NOTICE

The quality of this microform is heavily dependent upon the quality of the original thesis submitted for microfilming. Every effort has been made to ensure the highest quality of reproduction possible.

If pages are missing, contact the university which granted the degree.

Some pages may have indistinct print especially if the original pages were typed with a poor typewriter ribbon or if the university sent us an inferior photocopy.

Reproduction in full or in part of this microform is governed by the Canadian Copyright Act, R.S.C. 1970, c. C-30, and subsequent amendments.

AVIS

La qualité de cette microforme dépend grandement de la qualité de la thèse soumise au microfilmage. Nous avons tout fait pour assurer une qualité supérieure de reproduction.

S'il manque des pages, veuillez communiquer avec l'université qui a conféré le grade.

La qualité d'impression de certaines pages peut laisser à désirer, surtout si les pages originales ont été dactylographiées à l'aide d'un ruban usé ou si l'université nous a fait parvenir une photocopie de qualité inférieure.

La reproduction, même partielle, de cette microforme est soumise à la Loi canadienne sur le droit d'auteur, SRC 1970, c. C-30, et ses amendements subséquents.

Electron Paramagnetic Resonance Studies of Single Crystals of Mn^{2+}-doped $(NH_4)_2SO_4$, Gd^{3+}-doped $NH_4Pr(SO_4)_2 \cdot 4H_2O$, VO^{2+}-doped $M(NH_4)_2(SO_4)_2 \cdot 6H_2O$ (M = Cd, Co, Fe, Mg, Zn) and $Mg(ND_4)_2(SO_4)_2 \cdot 6D_2O$, and Cu^{2+}-doped $MNa_2(SO_4)_2 \cdot 4H_2O$ (M = Co, Mg)

Jiansheng Sun

A Thesis
in
The Department
of
Physics

Presented in Partial Fulfillment of the Requirements
for the Degree of Doctor of Philosophy at
Concordia University
Montréal, Québec, Canada

March 1991

ISBN 0-315-64658-6

ABSTRACT

Electron Paramagnetic Resonance Studies of Single Crystals of Mn^{2+}-doped $(NH_4)_2SO_4$, Gd^{3+}-doped $NH_4Pr(SO_4)_2\cdot 4H_2O$, VO^{2+}-doped $M(NH_4)_2(SO_4)_2\cdot 6H_2O$ (M = Cd, Co, Fe, Mg, Zn) and $Mg(ND_4)_2(SO_4)_2\cdot 6D_2O$, and Cu^{2+}-doped $MNa_2(SO_4)_2\cdot 4H_2O$ (M = Co, Mg)

Jiansheng Sun, Ph.D.
Concordia University, 1991

Detailed X-band electron paramagnetic resonance (EPR) measurements on single crystals of Mn^{2+}-doped $(NH_4)_2SO_4$, Gd^{3+}-doped $NH_4Pr(SO_4)_2\cdot 4H_2O$, VO^{2+}-doped $M(NH_4)_2(SO_4)_2\cdot 6H_2O$ (M = Cd, Co, Mg, Fe, Zn) and $Mg(ND_4)_2(SO_4)_2\cdot 6D_2O$, and Cu^{2+}-doped $MNa_2(SO_4)_2\cdot 4H_2O$ (M = Mg, Co) are made at variable temperatures. The spin-Hamiltonian parameters for Mn^{2+}, Gd^{3+}, VO^{2+} and Cu^{2+} ions are evaluated using a least-squares-fitting procedure. The positions and local symmetries of the impurity ions in these hosts have been well deduced.

The ferroelectric transition in $(NH_4)_2SO_4$ has been extensively studied via the splittings of Mn^{2+} EPR lines, leading to the determination of the critical exponent β. The existence of two inequivalent sublattices in the $(NH_4)_2SO_4$ crystal is confirmed.

Temperature variation of Gd^{3+} EPR spectra reveal two first-order phase transitions in the $NH_4Pr(SO_4)_2\cdot 4H_2O$ crystal. The host-ion spin-lattice relaxation (SLR) times

(τ) of Pr^{3+} have been estimated via the EPR linewidths of Gd^{3+} impurity ions using an appropriate expression. The predominant processes of SLR of Pr^{3+} host-ions have been deduced.

The superhyperfine structures of VO^{2+} EPR spectra in the hydrated Tutton-salt hosts $M(NH_4)_2(SO_4)_2 \cdot 6H_2O$ have been well explained by comparison with the VO^{2+} EPR spectra in the deuterated host crystal $Mg(ND_4)_2(SO_4)_2 \cdot 6D_2O$. Using the VO^{2+} EPR and optical-absorption spectra, the bonding coefficients of the $[VO(H_2O)_5]^{2+}$ complex have been estimated. The systematics of EPR of the VO^{2+} ion in this series of Tutton salts is analyzed.

The impurity-host exchange-interaction constant of VO^{2+}-Fe^{2+} pair is determined in the $Fe(NH_4)_2(SO_4)_2 \cdot 6H_2O$ host, using the g-shift due to the exchange interaction and the shape of the crystal at liquid-helium temperature. The τ values of Fe^{2+} and Co^{2+} in the $Fe(NH_4)_2(SO_4)_2 \cdot 6H_2O$ and $Co(NH_4)_2(SO_4)_2 \cdot 6H_2O$ hosts, respectively, have been estimated.

The symmetry of the $\tilde{g}$ matrix and temperature dependence of the $\tilde{g}$ principal values of Cu^{2+} in the $MNa_2(SO_4)_2 \cdot 4H_2O$ hosts have been explained by taking into account the pseudo-static Jahn-Teller effect (JTE) at room and lower temperatures, and dynamic JTE at higher temperatures, experienced by the $CuO_2(H_2O)_4$ complex.

ACKNOWLEDGMENTS

The author expresses his deep gratitude and sincere appreciation to Professor S. K. Misra for suggesting the research problems included in this thesis. Without Dr. Misra's continued availability and active guidance the completion of this thesis would not have been possible. Further, it was due to Dr. Misra's efforts that he was invited as an exchange student by Concordia University, thus providing him with the opportunity to pursue an advanced scientific study in Canada.

The author is grateful to Natural Sciences and Engineering Research Council of Canada for partial financial support (Dr. Misra's grant No. OGP0004485). He acknowledges the teaching assistantship received from the Physics Department, as well as the research fellowship from the Vice Rector (Academic) of Concordia University.

The author is thankful to the Center of Materials Analysis, Nanjing University, People's Republic of China to grant a leave of absence for him to study in Canada. He thanks Professors Zhai Hongru, Jin Tongzheng and Han Shiying at Nanjing University for their continued encouragement.

In concluding, the author wishes to extend his appreciation to his parents, his wife Yu, and his daughter Juemeng for their patience and continued encouragement throughout the progress of this thesis.

TABLE OF CONTENTS

GLOSSARY OF SYMBOLS ——— ix

I INTRODUCTION ——— 1

II SAMPLE PREPARATION AND CRYSTAL STRUCTURE ——— 10

II.1 Sample Preparation ——— 10

II.2 Crystal Structure ——— 16

III EXPERIMENTAL ARRANGEMENT AND DETAILS OF EPR SPECTRA ——— 24

III.1 Experimental Apparatus and General Features of EPR Spectra ——— 24

III.2 Mn^{2+}-doped $(NH_4)_2SO_4$ (AS) ——— 30

III.3 Gd^{3+}-doped $NH_4Pr(SO_4)_2 \cdot 4H_2O$ (APST) ——— 37

III.4 VO^{2+}-doped $M(NH_4)_2(SO_4)_2 \cdot 6H_2O$ (M = Cd, Mg, Zn, Fe, Co; referred to as CASH, MASH, ZASH, FASH, COASH) and $Mg(ND_4)_2(SO_4)_2 \cdot 6D_2O$ (MDSD) ——— 41

III.5 Cu^{2+}-doped $MNa_2(SO_4)_2 \cdot 4H_2O$ (M = Mg, Co; referred to as MNST, CNST) ——— 55

IV SPIN-HAMILTONIAN AND EVALUATION OF PARAMETERS ——— 61

IV.1 Evaluation of SHP by LST technique ——— 61

IV.2 Mn^{2+} in $(NH_4)_2SO_4$ ——— 66

IV.3 Gd^{3+} in $NH_4Pr(SO_4)_2 \cdot 4H_2O$ ——— 69

IV.4 VO^{2+} in $M(NH_4)_2(SO_4)_2 \cdot 6H_2O$ (M = Cd, Mg, Zn, Fe, Co) and $Mg(ND_4)_2(SO_4)_2 \cdot 6D_2O$ ——— 72

IV.5 Cu^{2+} in $MNa_2(SO_4)_2 \cdot 4H_2O$ (M = Mg, Co) ——— 82

V POSITION AND LOCAL SYMMETRY OF IMPURITY IONS ——— 86

V.1 Mn^{2+} in $(NH_4)_2SO_4$, Two Inequivalent Sublattices ——— 86

V.2 Gd^{3+} in $NH_4Pr(SO_4)_2 \cdot 4H_2O$, A Superposition-model

Calculation ——— 88

V.3 VO^{2+} in $M(NH_4)_2(SO_4)_2 \cdot 6H_2O$ (M = Cd, Mg, Zn, Fe, Co), $[VO(H_2O)_5]^{2+}$-complex Model ——— 93

V.4 Cu^{2+} in $MNa_2(SO_4)_2 \cdot 4H_2O$ (M = Mg, Co), Jahn-Teller Distortion ——— 95

VI PHASE TRANSITIONS ——— 97

VI.1 Ferroelectric Phase Transition in $(NH_4)_2SO_4$ ——— 97

VI.2 First-order Structural Phase Transitions in $NH_4Pr(SO_4)_2 \cdot 4H_2O$ ——— 107

VII SUPERHYPERFINE INTERACTION ——— 113

VII.1 Principal Values and Axes of SHF Interaction Tensor ——— 113

VII.2 Origin of SHF Interaction in VO^{2+}-doped $M(NH_4)_2(SO_4)_2 \cdot 6H_2O$ (M = Cd, Mg, Zn, Fe, Co) ——— 116

VII.3 Density of Unpaired Electron of VO^{2+} at Ligand Proton Sites ——— 119

VIII HOST-IMPURITY EXCHANGE INTERACTION ——— 121

VIII.1 g-shift and Shape Effect ——— 121

VIII.2 g-shift and Exchange Interaction ——— 122

VIII.3 Estimation of Exchange Constant of VO^{2+}-Fe^{2+} in $Fe(NH_4)_2(SO_4)_2 \cdot 6H_2O$ ——— 124

IX HOST-ION SPIN-LATTICE RELAXATION TIME (τ) ——— 126

IX.1 Theoretical Expression for τ ——— 126

IX.2 Pr^{3+} in $NH_4Pr(SO_4)_2 \cdot 4H_2O$ ——— 127

IX.3 Fe^{2+} in $Fe(NH_4)_2(SO_4)_2 \cdot 6H_2O$ ——— 137

IX.4 Co^{2+} in $Co(NH_4)_2(SO_4)_2 \cdot 6H_2O$ ——— 139

IX.5 Co^{2+} in $CoNa_2(SO_4)_2 \cdot 4H_2O$ ——— 140

X JAHN-TELLER EFFECT ——— 142

X.1 Ground State of Cu^{2+} in $MNa_2(SO_4)_2 \cdot 4H_2O$ (M = Mg, Co) ——— 142

X.2 Pseudo-static Jahn-Teller Effect ——— 143

X.3 Dynamic Jahn-Teller Effect ——— 145

X.4 Comparison of Cu^{2+} EPR Spectra of $MNa_2(SO_4)_2 \cdot 4H_2O$ (M = Mg, Co) ——— 147

XI OPTICAL ABSORPTION AND BONDING COEFFICIENTS ——— 148

XII SYSTEMATICS OF VO^{2+} EPR SPECTRA IN $M(NH_4)_2(SO_4)_2 \cdot 6H_2O$ (M = Cd, Mg, Zn, Fe, Co) ——— 155

XIII CONCLUSIONS ——— 159

XIII.1 Mn^{2+}-doped $(NH_4)_2SO_4$ ——— 159

XIII.2 Gd^{3+}-doped $NH_4Pr(SO_4)_2 \cdot 4H_2O$ ——— 160

XIII.3 VO^{2+}-doped $M(NH_4)_2(SO_4)_2 \cdot 6H_2O$ (M = Cd, Mg, Zn, Fe, Co) and $Mg(ND_4)_2(SO_4)_2 \cdot 6D_2O$ ——— 161

XIII.4 Cu^{2+}-doped $MNa_2(SO_4)_2 \cdot 4H_2O$ (M = Mg, Co) ——— 164

REFERENCES ——— 166

APPENDIX I PUBLICATIONS ——— 176

APPENDIX II COMPUTER PROGRAMS ——— 231

GLOSSARY OF SYMBOLS

$\tilde{A}$:	Hyperfine interaction matrix
$\tilde{A}^{L}$:	Superhyperfine interaction matrix
ACST:	$NH_4Ce(SO_4)_2 \cdot 4H_2O$
ALST:	$NH_4La(SO_4)_2 \cdot 4H_2O$
ANST:	$NH_4Nd(SO_4)_2 \cdot 4H_2O$
APST:	$NH_4Pr(SO_4)_2 \cdot 4H_2O$
ASST:	$NH_4Sm(SO_4)_2 \cdot 4H_2O$
AS:	$(NH_4)_2SO_4$
$\vec{B}$:	External magnetic field
b_{ℓ}^{m}:	Fine-structure spin-Hamiltonian parameter
CASH:	$Cd(NH_4)_2(SO_4)_2 \cdot 6H_2O$
COASH:	$Co(NH_4)_2(SO_4)_2 \cdot 6H_2O$
CNST:	$CoNa_2(SO_4)_2 \cdot 4H_2O$
EPR:	Electron paramagnetic resonance
FASH:	$Fe(NH_4)_2(SO_4)_2 \cdot 6H_2O$
f_s:	Density of unpaired electron at site of ligand protons
hf	Hyperfine
$\vec{I}$:	Nuclear spin vector
$\vec{I}_L$:	Total spin vector of the ligand protons
J_p:	Impurity-host pair-exchange constant
JTE:	Jahn-Teller Effect
LHT:	Liquid-helium temperature
LNT:	Liquid-nitrogen temperature

LSF:	Least-squares fitting
MASH:	$Mg(NH_4)_2(SO_4)_2 \cdot 6H_2O$
MDSD:	$Mg(ND_4)_2(SO_4)_2 \cdot 6D_2O$
MNST:	$MgNa_2(SO_4)_2 \cdot 4H_2O$
NASH:	$Ni(NH_4)_2(SO_4)_2 \cdot 6H_2O$
RT:	Room temperature
$\vec{S}$:	Electronic spin vector
S.H.	Spin Hamiltonian
SHF:	Superhyperfine
SHP:	Spin-Hamiltonian parameters
T_c:	Phase-transition temperature
ZASH:	$Zn(NH_4)_2(SO_4)_2 \cdot 6H_2O$
ZNST:	$ZnNa_2(SO_4)_2 \cdot 4H_2O$
β:	Critical exponent
β_1^2:	σ-bonding parameter
γ^2:	π-bonding parameter
ΔB:	EPR linewidth
ΔE:	Energy difference between the pairs of energy levels participating in resonance
$<\Delta\nu^2>$:	Second moment related the EPR linewidth
λ:	Spin-orbit coupling constant
μ_B:	Bohr magneton
ν:	Klystron frequency
$\mathcal{H}$:	Spin-Hamiltonian
τ:	Host-ion spin-lattice relaxation time

CHAPTER I

INTRODUCTION

Electron paramagnetic resonance (EPR) spectra of the transition-metal and rare-earth impurity ions, doped into various host lattices, have been widely studied in order to understand the electronic structures and other related physical properties of these compounds [1, 2, 3]. The X-band EPR data considered in the present thesis, have been obtained on Mn^{2+}-doped $(NH_4)_2SO_4$ (AS, hereafter) [4], Gd^{3+}-doped $NH_4Pr(SO_4)_2 \cdot 4H_2O$ (APST, hereafter) [5, 6], VO^{2+}-doped Tutton salts $M(NH_4)_2(SO_4)_2 \cdot 6H_2O$ (M = Cd, Mg, Zn, Fe and Co; hereafter referred to as CASH, MASH, ZASH, FASH and COASH, respectively) [7, 8, 9, 10], $Mg(ND_4)_2(SO_4)_2 \cdot 6D_2O$ (MDSD, hereafter) and Cu^{2+}-doped $MNa_2(SO_4)_2 \cdot 4H_2O$ (M = Mg, Co; referred to as MNST and CNST, respectively) single crystals at room, below-room and above-room temperatures. These results have been exploited in this thesis to: (i) study the structural and ferroelectric phase transitions; (ii) estimate spin-Hamiltonian parameters (SHP), including the fine-structure parameters, hyperfine (hf) interaction and ligand-superhyperfine (SHF) interaction tensors of the impurity ion in the various crystals investigated; (iii) determine the impurity-host exchange-interaction constants in host crystals consisting of paramagnetic ions; (iv) estimate the host-ion spin-lattice relaxation times (τ) in

the paramagnetic host crystals; and (v) study Jahn-Teller effect (JTE) in MNST and CNST.

The temperature variation of EPR spectra can be easily used for a study of the phase transitions undergone by the host crystal. Since EPR is a microscopic probe of the local environment around a specific ion, it provides considerable insight into the nature of the phase transition, as well as the structural character of the various phases [11, 12]. Mn^{2+} and Gd^{3+} ions are very effective EPR probes of the environment around them. Since their electronic spins S = 5/2 and 7/2, being greater than 1/2, they monitor the crystalline field directly via the SHP b_ℓ^m. Both the Gd^{3+} and Mn^{2+} can be doped into host lattices easily, and their EPR spectra can be readily observed at very low, as well as very high, temperatures. The phase transitions in Mn^{2+}- and Gd^{3+}-doped crystals can be detected by the changes in the EPR linewidths and intensities, and the splittings of the EPR line positions [11, 12, 13, 14].

The vanadyl ion (VO^{2+}) is the most stable cation, among the few molecular paramagnetic transition-metal ions; it can exist in a variety of ligand-field environments. The VO^{2+} EPR spectrum is very sensitive to crystalline-field environment [15, 16]. SHF structure of the EPR spectra of VO^{2+}, due to the interaction of the unpaired electron of the vanadyl ion with its ligands, has been observed in a few single crystals [17, 18, 19, 20]. The SHF structure can be

used to determine the orientation of the bond axis of VO^{2+} ions in the unit cell; this is because the maximum SHF splitting occurs when the direction of the external magnetic field is parallel to the bond axis between the paramagnetic ions and the closest ligand ion [1]. The local symmetry of the VO^{2+} ion has been, generally, found to be rather high in the host crystals [20, 21]. The bonding coefficients of the $[VO(H_2O)_5]^{2+}$ complex have been related to the electronic energy levels of VO^{2+} ion, which can be calculated from the optical-absorption spectra, and to the principal values of the $\tilde{g}$ and $\tilde{A}$ matrices in the vanadyl complex, which can be evaluated from the EPR line positions, by the use of well-known theoretical models [22, 23, 24, 25, 26]. Thus, information on the nature of bonding of the central molecular ion VO^{2+} with its nearest-neighbors can be drawn from optical-absorption and EPR data.

When a paramagnetic impurity ion is introduced in a host lattice containing paramagnetic ions, it experiences a shift in its g value from that in an isostructural host containing diamagnetic ions at low temperatures due to the exchange interaction between the impurity and host paramagnetic ions [1], over and above that caused by the shape of the paramagnetic crystal [27]. Misra et al. [28, 29, 30, 31] estimated the Mn^{2+}-Ni^{2+}, Mn^{2+}-Fe^{2+}, Co^{2+}-Ni^{2+} and Gd^{3+}-Yb^{3+} exchange interaction constants from their EPR measurements. No report has, so far, been published on the

estimate of exchange interaction between the molecular paramagnetic impurity ion, VO^{2+}, and host paramagnetic ions, e.g., VO^{2+}-Fe^{2+} and VO^{2+}-Co^{2+} pairs, as estimated in the present study.

The impurity-ion EPR linewidths can be used to estimate spin-lattice relaxation times (τ) of the host paramagnetic ions [32]. However, in the literature, an incorrect expression has been used to estimate τ of host ions [32]. This expression published in the literature is applicable only to the systems containing a single paramagnetic species, because it disregards the important dipolar and exchange interactions between the impurity and paramagnetic host ions. Estimation of τ using this published expression has usually led to a longer value of τ, by up to three orders [6, 33]. Misra et al. [33] derived the correct expression for τ, valid for a typical EPR situation, where there are present two different kinds of magnetic ions in the system, e.g., VO^{2+} and Fe^{2+} in VO^{2+}-doped FASH lattice [9], VO^{2+} and Co^{2+} in VO^{2+}-doped COASH lattice [10], or Gd^{3+} and Pr^{3+} in Gd^{3+}-doped APST lattice [6].

The EPR technique has been extensively employed to study the JTE [1, 113, 114, 115]. Many observations of the JTE have been reported on Cu^{2+}-doped single crystal characterized by a relatively high-symmetry host site for the Cu^{2+} ion. JTE deals with complicated systems, which involve the phonons, and degenerate electronic ground

states, as well as internal strains of variable strength distributed over the crystal. When the kinetic energy of the ligand ions can be neglected, a static JTE is observed, otherwise a dynamic JTE manifests itself. The present EPR studies on Cu^{2+}-doped MNST and CNST crystals are made in the 113 - 398 K temperature range, making it possible to observe both the pseudo-static JTE and the dynamic JTE, in the MNST host consisting diamagnetic ions as well as in the CNST host consisting paramagnetic ions.

The AS crystal becomes ferroelectric below T_c (=223 K) [34]. Unusual ferroelectric properties, e.g. a low value of the Curie-Weiss constant [33] and a large spontaneous strain [36, 37], generate a great deal of interest in AS. Further, the AS crystal is ferroelastic, both in the paraelectric ($T > T_c$) and ferroelectric ($T < T_c$) phases [38]. Three kinds of ferroelastic domains in AS have been frequently observed [39]. In order to understand the transition mechanism responsible for the phase transition, many experimental techniques have been used to study AS [40, 41, 42, 43, 44]. Theoretically, different mechanisms have been invoked to explain the mechanism of the phase transition in AS [40, 45, 46, 47, 48, 49, 50]. Despite so many studies, the phase transition mechanism in AS still remains controversial. EPR studies, using many different paramagnetic ions, such as Mn^{2+}, Cu^{2+}, SeO_3^-, VO^{2+}, CrO_4^{3-}, CrO_4^{2-}, NH_3^+ [50, 51, 52, 53, 54, 55, 56, 57, 58, 59, 60, 61, 62], have been made to

understand the phase transition mechanism in AS. However, some of these studies have been confined to either temperatures above T_c, or both above and below T_c, but not systematically as a function of temperature in the range including T_c [51, 56, 60, 62]. Similar to the finding of the other techniques, a lot of controversy exists in the EPR results on AS as well; even different values of T_c have been reported [51, 52]. This thesis reports a much more detailed and systematic X-band EPR study on a Mn^{2+}-doped AS crystal in the 113 - 398 K temperature range. A detailed discussion of the dynamic behavior of the two different Mn^{2+} centers, which belong to two inequivalent sublattices, is provided [4].

The APST crystal belongs to the series of isostructural crystals of the double sulfates $NH_4R(SO_4)_2 \cdot 4H_2O$ (R = rare-earth, e.g., Ce, Nd, Sm, La; referred as ACST, ANST, ASST and ALST, respectively) [63], which are of analytical significance, because they can be used to separate the light and heavy lanthanides [64]. These crystals are interesting for EPR studies, since they exhibit a series of phase transitions below room-temperature (RT) [65, 66, 67, 68]. Infrared (IR) and differential scanning calorimetry (DSC) studies on these crystals have been reported [63, 67, 68]. As for APST, no EPR studies have so far been reported. IR and DSC measurements have revealed the two phase transitions in APST, occurring at about 230 K and

150 K [68]. This thesis reports an extensive X-band EPR study of a Gd^{3+}-doped APST crystal in the 4.2 - 410 K temperature range, with particular emphasis on the explanation of the values of SHP of Gd^{3+} in this crystal, as well as on the detection of the phase transitions experienced by the APST lattice [5]. The host-ion spin-lattices relaxation time (τ) of Pr^{3+} in APST lattice, is estimated presently using the correct expression [33], employing experimentally-observed Gd^{3+} impurity-ion EPR linewidths. The power-law temperature dependence of the values of τ for Pr^{3+} has been used to discern the spin-lattice relaxation processes governing the host Pr^{3+} ions in the APST lattice [6].

Tutton salts form an isostructural series of hydrated double sulfates which have been studied by many techniques [69, 70], because they are easily grown, and are interesting for many reasons. The previous studies of VO^{2+}-doped Tutton salts were usually confined to RT; as well, reported interpretation of experimental data have not been consistent with each other. The SHF splittings observed previously were deduced to be due to the interaction between the unpaired electron of VO^{2+} ion and the ligand protons; this has not been previously confirmed experimentally. To this end, deuterated sample MDSD, which does not have any protons has been presently investigated to confirm that the SHF interaction is, indeed, due to the protons. This thesis

reports detailed X-band EPR studies, in the 4.2 - 413 K temperature range, of VO^{2+}-doped Tutton salts, CASH, MASH, ZASH, FASH and COASH single crystals, respectively, estimating, among other things, ligand SHF interaction and the density of the unpaired electron at the site of ligand protons, impurity-host exchange interaction of VO^{2+}-Fe^{2+} pair, and host-ion spin-lattice relaxation times (τ) of Fe^{2+}, Co^{2+} ions. Using the EPR and optical-absorption data, recorded presently, the bonding coefficients of the $[VO(H_2O)_5]^{2+}$ complexes in this series of Tutton salts are estimated [7, 8, 9, 10]. After a careful comparison, the systematics of EPR in VO^{2+}-doped Tutton salts is presented [10].

MNST and CNST crystals belong to a family of hydrated double sulfates other than Tutton salts, known as astrakanites [116]. Unlike the case of Tutton salts, little mention has been made in the literature of the EPR of astrakanite family, although some papers have been published on the EPR studies of isostructural $ZnNa_2(SO_4)_2 \cdot 4H_2O$ (ZNST) crystal [117, 118, 119, 120, 121, 122]. No EPR work on MNST has been, so far, published. As for CNST, Jain et al. [123] estimated τ of host-ion Co^{2+}, from the EPR linewidth of impurity-ion Mn^{2+}, using an incorrect formula. This thesis reports detailed X-band EPR studies of Cu^{2+}-doped MNST and CNST crystals, in the 113 - 398 K temperature range with particular emphasis on the determination of ground state of

Cu^{2+} ion, the observation of Jahn-Teller effect and estimation of spin-lattice relaxation time (τ) of host-ion Co^{2+} in CNST from Cu^{2+} EPR linewidths.

The organization of this thesis is as follows. The descriptions of sample preparations and crystal structures are given in Chapter II. The experimental arrangement and details of the EPR spectra are described in chapter III. Chapter IV discusses the spin Hamiltonian (S.H.) and evaluation of SHP for the impurity ion in the various samples. The positions and local symmetries of impurity ions in the host lattices are discussed in Chapter V. The data and interpretation of phase transitions in AS and APST lattices; SHF interaction in the VO^{2+}-doped Tutton salts; host-impurity pair-exchange interaction of Fe^{2+}-VO^{2+} in FASH host; the host-ion spin-lattice relaxation times (τ) of Pr^{3+}, Fe^{2+} and Co^{2+}; and JTE in Cu^{2+}-doped MNST and CNST crystals are discussed in Chapters VI, VII, VIII, IX and X, respectively. The optical-absorption spectra, bonding coefficients of the $[VO(H_2O)_5]^{2+}$ complex and systematics of VO^{2+} EPR spectra in the series of Tutton salts $M(NH_4)_2(SO_4)_2 \cdot 6H_2O$ (M = Cd, Mg, Zn, Fe, Co) are described in Chapters XI and XII. The conclusions are given in Chapter XIII. The published papers, reporting the EPR studies included in this thesis, are provided in Appendix I. The computer programs used to evaluate SHP are listed in Appendix II.

CHAPTER II

SAMPLE PREPARATION AND CRYSTAL STRUCTURE

II.1 Sample Preparation

II.1.1 Mn^{2+}-doped $(NH_4)_2SO_4$ (AS)

The crystals of AS, used for the present EPR measurements, were grown by slow evaporation, at room temperature (RT), of an aqueous solution of $(NH_4)_2SO_4$, to which 0.5 at. % of $MnSO_4$ was added. Good-quality crystals with dimensions suitable for measurements, about 3x2x8 mm^3, were obtained after about eight weeks. It was found that Mn^{2+} does not enter the crystal lattice of AS in large amounts. Thus the actual amount of Mn^{2+} in AS crystals is much less than that present in the mother liquor. The crystals so obtained were colorless, had excellent cleavage in the (100) plane, and were almost ferroelastically monodomain, as verified under a polarizing microscope. The growth habit of AS crystals is shown in Fig. 2.1.

II.1.2 Gd^{3+}-doped $NH_4Pr(SO_4)_2 \cdot 4H_2O$ (APST)

APST crystals, doped with Gd^{3+}, were grown by slow evaporation at RT, of an aqueous solution, containing $Pr_2(SO_4)_3 \cdot 8H_2O$ and $(NH_4)_2SO_4$ mixed in the molar ratio of 1:4, to which a small quantity of $Gd_2(SO_4)_3 \cdot 8H_2O$ powder was added, so that there was one Gd^{3+} ion for every 100 Pr^{3+} ions in the solution. An amount greater than the

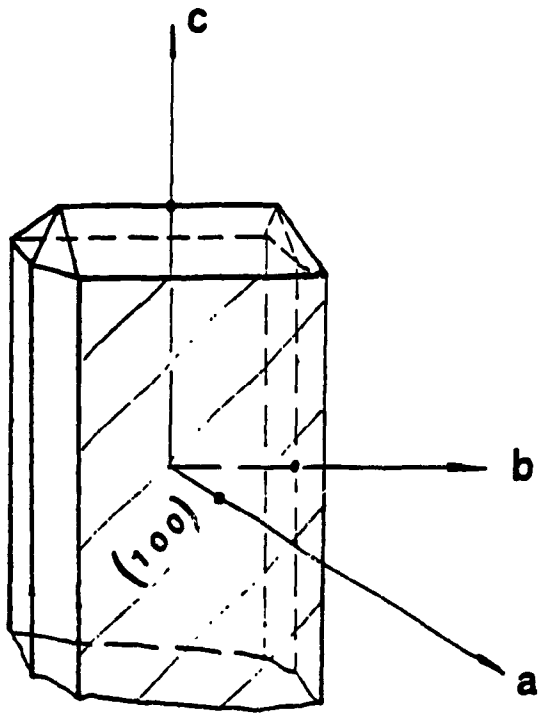

Fig. 2.1 The growth habit and crystallographic axes a, b and c of AS single crystal. The (100) plane, which exhibits a perfect cleavage, is shaded by oblique lines.

stoichiometric amount of $(NH_4)_2SO_4$ was used, since it has a strong tendency to creep out of the container [66, 67]. Also, a few drops of sulfuric acid (H_2SO_4) were added to the solution in order to prevent hydrolysis. Prismatic crystals, with green characteristic color of the Pr^{3+} ions, were obtained in about three weeks; one of approximate size 3.0x2.0x1.0 mm^3 was chosen for the present measurements. The crystals were stored in oil to avoid dehydration. So far, no information about the crystal-growth habit for APST is available.

II.1.3 VO^{2+}-doped $M(NH_4)_2(SO_4)_2 \cdot 6H_2O$ (M = Cd, Mg, Zn, Fe, Co; referred to as CASH, MASH, ZASH, FASH, COASH) and $Mg(ND_4)_2(SO_4)_2 \cdot 6D_2O$ (MDSD)

Single crystals of CASH, MASH, ZASH, FASH and COASH, doped with VO^{2+}, were grown at RT by slow evaporation from saturated aqueous solutions, containing stoichiometric amounts of MSO_4 (M = Cd, Mg, Zn, Fe, Co) and $(NH_4)_2SO_4$, to which a small quantity of $VOSO_4 \cdot 2H_2O$ powder was added, so that there was one VO^{2+} ion for every 100 M^{2+} (M = Cd, Mg, Zn, Fe, Co) ions in the solutions. VO^{2+}-doped $Mg(ND_4)_2(SO_4)_2 \cdot 6D_2O$ (MDSD) crystals were grown, using the same technique, from the saturated heavy-water solution, containing stoichiometric amounts of $MgSO_4$ and $(ND_4)_2SO_4$. Crystals, suitable for EPR measurements, grew in about two weeks; those of approximate size 3.0x2.5x1.0 mm^3 were chosen

for the present measurements. CASH crystals were stored in oil to avoid dehydration.

The crystals of CASH, MASH, ZASH, FASH, COASH and MDSD have the same growth habits. Fig. 2.2 shows the crystal-growth habit of CASH. Since the (010) plane of the CASH crystals is well developed in the form of a rectangular flat surface, the b axis is easy to identify (b is perpendicular to the (010) plane, which contains the a^* and c axes) [29]. For other crystals, b can be identified similarly [7, 8, 9, 10].

II.1.4 Cu^{2+}-doped $MNa_2(SO_4)_2 \cdot 4H_2O$ (M = Mg, Co; referred to as MNST and CNST)

Single crystals of MNST and CNST, doped with Cu^{2+}, were grown at RT by slow evaporation from saturated aqueous solutions, containing stoichiometric amounts of $MgSO_4 \cdot 7H_2O$ and $CoSO_4 \cdot 7H_2O$, respectively, and Na_2SO_4, to which a small quantity of $CuSO_4 \cdot 5H_2O$ powder was added, so that there was one Cu^{2+} ion for every 100 M^{2+} (M = Mg, Co) ions in the solutions. Crystals, suitable for EPR measurements, grew in about four weeks; those of approximate size 3.0x2.0x2.0 mm^3 were chosen for the present measurements. The growth habit of MNST and CNST is shown in Fig. 2.3. These crystals were stored in oil to prevent dehydration.

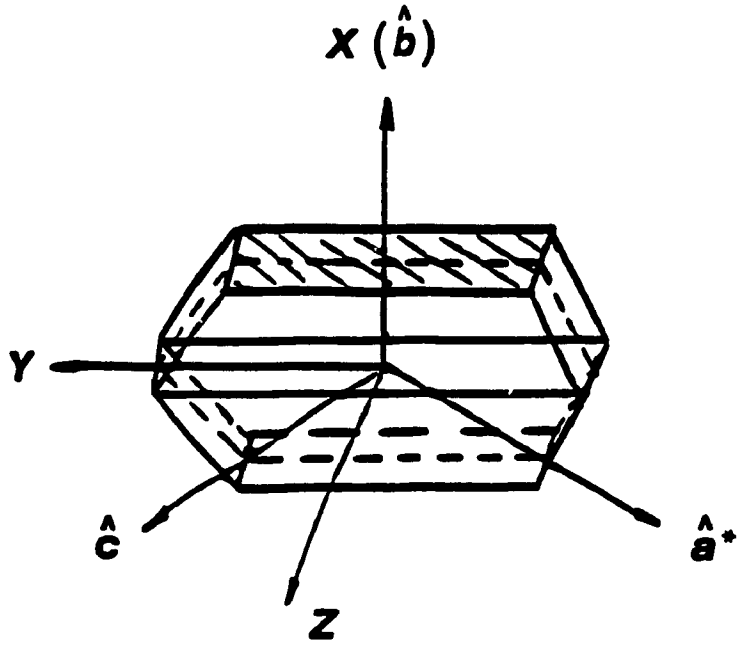

Fig. 2.2 Crystal-growth habit of CASH single crystal used for the present EPR measurements. The orientations of the laboratory axes X, Y and Z with respect to the crystal faces have been indicated. The (010) plane bas been shaded.

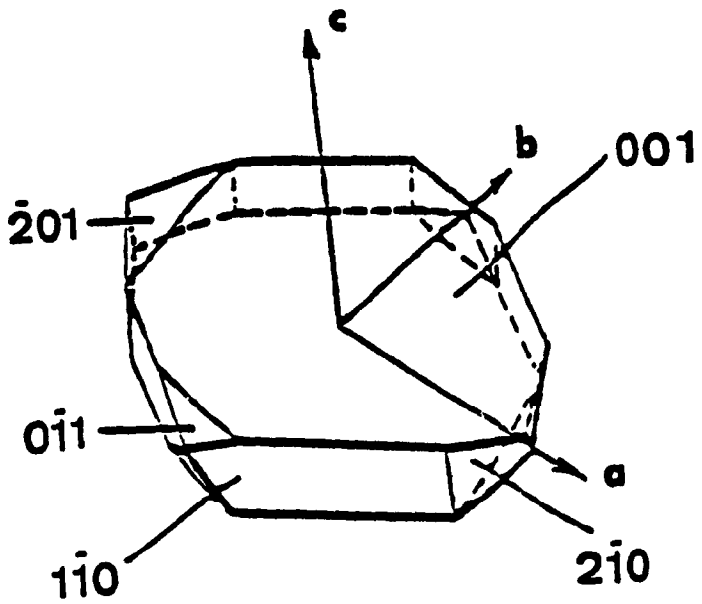

Fig. 2.3 The growth habit of MNST and CNST crystals [119].

II.2 Crystal Structure

II.2.1 $(NH_4)_2SO_4$

The crystal structure of AS is the same as that of K_2SO_4 [41]. At RT, the crystal possesses orthorhombic symmetry (space group P_{nam}), with the unit cell parameters: a = 0.7782 nm, b = 1.064 nm, c = 0.5993 nm [41]. (Some AS crystals show a superstructure at RT, characterized by the b and c dimensions doubled [71].) Below T_c, the reflection planes of AS crystal disappear, the space group changing to $P_{na2'}$ while the crystal still possesses orthorhombic symmetry; the c-axis becomes the axis of electric polarization. The unit cell parameters of AS below T_c are: a = 0.7837 nm, b = 1.061 nm, c = 0.5967 nm [41].

At RT, the unit cell of AS contains four formula units (Z = 4). There are present two crystallographically different NH_4^+(I) and NH_4^+(II) ions. NH_4^+(I) ions, with five SO_4^{2-} ions surrounding them, are designated as α ammonium ions; while NH_4^+(II) ions, located in the middle of a distorted octahedra of SO_4^{2-} ions, are designated as β ammonium ions. The directions of the two NH_4^+(I)-NH_4^+(II) (α-β) pairs make the following angles, relative to the crystallographic axes: $(\hat{a},\hat{Z}) = \pm 71.2^0$, $(\hat{b},\hat{Z}) = \pm 55.5^0$, $(\hat{c},\hat{Z}) = \pm 40.5^0$ [51]. These directions are found to be almost coincident with the magnetic Z axes corresponding to the two Mn^{2+} centers, as seen in Chap. III below.

II.2.2 $NH_4Pr(SO_4)_2 \cdot 4H_2O$

At RT, an APST crystal is monoclinic, characterized by the space group C_{2h}^5, containing four formula units per unit cell [63]; the unit-cell parameters are: a = 0.6444 nm, b = 1.8963 nm, c = 0.8798 nm and $\beta = 97.18^0$. The Pr^{3+} ion is coordinated to nine oxygen ions as shown in Fig. 2.4a, of which six belong to sulfate ions and three to three water molecules. The fourth water molecule is held between the sulfate layers by hydrogen bonding. The polyhedron of the nine-coordinated oxygens can be considered to be equivalent to a distorted monocapped square antiprism (C_2 or approximately "C_{4v}" site symmetry). In the absence of reported experimental data for the positions of the four Pr^{3+} ions in the unit cell, the Pr^{3+} positions have been presently deduced, using the information provided in the literature [63], to be (0.5, 0.1321, 0.0), (0.5, 0.3677, 0.5), (0.5, 0.6323, 0.5), and (0.5, 0.8678, 0.0) [5], labelled as 1, 2, 3, and 4, respectively, as depicted in Fig. 2.4b. The Pr^{3+} ions 1 and 2 belong to a pair, having parallel orientations of the respective C_{4v} axes, which is the Pr^{3+}-O(4) bond axis, making angles of about (51^0, 45^0, 72^0) relative to the (a, b, c) axes. The pair of ions 1, 2 is symmetrically related to the other pair (ions 3, 4) by the ac inversion plane. No crystal-structure data have been reported for the phases different from the RT phase.

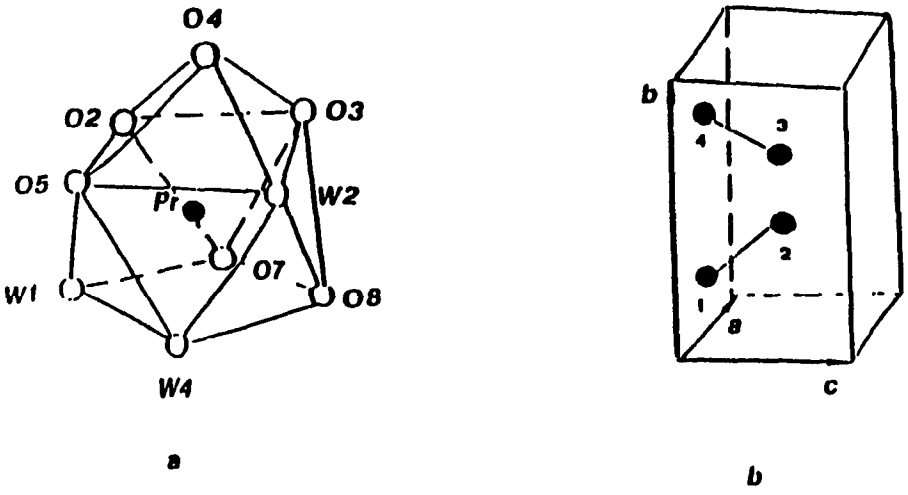

Fig. 2.4 Crystal structure of APST at RT. (a) The coordination polyhedron about a Pr^{3+} ion for APST: a monocapped square anti-prism. Wn indicates an oxygen ion belonging to a water molecule, while On an oxygen ion belonging to a sulfate ion. Only the oxygen ions nearest to Pr^{3+} ion have been shown. (b) Positions of the four Pr^{3+} ions in the unit cell of APST.

II.2.3 $M(NH_4)_2(SO_4)_2 \cdot 6H_2O$ (M = Cd, Mg, Zn, Fe, Co) and $Mg(ND_4)_2(SO_4)_2 \cdot 6D_2O$

CASH, MASH, ZASH, FASH and COASH crystals, being Tutton salts, are characterized by monoclinic symmetry, with the space group $P2_1/a$ [69, 72, 73, 74]. The unit-cell dimensions are listed in Table 2.1. The unit cell of a Tutton salt contains two divalent metal ions, each of which is surrounded by six water molecules, forming closely an octahedron. The octahedron at the site (1/2, 1/2, 0) is derived from that at (0, 0, 0) by a translation to (1/2, 1/2, 0) followed by a reflection in the a^*c plane ($a^* = a \sin\beta$). The six water molecules surrounding a divalent metal ion are labelled, as seen in Fig. 2.5 for CASH as an example, as $H_2O(7)$, $H_2O(8)$ and $H_2O(9)$ in pairs, each H_2O of a pair has the same distance from the metal ion (M^{2+}). The distances for M-O(7), M-O(8) and M-O(9), for each Tutton-salt sample, are also listed in Table 2.1. For MDSD, the $H_2O(7)$, $H_2O(8)$ and $H_2O(9)$ molecules are replaced by $D_2O(7)$, $D_2O(8)$ and $D_2O(9)$ molecules, respectively, with the same unit-cell dimensions as those of MASH.

II.2.4 $MNa_2(SO_4)_2 \cdot 4H_2O$ (M = Mg, Co)

MNST and CNST crystals are isostructural to ZNST, which is known to be monoclinic with space group $P2_1/a$, containing two formula units per unit cell [116]. The

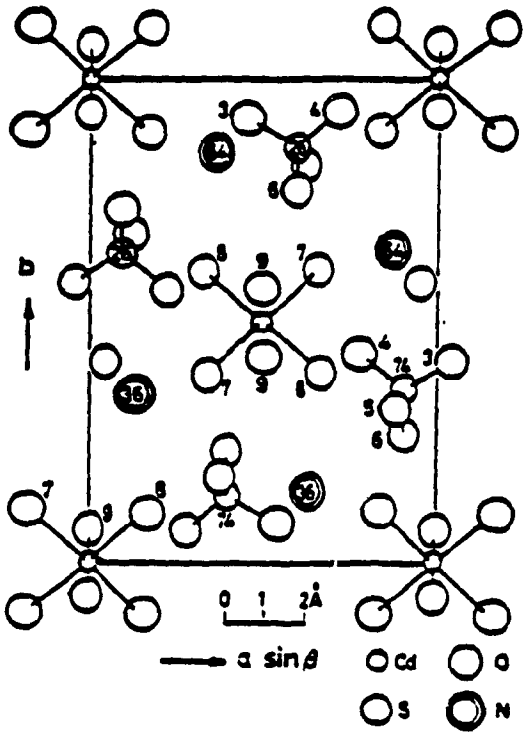

Fig. 2.5 The structure of CASH crystal as projected onto the the a*b plane [75].

Table 2.1 Unit-cell dimensions (nm) of $M(NH_4)_2(SO_4)_2 \cdot 6H_2O$ (M = Cd, Mg, Zn, Fe, Co) crystals and the distances (nm) of M-O(7), M-O(8) and M-O(9) for all crystals.

M	a	b	c	β	M-O(7)	M-O(8)	M-O(9)
Cd	0.943	1.282	0.629	106.87^{o}	0.2298	0.2297	0.2241
Mg	0.932	1.260	0.621	107.14^{o}	0.208	0.207	0.205
Zn	0.928	1.257	0.625	107.8^{o}	0.2138	0.2117	0.2066
Fe	0.932	1.265	0.624	106.8^{o}	0.216	0.214	0.209
Co	0.923	1.249	0.623	106.9^{o}	0.2107	0.2106	0.2070

unit-cell parameters for MNST are: a = 1.104 nm, b = 0.815 nm, c = 0.549 nm, β = 100.66^{0} [116], being not very different from those for $ZnNa_2(SO_4)_2 \cdot 4H_2O$ (ZNST). For CNST, the unit-cell parameters have not been reported, Vegard's law [90] has been used presently to determine these values. As seen from Fig. 2.6, an M^{2+} (M = Mg, Co) ion is surrounded by four oxygens lying approximately in a plane, of which two come from two water molecules [referred to as $H_2O(1)$] and the other two are contributed by the two sulfate groups [referred to as O(3)]. The M^{2+}-O^{2-} distance in the plane is about 0.202 nm. Perpendicular to this plane, the oxygens of the two water molecules [referred to as $H_2O(2)$] are coordinated to the M^{2+} ion at a distance about 0.224 nm. The symmetry of $MO_2(H_2O)_4$ complex, forming an elongated tetragonally-distorted octahedron, corresponds to the point group C_{4v} approximately. The positions of the two M^{2+} ions are at (0, 0, 0) and (1/2, 1/2, 0), similar to the case of Tutton salts.

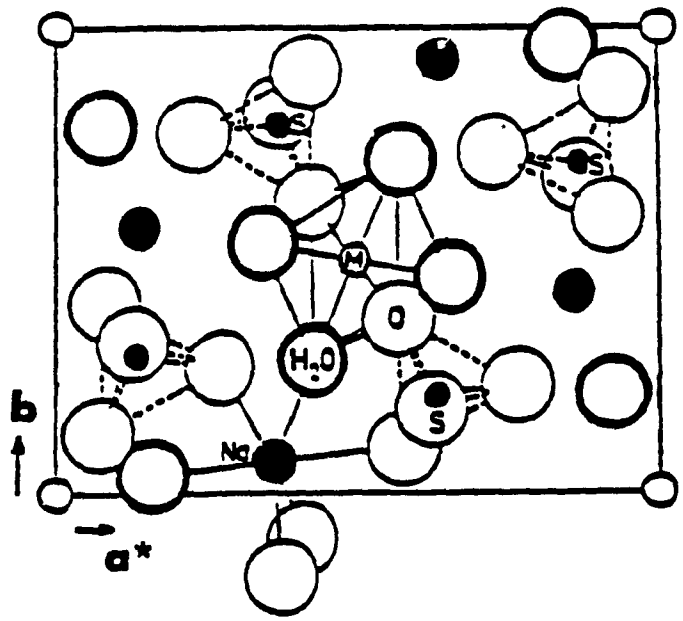

Fig. 2.6 The structure of MNST and CNST crystals as projected onto the the a^*b plane [118].

CHAPTER III

EXPERIMENTAL ARRANGEMENT AND DETAILS OF EPR SPECTRA

III.1 Experimental Apparatus and General Features of EPR Spectra

III.1.1 Experimental Apparatus

The EPR spectra were recorded on a reflection microwave cavity X-band Varian V4506 spectrometer, consisting of a 12-inch Varian low-impedance electromagnet (model no. V-3900), powered by a Bruker supply (model B-MN-50/200), and controlled by a Bruker field controller (B-H-15). The recorder of the EPR signal is a Graphtec X-Y plotter. A block diagram of the spectrometer is shown in Fig. 3.1. The description of the instrument and details of operation have been given in the instruction manual of the spectrometer. The following is a simplified discussion.

The klystron inside the microwave bridge (model V-4500-42) for X-band generates a microwave field at a frequency of about 9.5 GHz. This microwave power is fed to the resonant cavity. The microwave frequency is locked to the resonant frequency of the cavity, using an automatic frequency control (AFC) locking system. The microwave bridge is well adjusted for balance in the absence of electronic resonance absorption. When a resonance occurs, the electronic spins in the sample flip, reaching a higher energy state, and absorbing power from the cavity. This

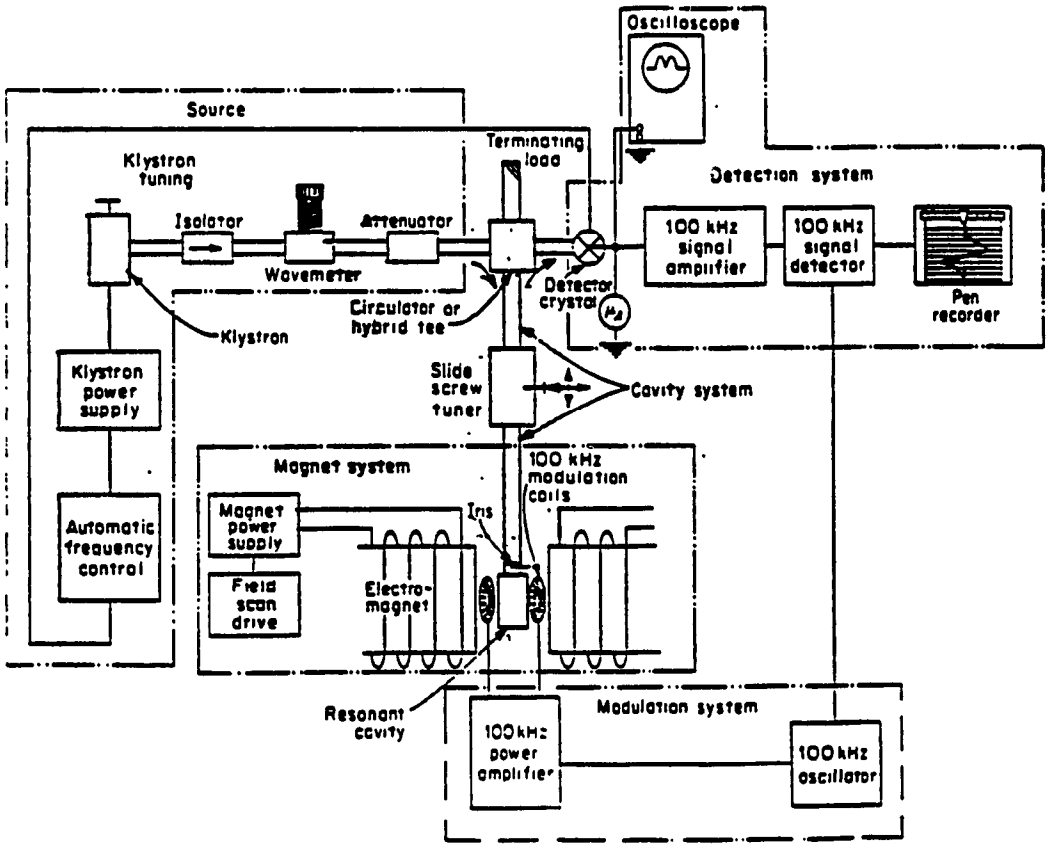

Fig. 3.1 Block diagram of the X-band EPR spectrometer.

energy change unbalances the microwave bridge, resulting in energy reaching the crystal detector. The d.c. magnetic field at the sample position is modulated with an a.c. field at a frequency of 100 kHz. The EPR signal reaching the crystal detector appears as an a.c. modulation on the power reflected from the cavity. This signal is then amplified and phase detected, and is applied to the graphic recorder for display. In more detail, the various important components of the spectrometer are described as follows.

EPR cavity. The crystal was placed inside a TE_{102}-type high Q-factor Varian cavity (model V-4531), which is a multipurpose cavity, so called because it can be used for fixed and variable temperature studies. It was designed for 100 kHz field modulation. The magnitude of the modulation field can be adjusted as required, the maximum value of peak-to-peak field modulation being 3.5 mT.

Klystron and X-band microwave bridge. The klystron, which is the source of microwave radiation, is supplied with resonator voltage by a Varian klystron power supply (model V-4500-20). The klystron was adjusted so that it operates in the mode corresponding to the highest power output. Besides the klystron, a microwave bridge contains the microwave distribution system and a crystal detector. Absorption of microwave power in the sample as a result of resonance unbalances the bridge. The unbalanced condition is detected by the crystal detector. The microwave frequency is measured

by a wavemeter consisting of a cylindrical resonant cavity, its length being adjustable by means of a micrometer.

Magnetic field and its measurement. The Bruker field controller (B-H-15) consists of a built-in microprocessor system to make it precise. It can be programmed for a specific field sweep within a desired period (sweep time). The resolution of controlling and measuring magnetic field is better than 0.01 mT. For higher accuracy, the magnetic field is measured using a Bruker NMR oscillator (model B-NM-20), with a resolution of 0.0001 mT. On the other hand, in all the EPR measurements presented in this thesis, a small amount of diphenyl picryl hydrazyl (DPPH) for which g = 2.0036 ± 0.0002 was used as a reference to check the accuracy of the resonant frequency and the magnetic-field values. The orientation of magnetic field with respect to the crystallographic axes of the sample can be changed, either by rotating the magnet around a vertical axis, or by rotating the sample itself around a vertical axis.

Signal detection system. A crystal detector is used in the EPR spectrometer to demodulate the microwave power which is transferred by a coaxial cable to a Varian lock-in amplifier (model V-4560). The resultant dc output from the lock-in amplifier was plotted on a Graphtec X-Y recorder (model Varian G-14A2). The EPR line position, as determined from the graph, had an accuracy of 0.05 mT.

Temperature Variation. Temperature, in the range of

113 - 420 K, was maintained at the sample by gently blowing nitrogen gas, passing respectively through the heater coils and coils immersed in liquid nitrogen, of a Varian temperature-controller unit (model E4540). The temperature stability was better than 0.5 K, as measured by an Omega Engineering Inc. microprocessor-based thermocouple meter (model 680), with a temperature resolution of 0.1 K. On the other hand, the temperatures, in the range of 4.2 - 120 K, were varied by the use of a heater resistor inside a commercial liquid-helium cryostat; the temperature was determined by measuring the resistances of the platinum and germanium resistors, using appropriate calibration charts, with a resolution of 0.5 K. In this case, a cavity with a lower Q value was used. As well, the modulation frequency was lower than that used at temperatures higher than 113 K, i.e., 400 Hz instead of 100 kHz was used.

Optical-absorption measurement. Optical-absorption spectrum was recorded on a Hewlett-Packard spectrometer (model 8452A) in the wavelength range 190 - 820 nm, i.e., from near ultra-violet to near infra-red. The size of crystals used for the optical measurements was the same as that for the EPR measurements. The absorption spectrum and the wavelengths of the absorbed peaks were recorded automatically via an IBM-XT microcomputer. All optical measurements were performed at room temperature.

III.1.2 General Features of EPR Spectra

In general, the number of observed EPR lines of a paramagnetic ion depend on (i) the electronic spin S and nuclear spin I (if the ion possesses a nucleus characterized by non-zero magnetic moment), and (ii) the number of magnetically inequivalent sites which the paramagnetic impurity ion can occupy in the host lattice.

Fine and Hyperfine Structure. For those impurity ions which have the electronic spin $S \geq 1/2$, the fine-structural EPR spectrum, having (2S) allowed lines, corresponding to the transitions $M \leftrightarrow M-1$, i.e., $\Delta M = \pm 1$ (M is the electronic magnetic quantum number), should be observed. Further, if their nuclear spin moment is not zero, a hyperfine (hf) EPR spectrum, in which each fine-structure line splits into (2I+1) allowed hf lines, corresponding to $m \leftrightarrow m$, i.e., $\Delta m = 0$ (m is the nuclear magnetic quantum number), is expected. Thus, a total of (2S) x (2I+1) hf EPR lines, corresponding to the transitions $M,m \leftrightarrow (M-1),m$, are observed. This thesis deals with single crystals doped with impurity ions Mn^{2+} ($S = 5/2$, $I = 5/2$), Gd^{3+} ($S = 7/2$, $I = 0$), VO^{2+} ($S = 1/2$, $I = 7/2$) and Cu^{2+} ($S = 1/2$, $I = 3/2$). The general features of the EPR spectrum for each of these impurity transition ions have been described at the beginning of each of following sections.

Physical and Magnetic Equivalences of Impurity Ions.

For the orientation of $\vec{B}$ in a general direction, one can observe more than one set of (2S) x (2I+1) EPR lines in a crystal, if there exist more than one magnetically inequivalent site which the impurity ion can occupy in the unit cell. Magnetically-inequivalent ions are those whose EPR spectra are distinguishable by the magnetic field. However, some of the sites may be physically equivalent, as well as magnetically equivalent, which means that the local surroundings of these impurity-ion sites are the same, thus they have the same EPR spectra for any orientation of $\vec{B}$. If there exist several physically-equivalent, but magnetically-inequivalent impurity-ion sites in the unit cell, the number of inequivalent sets of EPR lines can be reduced if one observes the EPR spectrum for $\vec{B}$ along a crystallographically-symmetric axis, or in a plane having an inversion symmetry in the unit cell of the crystal.

III.2 Mn^{2+}-doped $(NH_4)_2SO_4$

In general, for each of the magnetically-inequivalent Mn^{2+} ions (electronic spin S = 5/2, nuclear spin I = 5/2) in a host crystal, the EPR spectrum consists of five allowed sextets of hyperfine (hf) lines: $M,m \leftrightarrow (M-1),m$; where M and m are, respectively, the electronic and nuclear magnetic quantum numbers. Fig. 3.2 shows a typical Mn^{2+} EPR spectrum which corresponds to the highest-field fine-structure sextets $M = 5/2 \leftrightarrow 3/2$ for the two magnetically-inequivalent

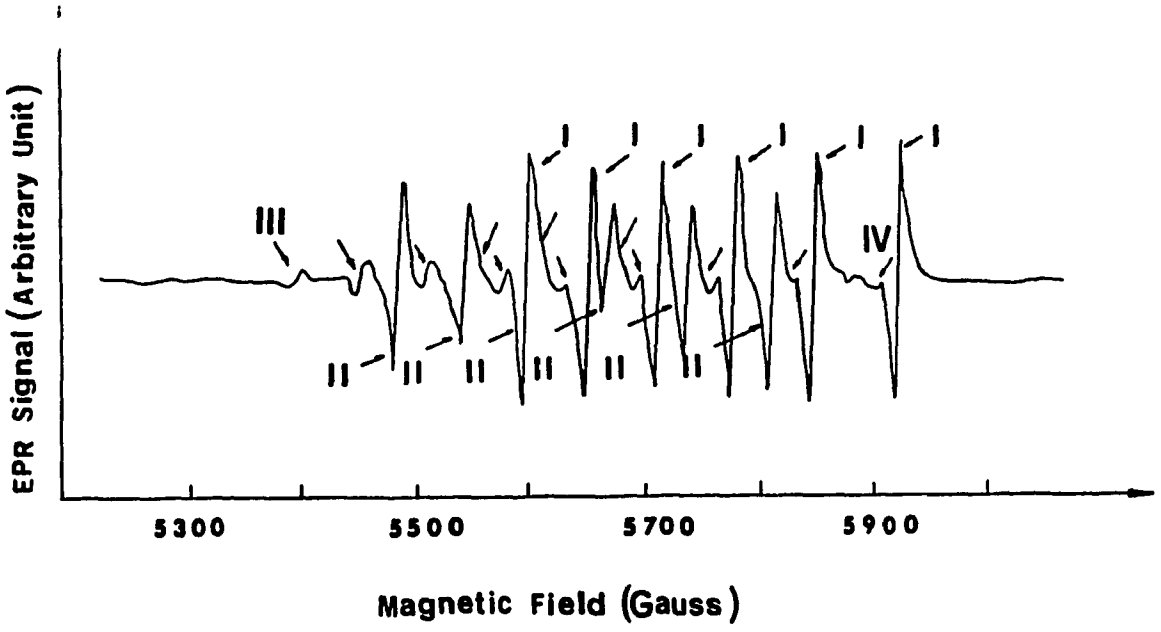

Fig. 3.2 EPR spectrum of Mn^{2+}-doped AS crystal for $\vec{B}$ in the ab plane, 23^{o} from the a-axis, showing the highest-field hf sextets (fine-structure transition 5/2 $\leftrightarrow$ 3/2), corresponding to the two Mn^{2+} centers (I and II) with almost the same intensity. There are also seen two weak centers (III and IV); these are due to other ferroelastic domains of relatively small volume.

Mn^{2+} ions in AS.

EPR spectra of Mn^{2+}-doped AS were recorded for the orientations of the external magnetic field ($\vec{B}$) in the ab, ac and bc planes. Fig. 3.2 exhibits the high-field EPR spectrum for the orientation of $\vec{B}$ in the ab plane, at 23^{o} from the a-axis; six strong hf lines of almost equal intensity, corresponding to the highest-field fine-structure sextets M = 5/2 $\leftrightarrow$ 3/2 for the two Mn^{2+} centers, designated as I and II, are clearly visible. The small difference in EPR line heights for Mn^{2+} centers I and II, as seen in Fig. 3.2, results from slightly larger linewidth of center II, as compared with that for center I (1.7 mT for center II and 1.4 mT for center I). This suggests somewhat bigger distortion of the surrounding of Mn^{2+} center II, as compared to that of center I. The almost equal intensities of the EPR lines corresponding to centers I and II imply that the occupation probabilities of the sites available to centers I and II are about the same. It is noted that, in addition, two other centers, of very weak intensity, designated as III and IV were observed; these are, most likely, due to additional ferroelastic domains of AS crystal, which were, however, not detected under a polarizing microscope, because of their negligible volume. (Centers III and IV have not, at all, been studied in the present thesis, because of their extremely weak intensities.)

Fig. 3.3 shows the angular variation of the high-field

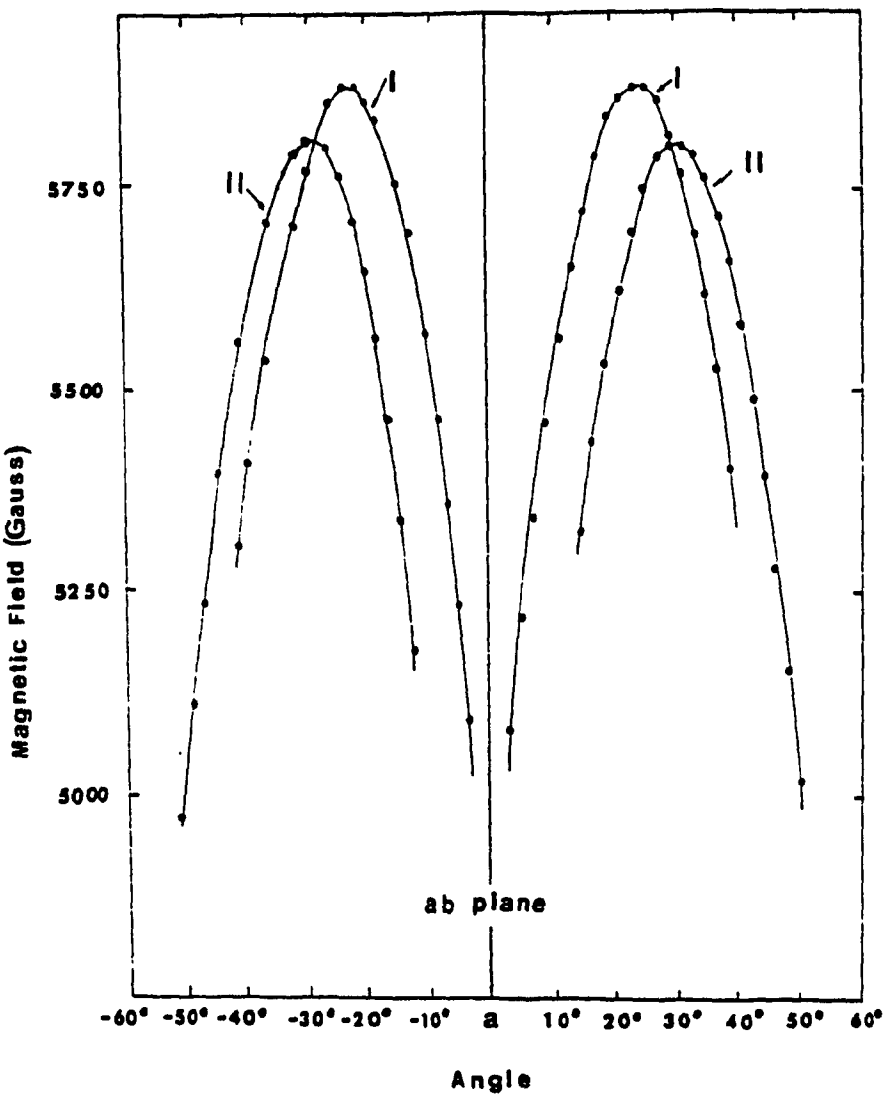

Fig. 3.3 Angular variation of the highest-field line of the highest-field hf sextet for Mn^{2+} centers I and II in Mn^{2+}-doped AS crystal at RT for the orientation of $\vec{B}$ in the ab plane. The continuous lines are smooth curves that connect data points.

EPR lines for centers I and II for the orientation of $\vec{B}$ in the ab plane. The lines corresponding to the two physically inequivalent Mn^{2+} centers (I and II) are clearly visible. This is possible because the principal axes and magnitudes of the zero-field splitting tensors b_2^m, corresponding to the two centers, are at definitive variance, albeit small, from each other.

Figs. 3.4 and 3.5 exhibit the angular variation of EPR spectra for the orientation of $\vec{B}$ in the bc and ac planes, respectively; they are found to be symmetric about the b and c axes, respectively, for the two centers, in accordance with the crystal symmetry. Figs. 3.4 and 3.5 confirm that there, indeed, exist two physically-inequivalent Mn^{2+} centers with almost the same intensity, but slightly different directions of the respective principal axes, and the values of the zero-field splitting tensors, b_2^m. These relative differences did not change much, upon increasing the temperature from RT to 398 K, except that the EPR line positions moved slightly towards higher magnetic fields for both the centers.

The orientations of the magnetic principal axes of the zero-field splitting tensor b_2^m, corresponding to centers I and II can be determined from the angular variation of spectra in the three mutually perpendicular planes. (The magnetic Z, X and Y axes of a Mn^{2+} complex are defined to be those directions of $\vec{B}$ for which the overall

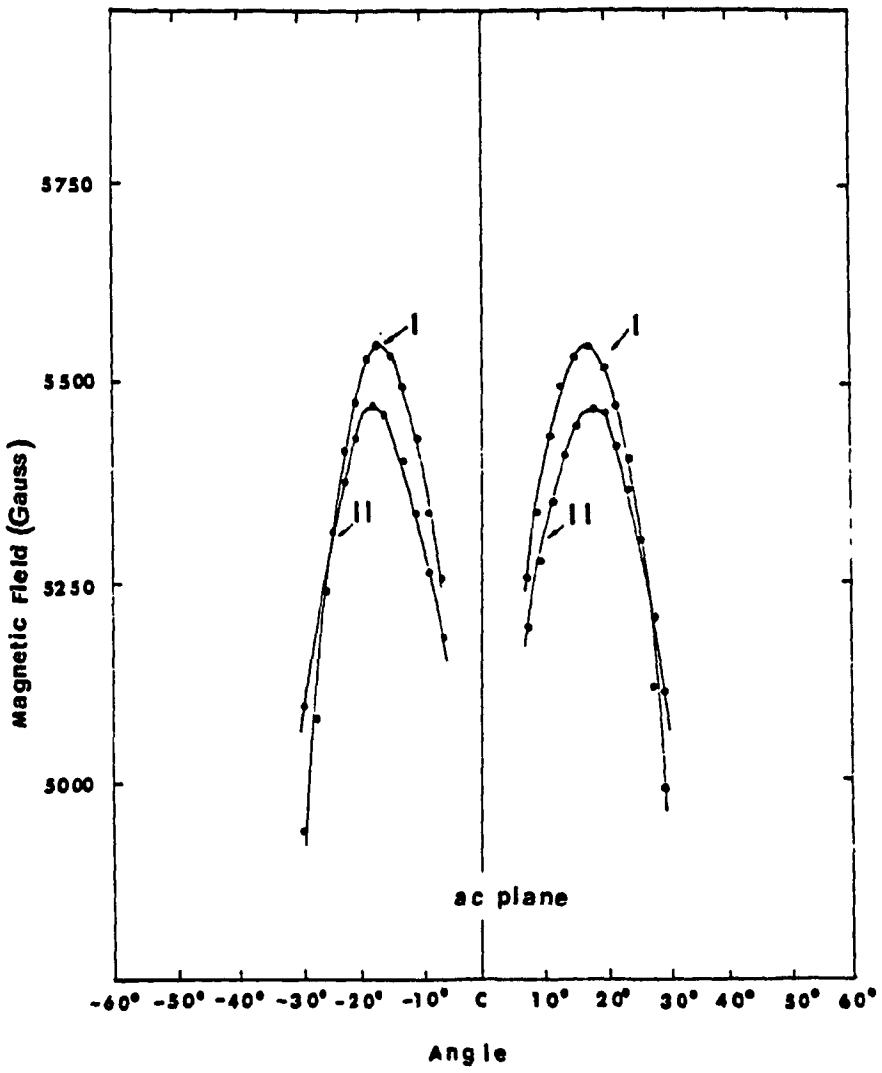

Fig. 3.4 Angular variation of the highest-field line of the highest-field hf sextet for Mn^{2+} centers I and II in Mn^{2+}-doped AS crystal at RT for the orientation of $\vec{B}$ in the ac plane. The continuous lines are smooth curves that connect data points arising out of the same transition.

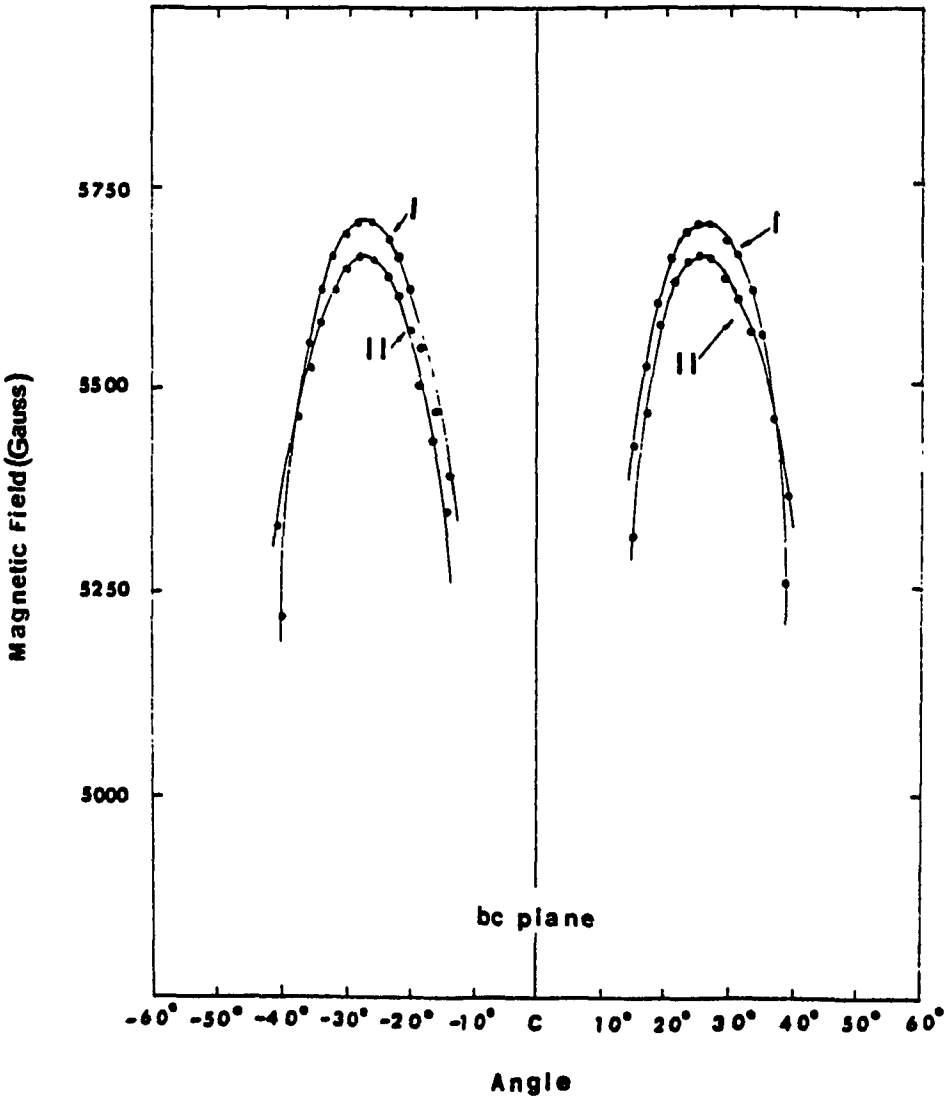

Fig. 3.5 Angular variation of the highest-field line of the highest-field hf sextet for Mn^{2+} centers I and II in Mn^{2+}-doped AS crystal at RT for the orientation of $\vec{B}$ in the bc plane. The continuous lines are smooth curves that connect data points arising out of the same transition.

separations of the allowed lines exhibit extrema; of these three, the overall separations occur in decreasing order for $\vec{B}$ along the Z, X and Y axes, respectively.) The results are as follows. Center I: $(\hat{Z},\hat{a}) = 75.6^0 \pm 0.5^0$, $(\hat{Z},\hat{b}) = 57.9^0 \pm 0.5^0$, $(\hat{Z},\hat{c}) = 35.9^0 \pm 0.5^0$. Center II: $(\hat{Z},\hat{a}) = 74.5^0 \pm 0.5^0$, $(\hat{Z},\hat{b}) = 62.8^0 \pm 0.5^0$, $(\hat{Z},\hat{c}) = 32.2^0 \pm 0.5^0$. Further, using the crystallographic data [51], it is found that the Z axis for center I is almost coincident with the direction of one of the two NH_4^+(I)-NH_4^+(II) pairs (within 5^0); while that for center II deviates slightly from this direction (about 9^0). The angle between the Z axes corresponding to Mn^{2+} centers I and II is about 6^0.

Unlike the previous findings [51, 52] of the presence of only one type of Mn^{2+} center in AS, two different types of Mn^{2+} centers have, indeed, been detected to exist simultaneously in the present studies; each of these two Mn^{2+} centers are characterized by EPR spectra which are symmetrical about c, b and a axes, for $\vec{B}$ in the ab, ac and bc planes respectively. (Figs. 3.3, 3.4 and 3.5.) (The term, "Mn^{2+} center", here, refers to a complex consisting of a Mn^{2+} ion with surrounding SO_4^{2-} groups and a nearest vacancy; see Chap. V for more details.)

III.3 Gd^{3+}-doped $NH_4Pr(SO_4)_2 \cdot 4H_2O$

It is expected that, for each of the magnetically-equivalent Gd^{3+} ions (electronic spin S = 7/2,

nuclear spin I = 0) in a host crystal, a set of seven allowed fine-structural EPR lines is observed. These lines correspond to $\Delta M = \pm 1$; here M is the electronic magnetic quantum number. Fig. 3.6 shows a typical Gd^{3+} EPR spectrum which corresponds to two sets of seven fine-structural lines for the two magnetically-inequivalent Gd^{3+} ion in APST.

EPR spectra of Gd^{3+}-doped APST were recorded at RT for the orientations of the external magnetic field ($\vec{B}$) in the principal ZX and ZY planes of the zero-field splitting tensor b_2^m of one of the magnetically inequivalent Gd^{3+} ions in the unit cell. [The principal axes (X, Y, Z) are defined in the same way as for Mn^{2+} in AS.] The spectra revealed the presence of two magnetically inequivalent Gd^{3+} ions. Each ion exhibited seven allowed transitions, corresponding to the electronic spin S = 7/2 of Gd^{3+}. The Gd^{3+} ions substitute with equal preference at the two magnetically inequivalent Pr^{3+} sites in the unit cell (Chap. II), because the intensities of the EPR spectra for $\vec{B}$ parallel to their respective $\vec{Z}$ axes are equal.

The EPR spectrum, for $\vec{B} \parallel \vec{Z}$ of one of the magnetically-inequivalent Gd^{3+} ions is shown in Fig. 3.6, while Figs. 3.7a and 3.7b exhibit the angular variations of the EPR lines for the same Gd^{3+} ion for $\vec{B}$ in its ZX and XY planes, respectively. The EPR linewidth for each of the two Gd^{3+} ions was found to be 5.3 ± 0.3 mT at RT. The four Pr^{3+} ions in the unit cell of APST, having the same nine-fold

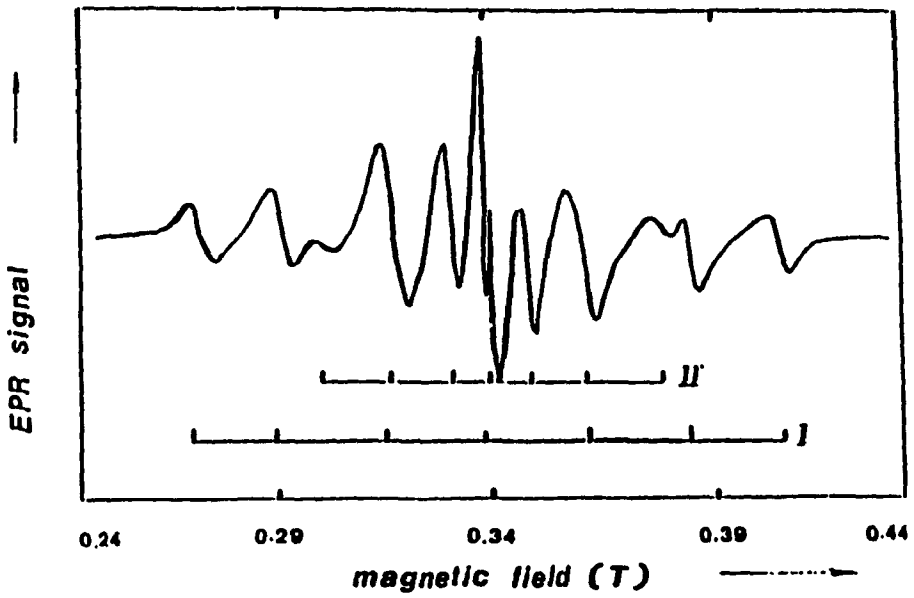

Fig. 3.6 EPR spectrum of Gd^{3+} in APST for $\vec{B} \parallel \vec{Z}$ for one of the magnetically-inequivalent Gd^{3+} ions (I), and $\vec{B} \parallel \vec{X}$ for the other magnetically-inequivalent Gd^{3+} ion (II) at RT.

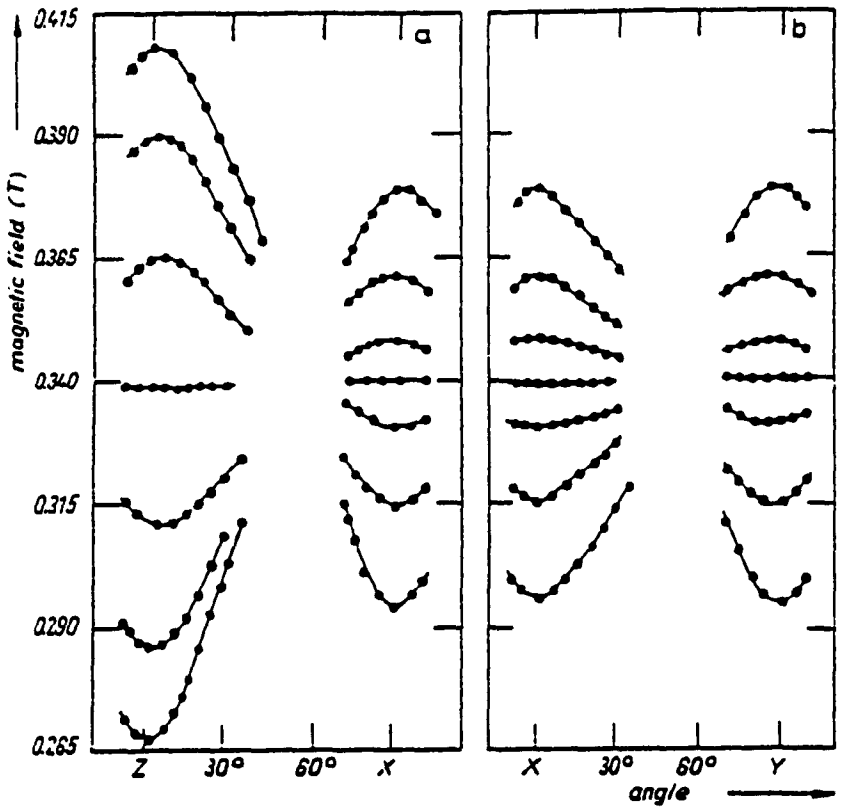

Fig. 3.7 Angular variation of EPR line positions for one of the magnetically-inequivalent Gd^{3+} ions at RT for (a) $\vec{B}$ in its ZX plane, and (b) for $\vec{B}$ in its XY plane.

coordinations with the ligand ions, were found to be physically equivalent, as revealed by the EPR spectra. For each of the two magnetically-inequivalent Gd^{3+} ions, the splittings for $\vec{B}$ along its X and Y axes were found to be about the same. The Z axis for one pair was found to be parallel to the X axis for the other pair, which is along one of the local C_{4v} axes (Chap. II), and vice versa; the Y axes for the two pairs, lying in the ac plane were observed to be parallel to each other, at 64^{0} from the a axis. Buckmaster et al. [65, 66, 67] also made the same observations in the isostructural ANST, ASST and ACST crystals. However, they did not relate the magnetic axes (Z, X, Y) to the crystal axes.

III.4 VO^{2+}-doped $M(NH_4)_2(SO_4)_2 \cdot 6H_2O$ (M = Cd, Mg, Zn, Fe, Co) and $Mg(ND_4)_2(SO_4)_2 \cdot 6D_2O$

In general, for each of the magnetically-inequivalent VO^{2+} ions in a host crystal, a set of eight VO^{2+} allowed hf EPR lines is expected. These correspond to $\Delta M = \pm 1$, $\Delta m = 0$; where M and m are, respectively, the electronic and nuclear magnetic quantum numbers; for VO^{2+} electronic spin S = 1/2 and nuclear spin I = 7/2. Fig. 3.8 shows a typical VO^{2+} EPR spectrum which corresponds to three sets of eight hf lines for the three magnetically-inequivalent VO^{2+} ions in FASH.

EPR spectra were recorded, for all the samples of VO^{2+}-doped CASH, MASH, ZASH, FASH and COASH single crystals,

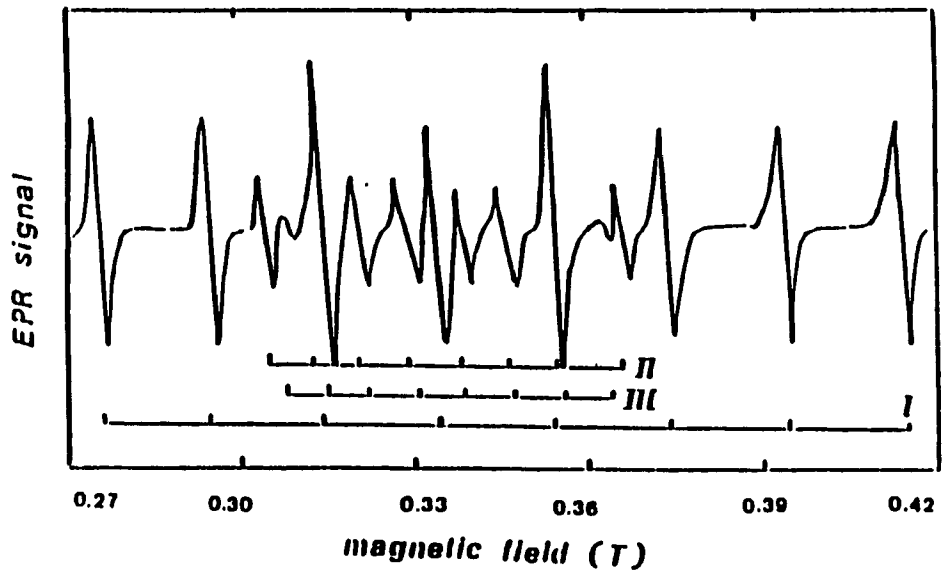

Fig. 3.8 RT VO^{2+} EPR spectrum in FASH, recorded for $\vec{B}$ in the ZY plane, at 25^0 from the Z axis. Due to inversion symmetry, the lines for each of the two physically-equivalent VO^{2+} pairs (I and II) merged into each other. The much weaker lines are due to the third pair of physically-equivalent VO^{2+} ion III.

at 295, 80 and 4.2 K (for COASH, at 295 K only) for the orientation of the Zeeman field, $\vec{B}$, in three mutually perpendicular planes, defined by the X, Y and Z axes. For CASH, the X axis was chosen to be parallel to the crystallographic b axis; the Y and Z axes were chosen to lie in the (010) plane of the crystal with Z axis perpendicular to the largest flat surface of the crystal, as exhibited in Fig. 2.2. Similar axis system was chosen for MASH, ZASH, FASH and COASH. EPR spectra were recorded by varying the orientation of the external magnetic field in each plane (ZX, ZY, XY) at every 5^0 interval. Similar measurements are made on the VO^{2+}-doped MDSD crystal.

III.4.1 Symmetry of VO^{2+} EPR Spectra

At a general orientations of $\vec{B}$, there were observed four intense distinct sets of eight VO^{2+} allowed hf lines each, at any temperature. These four sets of hf lines can be divided into two groups which can be obtained from each other by symmetry operations, i.e., these two groups are physically equivalent to each other. For $\vec{B}$ in the ZY plane, as well as for $\vec{B} \parallel \vec{X}$, two distinct sets of eight hf lines each were observed, consistent with the physical symmetry. Thus, there were present four magnetically-inequivalent, i.e., distinguishable by $\vec{B}$, VO^{2+} molecular ions, in the unit cell of CASH, MASH, ZASH, FASH and COASH, with intense EPR spectra for an arbitrary orientation of $\vec{B}$. These correspond

to two pairs of physically-equivalent VO^{2+} molecular ions in the unit cell, referred to as I and II. In addition, some weak lines were also observed, which were presumably due to a third possible pair of physically-equivalent VO^{2+} molecular ions, referred to as III, with different orientation of its axis, also occupying an M^{2+} (M = Cd, Mg, Zn, Fe, Co) site. In conclusion, each of the two M^{2+} sites in the unit cell of CASH, MASH, ZASH, FASH and COASH is occupied by VO^{2+} ions with three different orientations of their molecular axes. The group of the three VO^{2+} ions occupying an M^{2+} site is physically equivalent to that occupying the other M^{2+} site in the unit cell of CASH, MASH, ZASH, FASH and COASH. (For more details see Chap. V.) The lines corresponding to the third ion were not studied at all for CASH, MASH, FASH and COASH, due to their much weaker intensities. For ZASH, the EPR lines corresponding to ion III were only studied in so far as their SHF splitting is concerned. For all the samples, the ratios of intensities of the VO^{2+} EPR lines corresponding to ions I, II and III were found to be about 10:6:1; these are somewhat different from that reported previously [20, 75]. This can be explained as follows. According to the model of the $[VO(H_2O)_5]^{2+}$ complex (Chap.V), when the VO^{2+} ion replaces an M^{2+} ion, the V^{4+}-O^{2-} bonds orient themselves along the M^{2+}-$H_2O(7)$, M^{2+}-$H_2O(8)$, or M^{2+}-$H_2O(9)$ direction; these orientations are occupied with different populations, one of them being very small, while

the other two being in the ratio of about 2:1.

A typical EPR spectrum, for $\vec{B}$ in the ZY plane, showing the presence of the various kinds of VO^{2+} ions in FASH, is exhibited in Fig. 3.8. Intense spectra from two VO^{2+} ions (I and II) and one weak spectrum from another VO^{2+} ion (III) are clearly seen. The angular variation of the EPR spectra for $\vec{B}$ in the ZY plane for FASH at RT is displayed in Fig. 3.9. It is seen from Fig. 3.9 that the separations of the adjacent hf lines for ion I are almost equal to each other for $\vec{B} \parallel \hat{Y}$, which is close to the direction of the maximum hf splitting for ion I. They become more unequal, the farther the orientation of $\vec{B}$ deviates from the Y axis. VO^{2+} EPR spectra for ion II, for $\vec{B}$ in the ZY plane, exhibited the same features as those for ion I for $\vec{B}$ in the ZY plane except that the maximum hf splitting for ion II occurred for the orientation of $\vec{B}$ at 90^0 from that at which the maximum splitting of hf lines occurs for VO^{2+} ion I. Also, the greater is the separation of the adjacent hf lines the higher is the external magnetic field value at which they occur for both the ions. Angular variation of the EPR spectra recorded for the orientation of $\vec{B}$ in the ZX and XY planes also confirmed the existence of two intensive and one weak physically-equivalent pairs VO^{2+} ions for each site.

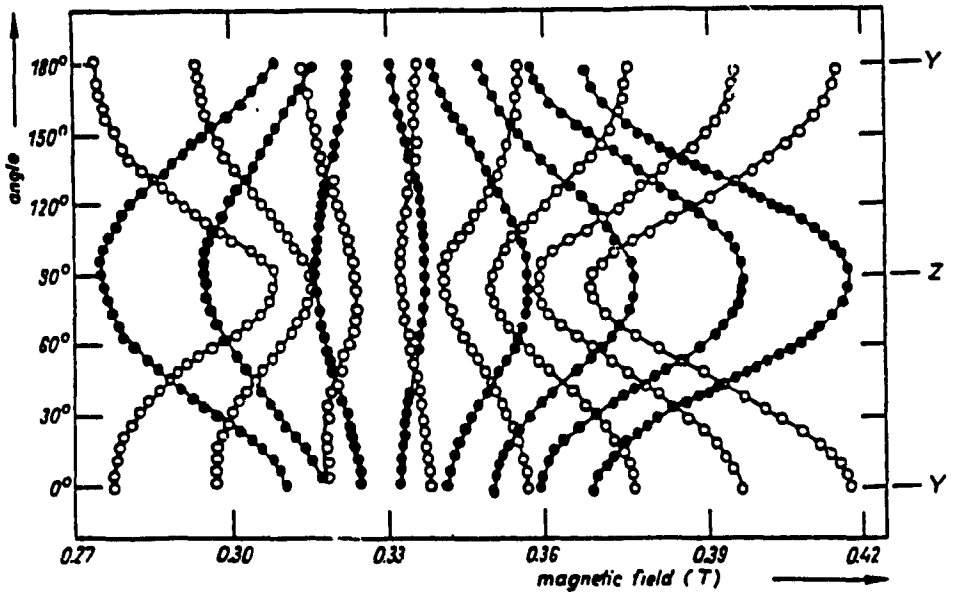

Fig. 3.9 Angular variation of EPR line positions observed at RT for $\vec{B}$ in the ZY plane for VO^{2+}-doped FASH crystal. The empty and solid circles represent experimental line positions corresponding to VO^{2+} ions I and II, respectively; the continuous lines are smooth curves that connect data points belonging to the same transition.

III.4.2 Superhyperfine (SHF) Structure and Temperature Dependence

The following features are common to the CASH, MASH and ZASH hosts at RT. Anisotropic quintet SHF splitting for both the VO^{2+} ions (I and II) was observed for $\vec{B}$ in the ZX and XY planes; no significant SHF splitting was observed for $\vec{B}$ in the ZY plane. The maximum SHF splitting, for ion I, was found to occur for $\vec{B}$ in the XY plane, at an angle of 45^0 from the X axis (referred to as the X_A axis); this direction is very close to the M^{2+}-$H_2O(7)$ direction. The SHF splitting for ion I is symmetric about the X_A axis for $\vec{B}$ in the XY plane. The EPR spectra for this orientation of $\vec{B}$ are shown in Fig. 3.10 for both the CASH and MASH hosts, and in Fig. 3.11 for ZASH host, exhibiting clearly that each hf line for ion I splits into five with the intensity ratios 1:4:6:4:1, the individual SHF linewidth being 0.4 mT. The farther is $\vec{B}$ from the X_A axis in the XY plane, the smaller is the observed SHF splitting for ion I. Finally, when $\vec{B}$ deviates from the X_A axis by more than 35^0, the SHF splitting for ion I is no longer resolved, the five SHF lines merge to form a single hf line. Further, the hf lines for ion I become narrower as $\vec{B}$ deviates farther from the X_A axis in the XY plane, while their peak-to-peak heights increase. The minimum width (0.7 mT) of the hf lines for ion I was attained when $\vec{B}$ was perpendicular to the X_A axis in the XY

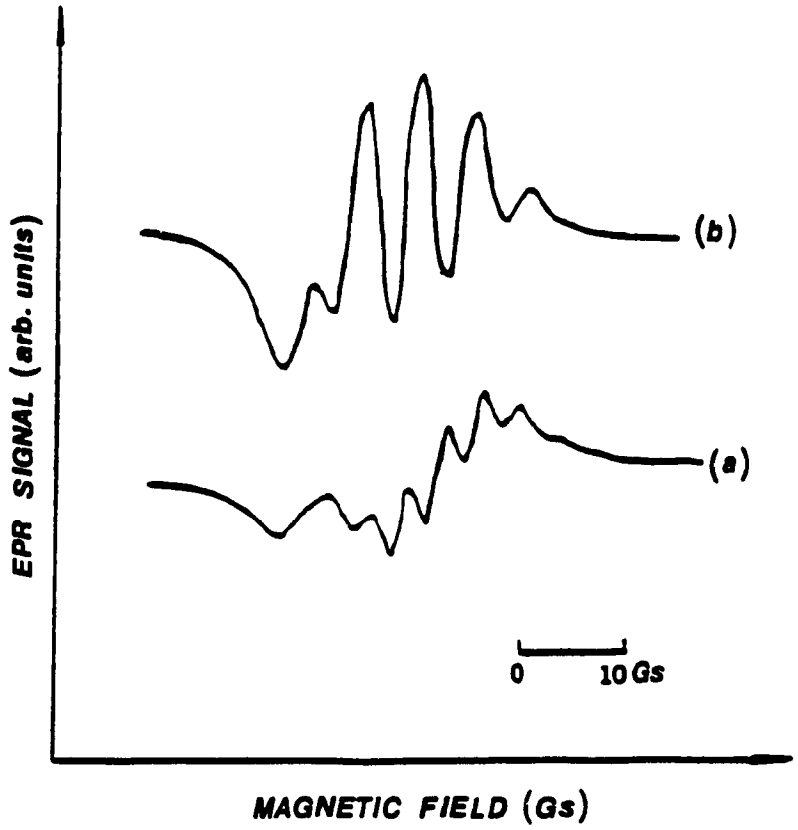

Fig. 3.10 EPR spectra, exhibiting the SHF structure for VO^{2+}-doped CASH and MASH single crystals, indicated by (a) and (b) respectively, at RT for the orientation of $\vec{B}$ for which maximum SHF splitting was observed. The intensity ratios of the five SHF lines are clearly seen to be 1:4:6:4:1.

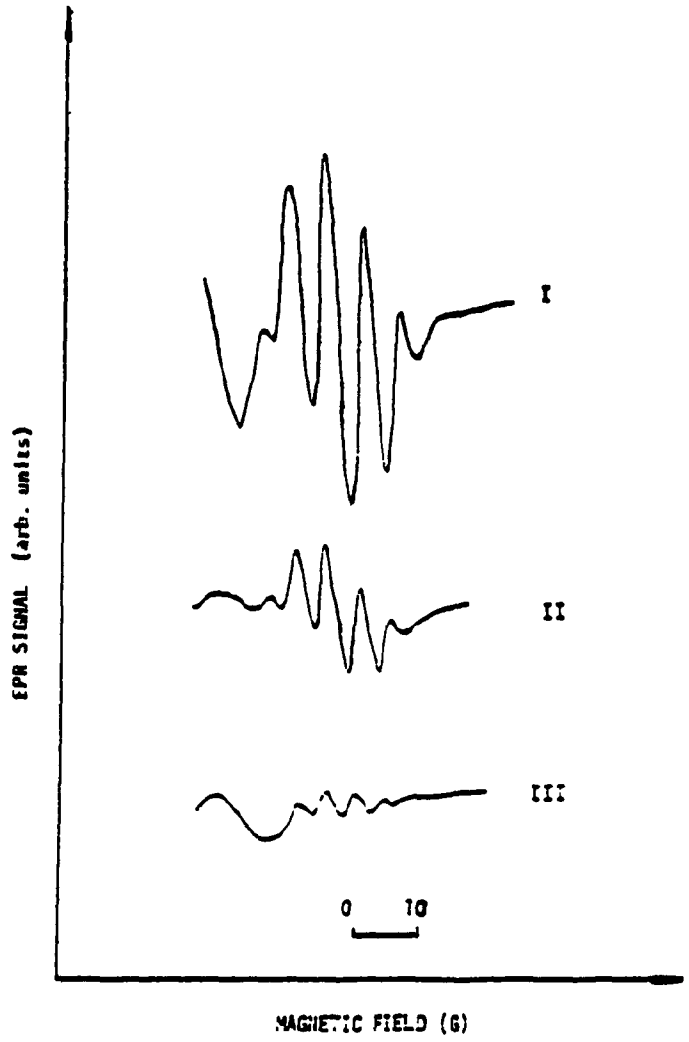

Fig. 3.11 RT EPR spectra of VO^{2+}-doped ZASH, exhibiting the SHF structure for the ions I, II and III, for the orientation of $\vec{B}$ for which the respective maximum SHF splittings were observed. It is seen that the SHF splitting for ion III is a bit smaller. The intensities of lines for ion III are much weaker than those for ions I and II.

plane. The extra linewidth of 0.3 mT over the individual SHF linewidth (0.4 mT) along this direction is due to inhomogeneous broadening of the unresolved SHF structure; this has been confirmed experimentally by measuring the VO^{2+} EPR spectra of a deuterated MDSD crystal, in which no protons exist thus no SHF interaction is involved. (See Sec. II.4.4 and Chap. VII for more details.) In the ZX plane the SHF splitting is the largest for $\vec{B} \parallel \hat{X}$, it decreases as $\vec{B}$ moves away from the X axis, being unresolved for $\vec{B} \parallel \hat{Z}$. For ion II, the maximum SHF splittings occurred for $\vec{B}$ in the XY plane, 90^0 away from X_A, and very close to, the M^{2+}-$H_2O(8)$ direction (the X_B axis). The features of the SHF splitting for $\vec{B}$ in the XY plane for ion II were found to be the same as those for ion I, except that here the symmetry is about the X_B axis.

For VO^{2+} ion III in ZASH, although the EPR lines were weak, their SHF splitting was still clearly observed (Fig. 3.11). The direction of $\vec{B}$ for which the maximum SHF splitting for ion III occurred was found to be perpendicular to those for the ions I and II, i.e., along the laboratory Z axis, which is close to the M^{2+}-$H_2O(9)$ direction.

The crystals of VO^{2+}-doped CASH, MASH and ZASH were then oriented so that $\vec{B}$ was along the direction for which the maximum SHF splitting for one of the two VO^{2+} ions (three VO^{2+} ions for ZASH) occurred, using the cavity with the higher Q, and the temperature was varied in the range

123 - 398 K. The SHF splitting for MASH and ZASH was found to be almost temperature independent. However, as the temperature was decreased, the resolution of the SHF splitting for CASH became poorer (Fig. 3.12); below 186 K, the five CASH SHF lines merged to form a single hf line. This implies a decrease in the value of SHF interaction tensor between VO^{2+} and ligand protons as the temperature is decreased. Above 350 K, the CASH crystal became destroyed due to dehydration.

At temperatures below 123 K, it was not possible to observe EPR characterized by well-resolved SHF splitting in any of VO^{2+}-doped CASH, MASH and ZASH, because of the use of a different cavity which had a lower Q. The other features of the spectra remained the same as those at RT. At liquid-helium temperature (LHT), it was necessary to reduce the microwave power considerably in order that the EPR lines did not broaden out due to the saturation effect by microwaves [1].

III.4.3 EPR Linewidths and Inhomogeneous Broadening of SHF Interaction

The EPR linewidths (ΔB) of VO^{2+} in FASH were found to be independent of temperature (T) in the range 4.2 - 393 K, being 1.4 ± 0.1 mT for the two VO^{2+} ions I and II, for any transition. These VO^{2+} EPR linewidths in FASH host consisting of paramagnetic ions are found to be twice those

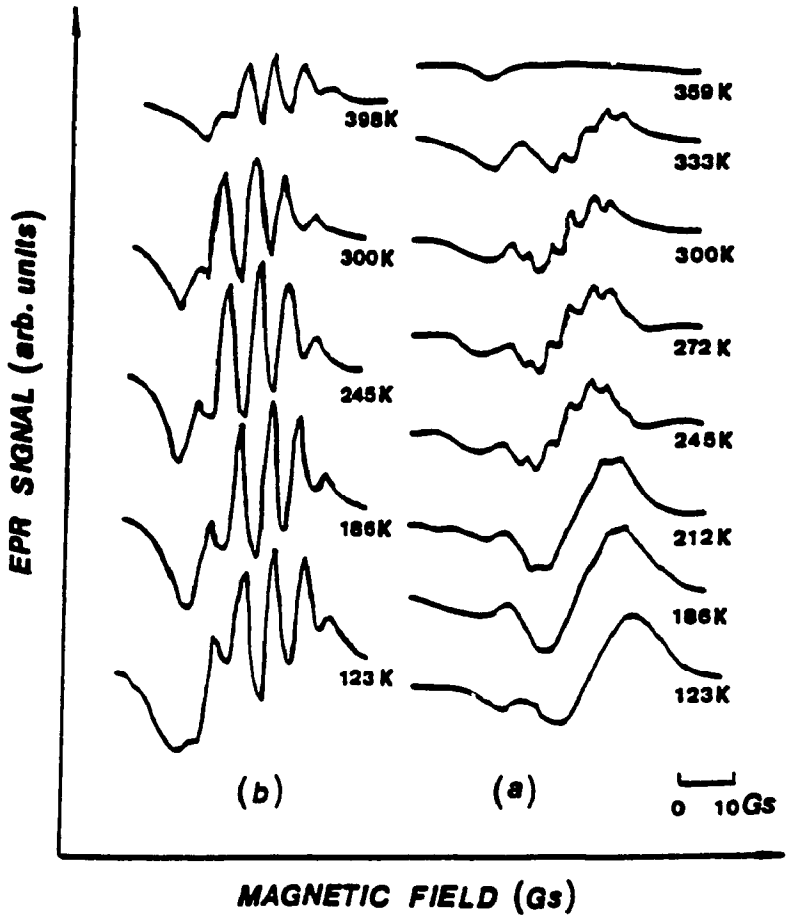

Fig. 3.12 EPR spectra exhibiting the temperature dependence of the maximum SHF splitting for CASH and for MASH, as indicated by (a) and (b) respectively.

in the ZASH, MASH and CASH hosts consisting of diamagnetic ions (0.7 mT at any temperature) [10,11].

For VO^{2+}-doped COASH, however, the VO^{2+} EPR linewidths (ΔB) were found to be very dependent on temperature (T), in the 117 - 413 K temperature range. At RT, ΔB for both the VO^{2+} ions I and II were 1.4 ± 0.1 mT, for any transition, and for any orientation of $\vec{B}$. Further, ΔB increased as T decreased; finally, VO^{2+} EPR lines were completely broadened out at and below 117 K. It was possible to measure ΔB clearly only above 143 K; at 143 K, ΔB = 2.6 ± 0.2 mT. For T higher than RT, ΔB were a little smaller, being 1.0 ± 0.1 mT at 400 K. Above 413 K, the crystal was destroyed due to heat.

Unlike VO^{2+}-doped CASH, MASH and ZASH hosts consisting diamagnetic ions, the SHF splitting of the VO^{2+} EPR lines was not resolved in the FASH and COASH hosts consisting of paramagnetic ions due to: (i) increased EPR linewidth (ΔB), and (ii) decreased SHF interaction. In the CASH, MASH and ZASH hosts consisting of diamagnetic ions, the maximum overall VO^{2+} SHF splitting was observed to be 2.0 mT, for $\vec{B}$ along one of the principal axes of the SHF tensor ($\vec{B}_{max}$ direction); the EPR lines are well resolved for $\vec{B} \parallel \vec{B}_{max}$ and the individual EPR linewidth (ΔB) is 0.4 mT. It is possible to estimate the contribution to individual linewidth due to inhomogenerous broadening using the following arguments. It is expected that the individual linewidth in the diamagnetic

hosts is independent of the orientation of $\vec{B}$. Further, when $\vec{B}$ was in the plane perpendicular to $\vec{B}_{max}$, the SHF structure was not resolved, only a single broadened line (ΔB = 0.7 mT at all temperatures) was observed, a situation similar to that exists in FASH or COASH hosts for any orientation of $\vec{B}$. Thus, for the CASH, MASH and ZASH hosts consisting diamagnetic ions, the extra linewidth of 0.3 mT over and above the individual linewidth of 0.4 mT, for $\vec{B}$ in the plane perpendicular to $\vec{B}_{max}$, should be due to the inhomogeneous broadening caused by the SHF interaction, which is expected to be the same in the FASH and COASH hosts. It is because in both the COASH and FASH hosts consisting of paramagnetic ions, the SHF structure was not resolved, only a single EPR line, with the same ΔB (1.4 mT), was observed for any orientation of $\vec{B}$. Finally, in order to estimate the contribution to EPR linewidth ($\Delta B'$) due only to the paramagnetism of the host Fe^{2+} and Co^{2+} ions, one has to subtract from the total linewidth the linewidth of an individual EPR line of VO^{2+} in diamagnetic hosts (0.4 mT at all temperatures), as well as the contribution to the linewidth by the broadening due to the SHF interaction (0.3 mT at all temperatures). This means that a total of 0.7 mT is to be subtracted at all temperatures from ΔB in order to estimate $\Delta B'$, to be used in eq. (9.1), in order to estimate the host-ion spin-lattice relaxation times (τ) (Chap. IX).

III.4.4 VO^{2+}-doped $Mg(ND_4)_2(SO_4)_2 \cdot 6D_2O$ (MDSD)

The main features of VO^{2+} EPR spectra and their temperature dependence in MDSD crystal were found to be the same as those for MASH crystal, except for the absence of SHF splitting of hf lines for MDSD crystal. The EPR linewidth for MDSD was observed to be about 0.4 mT, being the same as that of an individual EPR SHF line in MASH, independent of the orientation of $\vec{B}$ and the temperature.

III.5 Cu^{2+}-doped $MNa_2(SO_4)_2 \cdot 4H_2O$ (M = Mg, Co)

In general, for each of the magnetically-inequivalent Cu^{2+} ions (electronic spin S = 1/2, nuclear spin I = 3/2) in a host crystal, a set of four allowed Cu^{2+} hf EPR lines is expected. These lines correspond to $\Delta M = \pm 1$, $\Delta m = 0$; here M, m are the electronic and nuclear magnetic quantum numbers, respectively. One often observes that each of Cu^{2+} hf line splits into two lines, which is due to the existence of two copper isotopes, specifically, ^{63}Cu (69.09% abundance) and ^{65}Cu (30.91% abundance). Fig. 3.13 shows a typical Cu^{2+} EPR spectrum which corresponds to two sets of four hf lines for the two magnetically-inequivalent Cu^{2+} ions in MNST.

For both the Cu^{2+}-doped MNST and CNST crystals, the angular variations of EPR line positions were recorded for $\vec{B}$ in three mutually perpendicular planes at 5^0 intervals. The largest flat plane (Fig. 2.3), which contains the

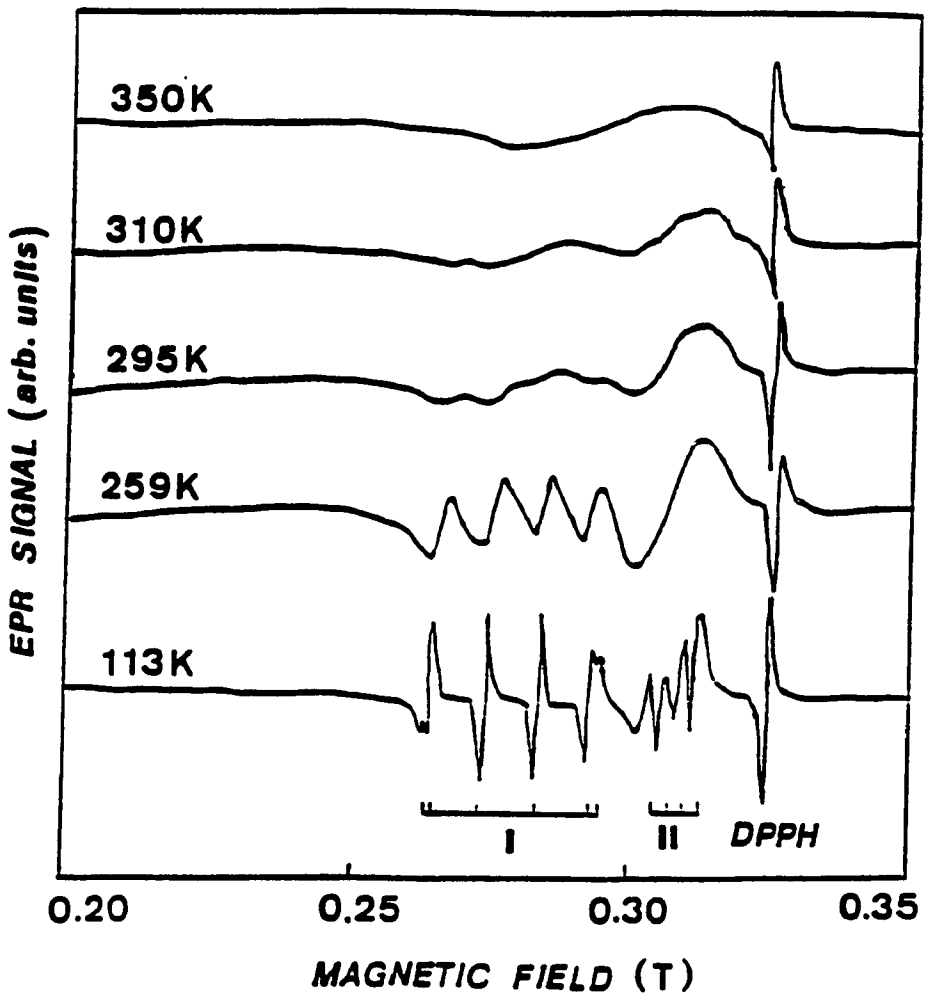

Fig. 3.13 Temperature variation of Cu^{2+} EPR spectra in MNST crystal, for $\vec{B}$ in the XY plane, 35^0 away from the Y axis. The hf lines due to the two isotopes (^{63}Cu and ^{65}Cu) are clearly resolved at 113 K. Above 347 ± 2 K, the four hf lines merge to form a single broad and isotropic line, corresponding to g = 2.20 ± 0.02.

crystallographic a and b axes, was chosen to define the XY plane with $\vec{Y} \parallel \vec{b}$. The Z axis is, accordingly, perpendicular to the ab plane and parallel to the crystallographic c axis.

III.5.1 Room-temperature EPR Spectra

For both Cu^{2+}-doped MNST and CNST crystals, RT EPR spectra showed that there are present two magnetically inequivalent, but physically equivalent, Cu^{2+} complexes in each of the unit cell of the MNST and CNST lattices. This is based on the following observations. For $\vec{B}$ in the ZY and XY planes, there were observed two sets of four allowed Cu^{2+} hf lines with the same intensities. The two sets hf lines were found to merge together for $\vec{B}$ along the Y ($\vec{b}$) axis. For $\vec{B}$ in the ZX (a^*c, $a^* = a \sin\beta$) plane, there was observed only one set of four Cu^{2+} hf lines, implying that the two sets of hf lines due to the two Cu^{2+} complexes overlapped each other perfectly. This is possible if the two sets of hf lines are symmetric about the ZX (a^*c) plane. Thus, the EPR spectra of the two Cu^{2+} ions, which substitute for the two M^{2+} (M = Mg, Co) ions in the unit cell of MNST and CNST (Chap. V), are consistent with the crystallographic symmetry [116].

At RT, the Cu^{2+} EPR linewidths in both MNST and CNST hosts were significantly larger than those of other impurity ions, e.g., Mn^{2+} and VO^{2+}, in the isostructural ZNST host [117, 118], being 4.0 mT (Fig. 3.13) and 8.5 mT, respectively. This is similar to the case of other

Cu^{2+}-doped hosts in which the spin-lattice relaxation of Cu^{2+} ions is enhanced by the tunneling effect between the different spin states of Cu^{2+} in the Jahn-Teller systems [1, 113, 124], resulting in shorter spin-lattice relaxation times of the impurity ion Cu^{2+}. Because of larger linewidths, the two sets of hf lines due to the two different isotopes, were not resolved. In the case of CNST, for $\vec{B}$ in the ZX and ZY planes, even the four hf lines were not clearly resolved, because of line broadening due to the effect of the host paramagnetic ions.

III.5.2 EPR Spectra at Lower Temperatures

As the temperature was decreased, EPR line positions of Cu^{2+} in both MNST and CNST did not change significantly, implying a temperature independence of their spin-Hamiltonian parameters. However, their linewidths (ΔB) did indicate a large change, as seen from Fig. 3.13. For MNST, the linewidth becomes much smaller at lower temperatures (at T = 113 K, ΔB = 1.2 mT). Because of narrow linewidth, the hf lines due to the two different isotopes were clearly resolved at 113 K. This narrower linewidth corresponds to longer spin-lattice relaxation time of the impurity ion Cu^{2+} at lower temperature. The τ of Cu^{2+} (τ_{Cu}), can be estimated by the use of the expression $\tau_{Cu} = \hbar/(g\mu_B \Delta B)$ [1, 124], which neglects the spin-spin interaction between Cu^{2+}-Cu^{2+} pairs, taking into account the fact that

width of Cu^{2+} lines in hosts consisting of diamagnetic ions is mainly due to the spin-lattice interaction. In this way, the value of τ_{Cu} in MNST was estimated to be 6.9×10^{-9} sec. at RT, and 2.7×10^{-8} sec. at 113 K.

On the other hand, for Cu^{2+}-doped CNST crystal consisting paramagnetic ions, the Cu^{2+} EPR linewidth was increased significantly as the temperature decreased. Below 280 K, the hf lines were no longer resolved. This is due to an increase of the τ of the host Co^{2+} ions (Chap. IX); this weakens the narrowing effect of the host-ion spin-lattice relaxation on the impurity ion Cu^{2+} EPR linewidth.

III.5.3 EPR Spectra at Higher Temperatures

As the temperature was increased above RT, the hf lines of Cu^{2+} in both MNST and CNST continued to become broader. Finally, at 347 ± 2 K and 339 ± 2 K for MNST and CNST, respectively, only one single, broad, isotropic line was observed (Fig. 3.13); both the position of the line center and the linewidth were independent of the orientation of $\vec{B}$. No further change in the linewidth was observed as the temperature was raised to 398 K, above which both MNST and CNST crystals became destroyed due to heat. The single isotropic line, for both MNST and CNST, corresponded to g = 2.20 ± 0.02, which is close to the average of the three principal values of $\tilde{g}$ matrix (Chap. IV). This can be well interpreted in terms of dynamic JTE. For more details, see Chap. X.

CHAPTER IV

SPIN HAMILTONIAN AND EVALUATION OF PARAMETERS

In this thesis, the spin-Hamiltonian parameters (SHP) of Mn^{2+} in AS ($\tilde{g}$, $\tilde{A}$ and b_ℓ^m), Gd^{3+} in APST ($\tilde{g}$, $\tilde{A}$ and b_ℓ^m), VO^{2+} in CASH, MASH, ZASH, FASH and COASH ($\tilde{g}$ and $\tilde{A}$) and Cu^{2+} in MNST and CNST ($\tilde{g}$ and $\tilde{A}$) host lattices have been evaluated from EPR line positions by the use of a least-squares fitting (LSF) procedure [76, 77, 78], in which all EPR line positions observed for several orientations of $\vec{B}$ are simultaneously fitted using a computer program.

IV.1 Evaluation of SHP by LSF Technique

Details of the LSF technique. The EPR data in this thesis have been analyzed using the LSF technique [76, 77, 78], in which the initially chosen set of SHP, represented by the components of the vector $\vec{a}_i$, are iteratively varied using a well-defined mathematical criterion. Explicitly, in each iteration the vector $\vec{a}_i$ is changed to $\vec{a}$ as follows:

$$\vec{a} = \vec{a}_i - (D'')^{-1}D'. \qquad (4.1)$$

The $\vec{a}$ so obtained is used as $\vec{a}_i$ for the next iteration. This process is continued until convergence is achieved. In eq. (4.1) D′ and D″ are the elements of the first and second derivatives of the quantity "chi-squared", χ^2, with respect to SHP, evaluated at $\vec{a}_i$;

$$(D')_j = (\partial\chi^2/\partial a_j)_{\vec{a}_i} , \tag{4.2}$$

and

$$(D'')_{jk} = (\partial^2\chi^2/\partial a_j \partial a_k)_{\vec{a}_i} , \tag{4.3}$$

where

$$\chi^2 \equiv \sum_i (|\Delta E_i| - \hbar\nu_i)^2/\sigma_i^2 . \tag{4.4}$$

In eq. (4.4), ΔE_i is the calculated energy difference between the pairs of energy levels participating in resonance, ν_i is the klystron frequency and $\hbar = h/2\pi$, where h is Planck's constant, while σ_i is an effective weight factor. The index i covers all the resonant line positions (data points), used simultaneously in the fitting.

Explicitly, from eq. (4.2) one has for the elements of D′ and D″:

$$(D')_j = 2 \sum_i (|\Delta E_i| - \hbar\nu_i)(\partial|\Delta E_i|/\partial a_j)/\sigma_i^2 \tag{4.5}$$

$$(D'')_{jk} = 2 \sum_i [(\partial|\Delta E_i|/\partial a_j)(\partial|\Delta E_i|/\partial a_k) + (|\Delta E_i| - \hbar\nu_i)(\partial^2|\Delta E_i|/\partial a_j \partial a_k)]/\sigma_i^2 \tag{4.6}$$

For the LSF method, one needs to calculate the derivatives of the eigenvalue difference $|\Delta E_i|$, either using the perturbation approximation, or using the matrix diagonalization method.

A detailed account of the LSF method has been given by Misra [76, 77, 78]. The method works equally well for both the case S > 1/2 and the case S = 1/2 (for which no fine-structural term appears in the spin Hamiltonian) which are coupled to one nuclear spin I ≥ 1/2. For the listings of computer programs, refer to Appendix II. In order to use these programs properly and to reduce the computing times significantly, the following should be noted: (i) for the case of S > 1/2, e.g., Mn^{2+} and Gd^{3+} ions, one has to find the principal axes (X, Y, Z) of the magnetic complexes in the crystal, then record the EPR spectra in the ZX, ZY and XY planes or fewer planes depending on site symmetry [76, 77]. (The principal Z, X and Y axes of a Mn^{2+}, or Gd^{3+}, complex, are defined to be those directions of $\vec{B}$ for which the overall separations of the allowed EPR lines exhibit extrema; of these three, the overall separations occur in decreasing order for $\vec{B}$ along the Z, X and Y axes.) On the other hand, for the case of S = 1/2, e.g., VO^{2+} and Cu^{2+} ions, the EPR spectra can be recorded for $\vec{B}$ in any three mutually perpendicular planes [78]. (ii) The initial value of the parameters should be carefully chosen, especially for the electron-nuclear spin-coupled systems, for which the spin-Hamiltonian (S. H.) matrix has a dimension of (2S+1)(2I+1) x (2S+1)(2I+1), the large number of EPR line positions fitted simultaneously making the total computer time required, prohibitively long. The various methods to

estimate the initial values of SHP have been described by Misra [76, 77, 78]. For example, in case of S = 1/2, e.g., VO^{2+}, or Cu^{2+}, one can first use the LSF procedure to find the approximate values of $\tilde{g}^2$ tensor from the fine line positions (assumed to lie at the center of a set of allowed hf line positions). The values of $\tilde{g}^2$ tensor so obtained, along with the typical values of $\tilde{A}^2$ tensor, were then used as initial values in a subsequent LSF procedure of the various hf line positions to obtain the exact values of $\tilde{g}^2$ and $\tilde{A}^2$ tensors.

Determination of signs of spin-Hamiltonian parameters. The LSF method gives the correct relative signs of the fine-structure, as well as those of the hyperfine-structural parameters. The absolute sign of fine-structural parameters can be determined by identifying the absolute sign of b_2^0, the largest fine-structural parameter, by comparing the observed line intensities of $\Delta M = \pm 1$ transitions at room and liquid-helium temperatures [1]. If the intensity of the high-field lines for $\vec{B} \parallel \vec{Z}$ increases (decreases) relative to the low-field lines as the temperature is reduced the absolute sign of b_2^0 is positive (negative). On the other hand, the absolute sign of hyperfine-structural parameters can be determined by comparing the EPR data with the hyperfine-interaction data obtained by the use of other techniques. See the following sections for more details.

Calculation of the errors of spin-Hamiltonian parameter.

The procedure for the determination of the errors of spin-Hamiltonian parameters in the fitting of EPR data, based on standard statistical analysis, has been described by Misra and Subramanian [79]. According to statistical analysis the parameter errors can be expressed as:

$$\Delta a_j = \sqrt{\varepsilon_{jj}} \ , \tag{4.7}$$

where a_j are SHP and ε_{jj} is the jth diagonal element of the error matrix $\tilde{\varepsilon}$, which is the inverse of the matrix whose elements A_{ij} are one-half of the matrix of second derivatives of χ^2, defined by eq. (4.4),

$$\tilde{\varepsilon} = \tilde{A}^{-1}, \tag{4.8}$$

where

$$A_{ij} = (1/2)(\partial^2\chi^2/\partial a_i \partial a_j)_{\vec{a}} \ . \tag{4.9}$$

When all σ_i in eq. (4.4) are equal, the parameter errors can be estimated from the following expression [79]:

$$\Delta a_j^2 = [\chi^2(1)/(N - r)]\varepsilon_{jj}(1), \tag{4.10}$$

where $\tilde{\varepsilon}(1)$ and $\chi^2(1)$ are the error matrix and chi-squared values, respectively, when all $\sigma_i = 1$; N is the number of data points fitted and r is the number of parameters. Eq. (4.10) is easily understood if one notes that the estimated variance of the data points, S^2, is expressed as [79]:

$$S^2 = \chi^2(1)/(N - r). \qquad (4.11)$$

The following sections report, in detail, the determination of SHP of the various impurity ions doped in different host crystals, by the LSF technique.

IV.2 Mn^{2+} in $(NH_4)_2SO_4$

The following spin Hamiltonian (S.H.), appropriate to orthorhombic symmetry, is applicable to Mn^{2+} in AS [1]:

$$\mathcal{H} = \mu_B[g_{\parallel}B_zS_z + g_{\perp}(B_xS_x + B_yS_y)] + \tfrac{1}{3}(b_2^0O_2^0 + b_2^2O_2^2) +$$

$$+ \tfrac{1}{60}(b_4^0O_4^0 + b_4^2O_4^2 + b_4^4O_4^4) + AS_zI_z + B(S_xI_x + S_yI_y) +$$

$$+ Q'[I_z^2 - \tfrac{1}{3}I(I + 1)] + Q''[I_x^2 - I_y^2]. \qquad (4.11)$$

In eq. (4.11), μ_B is the Bohr magneton, and the O_ℓ^m are spin operators, as defined by Abragam and Bleaney [1]. A rigorous LSF procedure [76, 77], utilizing numerical diagonalization of the S.H. matrix on a digital computer, in which all clearly-resolved allowed Mn^{2+} line positions, observed for several orientations of $\vec{B}$ in its ZX plane, were simultaneously fitted to evaluate the nine SHP $g_{\parallel}$, $g_{\perp}$, b_2^0, b_2^2, b_4^0, b_4^2, b_4^4, A and B. (The parameters Q' and Q" could not be determined, since the allowed line positions do not depend upon them, to first-order in approximation.) The

errors of the parameters were determined by the use of a statistical method [79]. Finally, a total of 140 line positions were used to evaluate the nine SHP. This included, generally, all the six lines of each of the first, second, fourth and fifth hf sextets for each of the orientations of $\vec{B}$ close to, and including, the Z axis (at 0^{o}, 2^{o}, 4^{o}, 6^{o}, 8^{o} and 10^{o} from Z axis), and all the six lines of each of the first and fifth hf sextets for each of the orientations of $\vec{B}$ close to, and including, the X axis (at 0^{o}, 2^{o}, 4^{o}, 6^{o} and 8^{o} from X axis). (Here, the sextets are referred to in increasing values of the Zeeman field, i.e., the first hf sextet lies at the lowest values of B, while the fifth hf sextet lies at the highest values of B.) The values of the SHP, so evaluated, are listed in Table 4.1, which also includes, the SHP reported by Abdulsabirov et al. [51] and by Shrivastava [52]. As for the absolute signs of the parameters, they could not be determined from the present data, since no relative-intensity data were available at LHT. The sign of b_2^0 was, then, assumed to be positive. The signs of the other fine-structure parameters, relative to that of b_2^0, as yielded by the LSF procedure, are correct. The signs of the hf parameters A, B were chosen to be negative, in accordance with the hyperfine-interaction data [80].

Although the values of the SHP as evaluated presently are for Mn^{2+} center I, those for center II are expected not

Table 4.1 RT Mn^{2+} SHP in AS crystal. The unit for b_ℓ^m, A and B values is GHz, while that for χ^2, GHz^2. n is the number of lines fitted simultaneously. For the data of Abdulsabirov et al. [51] and Shrivastava [52], χ^2 are as calculated using their reported parameters and the line positions observed presently.

Parameter	Present	Ref. [51]	Ref. [52]
$g_{\parallel}$	2.0014 ± 0.0004	g_z = 2.0009	g = 1.9959
$g_{\perp}$	2.0176 ± 0.0079	g_x = 2.0009	
		g_y = 2.0014	
b_2^0	2.153 ± 0.003	-2.183	1.454
b_2^2	-0.714 ± 0.027	1.108	-0.717
b_4^0	0.001 ± 0.001	0.008	-0.006
b_4^2	0.699 ± 0.045	0.000	——
b_4^4	-0.281 ± 0.180	0.039	——
A	-0.258 ± 0.003	0.259	-0.256
B	-0.281 ± 0.003	0.263	-0.250
C	——	0.263	——
χ^2/n	0.003	0.096	3.064
n	140	140	140

to be much different from these, because of the very close proximity of the environments of the two centers, as discussed in Chap. V below.

IV.3 Gd^{3+} in $NH_4Pr(SO_4)_2 \cdot 4H_2O$

A S.H., appropriate to monoclinic symmetry, with the two-fold axis $C_2 \parallel \vec{Z}$, was chosen to fit the EPR line positions of Gd^{3+} in APST. This is consistent with the site symmetry, since the Z axis, as discussed in Chap. II, lies along the local "C_{4v}" axis, which is oriented very close to the crystal C_2 axis (b axis). (In the previously reported EPR studies on Gd^{3+}-doped isostructural ACST, ANST and ASST [65, 66, 67], an incorrect S.H., applicable to orthorhombic site symmetry, was used.) Accordingly [1, 81],

$$\mathcal{H} = \mu_B[g_\parallel B_z S_z + g_\perp (B_x S_x + B_y S_y)] + \sum_{m=0,\pm2} (1/3)\, b_2^m O_2^m + \\ + \sum_{m=0,\pm2,\pm4} (1/60)\, b_4^m O_4^m + \sum_{m=0,\pm2,\pm4,\pm6} (1/1260)\, b_6^m O_6^m \,, \tag{4.12}$$

In eq. (4.12), $g_\parallel$, $g_\perp$ and b_ℓ^m are the SHP. [The monoclinic S.H. appropriate to $C_2 \parallel \vec{X}$ and $C_2 \parallel \vec{Y}$ [81], where the negative (for $C_2 \parallel \vec{X}$) or positive (for $C_2 \parallel \vec{Y}$) odd-m O_ℓ^m terms instead of negative even-m O_ℓ^m terms (for $C_2 \parallel \vec{Z}$) in eq. (4.12) were included, as well as a S.H. for orthorhombic symmetry [81], which did not include any positive or negative odd-m, or negative even-m O_ℓ^m terms needed to

represent the monoclinic symmetry, were also used to fit the EPR line positions; however, they gave much larger least-squares χ^2 values, and thus were excluded.]

A rigorous LSF procedure [76, 77], in which all clearly-resolved Gd^{3+} allowed line positions, observed for several orientations of $\vec{B}$ in the ZX and XY planes, were simultaneously fitted to evaluate the 17 SHP, $g_{\parallel}$, $g_{\perp}$ and b_{ℓ}^{m}. Finally, a total of 154 line positions were used to evaluate the 17 SHP; they are listed in Table 4.2. As for the absolute signs of the parameters, they could not be determined from the present data, since no relative-intensity data are available at LHT; because at LHT, the crystal is in a different phase (Chap. VI). The sign of b_2^0 was, then, assumed to be positive, which is consistent with the results of the superposition-model calculation (Chap. V). The signs of the other fine-structure parameters (b_{ℓ}^{m}), relative to that of b_2^0, as yielded by the LSF procedure, are, of course, correct.

It was not possible to evaluate the SHP below the phase-transition temperature 266 K (Chap. VI), since the orientations of the magnetic axes changed below 266 K, and experimental arrangement did not permit variation of the magnetic field orientation in the magnetic ZX, XY planes at low temperatures, to provide the EPR line positions, required for the evaluation of SHP.

Table 4.2 RT Gd^{3+} SHP in the APST single crystal. For other details see the caption of Table 4.1.

parameter	value	parameter	value
$g_{\parallel}$	1.9950 ± 0.0004	b_6^0	0.0006 ± 0.0005
$g_{\perp}$	1.9948 ± 0.0004	b_6^2	0.0001 ± 0.0034
b_2^0	0.3469 ± 0.0009	b_6^4	-0.0215 ± 0.0060
b_2^2	-0.0003 ± 0.0013	b_6^6	0.0075 ± 0.0054
b_2^{-2}	0.0914 ± 0.0041	b_6^{-2}	-0.0796 ± 0.0043
b_4^0	-0.0087 ± 0.0004	b_6^{-4}	-0.0085 ± 0.0001
b_4^2	-0.0002 ± 0.0020	b_6^{-6}	0.0176 ± 0.0069
b_4^4	-0.0284 ± 0.0022	n	154
b_4^{-2}	0.0328 ± 0.0049	χ^2/n	0.0037
b_4^{-4}	0.0014 ± 0.0032		

IV.4 VO^{2+} in $M(NH_4)_2(SO_4)_2\cdot 6H_2O$ (M = Cd, Mg, Zn, Fe, Co) and $Mg(ND_4)_2(SO_4)_2\cdot 6D_2O$

For VO^{2+} ion the effective electronic spin S = 1/2 and its nuclear spin I = 7/2. The S.H. characterizing the VO^{2+} ion in the Tutton salts, without the assumption, which was made in previous studies [82, 83], of axial symmetry or coincidence of the principal axes of the $\tilde{g}^2$ and $\tilde{A}^2$ tensors, can be expressed as [1]:

$$\mathcal{H} = \mu_B \vec{S}\cdot\tilde{g}\cdot\vec{B} + \vec{S}\cdot\tilde{A}\cdot\vec{I} + \vec{S}\cdot\tilde{A}^L\cdot\vec{I}_L \ . \qquad (4.13)$$

In eq. (4.13), the successive terms represent electronic Zeeman, hf interaction and SHF interaction with the ligand protons, respectively, while $\tilde{A}$, $\tilde{A}^L$ and I_L are, respectively, the hyperfine-interaction matrix, the SHF matrix and the resultant spin (= 2) of the four ligand protons. In the case of $Mg(ND_4)_2(SO_4)_2\cdot 6D_2O$ (MDSD) the third term does not apply because there are present no ligand protons. In eq. (4.13), the quadruple-interaction term has been omitted, as it has negligible effect.

The principal values of the $\tilde{g}^2$ ($\equiv \tilde{g}^T\cdot\tilde{g}$; T denotes transpose of a matrix) and $\tilde{A}^2$ ($\equiv \tilde{A}^T\cdot\tilde{A}$) tensors were evaluated by the use of a LSF procedure [78], applicable to the cases with non-coincident $\tilde{g}^2$ and $\tilde{A}^2$ tensors. In summary, a total of 384 allowed hf line positions (averaged over SHF splitting in the cases of CASH, MASH and ZASH), observed for

the VO^{2+} complex for any VO^{2+} ion (I or II), were fitted simultaneously to evaluate the principal values of the $\tilde{g}$ and $\tilde{A}$ matrices and their direction cosines, which are the eigenvectors of the respective matrices. [It should be noted that the principal values of $\tilde{g}$ and $\tilde{A}$ matrices are the square roots of the principal values of $\tilde{g}^2$ and $\tilde{A}^2$ tensors with the same direction cosines.] The values so obtained, for the two VO^{2+} ions, are listed in Tables 4.3, 4.4, 4.5, 4.6, 4.7 and 4.8 for CASH, MASH, ZASH, FASH, COASH and MDSD, respectively. The absolute signs of the principal values of $\tilde{A}$ have been assumed to be negative in accordance with those determined by Muncaster and Parke [84]. At temperatures below 123 K, SHF splitting for CASH, MASH and ZASH was not observed because a low-Q cavity was used; thus no averaging of line positions was necessary in order to estimate $\tilde{g}$ and $\tilde{A}$. It is seen from Tables 4.3, 4.4, 4.5, 4.6, 4.7 and 4.8 that the principal axes for the $\tilde{g}^2$ and $\tilde{A}^2$ tensors are almost coincident, for all the samples. The present values of SHP of VO^{2+} in CASH, MASH, ZASH, ZASH, COASH and MDSD are temperature independent to within 1% for principal values of $\tilde{g}$ and to within 3% for principal values of $\tilde{A}$. This temperature independence is typical of vanadyl complexes, whose EPR spectra are characterized by an axial symmetry of the ligand field with small distortion, as revealed by the slightly unequal principal values $A_{x''}$ and $A_{y''}$ of the hyperfine-interaction matrix, $\tilde{A}$. The previously-reported

Table 4.3 Principal values and direction cosines of the $\tilde{g}$ and $\tilde{A}$ matrices of VO^{2+}-doped CASH single crystal. The principal values of $\tilde{g}$ are dimensionless, while those of $\tilde{A}$ are expressed in GHz. The direction cosines of the $\tilde{g}^2$ tensor (X′, Y′, Z′) are given with respect to the X, Y and Z axes (Fig. 2.2), while those of the $\tilde{A}^2$ tensor (X″, Y″, Z″) are expressed relative to (X′, Y′, Z′). The numbers in brackets are those reported by Satyanarayana et al. [75].

Ion Temperature (K)	Principal Values		Direction Cosines Z/Z′	X/X′	Y/Y′
295 I	$g_{z'}$ =	1.9363±0.0020 (1.947)	0.7399	-0.6500	-0.1734
	$g_{x'}$ =	1.9810±0.0020 (1.999)	-0.6550	0.7548	0.0348
	$g_{y'}$ =	1.9847±0.0020 (1.992)	0.1535	0.0879	0.9842
	$A_{z''}$ =	-0.5343±0.0050 (0.5178)	0.9973	0.0421	0.0595
	$A_{x''}$ =	-0.2159±0.0050 (0.2068)	-0.0538	0.9761	0.2106
	$A_{y''}$ =	-0.1997±0.0050 (0.2007)	0.0493	0.2132	-0.9758
II	$g_{z'}$ =	1.9422±0.0020 (1.945)	0.2660	0.6560	-0.6941
	$g_{x'}$ =	1.9800±0.0020 (1.998)	-0.3179	0.7674	0.4829
	$g_{y'}$ =	1.9846±0.0020 (1.993)	0.9101	-0.0924	0.4034
	$A_{z''}$ =	-0.5358±0.0050 (0.5172)	0.9962	-0.0742	-0.0742
	$A_{x''}$ =	-0.2189±0.0050 (0.2069)	-0.0356	0.9920	0.1214
	$A_{y''}$ =	-0.2028±0.0050 (0.2008)	0.0790	-0.1183	0.9898

Table 4.3 (continued)

80	I	$g_{z'}$ = 1.9481±0.0020	0.7405	-0.6200	-0.2771
		$g_{x'}$ = 1.9961±0.0020	-0.6660	0.7574	0.0530
		$g_{y'}$ = 1.9944±0.0020	0.0668	0.2741	0.9594
		$A_{z''}$ = -0.5328±0.0050	0.9988	-0.0046	0.0484
		$A_{x''}$ = -0.2224±0.0050	-0.0162	0.9698	0.2432
		$A_{y''}$ = -0.2021±0.0050	0.0458	0.2437	-0.9688
	II	$g_{z'}$ = 1.9488±0.0020	0.3373	0.6427	-0.6879
		$g_{x'}$ = 1.9948±0.0020	-0.3441	0.7868	0.4124
		$g_{y'}$ = 1.9940±0.0020	0.9303	-0.3394	0.1390
		$A_{z''}$ = -0.5607±0.0050	0.9863	0.1632	-0.0233
		$A_{x''}$ = -0.2191±0.0050	-0.0763	0.9774	0.1129
		$A_{y''}$ = -0.1983±0.0050	0.1461	-0.1000	0.9820
4.2	I	$g_{z'}$ = 1.9384±0.0020	0.6851	-0.6838	-0.2511
		$g_{x'}$ = 1.9993±0.0020	-0.7282	0.6344	0.2592
		$g_{y'}$ = 1.9894±0.0020	0.0179	0.3604	0.9326
		$A_{z''}$ = -0.5514±0.0050	0.9975	0.0431	0.0556
		$A_{x''}$ = -0.2337±0.0050	-0.0480	0.9948	0.0903
		$A_{y''}$ = -0.1935±0.0050	0.0514	0.0927	-0.9948
	II	$g_{z'}$ = 1.9418±0.0020	0.3869	0.6238	-0.6821
		$g_{x'}$ = 1.9902±0.0020	-0.2186	0.7756	0.4180
		$g_{y'}$ = 1.9918±0.0020	0.9377	-0.2181	0.1875
		$A_{z''}$ = -0.5585±0.0050	0.9829	0.1836	-0.0109
		$A_{x''}$ = -0.2397±0.0050	-0.0109	0.9763	0.2235
		$A_{y''}$ = -0.1949±0.0050	0.1812	-0.2286	0.9380

Table 4.4 Principal values and direction cosines of the $\tilde{g}$ and $\tilde{A}$ matrices of VO^{2+}-doped MASH single crystal. These values are the same at all temperatures in the 4.2 - 295 K range. The numbers in brackets are those reported by Jayaram et al. [83]. For other details see the caption of Table 4.3.

Ion	Principal Values	Direction Cosines		
		Z/Z′	X/X′	Y/Y′
I	$g_{z'}$ = 1.9424±0.0020 (1.9420)	0.8666	0.4906	-0.0909
	$g_{x'}$ = 1.9826±0.0020 (2.0062)	-0.4940	0.8182	0.2940
	$g_{y'}$ = 1.9859±0.0020 (1.9875)	0.0698	0.2997	0.9515
	$A_{z''}$ = -0.5226±0.0050 (0.562)	0.9954	-0.0209	0.0935
	$A_{x''}$ = -0.2216±0.0050 (0.220)	-0.0593	0.9724	0.1724
	$A_{y''}$ = -0.2072±0.0050 (0.225)	0.0753	0.1744	-0.9783
II	$g_{z'}$ = 1.9384±0.0020 (1.9372)	0.1647	0.5420	-0.8241
	$g_{x'}$ = 1.9827±0.0020 (2.0025)	0.2389	0.7888	0.5665
	$g_{y'}$ = 1.9862±0.0020 (1.9972)	0.9570	-0.2902	0.0004
	$A_{z''}$ = -0.5319±0.0050 (0.554)	0.9989	0.0420	-0.0224
	$A_{x''}$ = -0.2229±0.0050 (0.221)	-0.0421	0.9991	0.0051
	$A_{y''}$ = -0.1942±0.0050 (0.248)	-0.0223	-0.0061	0.9997

Table 4.5 Principal values and direction cosines of the $\tilde{g}$ and $\tilde{A}$ matrices of VO^{2+}-doped ZASH single crystal for ions I and II. These values are the same at all temperatures in the 4.2 - 295 K range. The numbers in brackets are those reported by Borcherts et al. [20]. For other details see the caption of Table 4.3.

Ion	Principal Values		Direction Cosines		
			Z/Z′	X/X′	Y/Y′
I	$g_{z'}$ =	1.9384±0.0020 (1.9331)	0.4582	0.8011	0.3852
	$g_{x'}$ =	1.9854±0.0020 (1.9813)	-0.8107	0.5543	0.1884
	$g_{y'}$ =	1.9742±0.0020 (1.9801)	0.3644	0.2260	0.9034
	$A_{z''}$ =	-0.5648±0.0050 (0.6081)	-0.9974	0.0248	0.0677
	$A_{x''}$ =	-0.2881±0.0050 (0.2381)	-0.0406	0.9692	0.2429
	$A_{y''}$ =	-0.1724±0.0050 (0.2420)	0.0596	-0.2450	0.9677
II	$g_{z'}$ =	1.9315±0.0020 (1.9361)	0.5299	0.2297	0.8164
	$g_{x'}$ =	1.9821±0.0020 (1.9808)	-0.7609	-0.2964	0.5773
	$g_{y'}$ =	1.9884±0.0020 (1.9797)	0.3745	-0.9271	0.0177
	$A_{z''}$ =	-0.5343±0.0050 (0.6096)	0.9948	0.1234	0.1221
	$A_{x''}$ =	-0.2588±0.0050 (0.2370)	-0.1423	0.9767	0.1608
	$A_{y''}$ =	-0.1676±0.0050 (0.2420)	0.0993	0.1758	-0.9794

Table 4.6 Principal values and direction cosines of the $\tilde{g}$ and $\tilde{A}$ matrices of VO^{2+} in FASH single crystal for the ions I and II. The numbers in brackets for the principal values are those reported by Upreti and Saraswat [82], who assumed $g_{x'} = g_{y'} = g_{\perp}$ and $A_{x''} = A_{y''} = A_{\perp}$ (RT). For other details see the caption of Table 4.3.

Ion	Principal Values	Direction Cosines		
Temperature (K)		Z/Z'	X/X'	Y/Y'
295 I	$g_{z'}$ = 1.9364±0.0020 (1.941)	0.7400	0.6499	-0.1734
	$g_{x'}$ = 1.9809±0.0020 (1.990)	-0.6550	0.7549	0.0345
	$g_{y'}$ = 1.9846±0.0020 (1.990)	0.1534	0.0880	0.9843
	$A_{z''}$ = -0.5344±0.0050 (0.540)	-0.9919	0.1124	0.0593
	$A_{x''}$ = -0.2136±0.0050 (0.220)	0.1098	0.9930	-0.0446
	$A_{y''}$ = -0.1813±0.0050 (0.220)	0.0639	0.0378	0.9972
II	$g_{z'}$ = 1.9371±0.0020 (1.941)	0.0408	0.7407	-0.6707
	$g_{x'}$ = 1.9801±0.0020 (1.990)	-0.3309	0.6343	0.6904
	$g_{y'}$ = 1.9741±0.0020 (1.990)	0.9428	0.1938	0.6904
	$A_{z''}$ = -0.5412±0.0050 (0.522)	0.9909	-0.0041	0.1347
	$A_{x''}$ = -0.2578±0.0050 (0.220)	0.0157	0.9963	-0.0850
	$A_{y''}$ = -0.1776±0.0050 (0.220)	0.1339	-0.0864	-0.9872

Table 4.6 (continued)

80	I	$g_{z'}$ = 1.9363±0.0020	0.7452	0.6466	-0.1630
		$g_{x'}$ = 1.9907±0.0020	-0.6514	0.7582	0.0292
		$g_{y'}$ = 1.9868±0.0020	0.1425	0.0844	0.9862
		$A_{z''}$ = -0.5318±0.0050	-0.9512	-0.2967	0.0856
		$A_{x''}$ = -0.2174±0.0050	-0.2983	0.9545	-0.0063
		$A_{y''}$ = -0.1835±0.0050	0.0793	0.0314	0.9964
	II	$g_{z'}$ = 1.9401±0.0020	0.0388	0.7407	-0.6707
		$g_{x'}$ = 1.9827±0.0020	-0.3319	0.6426	0.6906
		$g_{y'}$ = 1.9661±0.0020	0.9425	0.1958	0.2708
		$A_{z''}$ = -0.5633±0.0050	0.9972	-0.0058	0.0742
		$A_{x''}$ = -0.2567±0.0050	0.0155	0.9912	-0.1312
		$A_{y''}$ = -0.2008±0.0050	0.0728	-0.1320	-0.9886
4.2	I	$g_{z'}$ = 1.9364±0.0020	0.7400	0.6499	-0.1734
		$g_{x'}$ = 1.9809±0.0020	-0.6550	0.7549	0.0345
		$g_{y'}$ = 1.9846±0.0020	0.1534	0.0880	0.9843
		$A_{z''}$ = -0.5344±0.0050	-0.9972	0.0378	0.0639
		$A_{x''}$ = -0.2136±0.0050	0.0446	0.9930	-0.1098
		$A_{y''}$ = -0.1813±0.0050	0.0593	0.1124	0.9919
	II	$g_{z'}$ = 1.9237±0.0020	0.0398	0.7413	-0.6699
		$g_{x'}$ = 1.9769±0.0020	-0.3310	0.6423	0.6913
		$g_{y'}$ = 1.9749±0.0020	0.9428	0.1942	0.2710
		$A_{z''}$ = -0.5238±0.0050	0.9915	-0.0027	0.1303
		$A_{x''}$ = -0.2373±0.0050	0.0010	0.9999	0.0129
		$A_{y''}$ = -0.1570±0.0050	0.1303	0.0127	-0.9914

Table 4.7 Principal values and direction cosines of the $\tilde{g}$ and $\tilde{A}$ matrices of VO^{2+} in COASH single crystal for the ions I and II. These values are the same at all temperatures in the 120 - 295 K range. The numbers in brackets for the principal values are those reported by Jayaram et al. [83]. For other details see the caption of Table 4.3.

Ion	Principal Values	Direction Cosines		
		Z/Z′	X/X′	Y/Y′
I	$g_{z'}$ = 1.9595±0.0020 (1.9381)	0.7400	0.6499	-0.1734
	$g_{x'}$ = 1.9960±0.0020 (2.0007)	-0.6550	0.7549	0.0345
	$g_{y'}$ = 1.9972±0.0020 (1.9902)	0.1534	0.0880	0.9843
	$A_{z''}$ = -0.5334±0.0050 (0.546)	-0.9974	0.0248	0.0677
	$A_{x''}$ = -0.1946±0.0050 (0.215)	-0.0406	0.9692	0.2429
	$A_{y''}$ = -0.1780±0.0050 (0.229)	0.0596	-0.2450	0.9677
II	$g_{z'}$ = 1.9533±0.0020 (1.9361)	0.2566	0.6593	0.7067
	$g_{x'}$ = 1.9847±0.0020 (2.0009)	0.2968	0.6421	-0.7068
	$g_{y'}$ = 1.9988±0.0020 (1.9906)	-0.9198	0.3911	-0.0309
	$A_{z''}$ = -0.5106±0.0050 (0.549)	0.9948	0.1234	0.1221
	$A_{x''}$ = -0.2530±0.0050 (0.215)	-0.1423	0.9767	0.1608
	$A_{y''}$ = -0.1658±0.0050 (0.220)	0.0993	0.1755	-0.9794

Table 4.8 Principal values and direction cosines of the $\tilde{g}$ and $\tilde{A}$ matrices of VO^{2+} in MDSD single crystal for the VO^{2+} ions I and II. These values are the same at all temperatures in the 113 - 410 K range. For other details see the caption of Table 4.3.

Ion	Principal Values	Direction Cosines		
		Z/Z′	X/X′	Y/Y′
I	$g_{z'}$ = 1.9461 ± 0.0020	0.7407	-0.6707	0.0388
	$g_{x'}$ = 1.9827 ± 0.0020	-0.6426	-0.6905	0.3319
	$g_{y'}$ = 1.9861 ± 0.0020	0.1958	0.2708	0.9425
	$A_{z'}$ = -0.5321 ± 0.0050	0.9972	-0.0057	0.0742
	$A_{x'}$ = -0.2240 ± 0.0050	0.0155	0.9912	-0.1312
	$A_{y'}$ = -0.1953 ± 0.0050	0.0728	-0.1320	-0.9886
II	$g_{z'}$ = 1.9391 ± 0.0020	0.0887	0.2905	-0.9528
	$g_{x'}$ = 1.9820 ± 0.0020	0.3386	0.8908	0.3039
	$g_{y'}$ = 1.9861 ± 0.0020	0.9358	-0.3498	0.0194
	$A_{z'}$ = -0.5328 ± 0.0050	0.9998	0.0009	0.0122
	$A_{x'}$ = -0.2230 ± 0.0050	-0.0025	0.9897	0.1431
	$A_{y'}$ = -0.2053 ± 0.0050	0.0121	0.1432	-0.9898

parameters [20, 75, 82, 83], determined at RT only, are also included in Tables 4.3, 4.4, 4.5, 4.6 and 4.7 for comparison. The principal values and direction cosines of $\tilde{g}$ and $\tilde{A}$ matrices for VO^{2+} in MDSD were found to be the same as those in MASH. (No parameters have been reported for VO^{2+}-doped MDSD.)

Specifically, it is seen from Table 4.5 that the principal axes of the $\tilde{g}^2$ and $\tilde{A}^2$ tensors for VO^{2+} in ZASH are almost coincident; in particular, no significant "in-plane anisotropy" [20, 85] exists, i.e., the principal X, Y axes for $\tilde{g}^2$ and $\tilde{A}^2$ are, indeed, coincident. This is consistent with the results of Strach et al. [85], and in disagreement with those of Borcherts et al. [20]. Thus, the present study has resolved the "in-plane anisotropy" controversy [15].

IV.5 Cu^{2+} in $MNa_2(SO_4)_2 \cdot 4H_4O$ (M = Mg, Co)

The EPR spectra of Cu^{2+} ion in MNST and CNST were fitted to the following S.H. [1]:

$$\mathcal{H} = \mu_B \vec{B} \cdot \tilde{g} \cdot \vec{S} + \vec{S} \cdot \tilde{A} \cdot \vec{I}, \qquad (4.14)$$

where S (= 1/2) is the electronic spin and I (= 3/2) is the nuclear spin of Cu^{2+} (for both ^{63}Cu and ^{65}Cu isotopes).

The principal values of the $\tilde{g}^2$ and $\tilde{A}^2$ tensors and their direction cosines were evaluated by the use of a least-squares fitting (LSF) procedure [77, 78]; they are listed in Tables 4.9 and 4.10. Since the EPR line positions

of Cu^{2+} in MNST and CNST did not change significantly with temperature, the SHP for the two samples are almost temperature independent. Further, it is seen from Tables 4.9 and 4.10 that the principal axes of the $\tilde{g}^2$ and $\tilde{A}^2$ tensors are coincident within the experimental errors.

It is also noted from Tables 4.9 and 4.10 that although a little difference is seen in the direction cosines of the $\tilde{g}$ matrices, the principal values of the $\tilde{g}$ and $\tilde{A}$ matrices of Cu^{2+} in MNST and CNST are extremely close to each other. This can be explained in the same way as that for VO^{2+} in Tutton salts (Chap. XI), arguing that the M^{2+} (M = Mg, Co) ions are not the nearest neighbors of the impurity ion Cu^{2+}; thus, they play little role in determining the SHP of Cu^{2+}.

Table 4.9 Principal values and direction cosines of the $\tilde{g}$ and $\tilde{A}$ matrices of Cu^{2+}-doped MNST single crystal at 113 K. The corresponding values of SHP at RT are found to be the same within experimental errors, except that the principal values of $\tilde{A}$ matrix are the average of those for ^{63}Cu and ^{65}Cu isotopes. For other details see the caption of Table 4.3.

Isotope	Principal Value	Direction Cosine Z/Z′	X/X′	Y/Y′
	$g_{z'}$ = 2.3991 ± 0.0030	0.0510	0.2027	0.9779
	$g_{x'}$ = 2.1979 ± 0.0030	0.7258	0.6651	-0.1758
	$g_{y'}$ = 2.0299 ± 0.0030	-0.6860	0.7187	-0.1132
^{65}Cu	$A_{z'}$ = 0.4430 ± 0.0060	0.9760	-0.0020	0.2176
	$A_{x'}$ = 0.2513 ± 0.0060	0.0097	0.9994	-0.0034
	$A_{y'}$ = 0.2060 ± 0.0060	-0.2174	0.0355	0.9755
^{63}Cu	$A_{z'}$ = 0.4202 ± 0.0060	0.9999	0.0017	-0.0024
	$A_{x'}$ = 0.2427 ± 0.0060	-0.0018	0.9988	-0.0499
	$A_{y'}$ = 0.1986 ± 0.0060	0.0023	0.0499	0.9988

Table 4.10 Principal values and direction cosines of the $\tilde{g}$ and $\tilde{A}$ matrices of Cu^{2+}-doped CNST single crystal at RT. Here the principal values of $\tilde{A}$ matrix are the average for the ^{63}Cu and ^{65}Cu isotopes, since the hf lines due to the two isotopes could not be separated because of large Cu^{2+} EPR linewidths observed in this host consisting of paramagnetic ions. For the other details see the caption of Table 4.3.

Principal Value	Direction Cosine		
	Z/Z′	X/X′	Y/Y′
$g_{z'} = 2.4023 \pm 0.0030$	0.0110	0.4282	0.9036
$g_{x'} = 2.1926 \pm 0.0030$	-0.3588	0.8452	-0.3961
$g_{y'} = 2.0256 \pm 0.0030$	-0.9334	-0.3198	0.1629
$A_{z'} = 0.3678 \pm 0.0060$	0.9999	-0.0146	0.0060
$A_{x'} = 0.2363 \pm 0.0060$	-0.0153	-0.9923	0.1233
$A_{y'} = 0.1679 \pm 0.0060$	-0.0041	0.1234	0.9924

CHAPTER V

POSITION AND LOCAL SYMMETRY OF IMPURITY IONS

V.1 Mn^{2+} in $(NH_4)_2SO_4$, Two Inequivalent Sublattices

V.1.1 Two Mn^{2+} centers

According to Abdulsabirov et al. [51], when the Mn^{2+} ion replaces a NH_4^+ ion in the lattice of $(NH_4)_2SO_4$ (AS), a neighbor NH_4^+ is displaced to create a vacancy for charge compensation; this is referred to as type-1 charge-compensation mechanism [86]. Abdulsabirov et al. [51] did not specify which of the NH_4^+ ions, in the α or β position, was replaced by Mn^{2+}, reporting the observation of only one Mn^{2+} center, with four physically equivalent orientations. However, in the present work, two physically inequivalent Mn^{2+} centers were, indeed, observed (Figs. 3.2, 3.3 and 3.4). This can be understood as follows. There exist two inequivalent, $NH_4^+(I)$ and $NH_4^+(II)$, ions in AS as verified by a neutron-diffraction experiment [41]. When a $NH_4^+(I)$ ion is replaced by Mn^{2+} a different Mn^{2+} center is created from that when the Mn^{2+} ion replaces a $NH_4^+(II)$ ion. This is due to the smaller space available around $NH_4^+(I)$ ion (α-position); the substitution of Mn^{2+} for $NH_4^+(I)$ causes greater distortion of the coordinations with the surrounding ligands than that caused when Mn^{2+} substitutes for $NH_4^+(II)$ ion. Assuming that the larger EPR linewidth of Mn^{2+} center II is due to the more distorted coordination, it appears

from the present experimental results that the Mn^{2+} ion, in center II, is in the α-position, which is surrounded by five SO_4^{2-} ions, with the β-position left as a vacancy. The Mn^{2+} ion in center I, replaces a NH_4^+(I) ion, which is in the β-position, surrounded by six SO_4^{2-} ions, forming a distorted octahedron, with the α-position left as vacancy. The α-position can also be considered, equivalently, to be surrounded by six SO_4^{2-} ions, one of them lying a little farther from the NH_4^+ ion, as compared with the remaining five SO_4^{2-} ions. Therefore, the environments of the α and β positions appear to be very close to each other.

Using the geometrical orientations of the SO_4^{2-} ions [48], and the assumption that SO_4^{2-} ions, being heavier than NH_4^+ ions, are responsible for the occurrence of a spontaneous strain (acoustic mode) in the AS crystal, it is presently concluded that there also exist two inequivalent SO_4^{2-} groups. This inequivalence may be caused by a <u>hypothetical</u> ferroelastic phase transition from hexagonal to orthorhombic symmetry, which is expected to take place at a temperature higher than 630 K in the AS crystal [39]. The NH_4^+ ions also respond to this hypothetical transition, resulting in the creation of two inequivalent, α and β, cations. It is, therefore, likely that the two inequivalent SO_4^{2-} groups, which ligand to Mn^{2+} ions, are responsible for the creation of two different Mn^{2+} centers in AS.

V.1.2 Two Inequivalent Sublattices

It is likely that the Mn^{2+} centers I and II belong to two inequivalent sublattices. Different EPR linewidths, and different temperature dependences of the EPR spectra for the two Mn^{2+} centers (Chap. VI), imply different distortions and different dynamic behaviours of these two sublattices. This conclusion is a logical consequence of the presence of two crystallographically-inequivalent NH_4^+ ions in the unit cell, which implies that there also exist two sets of inequivalent SO_4^{2-} ions in the lattices of AS, since the two α- and β-NH_4^+ groups are surrounded by different SO_4^{2-} groups. The existence of two inequivalent sublattices in AS has also been proposed from temperature dependence of the reported spontaneous polarization, and softening of a coupled-lattice vibration mode by Fujimoto et al [59]. As for the EPR studies on AS, the two-sublattices model was proposed only from the EPR of SeO_3^- ions in AS, namely, from the observation of two inequivalent SeO_3^- ions, which substitute for the SO_4^{2-} ions, by Fujimoto and Jerzak [58].

V.2 Gd^{3+} in $NH_4Pr(SO_4)_2 \cdot 4H_2O$, A Superposition-model Calculation

As mentioned in Chap. III, a Gd^{3+} ion enters the site of a Pr^{3+} ion in APST substitutionally. It is noted that the value of the zero-field splitting parameter b_2^0 of Gd^{3+} in

APST (~ 0.35 GHz), which is about the same as those in the isostructural ACST, ANST and ASST hosts [65, 66, 67], is much smaller compared to those in other host crystals, e.g. $|b_2^0|$ = 2.4 - 2.6 GHz in $LiYb_xY_{1-x}F_4$ (x = 0.0 - 1.0) [87] and $|b_2^0|$ = 0.7 - 0.8 GHz in RF_3 (R = La, Ce, Pr, Nd) [88]. Buckmaster et al. [65, 66, 67] suggested that a lower symmetry would lead to a larger value of b_2^0, which is in disagreement with the present case of a local symmetry lower than C_{4v} at the Gd^{3+} ion, for which the value of b_2^0 is rather small.

The presently-estimated small value of b_2^0 can be well explained by the superposition model of Newman [88, 89]. In the superposition model, the SHP (b_ℓ^m) can be expressed as linear combinations of single-ligand contributions via the intrinsic parameters $\bar{b}_\ell(R_0)$, as follows:

$$b_\ell^m = \sum_i \bar{b}_\ell(R_i)\ K_\ell^m(\theta_i,\phi_i), \tag{5.1}$$

where

$$\bar{b}_\ell(R_i) = \bar{b}_\ell(R_0)(R_0/R_i)^{t_\ell}. \tag{5.2}$$

In eqs. (5.1) and (5.2), (R_i, θ_i, ϕ_i) are the coordinates of ligand i, and R_0 is a particular reference bond length, which has been presently chosen to be 0.2499 nm, namely, the length of the Pr^{3+}-O(2) bond. The $K_\ell^m(\theta,\phi)$ are angular functions. Specifically [89],

$$K_2^0(\theta,\phi) = (3\cos^2\theta - 1)/2,$$

$$K_4^0(\theta,\phi) = (35\cos^4\theta - 30\cos^2\theta + 3)/8,$$

$$K_4^4(\theta,\phi) = (35\sin^4\theta\cos 4\phi)/8.$$

For an APST crystal, one takes into account the nine ligand-oxygen ions, forming a distorted-monocapped square antiprism (Chap. II), being the nearest neighbors to the Gd^{3+} ion, which substitutes for a Pr^{3+} ion (Fig. 2.4a). In the absence of crystal-structure data for APST, the values of (R_i,θ_i,ϕ_i) for APST can be calculated from the reported crystal-structure data for the isostructural ASST [63], by the use of Vegard's law [90]. Finally,

$$\bar{b}_\ell(R_0) = b_\ell^m / [\sum_i (R_0/R_i)^{t_\ell} K_\ell^m(\theta_i, \phi_i)]. \qquad (5.3)$$

The intrinsic parameter $\tilde{b}_2$ and value of t_2 can now be determined, according to the following procedure [88]. For a chosen value of t_2 one can determine $\tilde{b}_2$ in two ways. (a) from eq. (5.3), for APST one has

$$\bar{b}_2(R_0) = b_2^0/[\sum_i (R_0/R_i)^{t_2} K_2^0(\theta_i, \phi_i)]. \qquad (5.4)$$

(b) If the relation (5.2) is indeed true it should be possible to express $\bar{b}_2(R_0)$ for APST in terms of that for the Gd^{3+} ion, denoted as $\bar{b}_2(Gd)$, in the isostructural $NH_4Gd(SO_4)_2\cdot 4H_2O$ lattice, in which Gd^{3+} ions are the host

ions. The required value of b_2^0 (= 0.380 GHz) for Gd^{3+} in this concentrated crystal was obtained since b_2^0 is linear in host-ion radius [88]. Thus one has

$$\bar{b}_2(R_0) = \bar{b}_2(Gd)(R_0^{Gd}/R_0)^{t_2}, \tag{5.5}$$

where R_0^{Gd} (= 0.229 nm) is the length of the Gd^{3+}-O(2) bond in the unit cell of the $NH_4Gd(SO_4)_2 \cdot 4H_2O$ crystal [63, 88]. The values of $\bar{b}_2$ as determined from eqs. (5.4) and (5.5) are referred to as $\bar{b}_2(A)$ and $\bar{b}_2(B)$, respectively. In order to find the best $\bar{b}_2$ and t_2 values for APST, the minimum of the function

$$E(t_2) = [\bar{b}_2(A) - \bar{b}_2(B)]/\bar{b}_2(B) \tag{5.6}$$

was computed. Finally, the values of $\bar{b}_2$ and t_2 turned out to be

$$\bar{b}_2 = -4.85 \text{ GHz} \quad \text{and} \quad t_2 = 9.5 \pm 1.0.$$

The intrinsic parameter $\bar{b}_2$ calculated here for Gd^{3+} in APST is very close to those calculated for Gd^{3+} in $LiYb_xY_{1-x}F_4$ (x = 0.0 - 1.0) [87] and RF_3 (R = La, Ce, Pr, Nd) [88]. The t_2 value determined here is close to that found for RF_3 (t_2 = 9) [88]. It is to be noted here, in particular, that the sign of the presently-calculated value of $\bar{b}_2$ is negative, the same as those in some other hosts, for which the sign of resulting b_2^0 has been determined to be positive from relative-intensity data at LHT [87, 88]. This fact supports

the present assumption of a positive absolute sign for b_2^0 in Chapter IV [89].

As for the value of the intrinsic parameter $\bar{b}_4$ (= 0.020 GHz), it was estimated using only the value of b_4^0 (= -0.0087 GHz), since the use of b_4^m with $m \neq 0$, requires the exact values of ϕ_i, which are not available. $\bar{b}_4$ was found to increase slowly with the increase in the value of t_4. The corresponding value of t_4 was found to be 27 ± 1, which is much larger than 14, the value calculated for RF_3 [88], and still much larger than that in the range 5 - 8 as calculated for MeF_2 hosts (Me = Cd, Ca, Sr, Pb, Ba) [91]. The value of t_4 for APST was, however, calculated without considering any distortions of the positions of the ligand oxygen ions, which are likely to be caused when a Gd^{3+} ion substitutes for a Pr^{3+} ion, since the two ions possess different ionic radii. In the absence of any knowledge of what these distortions are, some simple distortions were considered in order to see the effect on t_4. For example, rather small, and same increases, by $\Delta\theta$ in the value of each of the nine angles θ_i for the oxygen ions, yields the t_4 values to be 15, 11, and 2 for $\Delta\theta$ equal to 1.5^0, 2^0 and 5^0, respectively. This means that the same small increase in the values of all θ_i by $\Delta\theta = 1.7^0$ yields a $t_4 = 14$ which is consistent with those for RF_3 and MeF_2 hosts.

Finally, a small absolute value of b_2^0 is quite plausible if one realizes that the different angular factors

$K_\ell^m(\theta_i,\phi_i)$ in eq. (5.1) for various oxygen ligands partially cancel each other for the nine-fold coordinated Gd^{3+} ion in APST. The same considerations should apply to the isostructural Gd^{3+}-doped ANST, ASST and ACST host crystals.

V.3 VO^{2+} in $M(NH_4)_2(SO_4)_2\cdot 6H_2O$ (M = Cd, Mg, Zn, Fe, Co): Model of $[VO(H_2O)_5]^{2+}$ Complex

The model of $[VO(H_2O)_5]^{2+}$ complex [20] explains well the features of the EPR spectra for VO^{2+}-doped CASH, MASH, ZASH, FASH and COASH crystals. The site of an M^{2+} ion in $M(NH_4)_2(SO_4)_2\cdot 6H_2O$ (M = Cd, Mg, Zn, Fe, Co) is the most probable site for substitution by a VO^{2+} ion, both being doubly ionized. The VO^{2+} ion enters the lattice to substitute for an M^{2+} ion and to form a $[VO(H_2O)_5]^{2+}$ complex with its nearest-neighbors (Fig. 5.1), which possesses a tetragonally-distorted octahedral symmetry. The two observed groups of symmetry-related EPR lines are due to two symmetrically-oriented $[VO(H_2O)_5]^{2+}$ complexes. The orientation of the principal Z axis of the $\tilde{g}^2$ tensor for any VO^{2+} complex is expected to be along its V^{4+}-O^{2-} bond [20, 92]. Using the direction cosines (Tables 3.3, 3.4, 3.5, 3.6 and 3.7) and the crystal-structural data, the principal Z axes of the $\tilde{g}^2$ tensor are found to be almost parallel to the M^{2+}-$H_2O(7)$ direction for ion I, and to the M^{2+}-$H_2O(8)$ direction for ion II. When a VO^{2+} ion substitutes for an M^{2+} ion in a $M(NH_4)_2(SO_4)_2\cdot 6H_2O$ lattice, it expels one of the

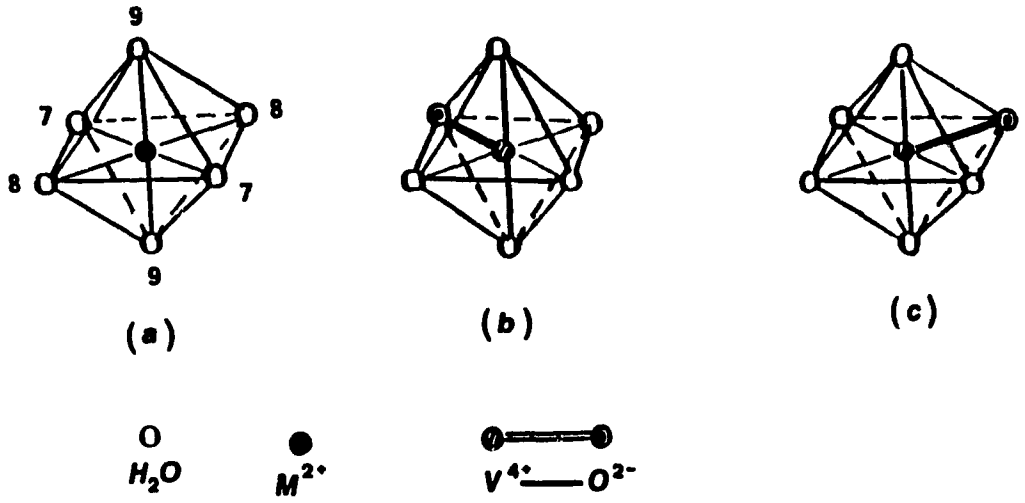

Fig. 5.1 Orientations of the VO^{2+} ions with respect to the $[VO(H_2O)_5]^{2+}$ complexes, in the CASH, MASH, ZASH, FASH and COASH lattices: (a) octahedral coordination of water molecules around M^{2+} ion, (b) V^{4+}-O^{2-} bond orientation for ion I, and (c) V^{4+}-O^{2-} bond orientation for ion II. (It is noted that the maximum SHF splitting occurs when $\vec{B}$ is along the V^{4+}-O^{2-} bond.)

$H_2O(7)$, or $H_2O(8)$, or $H_2O(9)$ molecules, forming the so-called $[VO(H_2O)_5]^{2+}$ complex [20], whose geometrical axis, i.e., the line joining the V^{4+} and O^{2-} ions, is oriented along the direction previously formed by the M^{2+}-$H_2O(7)$ pair for ion I, and by the M^{2+}-$H_2O(8)$ pair for ion II. (Jayaram et al. [83] suggested, incorrectly, that the axis of the VO^{2+} ion II was along the M^{2+}-$H_2O(9)$ direction for MASH and COASH.) The orientations of $\vec{B}$, for which the maximum SHF splitting occurs, i.e., X_A and X_B, also support this contention, as discussed in Chap. VII below. There is a finite, though small, probability, in agreement with the experimental data, for a VO^{2+} ion (ion III in the present case) to orient itself along the M^{2+}-$H_2O(9)$ direction; the M^{2+}-$H_2O(9)$ distance is the smallest of the three, M^{2+}-$H_2O(i)$, i = 7, 8, 9, distances. As for a VO^{2+}-doped MDSD crystal (Table 3.8), replacing $H_2O(i)$ by $D_2O(i)$ to form a $[VO(D_2O)_5]^{2+}$-complex does not change the orientations of V^{4+}-O^{2-} bonds (Chap. IV).

V.4 Cu^{2+} in $MNa_2(SO_4)_2 \cdot 4H_2O$ (M = Mg, Co), Jahn-Teller Distortion

From the crystal structure of MNST and CNST, it appears that the site of an M^{2+} (M = Mg, Co) ion, the center of $MO_2(H_2O)_4$ complex, is the most probable site for substitution by a Cu^{2+} ion, forming a $CuO_2(H_2O)_4$ complex. Sastry et al. [121] concluded, from the EPR study of

Cu^{2+}-doped ZNST, that the orientation of the maximum principal value of the $\tilde{g}$ matrix, g_z, is along the Zn^{2+}-$H_2O(1)$ direction. The presently-determined direction cosines of $\tilde{g}$ matrices for both MNST and CNST (Chap. IV) do not suggest a correlation between the orientations of the principal axes of $\tilde{g}$ matrices and the bond directions in the $MO_2(H_2O)_4$ complex of the MNST and CNST crystals. Similar considerations apply to Gd^{3+} in ZNST host [120].

When a Cu^{2+} ion substitutes for an M^{2+} ion to convert a $MO_2(H_2O)_4$ complex to a $CuO_2(H_2O)_4$ complex, it introduces a local distortion due to the difference in the ionic radii between M^{2+} and Cu^{2+} ions. Further, the Cu^{2+} ion, being a Jahn-Teller ion, causes an additional distortion, which is referred to as Jahn-Teller effect (JTE) (Chap. X). Due to distortions, the three principal values of the $\tilde{g}$ matrices of Cu^{2+}, in both MNST and CNST, are all different from each other at room and lower temperatures (Chap. IV), indicating a lower symmetry of the Cu^{2+} complex [i.e., $CuO_2(H_2O)_4$ complex], namely, orthorhombically-distorted octahedral symmetry.

CHAPTER VI

STUDY OF PHASE TRANSITIONS

VI.1 Ferroelectric Phase Transition in $(NH_4)_2SO_4$

VI.1.1 Temperature Variation of Mn^{2+} EPR Spectra

Fig. 6.1 exhibits the variation of the highest-field line position of the highest-field hf sextet corresponding to center I, as well as that of the lowest-field line position of the highest-field hf sextet corresponding to center II, for the orientation of the external magnetic field $\vec{B}$ in the ab plane, 25^0 away from the a-axis, in the 113 - 398 K temperature range. (These hf lines are particularly chosen, because they are not flanked by other lines, and are easy to identify.) It is clearly seen from Fig. 6.1 that, as the temperature is decreased, the line positions corresponding to center I show an abrupt jump to higher magnetic fields at T_c = 223 K, thereafter, each line splits into two lines below T_c, characterizing a first-order phase transition of the sublattice of AS crystal, to which it belongs. On the other hand, the line positions corresponding to center II do not at all undergo any jumps at T_c, as the temperature is decreased, each of them experiences only a splitting into two lines below T_c; this indicates a second-order phase transition of the sublattice of AS, to which center II belongs. Further, as seen from Fig. 6.1, the splittings of the lines corresponding to

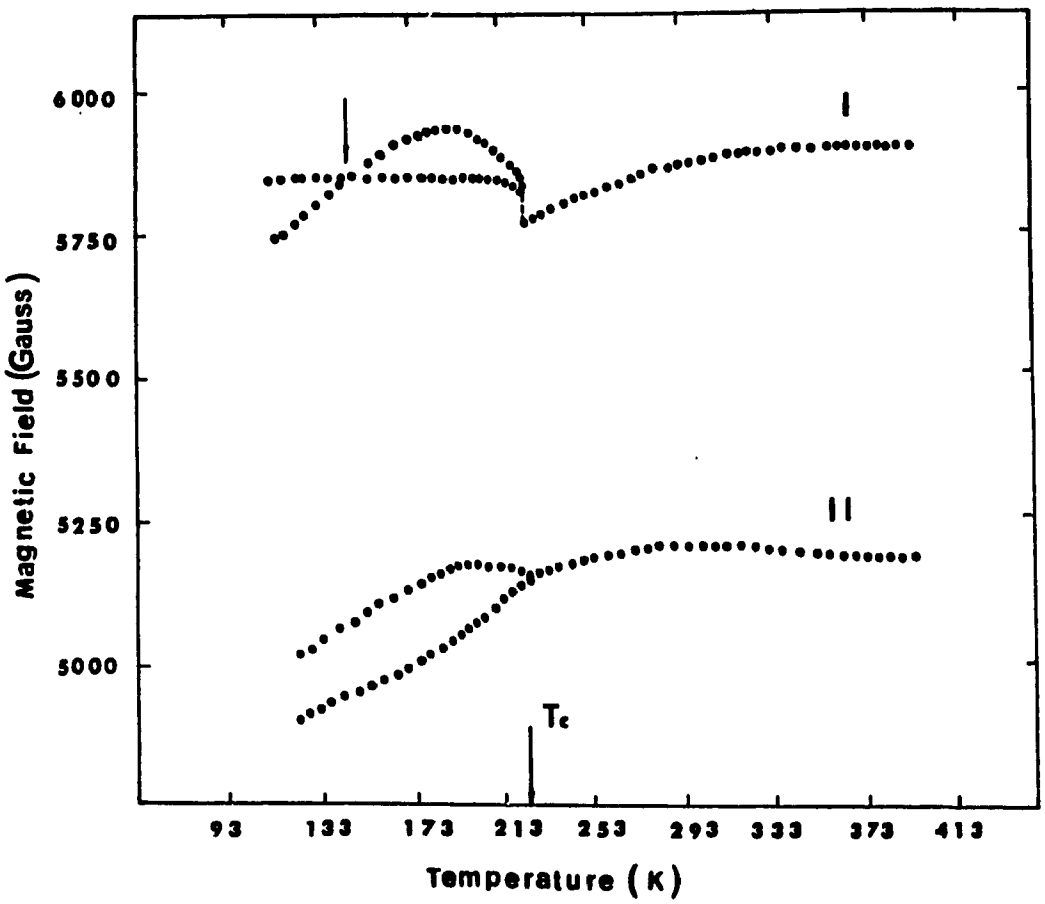

Fig. 6.1 Temperature variation of the highest-field and the lowest-field hf EPR line positions for the highest-field hf sextets for Mn^{2+} centers I and II in AS, respectively, from 113 K to 398 K, for $\vec{B}$ in the ab plane, 25^{0} from the a-axis. At T_c = 223 K, a jump of the line position for center I and a continuous change of line position for center II, are clearly exhibited. As well unusual crossing of split lines for Mn^{2+} center I at 147 K is clearly visible.

center I exhibit a unique feature never reported previously; the line splitting first increases with decreasing temperature below T_c, then it starts to diminish, finally becoming zero at about 147 K. It splits again below 147 K in the opposite direction. This feature is not exhibited by the splitting of the EPR lines, which correspond to center II.

Fig. 6.2 exhibits detailed EPR spectra for $\vec{B}$ in the ab plane, 25^0 from the a axis, over a temperature region, including T_c, confirming the conclusions drawn from Fig. 6.1. Another feature that is apparent from Fig. 6.2 for center I, is that at 223.5 K (just above T_c), some weak lines of the ferroelectric phase, that exists below T_c, are also observed, although the EPR lines of the paraelectric phase, that exists above T_c, are dominant. This indicates a coexistence of the paraelectric and ferroelectric phases just above T_c. Fig. 6.3 displays a detailed temperature dependence of the EPR spectra for $\vec{B}$ in the ab plane, 25^0 from the a axis, over a temperature region including 147 K; the EPR lines corresponding to center I show crossing of split lines, in accordance with that exhibited by Fig. 6.1. On the other hand, the lines corresponding to center II continue to remain split, without reversing their splitting, or crossing, at all temperatures below T_c.

Variable-temperature EPR measurements were made for the orientation of $\vec{B}$ in the bc and ac planes also; similar results to those observed for the orientation of $\vec{B}$ in the ab

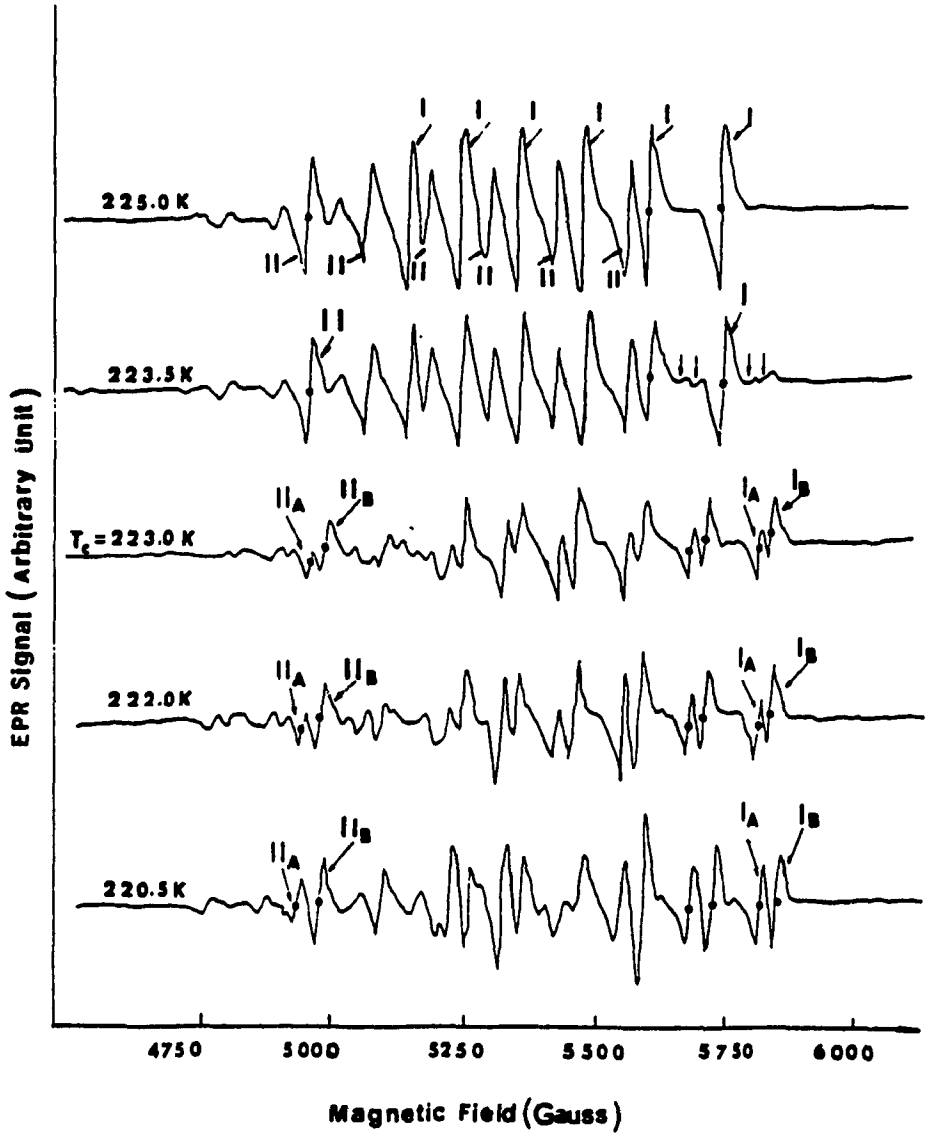

Fig. 6.2 EPR spectra for the highest-field Mn^{2+} sextet in AS single crystal, in the temperature range, covering T_c = 223 K, for $\vec{B}$ in the ab plane, 25^0 from the a-axis. I_A and I_B indicate the spectra from the two sub-sublattices to which center I belongs below T_c; the same applies to II_A and II_B for center II.

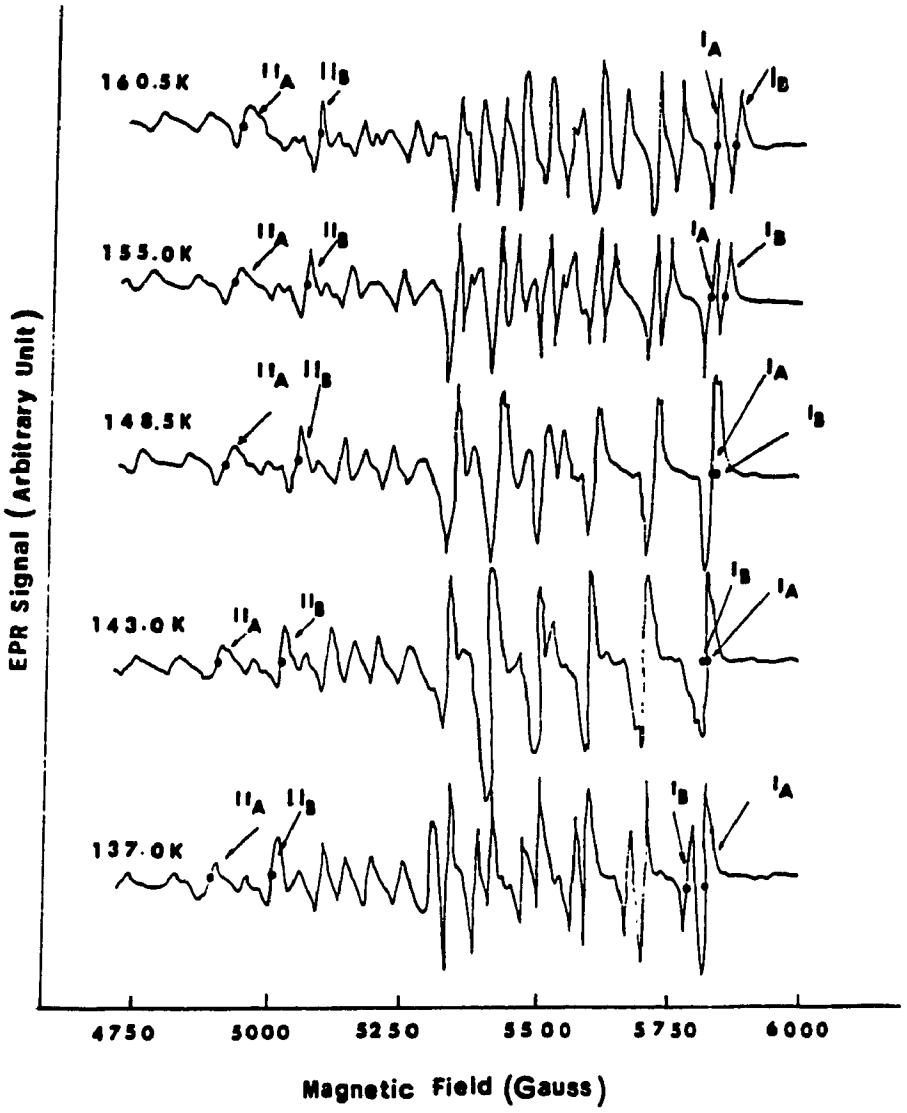

Fig. 6.3 EPR spectra, for the highest-field Mn^{2+} hf sextet in AS single crystal in a temperature range covering 147 K, for $\vec{B}$ in the ab plane, 25^0 from the a-axis. Mn^{2+} center I exhibits an unusual crossing of split lines at 147 K, as indicated by the relative positions of the solid circles identifying the lines corresponding to center I on the highest-field side. I_A and I_B indicate the spectra from the two sub-sublattices to which center I belongs below T_c; the same applies to II_A and II_B for center II.

plane were found, except for the fact that no crossing of split lines was observed below T_c for any Mn^{2+} center.

VI.1.2 Critical Exponents

For both the centers I and II, the critical exponent β is presently found to be 0.49 ± 0.03 from the line splitting (ΔB), in the region ($0 < (T_c - T) < 10$ K). This is clear from Fig. 6.4, exhibiting log-log straight-line plots of ΔB versus ($T_c - T$), the slopes being β. The result for center II is in agreement with the that reported by Misra and Shrivastava [53], where a second-order transition was considered, while that for center I it is in agreement with that reported by Bhat et al. [61] for CrO_4^{3-}-doped AS crystal for the CrO_4^{3-} center, which undergoes a first-order phase transition.

VI.1.3 Scaling Law and Rushbrooke Inequality

There exists a relation, $(\alpha + 2\beta + \gamma) = 2$, involving the critical exponents α and γ for $T > T_c$ and β for $T < T_c$, referred to as a <u>scaling</u> law [11]. It is interesting to examine the fulfillment of this law for AS. The value of critical exponent β is determined presently to be 0.5. The critical exponents α and γ are defined, for $T > T_c$, from the relations $C \propto (T - T_c)^{-\alpha}$ and $\chi \propto (T - T_c)^{-\gamma}$, where C and χ are specific heat and susceptibility, respectively [93]. For the AS crystal, γ has been reported to be - 1.0 [70]. As for α, it has been determined by Hoshino et al. [36], to be

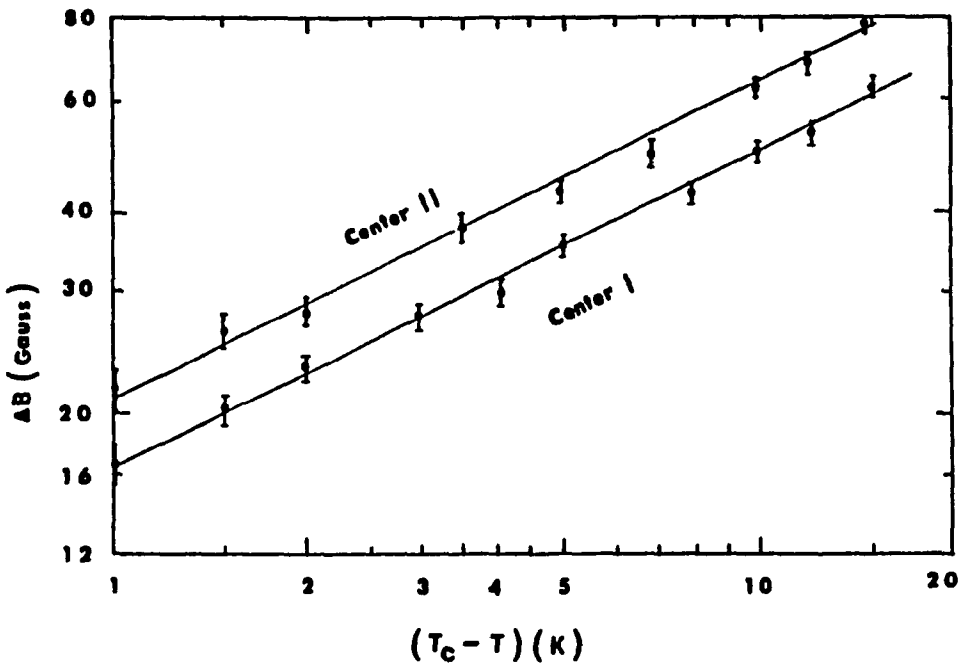

Fig. 6.4 Log-log plot of the temperature dependence of the line splitting, ΔB, for Mn^{2+} centers I and II in AS, below the ferroelectric transition temperature, T_c. The straight lines show that $\Delta B \propto (T_c - T)^{\beta}$, with $\beta = 0.49 \pm 0.03$ and $T_c = 223$ K, for both the centers in the range 0 K < $(T_c - T)$ < 10 K; this is consistent with Laudau theory [11].

almost 0.0, for $T > T_c$. Thus, for AS, $\alpha + 2\beta + \gamma \cong 2$. This is in agreement with the scaling law. For $T < T_c$, there exists only one inequality: $\alpha' + 2\beta + \gamma' \geq 2$, known as Rushbrooke inequality [93]. Here the exponents α' and γ' are defined from the relations $C \propto (T_c - T)^{-\alpha'}$ and $\chi \propto (T_c - T)^{-\gamma'}$ [93]. For the AS crystal, γ' and α' have been reported to be ~ 1.0 [70], and - 0.2 [36], respectively. Thus for AS, $\alpha' + 2\beta + \gamma' \cong 2.2$. This is in good agreement with Rushbrooke inequality.

VI.1.4 Mechanism of Phase Transition in $(NH_4)_2SO_4$

Unruh et al. [37] concluded, from their measurement of the spontaneous polarization, P_s, of AS, which changes sign below 85 K, that P_s should not be treated as an order parameter of phase transition, and, thus, considered the transition to be <u>ferrielectric</u>, implying that the two sublattices contribute differently to the resultant spontaneous polarizations. Since P_s, which is related to the optical mode of lattice vibration, is not an order parameter, some other mode must be responsible for the occurrence of the phase transition. This other mode is presently suggested to be the acoustic mode, related to the existence of ferroelasticity in the paraelectric phase of the AS crystal above T_c. The high value of the spontaneous strain may cause additional crystal distortion, leading to ferroelastic domains. This creates additional weak lines in

the Mn^{2+} spectra at room-temperature in AS, over and above those already mentioned. It is likely that the coupling to the spontaneous strain (acoustic mode) is different for the two sublattices. It is suggested presently that the sublattice, to which Mn^{2+} center I belongs, which undergoes first-order transition, is strongly coupled to the acoustic mode, while the sublattice to which center II belongs, which undergoes second-order transition, is only weakly coupled to the acoustic mode. This explains qualitatively why these Mn^{2+} ions which belong to different sublattices behave differently at T_c. Bhat et al. [61] also noticed the coexistence of discontinues (the same as that of center I) and continuous (the same as that of center II), behaviours of the EPR lines in CrO_4^{3-}-doped AS crystal at T_c. However, they did not invoke the two-inequivalent-sublattices model, which would have provided the correct explanation of their spectra.

The EPR linewidths for Mn^{2+} were measured for the two centers in the 113 - 398 K temperature range. Center II is characterized by a slightly larger linewidth than that of center I. The EPR linewidth for center I is 1.4 ± 0.1 mT above T_c, while it is 1.6 ± 0.1 mT below T_c. On the other hand, the linewidth for center II remains 1.7 ± 0.1 mT at all temperatures. The fact that only the linewidth corresponding to center I experiences a change at T_c supports the contention that only one sublattice in AS,

namely, the one to which center I belongs, is responsible for the onset of ferroelectric phase transition; the other sublattice, the one to which center II belongs, just follows this phase transition.

The reversal of the sign of polarization, P_s, at low temperatures, as observed by Unruh [37], can be explained as follows. As the temperature is lowered below T_c, the sublattice, to which center I belongs, splits further into two sublattices with opposite polarizations; these polarizations exhibit different temperature dependences. The crossing of split lines for center I occurs when these two polarizations are equal and opposite, i.e., at 147 K. (Fig. 6.3).

The two-inequivalent-sublattices model, as proposed presently, is not the same as that postulated by Sawada et al. [48], in which no further splittings of the sublattices below T_c was predicted, contrary to the present finding for AS, wherein each of the two sublattices, above T_c, splits into two sub-sublattices below T_c. For, otherwise, the observed polarization behavior below T_c could not be correctly explained, as discussed above. In the model proposed presently, the SO_4^{2-} ions are also considered to be inequivalent, contrary to the assumption of Sawada et al. [48]. The SO_4^{2-} ions play an important role in the splitting of each of two sublattices, which exist above T_c, into two sublattices below T_c. The effectiveness of SO_4^{2-} ions in the

ferroelectric phase transition has also been suggested by Sawada et al. [39], and by Bhat et al. [61].

The present results and interpretation are similar to those drawn by Fujimoto and Jerzak [58] from the EPR of SeO_3^- ions in AS crystal. According to them, two inequivalent centers of SeO_3^- radical in AS belong to two coupled sublattices; the EPR lines, above T_c, of one center are very strongly temperature dependent, while those of the other almost temperature independent.

VI.2 First-order Structural Phase Transitions in $NH_4Pr(SO_4)\cdot 4H_2O$

VI.2.1 Temperature Variation of EPR Spectra

EPR spectra were recorded, for $\vec{B}$ parallel to the RT Z axis of one of the magnetically-inequivalent Gd^{3+} ions in APST, in the 4.2 - 410 K temperature range. (Above 410 K the crystal is destroyed due to dehydration.) Figs. 6.5a and 6.5b display, respectively, the temperature variations of the overall splitting and linewidth of the EPR spectra.

(i) <u>T > RT</u>. As seen from Figs. 6.5a and 6.5b, the main features of the EPR spectra remain the same at temperatures higher than RT as those at RT. However, at higher temperature, the overall splitting decreases significantly, implying that the zero-field splitting parameter, b_2^0, decreases as the temperature increases. For example, at 374 K, b_2^0 was estimated to be 0.297 ± 0.002 GHz using the EPR

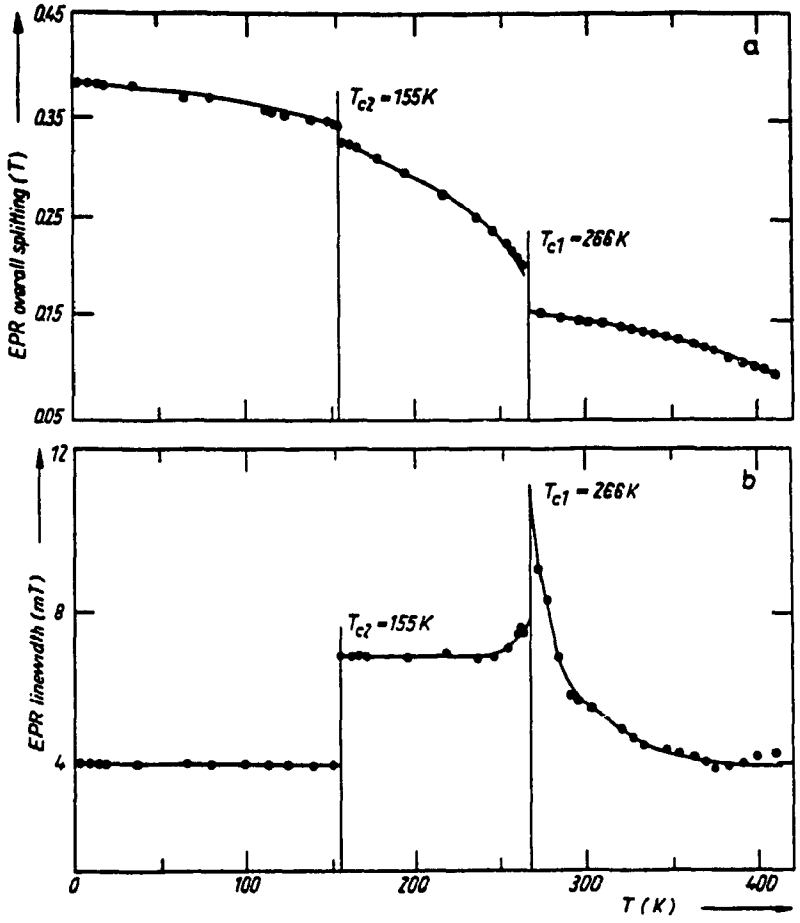

Fig. 6.5 Temperature variation of (a) the overall splittings of the EPR spectra and (b) the EPR linewidth for $\vec{B}$ along the RT Z axis of one of the magnetically-inequivalent Gd^{3+} ions. The two phase transitions, occurring at T_{c1} = 266 K and T_{c2} = 155 K, are clearly seen.

line positions for $\vec{B} \parallel \vec{Z}$ and $\vec{B} \parallel \vec{X}$, being 14.2% less than the RT value. This behavior is similar to that for Gd^{3+}-doped $LiYb_xY_{1-x}F_4$ ($x = 0.0 - 1.0$) crystals [87], where the temperature dependence of b_2^0 has been accounted for by the spin-phonon interaction and thermal expansion. Further, the EPR linewidth decreases as the temperature is increased, indicating a decrease in the host-ion spin-lattice relaxation time (τ) of Pr^{3+} (Chap. IX).

(ii) T < RT. As the temperature was decreased below RT, the overall splitting of the spectrum for $\vec{B} \parallel \vec{Z}$ increased, associated with an increase in the linewidths of each of the 14 allowed lines corresponding to the two magnetically-inequivalent Gd^{3+} ions. The linewidths for all the lines were the same at any temperature. At 267 ± 0.5 K, only 7 broad lines could be observed. A new spectrum with 14 lines, characterized by a much larger overall splitting, appeared below T_{c1} = 266 ± 0.5 K, indicating that a phase transition had occurred at T_{c1}. Below T_{c1}, the EPR spectra were much better resolved than those observed between RT and 267 K. The Z axis of one of the magnetically-inequivalent Gd^{3+} ions had about the same orientation as that in the RT phase. However, the magnetic Z axes corresponding to the two magnetically-inequivalent Gd^{3+} ions were no longer perpendicular to each other, as was the case at RT, perhaps due to the disappearance of the inversion plane that existed in the RT phase. No significant change in the spectra was

observed in the 266 - 156 K temperature range, except that the overall splitting continued to increase monotonically as the temperature was lowered. At T_{c2} = 155 ± 0.5 K another phase transition occurred, since the spectrum showed a drastic change, as revealed by the appearance of a well-resolved spectrum, with very narrow linewidths, below T_{c2}. The EPR line intensities increased abruptly as the temperature was lowered below T_{c2}; a total of 56 lines corresponding to eight magnetically-inequivalent Gd^{3+} ions were observed. Below T_{c2}, as $\vec{B}$ was rotated in the ZX plane of the RT phase, eight maxima of the overall splitting were observed. Below T_{c2}, the overall splitting of the EPR spectra increased; however, no further drastic changes were found down to 4.2 K.

The abrupt changes of the overall splittings and the linewidths, exhibited in Figs. 6.5a and 6.5b, indicate that the two phase transitions, occurring at T_{c1} and T_{c2}, are each of first-order.

As the temperature was increased from 4.2 K to RT, all the spectra and the phase transitions as observed with the lowering of temperature were found to repeat themselves, except that the values of the phase-transition temperatures T_{c1}, T_{c2} were found to be about 2 K higher than those determined when decreasing the temperature.

(iii) Comparison with previously-reported data on the phase transitions in the isostructural ACST and ASST

crystals. Buckmaster et al. [66, 67] reported the occurrences of three phase transitions in the 97 - 304 K temperature range for the isostructural ACST and ASST crystals. For the APST crystal, the present EPR study revealed only the existence of two phase transitions in this temperature range with different values of T_{c1} and T_{c2} from those for ASST and ACST. However, the present results are in agreement with those found by the IR and DSC measurements for the APST crystal, which also yielded two transitions; although, they occurred at lower temperatures; T_{c1} and T_{c2} being 36 K and 5 K lower, respectively [68].

VI.2.2 Nature of the Phase Transitions in $NH_4Pr(SO_4)_2 \cdot 4H_2O$

Some conclusions regarding the nature and physical mechanisms of the phase transition, can be made for APST, based on the present and previously-reported EPR data on the isostructural ACST, ANST and ASST host crystals [65, 66, 67], in conjunction with the crystal-structure and IR data on APST. These are described as follows:

(i) Between T_{c1} and T_{c2}, the Z axes of the two magnetically-inequivalent Gd^{3+} centers were no longer observed to be perpendicular to each other, implying the disappearance of the inversion plane that existed at RT.

(ii) Below T_{c2}, there were observed eight magnetically-inequivalent Gd^{3+} ions, implying the breakdown of the Pr^{3+} pairs that existed above T_{c2}, and the appearance

of a doubled unit cell, wherein one of the three unit cell parameters (a, b, c) becomes doubled, forming the so-called "superstructure".

(iii) At temperatures just above T_{c1} (266 K), the broadening of EPR lines is similar to that observed for the Cr^{3+} impurity ion in the $(NH_4)Al(SO_4)_2 \cdot 12H_2O$ alum, reported by Owens [94], attributed to the fluctuations in the fine-structure tensor due to the dipoles corresponding to H_2O molecules. Further, the behaviours of the H_2O molecules and the NH_4^+, SO_4^{2-} ions change at low temperatures, thereby affecting the EPR spectra. As revealed by infrared (IR) studies [63, 67], the NH_4^+ ions rotate freely in the RT phase, but not below T_{c1}. Below T_{c2}, new bands in the IR spectra, due to the H_2O molecules and SO_4^{2-} ions, were observed [67], as compared to that at RT.

(iv) The sudden increase in the intensity of the EPR lines below T_{c2} is due to a decrease in the dielectric constant of the sample [11], since a sudden decrease in the leakage current of the microwave power reflected from the EPR cavity was observed upon cooling the sample below T_{c2}.

CHAPTER VII

SUPERHYPERFINE INTERACTION

VII.1 Principal Values and Axes of SHF Interaction Tensor

The superhyperfine (SHF) interaction is the interaction between the electronic magnetic moment of the impurity ion and nuclear magnetic moment of the ligand ions in the host lattice. It causes further splitting of each of the EPR hyperfine lines of the impurity ion, known as the SHF splitting. In this chapter, the SHF interaction between the impurity ion VO^{2+} and the ligand protons is considered. The observed SHF splittings of the VO^{2+} EPR lines in the hydrated Tutton salts have been described, in detail, in Chapter III.

The maximum principal values, $A_{\parallel}^{L}$, of the SHF coupling tensor, $\tilde{A}^{L}$, for the interaction of VO^{2+} ion with the protons of the nearest-neighbor water molecule in CASH, MASH and ZASH lattices, for the two VO^{2+} ions [three VO^{2+} ions in the case of ZASH (Chap. III)], are listed in Table 7.1, as evaluated from the respective maximum SHF splittings, using the expression which takes into account the quintet splitting:

$$A_{\parallel}^{L} = (1/4)\mu_B g_{\perp}(B^{-} - B^{+}), \qquad (7.1)$$

where $(B^{-} - B^{+})$ is the overall SHF splitting. For ion I of CASH, MASH or ZASH, the maximum VO^{2+} SHF splitting occurred

Table 7.1 The principal values (in MHz) of SHF interaction tensor, $\tilde{A}^L$, and values (dimensionless) of density of the unpaired electron of VO^{2+} at the site of a ligand proton, f_s, for VO^{2+} in $M(NH_4)_2(SO_4)_2 \cdot 6H_2O$ (M = Cd, Mg, Zn, Fe, Co) host lattices. Here $A_{\parallel}^L = A_z^L$ and $A_{\perp}^L = A_x^L = A_y^L$.

M	ion	$A_{\parallel}^L$	$A_{\perp}^L$	f_s
Cd	I	12.3	1.9	0.28%
	II	12.3	1.9	0.28%
Mg	I	14.6	1.9	0.34%
	II	14.6	1.9	0.34%
Zn	I	14.6	1.9	0.34%
	II	14.6	1.9	0.34%
	III	12.9	1.9	0.30%
Fe	I	1.9	1.9	0.11%
	II	1.9	1.9	0.11%
Co	I	1.9	1.9	0.11%
	II	1.9	1.9	0.11%

for $\vec{B}$ at 45^0 from the X axis in the XY plane. The lines corresponding to the SHF splittings for $\vec{B}$ along two orthogonal directions to this, i.e. at 135^0 from the X axis in the XY plane and along the Z axis, were not resolved. However, the two principal values of $\tilde{A}^L$ for the orientation of $\vec{B}$ that produces the minimum SHF splitting for $\vec{B}$ can be estimated, by appropriately taking into account the inhomogeneously-broadened EPR linewidths (Chap. III). Thus, the two principal directions of the SHF tensor, $\tilde{A}^L$, for VO^{2+} ion I in CASH, MASH, or ZASH are very close to 45^0 and 135^0 from the X axis in the XY plane, while the third principal direction is along the Z axis; for example, for CASH the corresponding principal values of $\tilde{A}^L$ are 12.3, 1.9 and 1.9 MHz. For ion II, the principal direction of the SHF tensor corresponding to the largest SHF splitting is perpendicular to that for icn I; it lies in the XY plane, with the same principal value as that for ion I. The maximum principal values of the SHF interaction tensor, i.e., 12.3 MHz for CASH, as found presently, is 25% lower than that reported previously by Satyanarayana et al. [75] (16.8 MHz). For MASH, the present value (14.6 MHz) is almost the same as that reported by Jayaram et al. [83] (14.0 MHz); however, the present minimum principal SHF value for MASH is different from that reported by Jayaram et al. [83] (8.3 MHz). For ion III of ZASH, the principal values and principal axes of the SHF tensor, $\tilde{A}^L$, are determined

similarly. In particular, the maximum principal SHF value for ion III in ZASH is smaller than those for ion I and II (Table 7.1), being observed for the orientation of $\vec{B}$ being perpendicular to the two directions which yielded the maximum SHF splittings when $\vec{B}$ was parallel to them for ions I and II.

For FASH and COASH crystals, consisting of paramagnetic host ions, the principal values of the SHF interaction tensor, assumed to be isotropic, are estimated from the EPR hyperfine linewidths, taking into account of the inhomogeneous broadening effect of the SHF interaction; this has been described in detail in Chapter III. The principal values are listed in Table 7.1. It can be seen from this table that the principal values of the SHF interaction tensor (isotropic) for FASH and COASH hosts are about 14% in magnitude of the maximum principal SHF value in the hosts consisting of diamagnetic ions.

VII.2 Origin of SHF Interaction in VO^{2+}-doped $M(NH_4)_2(SO_4)_2 \cdot 6H_2O$ (M = Cd, Mg, Zn, Fe, Co)

The interaction between the magnetic electron of VO^{2+} ion, which is localized on the central magnetic ion, and the ligand nuclei, i.e. the protons of the neighboring H_2O molecules, is dipolar [1]. There is a non-zero probability that this unpaired electron is localized on the ligand ions. The combined effect of the dipolar and Fermi-contact

interactions is responsible for the SHF splitting in the present case. It should be noted that the nearest-neighbor ligands to a VO^{2+} ion for both the sites are four protons of the two $H_2O(9)$ molecules, which determine predominantly the SHF splitting for the ions I and II, as discussed in Chap. V. The resulting EPR spectra should, then, consist of five SHF lines, due to the combined spin $I_L = 2$ of the four protons of nuclear spin 1/2 each, with the intensity ratios of 1:4:6:4:1 [20]; this is in accordance with the present data. Further, the SHF splitting should possess axial symmetry about the bond axis [1], i.e., the line though the center of magnetic electron of the VO^{2+} ion (I or II) and the center of the four protons of two $H_2O(9)$ molecules (a M^{2+} site), for the two sites. The combined effect of the four protons results in the experimental maximum SHF splitting to occur for $\vec{B}$ along the M^{2+}-$H_2O(7)$ direction for ion I, and along the M^{2+}-$H_2O(8)$ direction for ion II, as verified from the crystallographic data. For ion I this axis lies in the XY plane, at about 45^0 from the X axis (i.e., the X_A axis). This is in accordance with the present EPR data, confirming that the VO^{2+} ion, indeed, substitutes for an M^{2+} ion in CASH, MASH or ZASH. There is a similar mechanism responsible for the resolved SHF splitting corresponding to ion III in ZASH, except that here the four protons responsible for this splitting belong either to the two $H_2O(7)$, or the two $H_2O(8)$, molecules. Since the

distances between the VO^{2+} ion and the ligand protons of the two $H_2O(7)$, or the two $H_2O(8)$, molecules are a little longer than that of $H_2O(9)$ molecules from the VO^{2+} ion, the resulting SHF interaction is a bit weaker than that of ions I and II, as confirmed presently. Satyanarayana et al. [75] also concluded that the maximum SHF splittings were observed for $\vec{B}$ along M^{2+}-$H_2O(7)$ and M^{2+}-$H_2O(8)$ directions for CASH, but they did not specify as to which four protons were responsible for the observed SHF interaction. Although, Jayaram et al. [83] did point out that the four protons of the two $H_2O(9)$ molecules were responsible for the SHF interaction, they did not report the orientations of $\vec{B}$ for which the maximum SHF splittings occur. All the features of the SHF interaction in VO^{2+}-doped Tutton salts have been presently explained.

The above explanation has been confirmed experimentally by measuring the EPR spectra of a VO^{2+}-doped MDSD crystal, in which no SHF splitting was observed. In a MDSD crystal the H_2O molecules of a MASH crystal, surrounding the VO^{2+} ion, are replaced by D_2O molecules. This indicates unequivocally that the SHF splitting is due to the interaction between the unpaired electron of the VO^{2+} ion and the ligand protons in MASH. For, when there are no protons surrounding a VO^{2+} ion, there occurs no SHF splitting.

VII.3 Density of Unpaired Electron of VO^{2+} at Ligand Proton Sites

The calculation to estimate the value of f_s, the probability density of the unpaired electron of VO^{2+} at the ligand site, from the SHF interaction, is described here.

The SHF interaction with axial symmetry,

$$\mathcal{H}_{SHF} = \vec{S}\cdot\tilde{A}^{L}\cdot\vec{I}^{L} = A_{\parallel}^{L}S_zI_z^{L} + A_{\perp}^{L}(S_xI_x^{L} + S_yI_y^{L}) \qquad (7.2)$$

can be rewritten as

$$\mathcal{H}_{SHF} = [A_s\vec{S}\cdot\vec{I}^{L}] + [2A_pS_zI_z^{L} - A_p(S_xI_x^{L} + S_yI_y^{L})], \qquad (7.3)$$

with

$$A_{\parallel}^{L} = A_s + 2A_p, \qquad (7.4)$$

and

$$A_{\perp}^{L} = A_s - A_p. \qquad (7.5)$$

In eq. (7.3), the first term represents the isotropic interaction between the ligand ions and the unpaired electron, whose wavefunction contains an admixture of the s and p states, while the second term represents the sum of the anisotropic interaction and the dipole-dipole interactions [95] of ligand ions with the unpaired electron in the p state.

The density f_s of the unpaired electron at the ligand ions is related to A_s as follows [95]:

$$A_s = (A_s^0/2S)\, f_s, \tag{7.6}$$

where S = 1/2 for VO^{2+} and

$$A_s^0 = \frac{8\pi}{3}\, g_e \mu_B g_N \mu_N |\Psi(0)|_s^2. \tag{7.7}$$

A_s^0 is the Fermi contact energy, which has been reported to be 1420 MHz for protons in the Tutton salts [83].

From eqs. (7.4) - (7.6), one obtains

$$f_s = (A_{\parallel}^L + 2A_{\perp}^L)/(3A_s^0/2S), \tag{7.8}$$

which can be estimated using the values of $A_{\parallel}^L$ and $A_{\perp}^L$, as determined presently from the EPR data.

Finally, the values of f_s as estimated for VO^{2+}-doped $M(NH_4)_2(SO_4)_2 \cdot 6H_2O$ (M = Cd, Mg, Zn, Fe, Co) are also listed in Table 7.1.

CHAPTER VIII

HOST-IMPURITY EXCHANGE INTERACTION

VIII.1 g-shift and Shape Effect

At low temperatures, the magnetization of paramagnetic FASH crystal causes a shift of the g value of the VO^{2+} impurity ion, which depends (i) on the shape of the crystal [2] and (ii) on the exchange interaction with the host Fe^{2+} ion, as described in VIII. 2 below.

In general, it is difficult to estimate the shape-dependent g shift for an arbitrary orientation of $\vec{B}$, and for an arbitrary crystal shape [28, 29, 30, 31]. However, for special orientations of $\vec{B}$, and for particular shapes of crystal, there exist simple expressions to calculate the g shift theoretically, e.g., when $\vec{B}$ is along one of the susceptibility axes. For FASH, one of the principal axes of magnetic susceptibility has been reported to be parallel to the crystal b axis, for which the susceptibility is χ_3 = 0.79 emu/mol at 4.2 K [29, 96]. For external magnetic field $\vec{B} \parallel \vec{b}$, the magnetization (in emu) is $M = \chi_3 Bd/A$, where d (= 1.864 g/cm^3) is the density of FASH crystal and A (= 394.14) is its gram molecular weight [29]. For the presently-used thin disk-shaped FASH crystal the demagnetization factor, N, for $\vec{B} \parallel \vec{b}$ is approximately zero [29]. Thus, the shape-dependent g shift for $\vec{B} \parallel \vec{b}$ is estimated, according to Kittel [27], to be, Δg =

$3M[(4\pi/3)-N]/2B = 2\pi\chi_3 d/A = 0.0023.$

VIII.2 g-shift and Exchange Interaction

At LHT, the exchange interaction of the VO^{2+} ion with the host Fe^{2+} ions is equivalent to the presence of an internal magnetic field at the VO^{2+} site, since magnetic moments are induced on the paramagnetic host ions (Fe^{2+}) due to the polarization effect of the external magnetic field. This results in a shift of the resonant-field value in the host consisting paramagnetic ions from that in an isostructural host lattice consisting of diamagnetic ions. This is equivalent to a g-shift which can be estimated by taking into account the effect of the VO^{2+}-Fe^{2+} exchange interaction in a perturbation calculation.

Assume a pairwise exchange interaction between a VO^{2+} ion with a neighbor Fe^{2+} ion. The total S.H. for the pair can be expressed as

$$\mathcal{H}_t = \mathcal{H} + \mathcal{H}' + \mathcal{H}_p \ , \tag{8.1}$$

where $\mathcal{H} = g_d \mu_B \vec{S}\cdot\vec{B}$ is the S.H. of the VO^{2+} ion neglecting the hf term, g_d is the effective g-factor of VO^{2+}, in an isostructural diamagnetic host, and

$$\mathcal{H}' = g'_{\parallel}\mu_B B_z S'_z + \Delta_x S'_x + \Delta_y S'_y \ , \tag{8.2}$$

is the S.H. of the non-Kramers' ion Fe^{2+}, where the

effective spin $S' = 1/2$, and $\Delta = (\Delta_x^2 + \Delta_y^2)^{1/2}$ represents the small zero-field splitting due to local distortion [1, 2, 97]. The third term in eq. (8.1),

$$\mathcal{H}_p = J_p \vec{S}\cdot\vec{S}', \tag{8.3}$$

exhibits the VO^{2+}-Fe^{2+} exchange interaction, where J_p is the exchange-interaction constant.

The wave functions of the total system can be expressed as product wave functions $\psi_1(M)\psi_2(M')$, where the values of the magnetic quantum numbers are $M = \pm 1/2$, and $M' = \pm 1/2$ for the VO^{2+} and Fe^{2+} ions, respectively. Thus, the S.H. of the pair system is a 4x4 matrix. The following expressions are derived for the energy levels $E(M,M')$, using perturbation theory, for $\vec{B}$ parallel to the principal axis of the $\tilde{g}^2$ tensor of the VO^{2+} ion, for the Fe^{2+} energy level ($M' = -1/2$), which lies the lowest at LHT:

$$E(+1/2,-1/2) = \mu_B g_d B/2 - (1/2)[(g'_\parallel \mu_B B)^2 + \Delta^2]^{1/2} - J_p/4 \tag{8.4}$$

$$E(-1/2,-1/2) = -\mu_B g_d B/2 - (1/2)[(g'_\parallel \mu_B B)^2 + \Delta^2]^{1/2} + J_p/4 \tag{8.5}$$

Using these energy levels, the resonance condition (for the transition $1/2,-1/2 \leftrightarrow -1/2,-1/2$) $\Delta E = h\nu = g_p \mu_B B$, where g_p is the impurity-ion g value in the host consisting

of paramagnetic ions, and taking into account the nearest and next-nearest neighbor Fe^{2+} ions to a VO^{2+} ion, one obtains, for the exchange constant, J_p, considering only the nearest- and next-nearest neighbors:

$$J_p = 2\mu_B B(g_d - g_p)/n', \tag{8.6}$$

where $\Delta g = g_p - g_d$ is the shift in the g value of the VO^{2+} ion in FASH host consisting paramagnetic ions from that in an isostructural host, ZASH, CASH or MASH, consisting of diamagnetic ions; it can be determined experimentally. In eq. (8.6), $n' = 6$ is the number of nearest and next-nearest neighbor Fe^{2+} ions to a VO^{2+} ion in FASH. To estimate J_p from eq. (8.6), B can be chosen to be 0.34 T, being close to the average magnetic field used in the present EPR measurements.

VIII.3 Estimation of Exchange Constant of VO^{2+}-Fe^{2+} in $Fe(NH_4)_2(SO_4)_2 \cdot 6H_2O$

The effective g factor for VO^{2+} for $\vec{B} \parallel \vec{X}$, which is one of the principal axes of magnetic susceptibility for FASH [29, 96], can be expresses as:

$$g_X = [g_{Z'}^2 \cos^2(\vec{Z}', \vec{X}) + g_{X'}^2 \cos^2(\vec{X}', \vec{X}) + g_{Y'}^2 \cos^2(\vec{Y}', \vec{X})]^{1/2}, \tag{8.7}$$

where $\vec{Z}'$, $\vec{X}'$, $\vec{Y}'$ are the directions of the principal axes of

the $\tilde{g}$ matrix, ($g_{Z'}$, $g_{X'}$, $g_{Y'}$) are the principal values of the $\tilde{g}$ matrix of the VO^{2+} ion in FASH, ($\vec{Z}'$,$\vec{X}$), etc. represent the angle between the Z' and X axes, etc. which can be calculated using the values of direction cosines given in Table 4.6.

Finally, for $\vec{B} \parallel \vec{X}$,

$$J_p = (2\mu_B B/n')(g_{d_X} - g_{p_X} + 2\pi\chi_3 d/A) \qquad (8.8)$$

For ZASH, MASH and CASH hosts, consisting of diamagnetic ions, the average $g_{d_X} = 1.9945$, while for paramagnetic FASH $g_{p_X} = 1.9622$ averaged over the VO^{2+} ions I and II, as determined presently. Then, the VO^{2+}-Fe^{2+} exchange-interaction constant, J_p, averaged over the nearest and the next-nearest neighbors is estimated to be 0.07 GHz in FASH. For comparison, Mn^{2+}-Fe^{2+} exchange interaction constant was reported to be -0.006 GHz [29].

CHAPTER IX

HOST-ION SPIN-LATTICE RELAXATION TIME (τ)

IX.1 Theoretical Expression for τ

Spin-lattice relaxation time (τ) of the host paramagnetic ions in doped crystals can be estimated, using the contribution to the EPR linewidth of the impurity ion due to the paramagnetism of the host ions, $\Delta B'$, from the following expression [33]

$$\tau = (3\Delta B' g^2 \mu_B)/(110\hbar g' \langle \Delta\nu^2 \rangle), \qquad (9.1)$$

where μ_B, h, g, and g' are respectively the Bohr magneton, Planck's constant, the impurity-ion Lande's factor, and the host-ion Lande's factor. In order to estimate $\Delta B'$, one should subtract, from the observed impurity-ion linewidth the linewidth of the impurity ion in an isostructural host consisting of diamagnetic ions, as well as the linewidth contribution due to inhomogeneous broadening, caused by the unresolved SHF structure, if any (Chap. III). For example, a total of 0.7 mT (at all temperatures) has to be subtracted from the observed VO^{2+} EPR linewidths in Tutton salts, consisting of paramagnetic ions, in order to obtain the values of $\Delta B'$ in FASH and COASH hosts to be used in eq. (9.1), where $\langle \Delta\nu^2 \rangle$ is the second moment for the impurity ion. Misra et al. [33] showed that $\langle \Delta\nu^2 \rangle$ for crystals

containing two different species of magnetic ions, for the case when the distances between the impurity ions are sufficiently large, and when the number of host-ion neighbors considered is limited to N, can be expressed as

$$\langle \Delta\nu^2 \rangle = \tfrac{1}{3} S'(S'+1) h^{-2} \left[N J_p^2 + g g' \mu_B^4 \mu_o^2 \sum_{k'}^{N} (1-3\gamma_{jk'}^2)^2 r_{jk'}^{-6} + \right.$$

$$\left. + 2 J_p g g' \mu_B^2 \mu_o \sum_{k'}^{N} (1-3\gamma_{jk'}^2) r_{jk'}^{-3} \right]. \qquad (9.2)$$

In eq. (9.2) S', J_p, μ_o, $r_{jk'}$, and $\gamma_{jk'}$ are the effective spin of the host-ion, the average impurity-host pair-exchange constant, the permeability constant, the distance between j and k′ ions and the direction cosines of $\vec{r}_{jk'}$ with the external Zeeman field, $\vec{B}$, respectively. (The primed quantities refer to the host ions while the unprimed ones to the impurity ions.)

IX.2 Pr^{3+} in Gd^{3+}-doped $NH_4Pr(SO_4)_2 \cdot 4H_2O$

IX.2.1 Estimation of τ of Pr^{3+} in $NH_4Pr(SO_4)_2 \cdot 4H_2O$

In order to compute τ of Pr^{3+} in APST, using eqs. (9.1) and (9.2), one first needs to know the values of the various quantities appearing therein. The values of $\Delta B'$ at different temperatures were determined, by subtracting the Gd^{3+} linewidth (2.3 mT) in the isostructural diamagnetic ALST host [98], as well as the linewidth contribution (0.2 mT) due to the inhomogeneous broadening, caused by the

unresolved SHF structure [98], from the observed EPR linewidths of Gd^{3+} in APST. A computer program was used to generate the APST lattice in order to calculate the distances $r_{jk'}$ and the corresponding direction cosines ($\gamma_{jk'}$) of the external field. For the calculation of the second moment, $\langle \Delta\nu^2 \rangle$, it was found sufficient to consider only up to the fifth-nearest neighbors (N = 9); the contributions of the farther-lying neighbors were found to be negligible. As for the values of S', g' and J_p, the following considerations were made. The effective spin of each of the non-Kramers' ion Pr^{3+}, is S' = 1/2 [1, 3]. (S' = 1/2 for Pr^{3+} for the case of lower local symmetry, being equivalent to the presence of local distortions superimposed on higher symmetry due to Jahn-Teller effect). Further, for Pr^{3+}, $g'_{\parallel} = 2\langle \xi_0 | S'_z | \xi_0 \rangle$, where $|\xi_0\rangle$ is one of the time-conjugate states for the ground state of Pr^{3+}, and $g'_{\perp} = 0$ [1]. No experimental g' values have been reported for the host ions in APST or in the isostructural crystals. On the other hand, the coordinations around a Pr^{3+} ion in APST lattice are the same as that of a Pr^{3+} ion in the $Y(C_2H_5SO_4)_3 \cdot 9H_2O$ lattice, so that the g' values for Pr^{3+} ions in the two lattices are expected to be about the same [2]; for $Y(C_2H_5SO_4)_3 \cdot 9H_2O$ the theoretically calculated values are $g'_{\parallel} = 1.6$, $g'_{\perp} = 0.0$ for Pr^{3+} in $Y(C_2H_5SO_4)_3 \cdot 9H_2O$ host [2, 99]. In the numerical estimates made presently for τ, the direction of the external field has been assumed to

be along the principal magnetic Z axis, i.e. the principal axis of the b_2^m tensor of the Gd^{3+} ion [5, 65, 66, 67]; which is along the 4-fold axis of a distorted-monocapped-square antiprism, making approximately the angles (51^0, 45^0, 72^0) relative to the (a, b, c) axes (Chap. III). However, the principal magnetic axes (Z') for the host Pr^{3+} ions are not necessarily parallel to the respective principal Z axes of the impurity Gd^{3+} ion. In this case, the averages of $g'_{\parallel}$ and $g'_{\perp}$ values, for the host ions were chosen for g' in eqs. (9.1) and (9.2) for estimating τ. This does not lead to any significant error in the calculated values of τ, because there exists some uncertainty in other factors as well. The value of J_p has not been determined experimentally for the Gd^{3+}-Pr^{3+} pair. In order to examine the effect of different values of J_p on τ, the values of τ have been calculated at room temperature for J_p = 0.1, 1.0, 5.0, 10.0 GHz, which cover the possible range of values; they are listed in Table 9.1. It is seen from Table 9.1 for Pr^{3+} ion, that the τ value fluctuates by three orders of magnitude, for choices of value of J_p ranging from 0.1 to 10 GHz. However, as seen from eqs. (9.1) and (9.2), the T power-law dependence of τ^{-1}, which enables one to discern the spin-lattice relaxation process is, in effect, independent of a particular J_p value. As for the values τ for the Pr^{3+} ion in APST at different temperatures, they are estimated in the 266 - 410 K temperature range for J_p = 5.0 GHz; they are

Table 9.1 Calculated RT spin-lattice relaxation time (τ) for Pr^{3+} ion in APST lattice. The values of S', g, g', J_p and $\Delta B'$, used in the present calculation, are also listed. τ values are expressed in seconds, while the figures inside the round brackets following τ are J_p values in GHz.

S'	1/2
g	1.9949
g'	0.80
ΔB (mT)	3.0
τ (0.1)	7.64×10^{-12}
τ (1.0)	2.23×10^{-12}
τ (5.0)	1.04×10^{-13}
τ (10.0)	2.57×10^{-14}

listed in Table 9.2, along with the required experimental linewidths at different temperatures. Fig. 9.1 exhibits the log-log plot of τ^{-1} vs. temperature in the 266 - 410 K range for J_p = 5 GHz. No estimates were made for τ for Pr^{3+} in APST host crystal at temperatures above 410 K, or below 266 K, because of the unavailability of $\Delta B'$ values. This is because below 266 K the crystal underwent a phase transition, while above 410 K the crystal deteriorated due to dehydration.

For Pr^{3+} host ions in APST, a T^7 dependence of τ^{-1} is found in the 266 - 296 K temperature range, while a T^2 dependence is noted in the temperature interval 296 - 410 K.

IX.2.2 Spin-lattice Relaxation Mechanism for Pr^{3+} in $NH_4Pr(SO_4)_2 \cdot 4H_2O$

A least-squares fitting of τ to temperature indicates that the τ values of Pr^{3+} in APST, as estimated presently can be fitted well to $\tau = BT^{-7}$ in the 266 - 296 K temperature range, and to $\tau = CT^{-2}$ in the 296 - 410 K temperature range. In particular for J_p = 5.0 GHz, B = 3.04×10^4 sec.K^7, C = 9.11×10^{-9} sec.K^2. It is now possible, from these T^7 and T^2 temperature dependences of τ^{-1}, to deduce as to which mechanisms are responsible for spin-lattice relaxation in the two temperature regions. Surveys of the various spin-lattice relaxation mechanisms have been provided by Abragam and Bleaney [1], and by

Table 9.2 The estimated spin-lattice relaxation times (τ) of the Pr^{3+} ion for J_p = 5 GHz and the contribution to the EPR linewidth of the impurity Gd^{3+} ion due to the paramagnetism of the host Pr^{3+} ions, $\Delta B'$, in the APST host at various temperatures (T). The error for $\Delta B'$ is ±0.2 mT.

T(K)	$\Delta B'$ (mT)	τ (sec)	T(K)	$\Delta B'$ (mT)	τ (sec)
266	9.3	3.23×10^{-13}	333	1.7	6.03×10^{-14}
269	8.3	2.88×10^{-13}	347	1.4	5.01×10^{-14}
271	7.3	2.53×10^{-13}	354	1.4	5.01×10^{-14}
273	7.2	2.50×10^{-13}	362	1.3	4.51×10^{-14}
278	6.2	2.15×10^{-13}	369	1.2	4.17×10^{-14}
285	4.4	1.53×10^{-13}	374	1.1	3.82×10^{-14}
292	3.2	1.11×10^{-13}	383	1.1	3.82×10^{-14}
296	3.0	1.04×10^{-13}	392	1.1	3.82×10^{-14}
303	2.4	8.32×10^{-14}	400	1.2	4.17×10^{-14}
319	2.1	7.30×10^{-14}	410	1.2	4.17×10^{-14}
326	1.9	6.60×10^{-14}			

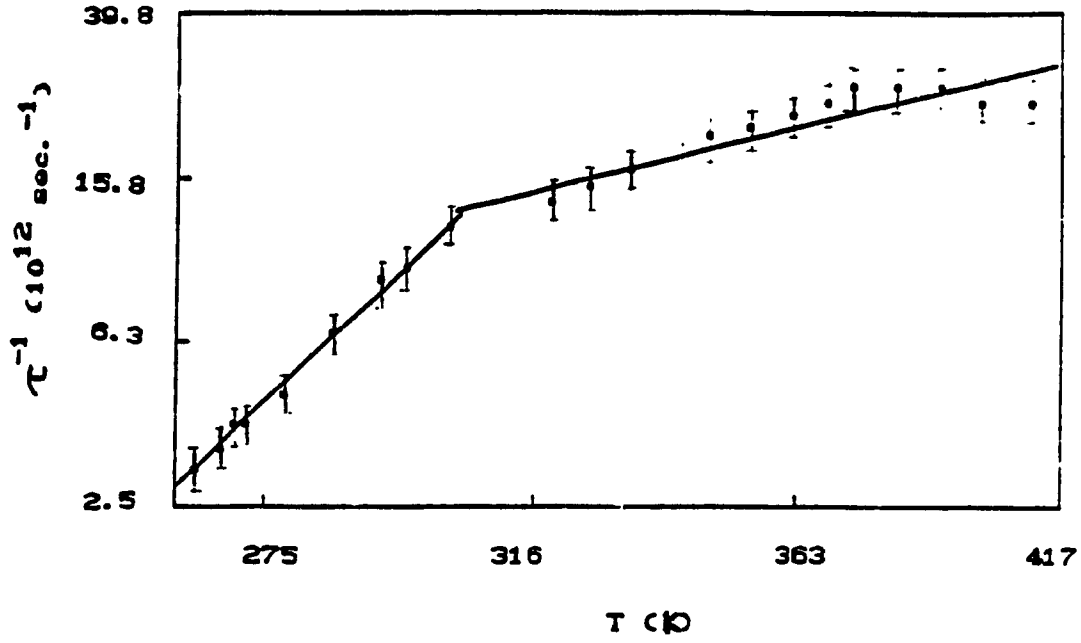

Fig. 9.1 A log-log plot of the inverse of the spin-lattice relaxation time (τ^{-1}) versus the temperature (T) in the 266 - 410 K range for the host paramagnetic ions Pr^{3+} in APST crystal for J_p = 5.0 GHz. [It is noted that the values of the slopes, determining as to which process of spin-lattice relaxation is effective, do not change for different values of J_p, as can be seen from eqs. (9.1) and (9.2).]

Shrivastava [100].

As for the T^7 dependence of τ^{-1} for a non-Kramers' ion, such as Pr^{3+}, it is caused by the following processes: (i) At <u>low</u> temperatures, by Raman processes, specifically Raman spin-one phonon interaction in second order, Raman spin-two-phonon interaction, and Raman process affected by short wave-length phonons. (ii) At <u>low</u> temperatures, by a process involving three phonons, described by Le Naour [101], in which first the small wave-vector approximation is used to obtain a transition from an upper level E_b to another upper level E_c by the emission of two phonons, and integration is made over all the phonons from 0 to Δ_c ($\Delta_c = E_c - E_a$, where E_a is the ground state). This is followed by the calculation of a Raman process using phonons from Δ_c to the Debye cutoff, thus making full use of the Debye spectrum. (iii) At <u>intermediate</u> temperatures, by the "sum" process [102, 103], in which a spin transition is achieved by means of emission or absorption of two phonons, the range of temperature being centered at about $0.14\ \Delta_c/k_B$ [103], depending very sensitively on the structure of levels in the host crystal [102, 103]. From the temperature ranges over which processes (i), (ii) and (iii) are applicable, it appears that the presently-observed T^7 behavior of τ^{-1} in the range 266 - 296 K may be explained to be due predominantly to the sum process, since this temperature range is more appropriately "intermediate", rather than

"low".

As for the T^2 behavior of τ^{-1} in the range 296 - 410 K, it can be explained to be due to any one of the various Raman processes, described above, as well as due to and the sum process, all of which predict T^2 dependence of τ^{-1} at high temperatures. However, the sum process has negligible contribution compared to that of the usual Raman process, particularly because in the sum process only the lowest-energy phonons are required, whose number diminishes considerably at high temperatures; in addition, the value of the integral required in the expression for τ^{-1} for the sum process becomes quite small at elevated temperatures [102, 103]. To explain further, at elevated temperatures, the number of phonons for which $\omega_1 - \omega_2 = \omega$, required for the usual Raman process, is extremely large compared to that for which $\omega_1 + \omega_2 = \omega$ required for the sum process. (Here $\hbar\omega$ is the difference in the two levels of the spin system and ω_1, ω_2 are the frequencies of the phonons involved in the Raman or sum processes.) This is because the energy density of phonons depends on temperature as $x^2/(e^x-1)$, where $x = \hbar\omega/k_BT$, which tends to zero as T approaches zero, or infinity, from an intermediate value [1]. Thus, the number of phonons required for the sum process, which come from the lowest part of the phonon spectrum, is negligible at high temperatures, while the number of phonons required for the Raman process is large, because they can belong to any part

of the phonon spectrum, including those belonging to the highest phonon density, as long as $\omega = \omega_1 - \omega_2$. Thus, the Raman process is the predominant mechanism for spin-lattice relaxation of host Pr^{3+} ions in APST in the 296 - 410 K temperature range. For Ce^{3+}, Nd^{3+} and Sm^{3+} ions in the isostructural hosts ACST, ANST and ASST, Malhotra et al. [67] and Buckmaster et al. [66] predicted an Orbach process. However, this conclusion at variance with the present deduction, was only guessed by comparison with other systems and not arrived by a study of temperature variation of τ, as only RT values of τ were estimated.

An interesting feature of the behaviour of τ versus temperature is that, as seen from Fig. 9.1, the τ^{-1} values for Pr^{3+} in APST exhibit a sudden transition from T^7 to T^2 behavior at 296 K as the temperature is increased. If only one of the processes, described above, is capable of explaining the presently-observed T^7 and T^2 dependences of τ^{-1} as one goes from low to high temperatures over the entire 266 - 410 K temperature range, a gradual, and not sudden, transition from the T^7 to T^2 behavior for τ^{-1} should be observed. The sudden transition of the T dependence of τ^{-1} is, therefore, most likely, due to the <u>simultaneous</u> presence of a number of competing spin-lattice relaxation mechanisms which are in force at the transition temperature 296 K, depending on the Pr^{3+} energy levels in a complex manner. Such a sudden transition, from T^{n_1} to T^{n_2} behavior

of τ^{-1}, is in conformity with the various experimental data exhibited in [1] and [100].

IX.3 Fe^{2+} in VO^{2+}-doped $Fe(NH_4)_2(SO_4)_2 \cdot 6H_2O$

FASH lattice was generated using a computer program in order to calculate the required distances between the impurity ion (VO^{2+}) and the neighbor host Fe^{2+} ions and the direction cosines ($\gamma_{jk'}$) of the external field, relative to the position vectors of the various ions. For the calculation of the second moment, required in eq. (9.2), it was found sufficient to consider only up to the fifth-nearest neighbors, i.e., a total of 20 Fe^{2+} ions (N = 20), the contributions of the farther-lying neighbors were found to be negligible.

In the estimation of τ from eqs. (9.1) and (9.2), the values of all the parameters required, except for S′ and g′, have been determined presently. For the values of S′ and g′ the following considerations were made. For Fe^{2+}, which is a non-Kramers′ ion, its S.H. for the case of lower symmetry (equivalent to the presence of local distortions superimposed on higher symmetry due to Jahn-Teller effect), as described by Abragam and Bleaney [1], is given by eq. (8.3), wherein Δ_x, Δ_y represent the distortion, $g'_{\parallel} = 2\langle\xi_0|S'_z|\xi_0\rangle$ where $|\xi_0\rangle$ is one of the time-conjugate states for the ground state of Fe^{2+}, and $g'_{\perp} = 0$. $g'_{\parallel}$ value has been reported to be 8.989 for FASH [2, 97]. In the numerical

estimates, made presently for τ, the direction of the external field was assumed to be along the Z (or parallel) magnetic axis of the VO^{2+} ion. However, the Z' magnetic axis for the host ion is not necessarily along the respective principal axis of the impurity VO^{2+} ion. Thus, the average of $g'_{\parallel}$ and $g'_{\perp}$ values (= 4.49) for the host ion was chosen for estimating τ. Using these values, the value of τ was estimated to be 7.20×10^{-15} sec. at RT.

The temperature independence of VO^{2+} EPR linewidth in FASH (Chap. III) does not necessarily imply that τ does not vary with temperature. For, it is well known that all processes of spin-lattice relaxation do depend on temperature [100]. Usually, EPR linewidth decreases as temperature increases due to the host-ion spin-lattice relaxation. Thus, there must exist other compensating processes which cause increase in EPR linewidth as temperature increases. Upreti and Saraswat [82] suggested that this compensating process might be the spin-quenching process, but they could not provide an appropriate justification. The population fluctuation of the crystal field levels of Fe^{2+} may cause the impurity-ion linewidth to decrease with decreasing temperature which could be the compensating process, similar to those for Tm^{3+}, Pr^{3+} and Tb^{3+} [104, 105, 106]. Further, it may be suggested here that the ordering of the host Fe^{2+} ions at low temperatures may also play this compensating role [107].

IX.4 Co^{2+} in VO^{2+}-doped $Co(NH_4)_2(SO_4)_2 \cdot 6H_2O$

Similar to the case of VO^{2+}-doped FASH, for the calculation of the second moment, $\langle \Delta\nu^2 \rangle$, in COASH using eq. (9.2), it was found sufficient to consider only up to the fifth-nearest neighbors, i.e., a total of 20 Co^{2+} ions (N = 20), the contributions of the farther-lying neighbors were found to be negligible.

In the estimation of τ, the values of all the parameters required have been determined presently, except for S', g' and J_p, for which the following is noted. Co^{2+} is a Kramer's ion with S' = 1/2 [1]. Bleaney et al. [108] have reported the principal g values of Co^{2+} in ZASH: $g_1' = 3.06$, $g_2' = 3.06$, $g_3' = 6.45$. The average of g_1', g_2' and g_3' values (g' = 4.19) for the Co^{2+} host ion was then chosen for estimating τ. The value of J_p for VO^{2+}-Co^{2+} has not been reported. In the present case, several choices for the values of J_p, in the range of 0.0 - 1.0 GHz, were used to calculate τ. However, variation of J_p in this range did not change the calculated value of τ significantly. This means that only the dipolar interaction in COASH is of importance in determining τ. Therefore, the value of J_p for VO^{2+}-Co^{2+} in COASH was chosen to be 0.07 GHz, the same as J_p that for VO^{2+}-Fe^{2+} exchange interaction in FASH (Chap. VIII). Finally, the value of τ for Co^{2+} ions in COASH was estimated to be 8.42×10^{-15} sec. at RT. For comparison, it is noted

that Jayaram et al. [83] reported $\tau = 5.5 \times 10^{-12}$ sec. for Co^{2+} in COASH at RT, using the incorrect formula, valid for the presence of only one kind of paramagnetic ion. This value of τ is three orders of magnitudes larger than that estimated presently.

The relaxation times, τ, as calculated from the EPR linewidth contribution due to the paramagnetism of the host ions ($\Delta B'$), using eqs. (9.1) and (9.2), for Co^{2+} in COASH can be fitted to temperature (T), within experimental error, to a straight line as follows: $\tau^{-1} = AT$, where $A = 2.35 \times 10^{11}$ $Sec.^{-1}K^{-1}$, in the 143 - 413 K temperature range. This temperature behavior of τ is consistent with that predicted for the direct process of spin-lattice relaxation [1, 100].

IX.5 Co^{2+} in $CoNa_2(SO_4)_2 \cdot 4H_2O$

For the calculation of the second moment $\langle \Delta\nu^2 \rangle$ in Cu^{2+}-doped CNST using eq. (9.2), it was found sufficient to consider only up to the fifth-nearest neighbors, i.e., a total of 20 Co^{2+} ions (N = 20). In the estimation of τ, g' value (= 3.866) is chosen to be average of the three principal values of $\tilde{g}$ matrix (g'_1, g'_2, g'_3) of Co^{2+} in ZNST host, reported previously [119]: $g'_1 = 2.652$, $g'_2 = 1.890$, $g'_3 = 7.442$. The value of J_p for Cu^{2+}-Co^{2+} has not been reported. Similar to the case of VO^{2+}-doped COASH, it was found that the variation of J_p in the range of 0.0 - 3.0 GHz did not change the calculated value of τ significantly,

confirming that only the dipolar interaction in CNST is of importance in determining τ. Therefore, the value of J_p was chosen to be 0.3 GHz. The values of $\Delta B'$ were obtained by subtracting from the Cu^{2+} EPR linewidth in CNST host consisting of paramagnetic ions, the Cu^{2+} linewidth in MNST host consisting of diamagnetic ions, at the same temperature, for the various temperatures considered in the 280 - 330 K temperature range. It was not possible to measure the Cu^{2+} EPR linewidth beyond this temperature range because of complete broadening of Cu^{2+} EPR lines.

Finally, the value of τ of host-ion Co^{2+} in CNST at RT was estimated to be 3.01×10^{-14} sec. For comparison, Jain et al. [123] reported the value of τ to be 1.66×10^{-12} sec. from the EPR linewidth of Mn^{2+} impurity ion in CNST, using the incorrect formula. Further, the present τ - T dependence can be fitted, within experimental errors, to be $\tau^{-1} = AT^9$, where $A = 5.64 \times 10^8$ sec.$^{-1}K^{-9}$, in the 280 - 330 K temperature range. This temperature behavior of τ is consistent with that predicted for the Kramer's Raman process of spin-lattice relaxation [1, 100].

CHAPTER X

JAHN-TELLER EFFECT

X.1 Ground State of Cu^{2+} in $MNa_2(SO_4)_2 \cdot 4H_2O$ (M = Mg, Co)

When the six ligands of a Cu^{2+} ion, in an octahedral six-fold coordination, form a regular octahedron, the ground state of the Cu^{2+} ion is the two-fold degenerate E_g state. The degeneracy of the ground state of the Cu^{2+} ion is usually removed by a Jahn-Teller distortion [1, 113]. In the present case, Cu^{2+} ions substitute for an M^{2+} (M = Mg, Co) ion in the MNST and CNST lattices. The M^{2+} sites originally have an elongated tetragonally-distorted octahedral coordination with the ligands. However, due to the Jahn-Teller distortion the principal values of the $\tilde{g}$ matrices of Cu^{2+} in MNST and CNST exhibit a lower, namely, orthorhombically distorted octahedral, symmetry at RT and lower temperatures. According to the crystal-field theory, the orbital doublet E_g of the Cu^{2+} ion is split in a field of orthorhombic symmetry, the lower state being either $|X^2-Y^2\rangle$ or $|3Z^2-r^2\rangle$; which one of these two is predominant can be determined from the value of the parameter R [113], which is defined as $R \equiv (g_x-g_y)/(g_z-g_x)$, where $g_z > g_x > g_y$, are the principal values of the $\tilde{g}$ matrix of Cu^{2+} in the host lattice. When the R-value is greater than unity, a predominantly $|3Z^2-r^2\rangle$ ground state is expected, while a predominantly $|X^2-Y^2\rangle$ ground state is expected when it is

less than unity. Since, in the present case, the calculated R-value is less than unity at RT and below, the predominant ground state of Cu^{2+} ion in both the MNST and CNST hosts, is $|X^2-Y^2>$ with an admixture of the excited state $|3Z^2-r^2>$.

X.2 Pseudo-static Jahn-Teller Effect

If the splitting between the ground state $|X^2-Y^2>$ and the excited state $|3Z^2-r^2>$, of Cu^{2+} is sufficiently small, a mixing of the two states by coupling with the lattice vibrations becomes quite possible. The vibronic mixing of the close-lying (pseudo-degenerate) levels $|X^2-Y^2>$ and $|3Z^2-r^2>$ due to the interaction of the Cu^{2+} ion with its ligands manifests itself as a pseudo JTE [113, 125].

The molecular and electronic structure of the Cu^{2+} ion, surrounded by six ligands of octahedral or trigonal distortion, is conventionally described in terms of Jahn-Teller coupling between the doubly degenerate electronic (E_g) and vibrational (ε_g) states of the octahedral complex [125]. Assuming a harmonic-vibrational potential, and taking into consideration only the linear coupling terms, leads to the well-known Mexican-hat potential surface. The geometry of the Cu^{2+} complex fluctuates between the various conformations of D_{4h} and D_{2h} symmetries, which are generated by linear combinations of Q_θ and Q_ε, the components of the ε_g vibrational mode. Q_θ and Q_ε are conventionally expressed as $Q_\theta = \rho \cos\phi$ and $Q_\varepsilon = \rho \sin\phi$

in terms of a polar coordination system (ρ,ϕ). When higher-order coupling terms are included, the perimeter of the Mexican hat becomes warped giving rise to three equivalent minima whose projections correspond to different ϕ values in the $(Q_\theta, Q_\varepsilon)$ space. Finally, the Mexican-hat potential results in three equivalent potential valleys. However, as pointed out by Ham [115], a strain, having a tetragonal component, that is prevalent in the present case as indicated by the three different principal values of the $\tilde{g}$ matrices of Cu^{2+} in MNST and CNST, destroys the equivalence of the three potential valleys. It is, therefore, expected that, for both MNST and CNST, one of the three inequivalent valleys lies much lower than the other two. When only the lowest potential valley is occupied at low temperatures, i.e., when $\Delta E > k_B T$ (ΔE is the energy difference between the lowest potential valley and the next-lying potential valleys), the principal values of the $\tilde{g}$ matrix of Cu^{2+} are not expected to be very temperature dependent, in accordance with the present observations. Further, in the present case, only one set of hf lines for each of the two magnetically inequivalent Cu^{2+} sites was observed, implying that only the lowest potential valley is occupied. For, otherwise, as seen in the case of Cu^{2+}-doped $Zn(C_4H_4N_2)SO_4 \cdot 3H_2O$ single crystal [126], three physically equivalent sets of hf lines should be observed for each magnetically-inequivalent Cu^{2+} site.

The above interpretation of the EPR spectra of Cu^{2+}-doped MNST and CNST at room and lower temperatures, in terms of pseudo-JTE, wherein the lowest-lying levels of the E state lie extremely close to each other but are not degenerate, is equivalent to that of the "static" JTE, wherein the lowest levels of the E state are degenerate, the degeneracy being lifted by a Jahn-Teller distortion, as described by Abragam and Bleaney [1]. This is consistent with the treatment of an E-state ion in a tetragonal crystal-field, by Bir [127], for a tetragonally distorted octahedral Cu^{2+} complex, such as $[Cu(H_2O)_6]^{2+}$.

X.3 Dynamic Jahn-Teller Effect

As the temperature was raised above RT, the hf lines of Cu^{2+} in both MNST and CNST became much broader because of decreased Cu^{2+} SLR times (Chap. III). At higher temperatures, k_BT is no longer smaller than ΔE, the separation between the two lowest-lying Jahn-Teller potential valleys. When $k_BT >> \Delta E$, the three potential valleys are almost equally occupied. This is consistent with the present observation of only a single isotropic line for $T > T_{JT}$, where T_{JT} is the transition temperature from static to dynamic Jahn-Teller state; they are 347 K and 339 K, for Cu^{2+} in MNST and CNST hosts, respectively. This is characteristic of type I dynamic JTE [115]. This occurs when the rate of tunneling though the barrier, at higher

temperatures, from one distorted configuration, or Jahn-Teller potential valley, of the complex to another exceeds the frequency difference between the corresponding EPR resonance lines for the different distorted configurations, i.e. that between the anisotropic spectra [115]. When dynamic JTE occurs $g_z = g_x = g_y = g_e - \frac{4\lambda}{\Delta}$, which is equal to the average of the three principal values of the $\tilde{g}$ matrix at $T < T_{JT}$, for both the Cu^{2+} ions I and II in the unit cell [126]. Here, g_e (= 2.0023) is the g-value of the free electron, λ is the spin-orbit coupling constant for the free Cu^{2+} ion (= -830 cm^{-1}) and Δ is the octahedral crystal-field constant for Cu^{2+} ion. For the typical value of $\lambda/\Delta = -0.05$ for Cu^{2+} ion [1], the value of $(g_e - \lambda/\Delta)$ is 2.20, being the same as the presently observed g-values at $T \geq T_{JT}$ for both the Cu^{2+} ions I and II in MNST and CNST and the average of the three principal values of $\tilde{g}$ at $T < T_{JT}$.

Since the EPR line position and linewidth for Cu^{2+} in each of MNST and CNST were independent of the orientation of $\vec{B}$ at higher temperatures ($T > T_{JT}$), the "oriented" and "random" strains should be very small compared to k_BT. This is because the center of the EPR line depends on the orientation of $\vec{B}$ if the "oriented" strains are large, while the EPR linewidth depends on the orientation of $\vec{B}$ if the "random" strains are large [115].

X.4 Comparison between Cu^{2+} EPR spectra of $MNa_2(SO_4)_2 \cdot 4H_2O$ (M = Mg, Co)

It is noted that the main features of Cu^{2+} EPR spectra in MNST, consisting of diamagnetic host ions and in CNST, consisting of paramagnetic host ions, crystals are very similar, except for a difference in the EPR linewidth and its temperature dependence (Chap. III). Both samples exhibited a pseudo-static JTE at room and lower temperatures, and a dynamic JTE at higher temperatures. The previous studies of JTE by Cu^{2+} EPR were mostly made in host lattices consisting of diamagnetic ions [113, 126]. Misra et al. [126] proposed a model to interpret the JTE observed in Cu^{2+}-doped diamagnetic crystals. The present studies indicate that the model is applicable to the occurrence of JTE in Cu^{2+}-doped hosts, consisting of paramagnetic ions, as well as in Cu^{2+}-doped hosts consisting diamagnetic ions. The reason why many JTE studies on Cu^{2+}-doped hosts consisting of paramagnetic ions have not been reported in the literature is perhaps due to larger EPR linewidth, resulting in poorer resolution of EPR spectra observed in these hosts.

CHAPTER XI

OPTICAL ABSORPTION AND BONDING COEFFICIENTS

EPR studies can provide a great deal of information about the bonding in vanadyl (VO^{2+}) complexes. The theoretical treatments, which relate the principal values of the $\tilde{g}$ and $\tilde{A}$ matrices to the energy levels and the bonding coefficients in vanadyl complexes, are by now well established [22, 23, 24, 25, 26]. The VO^{2+} ion has the electronic configuration $(A).3d^1$, where (A) stands for the closed Argon shell. The description of the molecular vanadyl ion, VO^{2+}, based on LCAO-MO [22] calculations of $[VO(H_2O)_5]^{2+}$ reveals that the ground state of the vanadyl ion is $(3d^1, {}^2D_{3/2})$. In an octahedral crystalline field, the ^2D term, with five-fold orbital degeneracy, splits into $^2T_{2g}$ and ^2E_g levels, of which $^2T_{2g}$ lies lower. Thus, only one band corresponding to $^2T_{2g} \leftrightarrow {}^2E_g$ transition is expected to be observed in the optical-absorption spectrum when the unpaired electron of the vanadyl ion is in an octahedral crystalline field [24]. In the tetragonal (C_{4v}) symmetry the $^2T_{2g}$ level splits further into $^2B_{2g}$ and $^2E_{2g}$ levels, while the ^2E_g level splits into $^2B_{1g}$ and $^2A_{1g}$ levels, out of those four levels $^2B_{2g}$ represents the lowest energy state. The first-excited energy level $^2E_{2g}$ is doubly degenerate. The relative positions of the energy levels have already been reported [22, 24]. These levels, in conjunction with their

designations, are shown in Fig. 11.1. The expected transitions in the optical-absorption spectra are, in order of increasing energy [23],

$$^2B_{2g} \longrightarrow {}^2E_{2g} = \Delta_\perp = -3D_s + 5D_t, \tag{11.1}$$

$$^2B_{2g} \longrightarrow {}^2B_{1g} = \Delta_\parallel = 100D_q, \tag{11.2}$$

$$^2B_{2g} \longrightarrow {}^2A_{1g} = \Delta = 10D_q - 4D_s - 5D_t. \tag{11.3}$$

In Fig. 11.1 the parameters D_q, D_s and D_t are referred to as the octahedral, the second- and fourth-order tetragonal field parameters, respectively. The vanadyl complex, with the C_{4v} symmetry, is expected to undergo the transitions (11.1) - (11.3). On the other hand, if the local symmetry of the VO^{2+} ion is lowered further, namely, to rhombic symmetry, the degenerate level will become more split. However, the optical-absorption spectrum did not exhibit the slightly-rhombic nature of the localization of the VO^{2+} ion in detail, because the energy level ^2E_g is insufficiently split to be observed. In this case, one expects to observe only three optical absorption bands.

Optical-absorption spectra have been observed presently for all VO^{2+}-doped Tutton salts CASH, MASH, ZASH, FASH and COASH. The measured energy-level differences, $\Delta_\perp$ and $\Delta_\parallel$, defined by eqs. (11.1) and (11.2) above, for VO^{2+} in the various hosts are listed in Table 11.1. The VO^{2+} ion

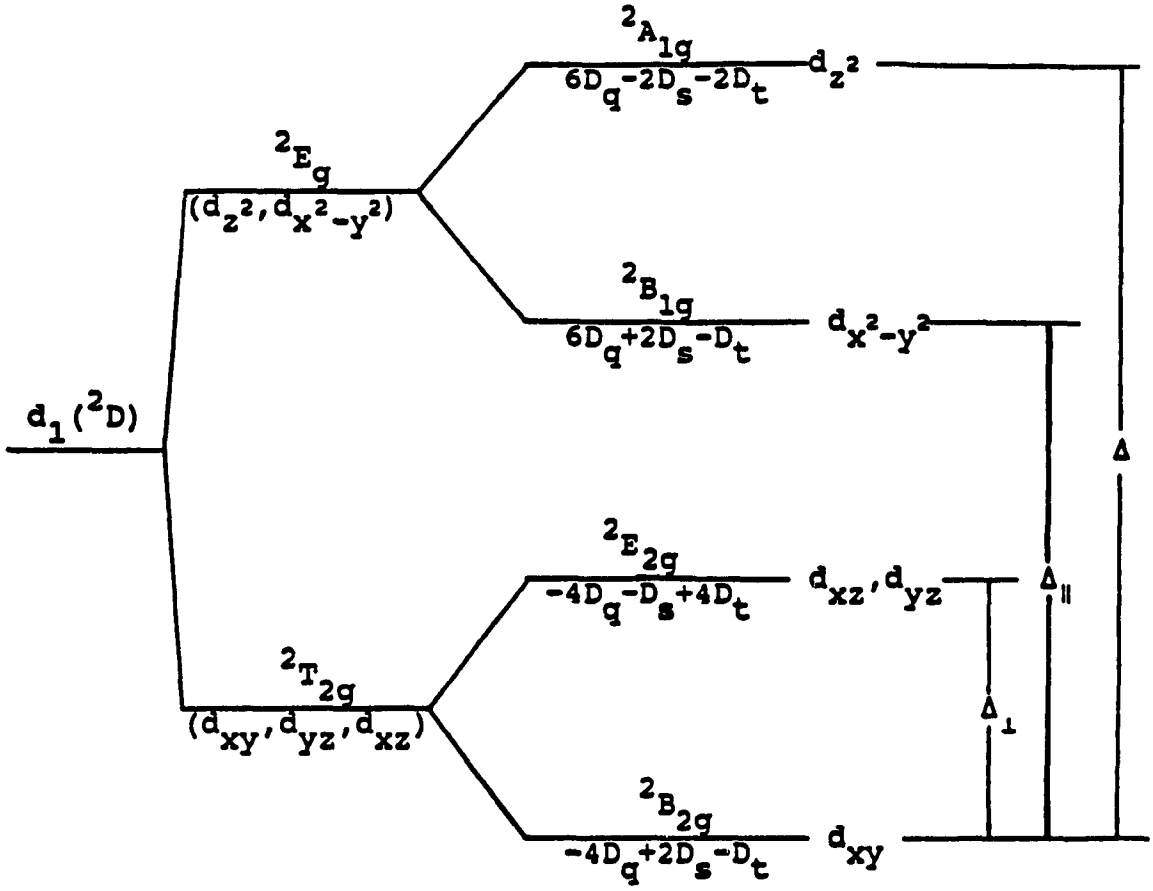

Fig. 11.1 Effect of tetragonal distortion upon the energy levels of a d^1 ion in an octahedral field.

enters a $M(NH_4)_2(SO_4)_2 \cdot 6H_2O$ (M = Cd, Mg, Zn, Fe, Co) lattice to substitute for an M^{2+} ion and to form a $[VO(H_2O)_5]^{2+}$ complex with its nearest-neighbors (Fig. 5.1), which possesses a tetragonally-distorted octahedral symmetry.

Since the VO^{2+} EPR and optical-absorption data suggest vanadyl complex with a nearly tetragonal symmetry, which implies $g_{xx} \cong g_{yy}$ and $A_{xx} \cong A_{yy}$ for both the VO^{2+} ions I and II, the bonding parameters for this complex can be estimated by the use of the following relations [22, 23, 24, 25, 26]:

$$g_e - g_{\parallel} = \frac{4g_e\lambda\beta_1^2\beta_2^2}{\Delta_{\parallel}}, \tag{11.4}$$

$$g_e - g_{\perp} = \frac{g_e\lambda\gamma^2\beta_2^2}{\Delta_{\perp}}, \tag{11.5}$$

$$A_{\parallel} = -PK - \left\{\frac{4}{7}\beta_2^2\right\}P - \left\{\frac{4g_e\lambda\beta_1^2\beta_2^2}{\Delta_{\parallel}}\right\}P - \frac{3}{7}\left\{\frac{g_e\lambda\gamma^2\beta_2^2}{\Delta_{\perp}}\right\}P, \tag{11.6}$$

and

$$A_{\perp} = -PK + \left\{\frac{2}{7}\beta_2^2\right\}P - \frac{11}{14}\left\{\frac{g_e\lambda\gamma^2\beta_2^2}{\Delta_{\perp}}\right\}P. \tag{11.7}$$

In eqs. (11.4) - (11.7), P is the direct dipolar term (dipole-dipole interaction of the electron and nuclear spins), K is the Fermi-contact term, proportional to the amount of unpaired electron density at the vanadium nucleus,

and λ is the spin-orbit coupling constant for the vanadium ion. Using g_e = 2.0023, λ = 170 cm^{-1} [92] and assuming β_2^2 = 1.00 for the present case, since the electronic orbital (d_{xy}) of the ground state ($^2B_{2g}$) of the vanadium ion is strictly non-(in-plane)-π-bonding, (here, "in-plane" means in the plane which is perpendicular to the direction of V^{4+}-O^{2-} bond in the $[VO(H_2O)_5]^{2+}$-complex), as as predicted by Ballhausen and Gray [22] and accepted by others [109, 110, 111]; the estimated values of the bonding parameters, using eqs. (11.4) - (11.7), are listed in Table 11.1. The values of $(1 - \beta_1^2)$ and $(1 - \gamma^2)$ are measures of covalency [110], (the weaker the covalent character of the bonding the closer are the values of the coefficients β_1^2 and γ^2 to unity), the former gives an indication of the influence of σ-bonding between the ion and the equatorial ligands, which varies from compound to compound, generally depending upon the σ donor strength of the ligand; it describes the bonding between the vanadium ion and $H_2O(9)$ molecules in the present case. While the latter indicates the influence of the π-bonding between the vanadium ion with the vanadyl oxygen. Here, the σ-bonding is defined to be the covalent bonding containing two electrons formed by endwise overlap of orbitals from the two ions such that the maximum charge density is along the bond axis. While the π-bonding is the covalent bonding containing two electrons formed by sidewise overlap of orbitals from the two ions such that the maximum

charge density is directed normal to the bond axis [1, 128, 129]. For σ-bonding, the molecular orbitals have cylindrical symmetry about the bond axis. On the other hand, for π-bonding, the molecular orbitals may have nodal planes through the bond axis [128, 129]. The values of $\beta_1^2 = \gamma^2 = 0.5$ corresponds to a complete sharing of the electron between the two atomic orbitals, namely, the orbital of the vanadium ion and that of the ligand.

Table 11.1 shows that the values of $(1 - \beta_1^2)$ and $(1 - \gamma^2)$ for CASH, MASH, ZASH, FASH and COASH are comparable to each other, being different from those for the alums $KAl(SO_4)_2 \cdot 12H_2O$ and $NH_4Al(SO_4)_2 \cdot 12H_2O$ [112], for which the covalency due to σ-bonding is much greater than that due to π-bonding. However, the present values are comparable to those reported by Misra et al. [19] for VO^{2+}-doped $Cd(COO)_2 \cdot 3H_2O$.

Table 11.1 The splittings of the VO^{2+} energy levels ($\Delta_\perp$, $\Delta_\parallel$) as determined from the optical-absorption data, and bonding coefficients (β_1^2, γ^2, P, K, β_2^2) of the $[VO(H_2O)_5]^{2+}$ complex for VO^{2+}-doped $M(NH_4)_2(SO_4)_2 \cdot 6H_2O$ (M = Cd, Mg, Zn, Fe, Co) Tutton salts. The units for $\Delta_\perp$, $\Delta_\parallel$ and P are 10^4 cm^{-1}, 10^4 cm^{-1} and GHz, while the other parameters are dimensionless.

Host	$\Delta_\perp$	$\Delta_\parallel$	β_1^2	γ^2	P	K	β_2^2
CASH	1.34	1.59	0.77	0.76	0.36	0.85	1.00
MASH	1.33	1.48	0.65	0.71	0.34	0.90	1.00
ZASH	1.36	1.52	0.74	0.80	0.36	0.90	1.00
FASH	1.39	1.52	0.74	0.80	0.37	0.81	1.00
COASH	1.30	1.60	0.58	0.66	0.39	0.76	1.00

CHAPTER XII

SYSTEMATICS OF VO^{2+} EPR SPECTRA IN $M(NH_4)_2(SO_4)_2 \cdot 6H_2O$ (M = Cd, Mg, Zn, Fe, Co)

As mentioned in the introduction (Chap. I), $M(NH_4)_2(SO_4)_2 \cdot 6H_2O$ (M = Zn, Cd, Mg, Fe, Co and Ni, i.e. ZASH, CASH, MASH, FASH, COASH and NASH, respectively), form a series of Tutton salts [69]. For NASH, VO^{2+}-doped sample did not exhibit any EPR signal at any temperature, implying that the VO^{2+} ion could not replace a Ni^{2+} ion in the NASH lattice. This is in contrast to the Mn^{2+} ion, which can, indeed, replace a host M^{2+} ions in the Tutton-salt lattice, exhibiting a well-defined EPR spectrum [28].

After a careful comparison, the following points, as far as the systematics of properties of VO^{2+} in the host lattices of the Tutton salts is concerned, are noted:

(i) The values of the $\tilde{g}^2$ and $\tilde{A}^2$ tensors for all the VO^{2+}-doped Tutton salts as seen from Tables 4.3 - 4.7 are very close to each other (within 5%). not depending significantly on the host divalent metallic ions. For all the samples, the principal values of the $\tilde{g}^2$, $\tilde{A}^2$ tensors indicate an axial symmetry of the ligand field, i.e. two $\tilde{g}$, and $\tilde{A}$, principal values being equal associated with a small distortion. As well, these values are almost temperature independent. (Except for a small g-shift due to the VO^{2+}-Fe^{2+} exchange interaction at LHT in FASH.) This can be

well explained by the model of the $[VO(H_2O)_5]^{2+}$ complex, in which the nearest-neighbor ions to the VO^{2+} ion are five water molecules whose crystal field determines the values of the $\tilde{g}^2$, $\tilde{A}^2$ tensors of the VO^{2+} ion. In a similar fashion, the bonding coefficients of the $[VO(H_2O)_5]^{2+}$ complex for all the VO^{2+}-doped Tutton salts are found to be about the same. The host M^{2+} ions are only the next-nearest-neighbors to a VO^{2+} ion; thus they have a rather weak effect on the $\tilde{g}^2$, $\tilde{A}^2$ tensors and the bonding coefficients, although different radii of M^{2+} ions cause slightly different distortions of the axial site symmetry seen by the VO^{2+} ion in these crystals. Also, replacing the $[VO(H_2O)_5]^{2+}$-complex by $[VO(D_2O)_5]^{2+}$-complex does not change the values of $\tilde{g}^2$ and $\tilde{A}^2$ tensors significantly, as seen in the case of VO^{2+}-doped MDSD crystal. This seems to suggest that the ligand oxygen ions play a dominant part in determining the VO^{2+} SHP values.

(ii) The SHF interactions in the hosts consisting of diamagnetic ions and hosts consisting of paramagnetic ions, are observed to be very different from each other. Paramagnetic host-ions may have an effect in reducing the SHF interaction between the VO^{2+} ion and the ligand protons. For each of the CASH, MASH and ZASH hosts consisting of diamagnetic ions, the maximum principal value of the SHF interaction tensor was determined to be about 14 MHz. However, for the FASH and COASH hosts consisting of

paramagnetic ions, the value of the SHF interaction tensor (isotropic) was estimated to be about 1.9 MHz, being about 14% of the maximum SHF value in the diamagnetic hosts. Accordingly, the values of f_s, density of the unpaired electron of VO^{2+} at the ligand site, for FASH and COASH hosts consisting of paramagnetic ions are also smaller than those for CASH, MASH and ZASH hosts consisting of diamagnetic ions.

(iii) The magnetic properties of the host M^{2+} ions do play important roles in determining the VO^{2+} EPR linewidths (ΔB) in various crystals. For the CASH, MASH and ZASH hosts, containing diamagnetic Cd^{2+}, Mg^{2+} and Zn^{2+} ions, smaller ΔB, independent of temperature, were observed. However, for the FASH and COASH lattices, containing the paramagnetic Fe^{2+} and Co^{2+} ions, ΔB values were found to be about twice as large as those in the diamagnetic hosts at RT.

(iv) The spin-lattice relaxation times (τ) for the host ions Fe^{2+} and Co^{2+} have been estimated from the VO^{2+} EPR linewidths, due to the paramagnetism of the host-ions in the FASH and COASH hosts, appropriately taking into account the dipolar and exchange interactions of the VO^{2+}-Fe^{2+} or VO^{2+}-Co^{2+} pairs. Although both FASH and COASH hosts contain paramagnetic ions, their temperature dependences of the VO^{2+} EPR linewidths are found to be very different from each other. For FASH, ΔB was almost independent of the temperature in the range of 4.2 - 393 K, the temperature

dependence of τ has been discussed in Chap. IX. In the case of Co^{2+} in COASH, $\tau^{-1} \propto T$ (143 K $\leq$ T $\leq$ 413 K), where the exponent (1.0) suggests the predominance of the direct process of spin-lattice relaxation. Further, similar to the case for the other host crystals containing Co^{2+} ions [1], a clearly-resolved VO^{2+} EPR spectrum for COASH was observed only above 117 K.

CHAPTER XIII

CONCLUSIONS

The conclusions drawn from the EPR studies of Mn^{2+}-doped AS, Gd^{3+}-doped APST, VO^{2+}-doped CASH, MASH, ZASH, FASH and COASH, and Cu^{2+}-doped MNST and CNST crystals, presented in this thesis, can be summarized as follows.

XIII.1 Mn^{2+}-doped $(NH_4)_2SO_4$

The following are the salient features of the present study:

(i) Two different Mn^{2+} centers, belonging to two inequivalent sublattices undergoing first- and second-order phase transitions, have been simultaneously observed in AS. Previously, either center I, or center II, but not both together, was observed. Above T_c, there exist two inequivalent sublattices in AS for each of the NH_4^+ and SO_4^{2-} ions which are coupled to each other; each of these split further into two sub-sublattices below T_c.

(ii) The ferroelectric phase transitions of different natures for the two sublattices are caused by couplings of different strengths of the two sublattices to the acoustic mode, effected by the spontaneous strain.

(iii) The unusual crossing of split lines, observed for Mn^{2+} center I below T_c, indicates that only one sublattice is responsible for the temperature variation of

the spontaneous polarization, P_s, since only one center exhibits a crossing of split EPR lines as the temperature changes.

(iv) The values of RT Mn^{2+} spin-Hamiltonian parameters (SHP), as reported presently, have been estimated by the use of a rigorous LSF procedure.

(v) The ferroelectric phase transition temperature, T_c, presently determined to be 223 K, is in agreement with the well-accepted value. The critical exponent (β) for both Mn^{2+} centers in AS has been determined. The ferroelectric phase transition in AS is found to satisfy both the scaling law and Rushbrooke inequality.

XIII.2 Gd^{3+}-doped $NH_4Pr(SO_4)_2 \cdot 4H_2O$

The main results of the present EPR studies on Gd^{3+}-doped APST are as follows:

(i) The orientations of the principal axes for the two magnetically-inequivalent Gd^{3+} ions, as well as the SHP of a monoclinic spin-Hamiltonian for Gd^{3+} have been determined for Gd^{3+} in APST at RT.

(ii) The superposition model has been satisfactorily exploited to explain the observed small values of b_2^0 in this crystal. Similar application should explain the small observed values of b_2^0 in the isostructural crystals $NH_4Ce(SO_4)_2 \cdot 4H_2O$, $NH_4Nd(SO_4)_2 \cdot 4H_2O$ and $NH_4Sm(SO_4)_2 \cdot 4H_2O$.

(iii) Two first-order phase transitions have been

deduced to occur at 266 and 155 K from the temperature variation of the overall EPR splittings and the EPR linewidths.

(iv) The host-ion spin-lattice relaxation time (τ) of Pr^{3+} in APST has been estimated by the use of EPR linewidths in the 296 - 410 temperature range, using the correct expression for crystals consisting of two different kinds of paramagnetic ions. Similar estimation has been done for τ of Ce^{3+}, Nd^{3+} and Sm^{3+} ions in the isostructural ACST, ANST and ASST lattices; much shorter τ values than those estimated using the incorrect expression [5] have been presently estimated.

(v) The power-law dependence on temperature of τ^{-1} values of the Pr^{3+} ion, which is independent of J_p, suggests the dominance of the sum relaxation process in APST crystal in the temperature range 266 - 296 K (T^7 dependence of τ^{-1}), and that of the Raman process in the 296 - 410 K range (T^2 dependence of τ^{-1}).

XIII.3 VO^{2+}-doped $M(NH_4)_2(SO_4)_2 \cdot 6H_2O$ (M = Cd, Mg, Zn, Fe, Co) and $Mg(ND_4)_2(SO_4)_2 \cdot 6D_2O$

They following are the main findings of the present EPR study on VO^{2+}-doped CASH, MASH, ZASH, FASH, COASH and MDSD crystals:

(i) The principal values of the $\tilde{g}$ and $\tilde{A}$ matrices, and those of the SHF interaction ($\tilde{A}^L$) matrix, as well as their

direction cosines, have been evaluated at different temperatures from the positions of the allowed hf lines. It is found that There is no significant temperature dependence exhibited by the $\tilde{g}$ and $\tilde{A}$ matrices. Further, replacing H_2O molecules, surrounding the VO^{2+} ion, with D_2O molecules does not change the VO^{2+} SHP significantly.

(ii) The VO^{2+} ion substitutes for a divalent metallic ion, referred to as M^{2+}, upon entering the CASH, MASH, ZASH, FASH, or COASH lattice, forming the $[VO(H_2O)_5]^{2+}$ complex. The V^{4+}-O^{2-} orientations of the three VO^{2+} ions I, II and III are deduced to be along the M^{2+}-$H_2O(7)$, M^{2+}-$H_2O(8)$ and M^{2+}-$H_2O(9)$ directions, respectively. The three VO^{2+} ions are physically inequivalent. This is also true in the case of VO^{2+}-doped MDSD crystal, where the model of $[VO(D_2O)_5]^{2+}$-complex applies. A mistake in one of the previously determined one of the V^{4+}-O^{2-} bond directions in VO^{2+}-doped MASH and COASH crystals has been corrected.

(iii) The SHF splitting for ions I and II originates as a result of the interaction between the VO^{2+} ion and the four protons of its nearest-neighbor pair of water molecules, $H_2O(9)$. As for ion III in ZASH, where one observed resolved SHF structure, the four protons responsible for SHF splitting belong either to the pair of water molecules $H_2O(7)$, or $H_2O(8)$. This has been confirmed experimentally by measuring the VO^{2+} EPR spectra of MDSD crystal.

(iv) The bonding parameters of the complex $[VO(H_2O)_5]^{2+}$ have been estimated from the present optical-absorption and EPR data on CASH, MASH, ZASH, FASH and COASH crystals. The density of the unpaired electron of the VO^{2+} ions at the site of ligand protons has also been estimated for all the crystals.

(v) The present study has resolved the "in-plane anisotropy" controversy, for VO^{2+}-doped ZASH, i.e. the non-coincidence of the principal axes of the $\tilde{g}$ and $\tilde{A}$ matrices. The principal axes of the $\tilde{g}$ and $\tilde{A}$ matrices in the XY plane are presently determined to be coincident, contrary to the previously-reported results.

(vi) The VO^{2+}-Fe^{2+} exchange-interaction constant has been estimated in FASH host consisting of paramagnetic ions, using the g-shift in the paramagnetic host from that in the isostructural $M(NH_4)_2(SO_4)_2 \cdot 6H_2O$ (M = Zn, Mg, Cd) hosts consisting of diamagnetic ions.

(vii) The host-ion spin-lattice relaxation times (τ) of Fe^{2+} and Co^{2+} in the FASH and COASH lattices, respectively, have been estimated, using an appropriate expression taking into account the presence of two kinds of paramagnetic ions from VO^{2+}-impurity-ion EPR linewidths. The predominant process of spin-lattice relaxation of Co^{2+} host ion has been deduced to be the direct process.

(viii) The present EPR and optical-absorption results have been analyzed with a view to deduce the systematics of

VO^{2+} EPR spectra in this series of Tutton salts. The paramagnetism of the host ions is found to have a significant effect on the linewidth and host-ion spin-lattice relaxation times, as well as on the SHF interaction of the VO^{2+} ion with the nearest protons.

XIII.4 Cu^{2+}-doped $MNa_2(SO_4)_2 \cdot 4H_2O$ (M = Mg, Co)

The main results of the present EPR studies on Cu^{2+}-doped MNST and CNST single crystals are as follows:

(i) Two magnetically inequivalent, but physically equivalent, Cu^{2+} complexes have been observed in both MNST and CNST hosts. The Cu^{2+} ion enters the site of an M^{2+} (M = Mg, Co) ion, forming a $CuO_2(H_2O)_4$ complex, which has an orthorhombically distorted octahedral symmetry, as exhibited by the three different principal values of $\tilde{g}$ matrices.

(ii) At room and lower temperatures, a pseudo-static Jahn-Teller effect (JTE) was observed for both the samples. Cu^{2+} occupies only the lowest Jahn-Teller potential valley, of the three potential valleys. At higher temperatures, a dynamic JTE was observed, wherein the Cu^{2+} ion occupies all the three Jahn-Teller valleys with equal probabilities. The transition between the two kinds of JTE was found to occur at 347 ± 2 K and 339 ± 2 K for MNST and CNST, respectively.

(iii) The temperature dependences of Cu^{2+} EPR linewidths for MNST and CNST have been explained to be due mainly to the spin-lattice relaxation processes of the

impurity-ion Cu^{2+} for the MNST host consisting of diamagnetic ions, and the host-ion Co^{2+} for the CNST host consisting of paramagnetic ions, respectively. The respective spin-lattice relaxation times, i.e., τ of Cu^{2+} in MNST and τ of Co^{2+} in CNST, have been estimated. The predominant spin-lattice relaxation process of host-ion Co^{2+} in CNST, in the 280 - 330 K temperature range, has been deduced to be Kramers' Raman process from the temperature dependence of $\tau^{-1} \propto T^{9}$.

REFERENCES

[1] A. Abragam and B. Bleaney, *Electron Paramagnetic Resonance of Transition Ions* (Clarendon, Oxford, 1970).

[2] S. A. Al'tshuler and B. M. Kozyrev, *Electron Paramagnetic Resonance in Compounds of Transition Elements*, Keter, Jerusalem (1974).

[3] S. A. Al'tshuler and B. M. Kozyrev, *Electron Paramagnetic Resonance*, (Academic Press, New York, 1964).

[4] S. K. Misra, J. Sun and S. Jerzak, Phys. Rev. B40, 74 (1989).

[5] S. K. Misra and J. Sun, Phys. Stat. Sol. (b)162, 265 (1990).

[6] S. K. Misra, U. Orhun and J. Sun, Solid St. Commun. 76, 949 (1990).

[7] S. K. Misra and J. Sun, Physica B162, 331 (1990).

[8] S. K. Misra and J. Sun, Phys. Rev. B42, 8601 (1990).

[9] S. K. Misra, J. Sun and U. Orhun, Phys. Stat. Sol. (b)162, 585 (1990).

[10] S. K. Misra, J. Sun and X. Li, Physica B167, to be published (1990).

[11] F. J. Owens, *Magnetic Resonance of Phase Transitions*, (eds. F. J. Owens, C. P. Poole Jr and H. Farach), Academic, New York (1979).

[12] G. C. Upreti and P. Chand, Mag. Reson. Rev. **12**, 245 (1987).

[13] S. K. Misra and J. Sun, Mag. Reson. Rev., to be published (1990).

[14] S. K. Misra and G. C. Upreti, Mag. Reson. Rev. **10**, 333 (1986).

[15] R. P. Kohin, Mag. Reson. Rev. **5**, 75 (1979).

[16] P. Chand, V. K. Jain and G. C. Upreti, Mag. Reson. Rev. **14**, 49 (1988).

[17] B. V. R. Chowdari, J. Phys. Soc. Jpn. **27**, 1135 (1969).

[18] B. V. R. Chowdari, J. Phys. Soc. Jpn. **29**, 105 (1970).

[19] S. K. Misra and C. Wang, Physica **B159**, 105 (1989).

[20] R. H. Borcherts and C. Kikuchi, J. Chem. Phys. **40**, 2270 (1964).

[21] S. Radhakrishna and M. Salagram, Solid St. Commun. **47**, 77 (1983).

[22] C. J. Ballhausen and H. B. Gray, Inorg. Chem. **1**, 111 (1962).

[23] N. Satyanarayana and S. Radhakrishna, Cryst. Latt. Def. and Amorph. Mat. **97**, 337 (1984).

[24] D. Kivelson and S. Lee, J. Chem. Phys. **41**, 1896 (1964).

[25] K. DeArmond, B. B. Garrett and H. S. Gutowsky, J. Chem. Phys. **42**, 1019 (1965).

[26] L. J. Boucher, E. C. Tynan and T. F. Yen, *Electron Spin Resonance of Metal Complexes*, (Edited by T. F. Yen, Plenum Press 1969).

[27] C. Kittel, Phys. Rev. **73**, 155 (1948).

[28] S. K. Misra and S. Z. Korczak, Phys. Rev. B35, 4625 (1987).

[29] S. K. Misra and S. Z. Korczak, Phys. Rev. B34, 3086 (1986).

[30] S. K. Misra, C. Wang, S. Han and S. Z. Korczak, Phys. Rev. B36, 3542 (1987).

[31] S. K. Misra, M. Kahrizi, P. Mikolajczak and L. Misiak, Phys. Rev. B32, 4738 (1985).

[32] S. K. Misra, Mag. Reson. Rev. **12**, 1919 (1987).

[33] S. K. Misra and U. Orhun, Phys. Rev. B39, 2856 (1989).

[34] V. T. Matthias and J. P. Remeika, Phys. Rev. **103**, 262 (1956).

[35] H. Ohshima and E. Nakamura, J. Phys. Chem. Solids 27, 481 (1966).

[36] S. Hoshino, K. Vedam, Y. Okaya and R. Pepinsky, Phys. Rev. **112**, 405 (1958).

[37] H. G. Unruh, Solid St. Commun. **8**, 1951 (1970).

[38] Y. Makita, A. Sawada, Y. Takagi, J. Phys. Soc. Jpn. 41, 167 (1976).

[39] A. Sawada, Y. Makita, Y. Takagi, J. Phys. Soc. Jpn. 41, 174 (1976).

[40] T. Ikada, K. Fujibashi, T. Nagai and K. Okayshi, Phys. Stat. Sol. (a)16, 279 (1973).

[41] E. O. Schlemper and W. C. Hamilton, J. Chem. Phys. 44, 4498 (1966).

[42] R. Blinc and I. Levstek, J. Phys. Chem. Solids **12**, 295 (1960).

[43] Y. S. Jain, H. D. Bist and G. C. Upreti, Chem. Phys. Lett. **22**, 572 (1973).

[44] Z. Iqbal and C. W. Christoe, Solid St. Commun. **18**, 269 (1976).

[45] D. E. O'Reilly and T. Tsang, J. Chem. Phys. **46**, 1291 (1967).

[46] A. Sawada, Y. Takagi and Y. Ishibashi, J. Phys. Soc. Jpn. **34**, 748 (1973).

[47] J. Petzelt, J. Grigas and I. Myerova, Ferroelectrics **6**, 225 (1974).

[48] A. Sawada, S. Ohya, Y. Ishibashi and Y. Takagi, J. Phys. Soc. Jpn. **38**, 1408 (1975).

[49] Y. S. Jain, P. K. Bajpai, R. Bhattachajee and D. Chowdhury, J. Phys. **C19**, 3789 (1986).

[50] B. Rakvin and N. S. Dalal, J. Chem. Phys. **85**, 6060 (1986).

[51] R. Yu. Abdulsabirov, Yu. S. Greznev and M. M. Zaripov, Sov. Phys. - Solid State **14**, 2894 (1973).

[52] K. N. Shrivastava, Phys. Stat. Solidi (a) **1**, K101 (1970).

[53] S. K. Misra and K. N. Shrivastava, Phys. Rev. **B37**, 2255 (1988).

[54] G. Chaddha, J. Phys. Soc. Jpn. **24**, 976 (1968).

[55] F. J. Owens, Chem. Phys. Lett. **38**, 106 (1976).

[56] C. V. Manjunath and R. Srinivasan, Phys. Stat. Sol. (a) **44**, 687 (1977).

[57] N. Shibata, R. Abe and I. Suzuki, J. Phys. Soc. Jpn. **41**, 2011 (1976).

[58] M. Fujimoto and S. Jerzak, unpublished.

[59] M. Fujimoto, L. A. Dressel and T. J. Yu, J. Phys. Chem. Solids **38**, 97 (1977).

[60] K. Chu, J. Mag. Reson. **21**, 151 (1976).

[61] S. V. Bhat, N. C. Mishra and R. Srinivasan, J. Phys. Chem. Solids **43**, 1157 (1982).

[62] C. V. Manjunath and R. Srinivasan, Phys. Stat. sol. (b) **87**, 395 (1978).

[63] B. Eriksson, L. O. Larsson, L. Niinisto and U. Skoglund, Inorg. Chem. **13**, 290 (1974).

[64] R. J. Callow, *The Industrial Chemistry of the Lanthanides: Yttrium, Thorium and Uranium*, (Pergamon Press, Oxford, 1967).

[65] V. M. Malhotra, H. D. Bist and G. C. Upreti, Chem. Phys. Lett. **28**, 390 (1974).

[66] H. A. Buckmaster, V. M. Malhotra and H. D. Bist, Can. J. Phys. **59**, 596 (1981).

[67] V. M. Malhotra, H. A. Buckmaster and H. D. Bist, Can. J. Phys. **58**, 1667 (1980).

[68] S. G. Jasty and V. M. Malhotra, EPR Symposium, Rocky Mountain Conference, Denver, Colorado (1988).

[69] R. W. G. Wyckoff, *Crystal Structures*, Vol. 3,

Interscience Publishers, New York (1963).

[70] Landolt-Bornstein Series: *Numerical Data and Functional Relationship in Science and Technology* Vol. 16 (Ferroelectric and Related Substance). Subvolume b: Non oxides, edited by T. Mitsui and E. Nakamura, Springer-Verlag, Berlin (1982).

[71] Y. Okaya, K. Vedam and R. Pepinsky, Acta Cryst. **11**, 307 (1958).

[72] M. Montgomery and E. C. Lingafelter, Acta Crystallogr. **20**, 728 (1966).

[73] T. N. Margulis and D. H. Templeton, Z. für Kristallographie **117**, 344 (1962).

[74] H. Montgomery, R. V. Chastain, J. J. Natt, A. M. Witkowska and E. C. Lingafelter, Acta Crystallogr. **22**, 775 (1967).

[75] N. Satyanarayana and S. Radhakrishna, J. Chem. Phys. **83**, 529 (1985).

[76] S. K. Misra, J. Mag. Reson. **23**, 403 (1976).

[77] S. K. Misra, Physica B **121**, 193 (1983).

[78] S. K. Misra, Physica **B124**, 53 (1983).

[79] S. K. Misra and S. Subramanian, J. Phys. C **15**, 7199 (1982).

[80] A. Steudel, *Hyperfine Interactions*, Academic Press, New York (1970).

[81] S. K. Misra and C. Rudowicz, Phys. Stat. Sol. (b)**147**, 677 (1988).

[82] G. C. Upreti and R. S. Saraswat, Phys. Stat. Sol. (b)122, K169 (1984).

[83] B. Jayaram and J. Sobhanadri, Cryst. Latt. Def. and Amorph. Mat. **10**, 47 (1983).

[84] R. Muncaster and S. Parke, J. Non-cryst. Solids **24**, 399 (1977).

[85] J. Strach and R. Bramley, Chem. Phys. Lett. **109**, 363 (1984).

[86] G. D. Watkins, Phys. Rev. **113**, 79 (1959).

[87] L. E. Misiak, S. K. Misra and P. Mikolajczak, Phys. Rev. B38, 8673 (1988).

[88] S. K. Misra, P. Mikolajczak and N. R. Lewis, Phys. Rev. B24, 3729 (1981).

[89] D. J. Newman and W. Urban, Adv. Phys. **24**, 793 (1975).

[90] L. Vegard, Z. Cryst. 67, 239 (1928).

[91] J. Kuriata and W. Pastusiak, Acta Phys. Pol. A66, 627 (1984).

[92] V. K. Jain, Phys. Stat. Sol. (b)97, 337 (1980).

[93] R. B. Griffiths, *Phase Transitions and Critical Phenomena*, Vol. **1**, (eds. C. Domb and M. S. Green), Academic, New York (1972).

[94] F. J. Owens, Phys. Stat. Sol. (b) 79, 623 (1977).

[95] F. J. Owens, Rep. Prog. Phys. **29**, 675 (1966).

[96] J. C. Gill and P. A. Ivey, J. Phys. C7, 1536 (1974).

[97] A. Bose, A. S. Chakravarty, and R. Chatterjee, Proc. R. Soc. London, A261, 207 (1961).

[98] S. K. Misra and X. Li, to be published.

[99] W. T. Gray IV and H. J. Stapleton, Phys. Rev. B9, 2863 (1974).

[100] K. N. Shrivastava, Phys. Stat. Sol. (b)117, 437 (1983).

[101] R. Le Naour, Phys. Rev. B1, 2007 (1970).

[102] K. N. Shrivastava, Phys. Stat. Sol. 42, K177 (1970).

[103] K. N. Shrivastava, Phys. Stat. Sol. (a)92, K19 (1979).

[104] K. Sugawara, C. Y. Huang, and B. R. Cooper, Phys. Rev. B11, 4455 (1975).

[105] K. Sugawara, C. Y. Huang, and B. R. Cooper, Phys. Rev. B28, 4955 (1983).

[106] B. R. Cooper, R. C. Fedder and D. P. Schumacher, Phys. Rev. 163, 506 (1967).

[107] S. K. Misra, U. Orhun, and J. Sun, to be published.

[108] B. Bleaney and D. J. E. Ingram, Proc. Roy. Soc. London A208 143 (1951).

[110] V. P. Seth, V. K. Jain, A. Yadav and R. S. Bansal, Phys. Stat. Sol. (b)132, K139 (1985).

[111] V. K. Jain, J. Phys. Soc. Jpn. 46, 1250 (1979).

[112] K. V. S. Rao, M. D. Sastry and P. Venkateswarlu, J. Chem. Phys. 49, 4984 (1969).

[113] S. K. Misra and C. Wang, Mag. Reson. Rev. 14, 157 (1990).

[114] H. Bill, *Observation of the Jahn-Teller Effect*, in

Dynamical Jahn-Teller Effect in Localized Systems, Ed. by Yu. E. Rerlin and M. Wager, Elsevier Science Publisher B. V. (1984).

[115] F. S. Ham, *Jahn-Teller Effects in Electron Paramagnetic Resonance Spectra*, in *Electron Paramagnetic Resonance*, Ed. by Geschwind, Plenum Press (1972).

[116] Von. M. Giglio, Acta Crystallogr. 11, 789 (1958).

[117] V. K. Jain and P. Venkateswarlu, J. Phys. C12, 865 (1979).

[118] V. K. Jain, J. Phys. C12, 1403 (1979).

[119] G. R. Bulka, S. V. Vedenin, V. M. Vinokurov, T. A. Zakharchenko, N. M. Nizamutdinov and R. S. Tukhvatullin, Sov. Phys. - Crystallogr. 16, 107 (1971).

[120] J. M. Gaite, G. R. Bulka, N. M. Hasanova, N. M. Nizamutdinov and V. M. Vinofurov, J. Phys. C19, 2077 (1986).

[121] B. A. Sastry and G. S. Sastry, J. Phys. C4, L347 (1971).

[122] B. A. Sastry, B. Madhu and K. M. Kar, Indian J. Phys. A62, 463 (1988).

[123] V. K. Jain and V. S. Yadav, Solid St. Commun. 69, 407 (1989).

[124] D. P. Breen, D. C. Krupka and F. I. B. Williams, Phys. Rev. 179, 241 (1969).

[125] B. Bersukev and V. Z. Polinger, in *The Dynamical Jahn-Teller Effect in Localized Systems*, (North-Holland, Amsterdam, 1984).

[126] S. K. Misra and C. Wang, J. Phys.: Condens. Matter, 1, 771 (1989).

[127] G. L. Bir, Scv. Phys. - Solid State, 18, 946 (1976).

[128] C. A. Hampel and G. G. Hawley, *The Encyclopedia of Chemistry*, 3rd Edition, Van Nostrand Reinhold Company, New York (1976).

[129] D. F. Shriver, P. W. Atkins and C. H. Langford, *Inorganic Chemistry,* W. H. Freeman and Company, New York (1990).

APPENDIX I

PUBLICATIONS

This appendix contains the published papers, reporting the EPR studies included in this thesis.

PHYSICAL REVIEW B VOLUME 40, NUMBER 1 1 JULY 1989

Mn^{2+} EPR study of the phase transition in an ammonium sulfate single crystal: Existence of two inequivalent sublattices

Sushil K. Misra, Jiansheng Sun,* and Stanislaw Jerzak†
Physics Department, Concordia University, 1455 de Maisonneuve Boulevard West, Montreal, Quebec, Canada H3G 1M8
(Received 14 December 1988)

Angular variations of X-band EPR spectra, for the magnetic field orientations in three mutually perpendicular planes, of a single crystal of Mn^{2+}-doped $(NH_4)_2SO_4$, have been recorded from 113 to 398 K. Two Mn^{2+} centers, the principal axes of whose zero-field splitting tensors (b_2^0) are found to be oriented very close to each other, exhibit ferroelectric phase transitions of entirely different natures, although occurring at the same transition temperature ($T_c = 223$ K). At T_c, the EPR lines corresponding to one center exhibit a jump (first-order transition), while those for the other a continuity (second-order transition). For both the centers each EPR hyperfine line splits into two below T_c. The Mn^{2+} spin-Hamiltonian parameters in $(NH_4)_2SO_4$ are evaluated at room temperature, using a rigorous least-squares-fitting procedure, combined with numerical diagonalization of the spin-Hamiltonian matrix. The present EPR data confirm the existence of two inequivalent sublattices in the $(NH_4)_2SO_4$ crystal. The unusual crossing of the EPR line positions, below T_c, for the Mn^{2+} center which undergoes a first-order phase transition at T_c, has been related to the reversal of the spontaneous polarization. The dynamic behavior of the two Mn^{2+} centers, in this ferroelastic crystal, has here been interpreted to be due to the deformation of the SO_4^{2-} groups and the spontaneous strain produced by the acoustic mode. The critical exponent β has been determined, for both the centers, to be 0.49 ± 0.03, from the line splitting below T_c. It has been verified that the scaling law and Rushbrooke inequality are well satisfied in $(NH_4)_2SO_4$.

I. INTRODUCTION

Ammonium sulfate [$(NH_4)_2SO_4$] (AS, hereafter) has been found to undergo a phase transition, becoming ferroelectric below 223 K, by Matthias and Remeika.[1] Unusual ferroelectric properties, e.g., a low value of the Curie-Weiss constant,[2] a large spontaneous strain,[3,4] provided a great deal of interest in AS. In order to understand the transition mechanism responsible for the phase transition, many experimental techniques, e.g., dielectric measurement,[5] neutron diffraction,[6] NMR,[7] EPR,[8–20] infrared,[21] and Raman spectroscopy,[22] have been used to study AS. Theoretically, different mechanisms, e.g., order-disorder,[23] displacive,[24] improper-ferroelectric,[5] "coupled-oscillator-relaxator" model,[25] two-inequivalent ferroelectric sublattices,[26] and, more recently, the molecular-distortion model[27] and weakly first-order Landau-type-transition model,[20] have been invoked to explain the mechanism of the phase transition in AS. Despite so many studies, the phase-transition mechanism in AS still remains controversial. Even the transition temperature T_c, the spontaneous polarization P_s, and its temperature dependence, have been reported to have different values; as well, the various explanations provided are at variance from each other. Hoshino *et al.*[3] reported that P_s was almost temperature independent in the neighborhood of the ferroelectric "Curie" temperature T_c (223 K), while Ikeda *et al.*[5] found the same result at a lower temperature (153 K). They explained it by the use of a phenomenological theory. Later, Unruh *et al.*[4] reported that P_s was strongly temperature dependent, changing the sign below 85 K; this was explained by Sawada *et al.*[26] to be due to the existence of two-inequivalent sublattices in AS. In the two-inequivalent-sublattices model, also referred to as the ferroelectric model, Sawada *et al.*[26] proposed that the two NH_4^+ ions in the unit cell of AS are crystallographically inequivalent, possessing different dipole moments, which are likely to be antiparallel along the c axis. Sawada *et al.*[26] further proposed that all the SO_4^{2-} ions in AS are equivalent.

The AS crystal is ferroelastic, both in the paraelectric ($T > T_c$) and ferroelectric ($T < T_c$) phases.[28] Makita *et al.*[28] reported that, at room temperature, AS crystals consisted of three domains, separated by {011} and {031} twin planes. These domains can be switched amongst themselves by an external stress. Group-theoretical analysis[29] of AS crystal symmetry suggests that the pseudohexagonal orthorhombic symmetry P_{nam} ($Z = 4$) in the paraelectric phase may be derived by a hypothetical phase transition of AS from a hexagonal (prototype) structure of symmetry $P6_3/mmc$ ($Z = 2$), supposed to exist at high temperatures.

EPR has been used in the study of the phase-transition mechanisms, in AS because of its high sensitivity to the local changes in the environment around the paramagnetic ions doped as microscopic probes. Many different paramagnetic ions, such as Mn^{2+},[8–10] Cu^{2+},[11–13] SeO_3^-,[14,15] VO^{2+},[16,17] CrO_4^{3-},[18] $(CrO_4)^{2-}$,[19] and NH_3^-[14,20] have been used to this end. However, some of these studies have been confined to either temperatures above T_c, or both above and below T_c, but not systemati-

cally as a function of temperature in the range including T_c.[11,13,17,19] Similar to the findings of the other techniques, a lot of controversy exists in the EPR results on AS as well.

Mn^{2+} is an important EPR probe of the environment around it since its spin ($S=5/2$), being greater than 1/2, experiences the crystalline field directly via the spin-Hamiltonian (SH) parameters b_2^m, b_4^m. As for the EPR studies of Mn^{2+}-doped AS single crystal, Abdulsabirov *et al.*[8] found four physically equivalent Mn^{2+} centers, (i.e., only one type of Mn^{2+} center); the magnitudes of the angles between the Z axes, defined to be the principal axis of the zero-field splitting tensor b_2^m, of the four Mn^{2+} centers and the crystallographic axes (a,b,c) were found to be about the same. The respective Z axes, were deduced to be along the NH_4^+(I)-NH_4^+(II) directions, depending on which NH_4^+ ion is replaced by the Mn^{2+} ion, with a type-1 charge-compensation mechanism being effective.[20] The temperature variation of the value of the zero-field splitting parameter (b_2^0) was found by Abdulsabirov *et al.*[8] to be discontinuous at 215 K; thus implying the occurrence of a first-order phase transition at 215 K. This temperature was assumed to be T_c, 8 K lower than the well-accepted value (223 K). Shrivastava[9] also found the existence of only one type of Mn^{2+} center, corresponding to four physically equivalent Mn^{2+} complexes in the AS crystal, associated with a transition temperature of 217.5 K, 5.5 K lower than the accepted value of T_c. He observed that the EPR lines just split below 217.5 K without experiencing any jump in their positions; implying that AS undergoes a second-order phase transition at 217.5 K. Based on the data of Ref. 9, Misra and Shrivastava[10] estimated the critical exponent β for this second-order transition from the line splitting (ΔB) below T_c: $\Delta B \propto (T_c - T)^\beta$, with $\beta=0.5$ and $T_c=217.5$ K. Both Abdulsabirov *et al.*[8] and Shrivastava[9] estimated the Mn^{2+} spin-Hamiltonian parameters in AS at room temperature, the *differences* between their values are significant (Table I). Furthermore, the parameters were evaluated, employing perturbation expressions, using the line positions obtained for one direction of the external magnetic field ($\mathbf{B}\|\hat{Z}$) by Shrivastava,[9] while for three directions ($\mathbf{B}\|\hat{Z},\hat{X},\hat{Y}$) by Abdulsabirov *et al.*[8]

The present paper reports yet much more detailed and systematic EPR experimental study on the Mn^{2+}-doped AS single crystal. The purpose is to verify the existence of two different Mn^{2+} centers, to determine T_c, to study the nature of the phase transition of AS at T_c (first and/or second order), to evaluate the room-temperature spin-Hamiltonian parameters for Mn^{2+} in AS by the use of a rigorous least-squares-fitting procedure employing exact numerical diagonalization of the spin-Hamiltonian matrix,[13] and to interpret the temperature dependences of the EPR spectra for the two Mn^{2+} centers. A detailed discussion of the dynamic behavior of the two different Mn^{2+} centers is provided. In addition, the value of the critical exponent β has been estimated from the line splittings of the two Mn^{2+} centers below T_c. As well, the validity of the scaling law and Rushbrooke inequality has been examined.

II. EXPERIMENTAL ARRANGEMENT, SAMPLE PREPARATION, AND CRYSTAL STRUCTURE

The EPR spectra were recorded on a X-band Varian V4506 spectrometer, consisting of a 12-in. Varian Associates electromagnet, a Varian power supply, and a Bruker

TABLE I. Room-temperature Mn^{2+} spin-Hamiltonian parameters in $(NH_4)_2SO_4$ crystal, as evaluated by the use of a rigorous least-squares-fitting procedure.[13] The results of Abdulsabirov *et al.*[8] and Shrivastava[9] are also included for comparison. The unit for b_l^m, A and B values is GHz, while that for χ^2, GHz^2 [$\chi^2 \equiv \sum_j (|\Delta E_j| - h\nu_j)^2$; here ΔE_j is the calculated energy difference between the pair of levels participating in resonance for the jth line position, ν_j is the corresponding klystron frequency, and h is Planck's constant]. n is the number of lines fitted simultaneously. For the data of Abdulsabirov *et al.*[8] and Shrivastava[9], χ^2 are as calculated using their reported parameters and the line positions observed presently.

Parameters	Present work	Abdulsabirov *et al.* (Ref. 8)	Shrivastava (Ref. 9)
g_x	2.0014±0.0004	$g_x=2.0009$	$g=1.9959$
g_y	2.0176±0.0079	$g_y=2.0009$	
		$g_z=2.0014$	
b_2^0	2.153 ±0.003	−2.183	1.454
b_2^1	−0.714 ±0.027	1.108	−0.717
b_4^0	0.001 ±0.001	0.008	−0.006
b_4^1	0.699 ±0.045	0.000	
b_4^4	−0.281 ±0.180	0.039	
A	−0.258 ±0.003	0.259	−0.256
B	−0.281 ±0.003	0.263	−0.250
C		0.263	
χ^2/n	0.003	0.096	3.064
n	140	140	140

field controller (B-NM-2). The crystal was placed inside a TE_{102} Varian cavity. Temperatures, above and below room temperature, were maintained at the sample by gently blowing nitrogen gas, passing respectively through the heater coils and coils immersed in liquid nitrogen, of a Varian temperature-controller unit (model E4540). The temperature stability was better than 0.5 K, as measured by an Omega Engineering Inc. microprocessor-based thermocouple meter (model 680), with a temperature resolution of 0.1 K.

The AS crystals, used for measurements, were grown by slow evaporation at room temperature of an aqueous solution of $(NH_4)_2SO_4$ to which a small amount of $MnSO_4$ (0.5 at. %) was added. Good-quality crystals with dimensions suitable for measurements (about $3\times2\times8$ mm^3) were obtained after about eight weeks. It was found that Mn^{2+} does not enter the crystal lattice of AS in large amounts. Thus the actual amount of Mn^{2+} in AS crystals is much less than that present in the mother liquor. The crystals so obtained were colorless, had excellent cleavage in the (100) plane, and were almost ferroelastically monodomain, as verified under a polarizing microscope.

The growth habit of AS crystals is shown in Fig. 1. The crystal structure of AS has been determined by Schlemper and Hamilton,[6] by neutron diffraction; it is the same as that of K_2SO_4. At room temperature, the crystal possesses orthorhombic symmetry (space group P_{nma}), with the unit-cell parameters being $a=7.782$, $b=10.64$, and $c=5.993$ Å.[6] (Some AS crystals show a superstructure at room temperature, i.e., characterized by the b and c dimensions doubled.[31]) Below T_c, the reflection planes of the AS crystal disappear, changing the space group to P_{na2_1}, while the crystal still possesses orthorhombic symmetry; the c axis becomes the axis of electric polarization. The unit-cell parameters of AS below T_c are $a=7.837$, $b=10.61$, and $c=5.967$ Å.[6]

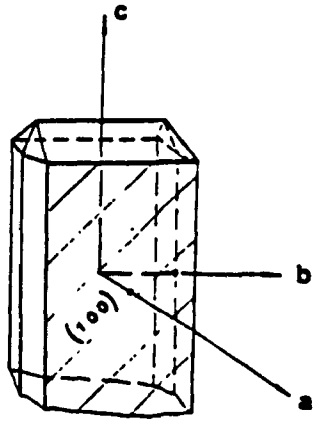

FIG. 1. The growth habit and crystallographic axes a, b, and c of $(NH_4)_2SO_4$ single crystal. The [100] plane, which exhibits a perfect cleavage, is shaded by oblique lines.

At room temperature, the unit cell of AS contains four formula units ($Z=4$). There are present two crystallographically different NH_4^+(I) and NH_4^+(II) ions. NH_4^+(I) ions, with five SO_4^{2-} ions surrounding them, are designated as α ammonium ions, while NH_4^+(II) ions, located in the middle of a distorted octahedra of SO_4^{2-} ions, are designated as β ammonium ions. The directions of the two NH_4^+(I)-NH_4^+(I) (or α-β) pairs make the following angles, relative to the crystallographic axes:[8] $(\hat{a},\hat{Z})=\pm71.2°$, $(\hat{b},\hat{Z})=\pm55.5°$, and $(\hat{c},\hat{Z})=\pm40.5°$. These directions are found to be almost coincident with the magnetic Z axes corresponding to the two Mn^{2+} centers, as seen in Sec. III below.

III. ROOM-TEMPERATURE EPR SPECTRA

EPR spectra were recorded for the orientations of the external magnetic field (B) in the ab, ac, and bc planes. Figure 2 exhibits the high-field EPR spectrum for the orientation of B in the ab plane, at 23° from the a axis; six strong hyperfine lines of almost equal intensity, corresponding to the highest-field fine-structure sextets $M=5/2\leftrightarrow3/2$ for the two Mn^{2+} centers, designated as I and II, are clearly visible. [For Mn^{2+}, $S=I=5/2$, where S and I are the electronic and nuclear spins, respectively. Therefore, for each Mn^{2+} center, the EPR spectrum consists of five allowed sextets $(M,m)\leftrightarrow(M-1,m)$, where M and m are, respectively, the electronic and nuclear magnetic quantum numbers.] The small difference in EPR line heights for Mn^{2+} centers I and II, as seen in Fig. 2, results from a slightly larger linewidth of center II, as compared with that for center I (17 G for center II and 14 G for center I). This suggests a somewhat bigger distortion of the surrounding of Mn^{2+} center II as compared to that of center I. The equality of the intensities of the EPR lines corresponding to centers I and II imply that the occupation probabilities of the sites available to centers I and II are about the same. (It is noted that there were observed, in addition, two other centers of very weak intensity designated as III and IV; these are, most likely, due to additional ferroelastic domains of AS crystal, which were, however, not detected under a polarizing microscope, because of their negligible volume. Centers III and IV have not at all been studied in the present paper because of their extremely weak intensities.)

Figure 3 shows the angular variation of the highest-field resonant lines for centers I and II for the orientation of B in the ab plane. The lines corresponding to the two magnetically inequivalent Mn^{2+} centers (I and II) are clearly visible in Fig. 3. This is possible because the principal axes and magnitudes of the zero-field splitting tensors b_2^m, corresponding to the two centers, are at definitive variance, albeit small, from each other.

Figures 4 and 5 exhibit the angular variation of EPR spectra for the orientation of B in the bc and ac planes, respectively; they are found to be symmetric about the b and c axes, respectively, for the two centers, in accordance with the crystal symmetry. Figures 4 and 5 confirm that there indeed exist two physically inequivalent Mn^{2+} centers with almost the same intensity

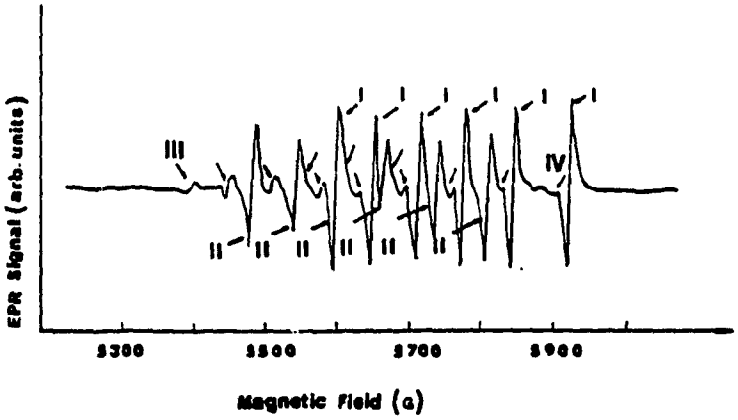

FIG. 2. EPR spectrum (first derivative) of Mn^{2+}-doped $(NH_4)_2SO_4$ crystal for B in the *ab* plane, 23° from the *a* axis, showing the highest-field hyperfine sextets (fine-structure transition $5/2 \leftrightarrow 3/2$), corresponding to the two Mn^{2+} centers, marked as I and II. The two centers have almost the same intensity. There are also seen two weak centers, marked as III and IV; these are due to another ferroelastic domain of relatively small volume.

but slightly different directions of the respective principal axes and the values of the zero-field splitting tensors b_2^m. These relative differences did not change much upon increasing the temperature from room temperature to 398 K, except that the EPR line positions moved slightly towards higher magnetic fields for both the centers.

The orientations of the principal axes of the zero-field splitting tensor b_2^m (i.e., the magnetic Z axes) corresponding to centers I and II can be determined from the angular variation of spectra in the three mutually perpendicular planes. (The magnetic Z, X, and Y axes of a Mn^{2+} complex are defined to be those directions of B for which

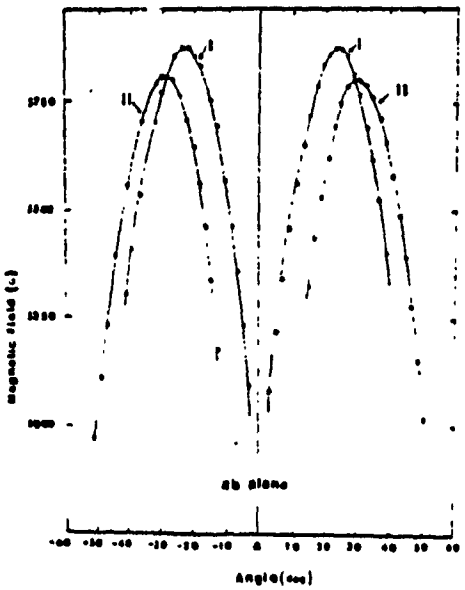

FIG. 3. Angular variation of the highest-field line of the highest-field hyperfine sextet for Mn^{2+} centers I and II in Mn^{2+}-doped $(NH_4)_2SO_4$ crystal at room temperature for the orientation of B in the *ab* plane. The continuous lines are smooth curves that connect data points.

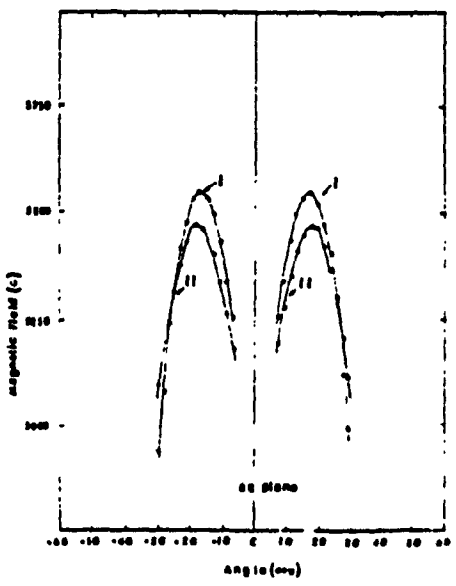

FIG. 4. Angular variation of the highest-field line of the highest-field hyperfine sextet for Mn^{2+} centers I and II in Mn^{2+}-doped $(NH_4)_2SO_4$ crystal at room temperature for the orientation of B in the *ac* plane. The continuous lines are smooth curves that connect data points.

the overall separations of the allowed lines exhibit extrema; of these three, the overall separations occur in decreasing order for B along the Z, X, and Y axes, respectively.) The results are as follows. Center I: $(\hat{Z},\hat{a})=75.6°\pm0.5°$, $(\hat{Z},\hat{b})=57.9°\pm0.5°$, and $(\hat{Z},\hat{c})=35.9°\pm0.5°$. Center II: $(\hat{Z},\hat{a})=74.5°\pm0.5°$, $(\hat{Z},\hat{b})=62.8°\pm0.5°$, and $(\hat{Z},\hat{c})=32.2°\pm0.5°$. Furthermore, using the crystallographic data,[4] it is found that the Z axis for center I is almost coincident with the direction of one of the two NH_4^+(I)-NH_4^+(II) pairs (within 5°); while that for center II deviates slightly from this direction (about 9°). The angle between the Z axes corresponding to Mn^{2+} centers I and II is about 6°.

Unlike the previous findings[8,9] of the presence of only one type of Mn^{2+} center in AS, two different types of Mn^{2+} centers have, indeed, been detected to exist simultaneously in the present studies; each of these two Mn^{2+} centers are characterized by EPR spectra which are symmetrical about c, b, and a axes, for B in the ab, ac, and bc planes, respectively (Figs. 3, 4, and 5). (The term, "Mn^{2+} center" here refers to a complex consisting of a Mn^{2+} ion with surrounding SO_4^{2-} groups and a nearest vacancy; see Sec. V for more details.)

IV. ROOM-TEMPERATURE SPIN-HAMILTONIAN PARAMETERS

In order to evaluate the spin Hamiltonian (SH) parameters, the EPR spectra were, specifically, recorded, at room temperature, for various orientations of the external magnetic field in the magnetic ZX plane, corresponding to the Mn^{2+} center I. The following spin Hamiltonian, appropriate to orthorhombic symmetry, is applicable to Mn^{2+} in AS[12]:

$$\mathcal{H}=\mu_B[g_1B_zS_z+g_1(B_xS_x+B_yS_y)]+\tfrac{1}{3}(b_2^0O_2^0+b_2^2O_2^2)+\tfrac{1}{60}(b_4^0O_4^0+b_4^2O_4^2+b_4^4O_4^4)+AS_zI_z+B(S_xI_x+S_yI_y)$$
$$+Q'[I_z^2-\tfrac{1}{3}I(I+1)]+Q''(I_x^2-I_y^2)\,. \qquad (4.1)$$

In Eq. (4.1), μ_B is the Bohr magneton, and the O_l^m are spin operators, as defined by Abragam and Bleaney.[12] A rigorous least-squares-fitting (LSF) procedure,[13] utilizing numerical diagonalization of the SH matrix on a digital computer, in which all clearly-resolved allowed Mn^{2+} line positions, observed for several orientations of B in its ZX plane, were simultaneously fitted to evaluate the nine SH parameters g_1, g_1, b_2^0, b_2^2, b_4^0, b_4^2, b_4^4, A, and B. (The parameters Q' and Q'' could not be determined since the allowed line positions do not depend upon them to first-order in approximation.) The errors of the parameters were determined by the use of a statistical method.[14] Finally, a total of 140 line positions were used to evaluate the nine SH parameters. This included, generally, all the six lines of each of the first, second, fourth, and fifth hyperfine (hf) sextets for each of the orientations of B close to, and including, the Z axis (at 0°, 2°, 4°, 6°, 8°, and 10° from the Z axis), and all the six lines of each of the first and fifth hf sextets for each of the orientations of B close to, and including, the X axis (at 0°, 2°, 4°, 6°, and 8° from the X axis). (Here, the sextets are referred to in increasing values of the Zeeman field, i.e., the first hf sextet lies at the lowest values of B, while the fifth hf sextet lies at the highest values of B.) The values of the SH parameters, so evaluated, are listed in Table I, which also include the SH parameters reported by Abdulsabirov *et al.*[4] and by Shrivastava.[9] As for the absolute signs of the parameters, they could not be determined from the present data since no relative-intensity data were available at liquid-helium temperature. The sign of b_2^0 was, then, assumed to be positive. The signs of the other fine-structure parameters, relative to that of b_2^0, as yielded by the LSF procedure, are correct. The signs of the hyperfine parameters A, B were chosen to be negative, in accordance with the hyperfine-interaction data.[15]

Although the values of the SH parameters as evaluated presently are for Mn^{2+} center I, those for center II are expected not to be much different from these because of the very close proximity of the environments of the two centers, as discussed in Sec. V below.

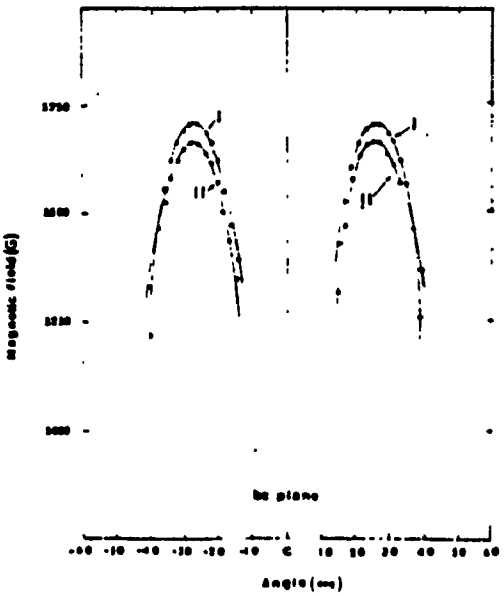

FIG. 5. Angular variation of the highest-field line of the highest-field hyperfine sextet for Mn^{2+} centers I and II in Mn^{2+}-doped $(NH_4)_2SO_4$ crystal at room temperature for the orientation of B in the bc plane. The continuous lines are smooth curves that connect data points.

V. INTERPRETATION OF Mn^{2+} CENTERS I AND II

A. Two Mn^{2+} centers

According to Abdulsabirov *et al.*,[4] when the Mn^{2+} ion replaces a NH_4^+ ion in AS, a neighbor NH_4^+ is dis-

placed to create a vacancy for charge compensation; this is referred to as a type-I charge-compensation mechanism.[11] The same charge-compensation mechanism was suggested by Chaddha,[17] for the case when Cu^{2+} replaces NH_4^+ in AS. Abdulsabirov *et al.*[4] did not specify which of the NH_4^+ ions, in the α or β position, was replaced by Mn^{2+}, reporting the observation of only one Mn^{2+} center, with four physically equivalent orientations. However, in the present work, two physically inequivalent Mn^{2+} centers were, indeed, observed (Figs. 3, 4, and 5). This can be understood as follows. There exist two inequivalent, NH_4^+(I) and NH_4^+(II), ions in AS as verified by neutron-diffraction measurement.[6] When a NH_4^+(I) ion is replaced by Mn^{2+}, a different Mn^{2+} center is created from that when the Mn^{2+} ion replaces a NH_4^+(II) ion. This is due to the smaller space available around the NH_4^+(I) ion (α position); the substitution of Mn^{2+} for NH_4^+(I) causes greater distortion of the coordinations with the surrounding ligands than that caused when Mn^{2+} substitutes for the NH_4^+(II) ion. Assuming that the larger EPR linewidth of Mn^{2+} center II is due to the more distorted coordination, it appears from the present experimental results that the Mn^{2+} ion, in center II, is in the α position, which is surrounded by five SO_4^{2-} ions with the β position left as a vacancy. The Mn^{2+} ion in center I replaces a NH_4^+(I) ion, which is in the β position surrounded by six SO_4^{2-} ions forming a distorted octahedron with the α position left as a vacancy. The α position can also be considered, equivalently, to be surrounded by six SO_4^{2-} ions, one of them lying a little farther from the NH_4^+ ion as compared with the remaining five SO_4^{2-} ions. Therefore, the environments of the α and β positions appear to be very close to each other.

Using the geometrical orientations of the SO_4^{2-} ions,[26] and the assumption that the SO_4^{2-} ions, being heavier than the NH_4^+ ions, are responsible for the occurrence of the spontaneous strain (acoustic mode) in the AS crystal, it is presently concluded that there also exist two-inequivalent SO_4^{2-} groups. This inequivalence may be caused by the *hypothetical* ferroelastic phase transition from hexagonal to orthorhombic symmetry which is expected to take place at a temperature higher than 630 K in the AS crystal.[29] [Although, actually, $(NH_4)_2SO_4$ changes into $(NH_4)HSO_4$ above 630 K, it is known that the other two isomorphous crystals, K_2SO_4 and K_2SeO_4, do, in fact, undergo such transitions at 860 and 745 K.[29]] The NH_4^+ ions also respond to this hypothetical transition, resulting in the creation of two-inequivalent α and β cations. It is, therefore, likely that the two-inequivalent SO_4^{2-} groups, which ligand to Mn^{2+} ions, are responsible for the creation of two different Mn^{2+} centers in AS.

B. Two inequivalent sublattices

It is likely that the Mn^{2+} centers I and II belong to two-inequivalent sublattices. Different EPR linewidths, and different temperature dependences of the EPR spectra for the two Mn^{2+} centers (Sec. VI), imply different distortions and different dynamic behaviors of these two sublattices. This conclusion is a logical consequence of the presence of two crystallographically inequivalent NH_4^+ ions in the unit cell, which implies that there also exist two sets of inequivalent SO_4^{2-} ions in the lattices of AS, since the two α- and β-NH_4^+ groups are surrounded by different SO_4^{2-} groups. The existence of two-inequivalent sublattices in AS has also been proposed from the temperature dependence of the reported spontaneous polarization, and the softening of a coupled-lattice vibration mode by Fujimoto *et al.*[16] As for the EPR studies on AS, the two-sublattices model was proposed only from the EPR of SeO_3^- ions in AS, namely, from the observation of two-inequivalent SeO_3^- ions, which substitute for the SO_4^{2-} ions by Fujimoto and Jerzak.[13]

VI. FERROELECTRIC PHASE TRANSITION AT 223 K

A. EPR spectra

Figure 6 exhibits the variation of the highest-field line position of the highest-field hyperfine sextet corresponding to center I, as well as that of the lowest-field line position of the highest-field hyperfine sextet corresponding to center II, for the orientation of the external magnetic field B in the *ab* plane, 25° away from the *a* axis, in the temperature range 113–398 K. (These hyperfine lines are particularly chosen, because they are *not* flanked by other lines, and are easy to identify.) It is clearly seen from Fig. 6 that, as the temperature is decreased, the line positions corresponding to center I show an abrupt jump to higher magnetic fields at $T_c = 223$ K, thereafter, each line split-

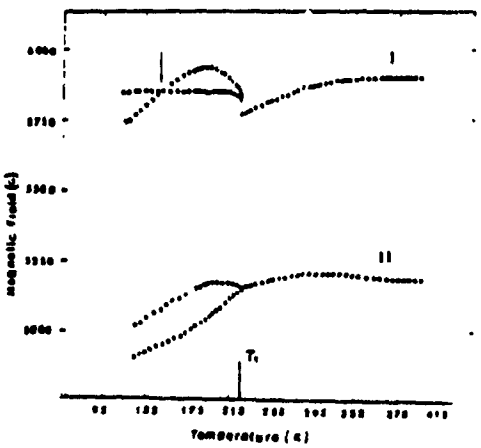

FIG. 6. Variation of the highest-field and the lowest-field hyperfine EPR line positions for the highest-field hyperfine sextets for Mn^{2+} centers I and II, respectively, as functions of temperature, from 113 K to 398 K, for B in the *ab* plane, 25° from the *a* axis. At $T_c = 223$ K, different natures of the phase transitions, i.e., a jump of the line position for center I and a continuous change of line position for center II, are clearly exhibited. As well, unusual crossing of split lines for Mn^{2+} center I at 147 K is distinctly visible.

ting into two lines below T_c, characterizing a first-order phase transition of the sublattice of AS crystal to which it belongs. On the other hand, the line positions corresponding to center II do not at all undergo any jumps at T_c, as the temperature is decreased, each of them experiences only a splitting into two lines below T_c; this indicates a second-order phase transition of the sublattice of AS, to which center II belongs. Furthermore, as seen from Fig. 6, the splittings of the lines corresponding to center I exhibit a unique feature *never* reported previously; the line splitting first increases with decreasing temperature below T_c, then it starts to diminish, finally becoming zero at about 147 K. It splits again below 147 K in the opposite direction. This feature is not exhibited by the splitting of the EPR lines, which correspond to center II.

Figure 7 exhibits detailed EPR spectra for **B** in the *ab* plane, 25° from the *a* axis, over a temperature region, including T_c, confirming the conclusions drawn from Fig. 6. Another feature that is apparent from Fig. 7 for center I, is that at 223.5 K (just above T_c), some weak lines of the ferroelectric phase that exists below T_c are also observed, although the EPR lines of the paraelectric phase that exist above T_c, are dominant. This indicates a coexistence of the paraelectric and ferroelectric phases just above T_c. Figure 8 displays a detailed temperature dependence of the EPR spectra, for **B** in the *ab* plane, 25° from the *a* axis, over a temperature region including 147 K; the EPR lines corresponding to center I show crossing of split lines, in accordance with that exhibited by Fig. 6. On the other hand, the lines corresponding to center II continue to remain split, without reversing their splitting, or crossing, at all temperatures below T_c.

Variable-temperature EPR measurements were made for the orientation of **B** in the *bc* and *ac* planes also; similar results to those observed for the orientation of **B** in the *ab* plane were found, except for the fact that no crossing of split lines was observed below T_c for any Mn^{2+} center.

B. Critical exponents

For both the centers I and II, the critical exponent β is presently found to be 0.49 ± 0.03 from the line splitting (ΔB), in the region $[0 < (T_c - T) < 10\ \text{K}]$. This is clear from Fig. 9, exhibiting log-log straight-line plots of ΔB versus $(T_c - T)$, the slopes being β. The result for center II is in agreement with that reported by Misra and

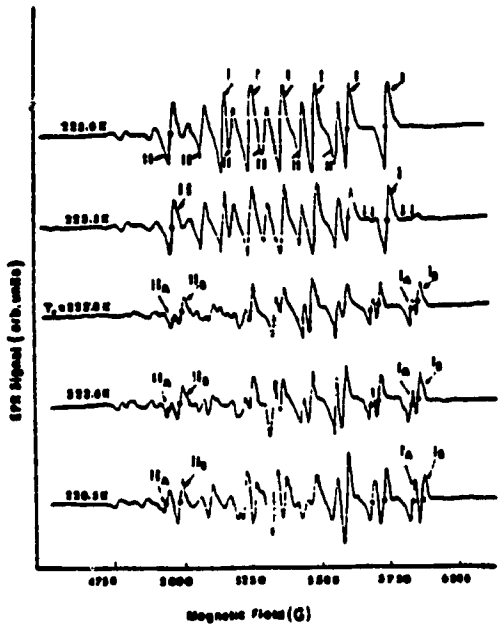

FIG. 7. EPR spectra (first derivative), for the highest-field Mn^{2+} sextet in $(NH_4)_2SO_4$ single crystal, in the temperature range, covering the ferroelectric transition temperature T_c (=223 K), for **B** in the *ab* plane, 25° from the *a* axis. As the temperature is lowered, the lines corresponding to Mn^{2+} center I show a jump at T_c, then each splits into two lines; the lines corresponding to Mn^{2+} center II, on the other hand, show only a splitting of each line into two at T_c, without undergoing jumps in line positions. (Some weak lines, indicated by arrows, belonging to the ferroelectric phase are also observed just above T_c.) I_A and I_B indicate the two subsublattices to which center I belongs below T_c; the same applies to II_A and II_B for center II.

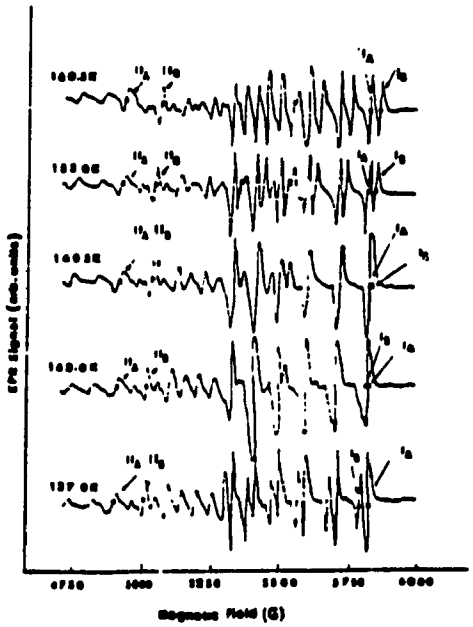

FIG. 8. EPR spectra (first derivative) for the highest-field Mn^{2+} hyperfine sextet in $(NH_4)_2SO_4$ single crystal in the temperature range covering 147 K, for **B** in the *ab* plane, 25° from the *a* axis. It is clearly seen that Mn^{2+} center I exhibits an unusual crossing of split lines at 147 K, as indicated by the relative positions of the solid circles identifying the lines corresponding to center I on the highest-field side, as functions of temperature. I_A and I_B indicate the two subsublattices to which center I belongs below T_c; the same applies to II_A and II_B for center II.

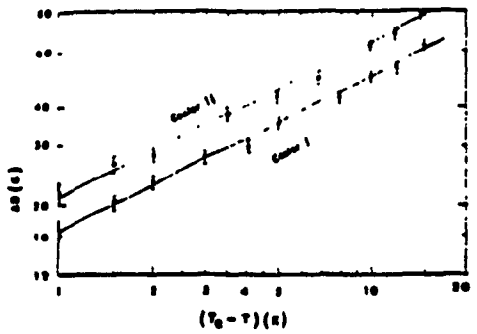

FIG. 9. Log-log plot of the temperature dependence of the line splitting, ΔB, for Mn^{2+} centers I and II, below the ferroelectric phase transition temperature, T_c. The straight lines show that $\Delta B \propto (T_c - T)^{\beta}$, with $\beta = 0.49 \pm 0.03$ and $T_c = 223$ K, for both the centers in the range $0 \text{ K} < (T_c - T) < 10$ K, consistent with Landau theory (Ref. 36).

Shrivastava,[10] where a second-order transition was considered, while that for center I is in agreement with that reported by Bhat *et al.*[18] for CrO_4^{3-}-doped AS crystal for the CrO_4^{3-} center, which undergoes a first-order phase transition.

C. Scaling law and Rushbrooke inequality

There exists a relation, $(\alpha + 2\beta + \gamma) = 2$, involving the critical exponents α and γ for $T > T_c$ and β for $T < T_c$, known as a *scaling* law.[36] It is interesting to examine the fulfillment of this law for AS. The critical exponent $\beta = 0.5$, as determined presently. The critical exponents α and γ are defined, for $T > T_c$, from the relations $C \propto (T - T_c)^{-\alpha}$ and $\chi \propto (T - T_c)^{-\gamma}$, where C and χ are specific heat and susceptibility, respectively.[38] For AS crystal, γ has been reported to be ~ 1.0.[37] As for α, it has been determined by Hoshino *et al.*[3] to be almost 0.0, for $T > T_c$. Thus, for AS, $\alpha + 2\beta + \gamma \simeq 2$. This is in agreement with the scaling law. For $T < T_c$, there exists only an inequality: $\alpha' + 2\beta + \gamma' \geq 2$,[38] known as the Rushbrooke inequality. Here the exponents α' and γ' are defined from the relations $C \propto (T_c - T)^{-\alpha'}$ and $\chi \propto (T_c - T)^{-\gamma'}$.[38] For the AS crystal, γ' and α' have been reported to be ~ 1.0,[37] and ~ 0.2,[3] respectively. Thus for AS, $\alpha' + 2\beta + \gamma' \simeq 2.2$. This is in good agreement with the Rushbrooke inequality.

D. Mechanism for phase transition

Unruh *et al.*[4] concluded from their measurement of the spontaneous polarization, P_s, of AS, that P_s could not be treated as the order parameter of the phase transition and thus called the transition *ferrielectric*, implying that the two sublattices contribute differently to the resultant spontaneous polarization. Since P_s, which is related to the optic mode of lattice vibration, is not the order parameter, some other mode must be responsible for the occurrence of the phase transition. This other mode is presently suggested to be the acoustic mode, related to the existence of ferroelasticity in the paraelectric phase of the AS crystal above T_c. The high value of the spontaneous strain may cause additional crystal distortion leading to ferroelastic domains. This creates additional weak lines in the Mn^{2+} spectra at room temperature in AS over and above those already mentioned. It is likely that the coupling to the spontaneous strain (acoustic mode) is different for the two sublattices. It is suggested presently that the sublattice to which Mn^{2+} center I belongs, which undergoes first-order transition, is strongly coupled to the acoustic mode while the sublattice to which center II belongs, which undergoes second-order transition, is only weakly coupled to the acoustic mode. This explains qualitatively why Mn^{2+} ions belonging to different sublattices behave differently at T_c. Bhat *et al.*[18] also noticed the coexistence of discontinuous (the same as that of center I) and continuous (the same as that of center II), behavior of the EPR lines in CrO_4^{3-}-doped AS crystal at T_c. However, they did not invoke the two-inequivalent-sublattices model, which would have provided the correct explanation of their spectra.

The reversal of the sign of polarization, P_s, at low temperatures, as observed by Unruh,[4] can be explained as follows. As the temperature is lowered below T_c, the sublattice, to which center I belongs, splits further into two sublattices with opposite polarizations; these polarizations exhibit different temperature dependences. The crossing of split lines for center I occurs when these two polarizations are equal and opposite, i.e., at 147 K (Fig. 8).

The two-inequivalent-sublattices model, as proposed presently, is not the same as that postulated by Sawada,[39] in which no further splittings of the sublattices below T_c was predicted, contrary to the present finding for AS, wherein each of the two sublattices above T_c splits into two sub-sublattices below T_c. Otherwise, the observed polarization behavior below T_c could not be correctly explained, as discussed above. In the model proposed presently, the SO_4^{2-} ions are also considered to be inequivalent, contrary to the assumption of Sawada *et al.*[39] The SO_4^{2-} ions play an important role in the splitting of each of two sublattices, which exist above T_c, into two sublattices below T_c. The effectiveness of SO_4^{2-} ions in the ferroelectric phase transition has also been suggested by Sawada *et al.*[39] and by Bhat *et al.*[18]

The present results and interpretation are similar to those drawn by Fujimoto and Jerzak[14] from the EPR of SeO_3^- ions in the AS crystal. According to them, two inequivalent centers of the SeO_3^- radical in AS belong to two coupled sublattices; the EPR lines above T_c of one center are very strongly temperature dependent, while those of the other are almost temperature independent.

VII. LINEWIDTH

The EPR linewidths for Mn^{2+} were estimated for the two centers in the temperature range 113–398 K. Center II is characterized by a slightly larger linewidth than that of center I. The EPR linewidth for center I is 14 ± 1 G above T_c, while it is 16 ± 1 G below T_c. On the other

hand, the linewidth for center II remains 17±1 G at all temperatures. The fact that only the linewidth corresponding to center I experiences a change at T_c supports the contention that only one sublattice in AS, namely, the one to which center I belongs, is responsible for the onset of ferroelectric phase transition; the other sublattice, the one to which center II belongs, just follows this transition.

VIII. CONCLUDING REMARKS

It has been possible here to identify the presence of the two different Mn^{2+} centers only because of the high sensitivity of the Mn^{2+} fine-structure EPR lines to even very small changes in the configuration of the SO_4^{2-} ligands to Mn^{2+} ions; the configurations of the surroundings of the α and β positions are quite close to each other.

The following are the salient features of the present study.

(i) Two different Mn^{2+} centers, belonging to two inequivalent sublattices undergoing first- and second-order phase transitions, have been simultaneously observed in AS. Previously, either center I, or center II, but not both together, was observed.

(ii) Above T_c, there exist two inequivalent sublattices in AS for each of the NH_4^+ and SO_4^{2-} ions which are coupled to each other; each of these split further into two subsublattices below T_c.

(iii) The ferroelectric phase transitions of different natures for the two sublattices are caused by couplings of different strengths of the two sublattices to the acoustic mode, effected by the spontaneous strain.

(iv) The unusual crossing of split lines, observed for Mn^{2+} center I below T_c, has not been reported previously in AS crystals, whether doped by Mn^{2+} or by any other paramagnetic ion.

(v) Only one sublattice is responsible for the temperature variation of the spontaneous polarization, P_s, since only one center exhibits a crossing of split EPR lines as the temperature changes.

(vi) The ferroelectric phase transition temperature T_c, presently determined to be 223 K, is in agreement with the well-accepted value.

(vii) The room-temperature Mn^{2+} spin-Hamiltonian parameters, as reported presently, have been evaluated by the use of a rigorous least-squares-fitting procedure.

(viii) The ferroelectric phase transition in AS is found to satisfy both the scaling law and Rushbrooke inequality.

ACKNOWLEDGMENTS

The authors are grateful to the Natural Sciences and Engineering Research Council of Canada for financial support (Grant No. A4485). The facilities of the Concordia University Computer Center were used to compute the spin-Hamiltonian parameters.

---

*On leave of absence from Center of Materials Analysis, Nanjing University, Nanjing, Jiangsu, People's Republic of China.

†Present address: Physics Department, York University, North York, Ontario, Canada M3J 1P3.

[1]V. T. Matthias and J. P. Remeika, Phys. Rev. 103, 262 (1956).

[2]H. Ohshima and E. Nakamura, J. Phys. Chem. Solids 27, 481 (1966).

[3]S. Hoshino, K. Vedam, Y. Okaya, and R. Pepinsky, Phys. Rev. 112, 405 (1958).

[4]H. G. Unruh, Solid State Commun. 8, 1951 (1970).

[5]T. Ikeda, K. Fujibayashi, T. Nagai, and K. Kobayashi, Phys. Status Solidi A 16, 279 (1973).

[6]E. O. Schlemper and W. C. Hamilton, J. Chem. Phys. 44, 4498 (1966).

[7]R. Blinc and I. Levstek, J. Phys. Chem. Solids 12, 295 (1960).

[8]R. Yu. Abdulsabirov, Yu. S. Gremev, and M. M. Zaripov, Sov. Phys.—Solid State 14, 2894 (1973).

[9]K. N. Shrivastava, Phys. Status Solidi A 1, K101 (1970).

[10]S. K. Misra and K. N. Shrivastava, Phys. Rev. B 37, 2255 (1988).

[11]G. Chaddha, J. Phys. Soc. Jpn. 24, 976 (1968).

[12]F. J. Owens, Chem. Phys. Lett. 38, 106 (1976).

[13]C. V. Manjunath and R. Srinivasan, Phys. Status Solidi A 44, 687 (1977).

[14]N. Shibata, R. Abe, and I. Suzuki, J. Phys. Soc. Jpn. 41, 2011 (1976).

[15]M. Fujimoto and S. Jerzak (unpublished).

[16]M. Fujimoto, L. A. Dressel, and T. J. Yu, J. Phys. Chem. Solids 38, 97 (1977).

[17]K. Chu, J. Magn. Reson. 21, 151 (1976).

[18]S. V. Bhat, N. C. Mishra, and R. Srinivasan, J. Phys. Chem. Solids 43, 1157 (1982).

[19]C. V. Manjunath and R. Srinivasan, Phys. Status Solidi B 87, 395 (1978).

[20]B. Rakvin and N. S. Dalal, J. Chem. Phys. 85, 6060 (1986).

[21]Y. S. Jain, H. D. Bist, and G. C. Upreti, Chem. Phys. Lett. 22, 572 (1973).

[22]Z. Iqbal and C. W. Christoe, Solid State Commun. 18, 269 (1976).

[23]D. E. O'Reilly and T. Tsang, J. Chem. Phys. 46, 1291 (1967).

[24]A. Sawada, Y. Takagi, and Y. Ishibashi, J. Phys. Soc. Jpn. 34, 748 (1973).

[25]I. Petzelt, J. Grigas, and I. Myerova, Ferroelectrics 6, 225 (1974).

[26]A. Sawada, S. Ohya, Y. Ishibashi, and Y. Takagi, J. Phys. Soc. Jpn. 38, 1408 (1975).

[27]Y. S. Jain, P. K. Bajpai, R. Bhattacharjee, and D. Chowdhury, J. Phys. C 19, 3789 (1986).

[28]Y. Makita, A. Sawada, and Y. Takagi, J. Phys. Soc. Jpn. 41, 167 (1976).

[29]A. Sawada, Y. Makita, and Y. Takagi, J. Phys. Soc. Jpn. 41, 174 (1976).

[30]G. D. Watkins, Phys. Rev. 113, 79 (1959).

[31]Y. Okaya, K. Vedam, and R. Pepinsky, Acta Crystallog. 11, 307 (1958).

[32]A. Abragam and B. Bleaney, *Electron Paramagnetic Reso-*

nance of Transition Ions (Clarendon, Oxford, 1970).
[45]S. K. Misra, J. Magn. Reson. 23, 403 (1976); Physica B 121, 193 (1983).
[46]S. K. Misra and S. Subramanian, J. Phys. C 15, 7199 (1982).
[47]A. Stoudel, *Hyperfine Interactions* (Academic, New York, 1970), p. 182.
[48]F. J. Owens, in *Magnetic Resonance of Phase Transitions*, edited by F. J. Owens, C. P. Poole, Jr., and H. Farach (Academic, New York, 1979).
[57]*Numerical Data and Functional Relationship in Science and Technology*, Vol. 16 of *Landolt-Börnstein Series*, edited by T. Mitsui and E. Nakamura (Springer-Verlag, Berlin, 1982), p. 105.
[58]R. B. Griffiths, in *Phase Transitions and Critical Phenomena*, edited by C. Domb and M. S. Green (Academic, New York, 1972).

PHYSICAL REVIEW B VOLUME 42, NUMBER 13 1 NOVEMBER 1990

Brief Reports

Brief Reports are accounts of completed research which, while meeting the usual Physical Review *standards of scientific quality, do not warrant regular articles. A Brief Report may be no longer than four printed pages and must be accompanied by an abstract. The same publication schedule as for regular articles is followed, and page proofs are sent to authors.*

EPR of a VO^{2+}-doped $Zn(NH_4)_2(SO_4)_2 \cdot 6H_2O$ single crystal: Ligand superhyperfine interaction

Sushil K. Misra and Jian-sheng Sun*
Department of Physics, Concordia University, 1455 de Maisonneuve Boulevard West, Montreal, Quebec, Canada H3G 1M8
(Received 27 December 1989; revised manuscript received 12 June 1990)

Detailed *X*-band electron-paramagnetic-resonance (EPR) studies of the VO^{2+} ion have been carried out on a single crystal of the Tutton salt $Zn(NH_4)_2(SO_4)_2 \cdot 6H_2O$ at 295, 80, and 4.2 K. The data are indicative of the presence of two physically equivalent VO^{2+} ions in the unit cell, each consisting of three magnetically inequivalent VO^{2+} ions, one of them being present with a much smaller probability. Each vanadyl hyperfine line is characterized by an anisotropic temperature-independent quintet superhyperfine (SHF) splitting, with the intensity ratios 1:4:6:4:1. The origin of the SHF splittings has been explained. The principal values and the orientations of the principal axes of the SHF-interaction tensor, as well as the density of the unpaired electron at the site of ligand protons, have been estimated. The "in-plane anisotropy" controversy has been resolved.

I. INTRODUCTION

Room-temperature (RT) EPR of VO^{2+}-doped $Zn(NH_4)_2 \cdot 6H_2O$ (ZASH, hereafter) single crystal has been previously reported by Borcherts *et al.*,[1] observing superhyperfine (SHF) structure for only one out of the three possible magnetically inequivalent VO^{2+} ions; no studies regarding the principal values and principal axes of the SHF-interaction tensor ($\tilde{A}^i$) were reported. Strach *et al.*,[2] from their zero-field EPR measurements, reported RT VO^{2+} hyperfine-interaction studies on ZASH. Thus far, no EPR study on VO^{2+}-doped ZASH single crystal has been reported below RT. Further, there exists the so-called "in-plane anisotropy" controversy, i.e., according to Borcherts *et al.*,[1] although the principal Z axes of the $\tilde{g}^i$ and $\tilde{A}^i$ tensors are coincident, their principal *X*, *Y* axes are not coincident,[1] which is contrary to the findings of Strach *et al.*[2] The present paper reports extensive *X*-band EPR study on VO^{2+}-doped ZASH single crystal at 295, 80, and 4.2 K, with particular emphasis on (i) the interpretation of the SHF splitting for the three magnetically inequivalent VO^{2+} ions in the unit cell of ZASH, (ii) resolution of the "in-plane anisotropy" controversy, and (iii) estimation of the density of the unpaired electron of VO^{2+} at the site of ligand protons.

II. SAMPLE PREPARATION AND CRYSTAL STRUCTURE

Single crystals of ZASH, doped with VO^{2+} (0.5 at. %), were grown at room temperature by slow evaporation of a saturated aqueous solution, containing stoichiometric amounts of $ZnSO_4 \cdot 7H_2O$ and $(NH_4)_2SO_4$, to which an appropriate amount of $VOSO_4 \cdot 2H_2O$ powder was added.

A ZASH crystal is characterized by monoclinic symmetry (space group $P2_1/a$).[1-3] The dimensions of the unit cell are $a = 9.28$ Å, $b = 12.57$ Å, $c = 6.25$ Å, and $\beta = 106.8°$; it contains two divalent metal ions, each of which is surrounded by six water molecules, labeled as $H_2O(7)$, $H_2O(8)$, and $H_2O(9)$ in pairs, forming closely an octahedron with distances $d_{Zn\text{-}O(7)} = 2.138$ Å, $d_{Zn\text{-}O(8)} = 2.117$ Å, and $d_{Zn\text{-}O(9)} = 2.066$ Å. A ZASH crystal has similar growth habits as that of the other Tutton salts:[4] the *b* axis is easy to identify, being perpendicular to the (010) plane, which is well developed in the form of a rectangular flat surface, containing the a^* ($= a \sin\beta$) and *c* axes.

III. EPR SPECTRA

EPR spectra were recorded at 295, 80, and 4.2 K for the orientation of the external Zeeman field ($\mathbf{B}$), in three mutually perpendicular planes, defined by the *X*, *Y*, and *Z* axes (laboratory frame). The *X* axis was chosen to be parallel to the crystallographic $\mathbf{b}$ axis, axis, while the *Y* and *Z* axes were chosen to lie in the (010) plane, of the crystal, with the *Z* axis being perpendicular to the largest flat face of the crystal.[4] For an arbitrary orientation of $\mathbf{B}$ and at any temperature, there were observed four sets of typical VO^{2+} spectra with strong intensity and two sets with much weaker intensity, characterized by eight VO^{2+} allowed hyperfine (HF) lines each. Figure 1 depicts a typical spectrum for VO^{2+} for $\mathbf{B}$ in the a^*-c plane at 30° from the *Z* axis. The six sets of HF lines can be divided

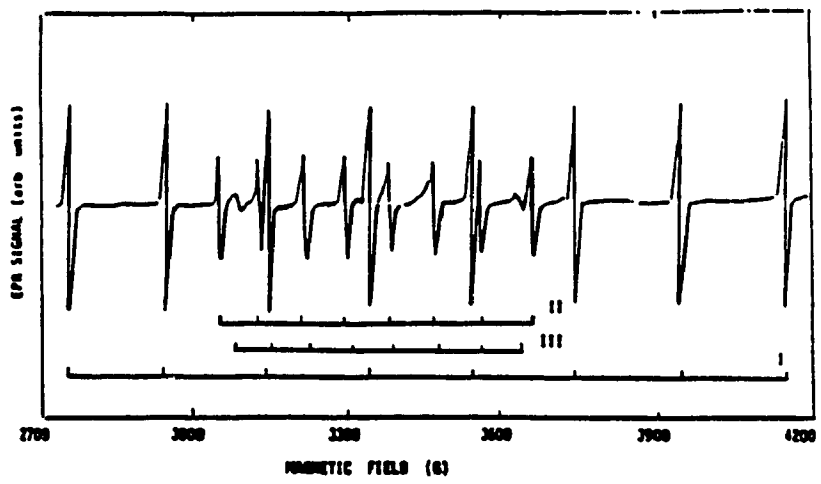

FIG. 1. First-derivative RT EPR spectrum, obtained for B in the Z-Y' (a^*-c) plane, 30° from the Z axis. Due to the inversion symmetry, only three sets of VO^{2+} HF lines were observed in this plane (the lines for the three groups of two physically equivalent VO^{2+} ions merged), although there were six sets of lines at an arbitrary orientation of B (Sec. III). The line positions for the three ions I, II, and III are clearly marked. For the ion III, three lines were seen; the other five lines were overlapped by the lines corresponding to ions I and II, having much larger intensities.

into three groups of two physically equivalent ions each (I, II with strong intensity, and III with much weaker intensity) which are obtained from each other by symmetry, conforming to the fact that the three VO^{2+} ions, which are located at each of the two Zn^{2+} sites, are physically equivalent, being situated symmetrically about the a^*-c plane. The lines corresponding to the ions III were only studied, insofar as their SHF splitting is concerned, due to their much weaker intensities. The ratios of the intensities of the VO^{2+} EPR lines corresponding to the ions I, II, and III were found to be about 10:5:1; these are different from those reported by Borcherts *et al.*,[1] which are 20:5:1.

A. SHF structures at room temperature

Figure 2 exhibits the SHF structure of VO^{2+} for ions I, II, and III for the orientation of B for which the respective maximum SHF splittings were observed. Anisotropic quintet SHF splittings, with the relative-intensity ratios 1:4:6:4:1, for ions I and II were observed for B in the Z-X and X-Y' planes; no significant SHF splitting was observed for B in the Z-Y' plane. The maximum SHF splitting for ion I was found to occur for B in the X-Y plane, at an angle of 50° with the X axis (referred to as the X_A axis); this direction is very close to the Zn^{2+}-$H_2O(7)$ direction. The SHF splitting for ion I was symmetric about the X_A axis for B in the X-Y plane. When B deviated by more than 35° from the X_A axis, the SHF splitting for ion I was no longer resolved and the five SHF lines merged to form a single HF line. For B in the Z-Y plane, the SHF splitting for ion I was the largest for $B \| \tilde{X}$; it decreases as B deviated from the $\tilde{X}$ axis, becoming unresolved for $B \| \tilde{Z}$. For ion II, the maximum SHF splitting occurred for B in the XY plane, 90° away from X_A, and very close to the Zn^{2+}-$H_2O(8)$ direction (X_B axis). The features of the SHF splitting for B in the XY plane for ion II were found to be the same as those for ion I, except that there the symmetry occurred about the X_B axis, which lies at 90° from the X_A axis. Although, for ion III, the EPR lines had the smallest intensity, their SHF splitting was still clearly observed. The direction of B for which the maximum SHF splitting for ion III occurred was found to be perpendicular to those for the ions I and II, i.e., the laboratory Z axis, which is the Zn^{2+}-$H_2O(9)$ direction.

B. Temperature dependence of SHF splitting

The crystal was orientated at RT for studying the temperature dependence of the SHF splitting in such a way that B was successively along the three directions for which the maxima of SHF splittings of lines occurred for one of the three physically equivalent VO^{2+} ions. The SHF splitting was observed to be independent of temperature in the 123–398 K range for any ion. (Below 123 K a cavity of small Q was used, which did not yield sufficient resolution of the EPR spectrum to exhibit SHF splitting. Above 398 K the crystal deteriorated.)

IV. SPIN HAMILTONIAN AND EVALUATION OF $\tilde{g}$ AND $\tilde{A}$ TENSORS

A. Spin Hamiltonian

The spin Hamiltonian describing the interactions of the VO^{2+} ion can be expressed as

$$\mathcal{H} = \mu_B \mathbf{S}\cdot\tilde{g}\cdot\mathbf{B} - \mathbf{S}\cdot\tilde{A}\cdot\mathbf{I} - \mathbf{S}\cdot\tilde{A}\cdot\mathbf{I}, \qquad (4.1)$$

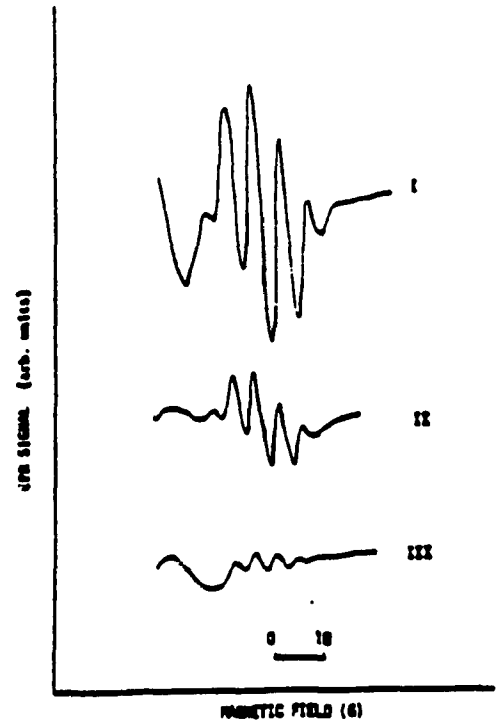

FIG. 2. X-band (klystron frequency ≈9.5 GHz) first-derivative RT EPR absorption spectra, exhibiting the SHF structure for the ions I, II, and III of VO^{2+}-doped ZASH single crystal, for the orientations of $\mathbf{B}$ for which the respective maximum SHF splittings were observed (Sec. III). The intensity ratios of the five SHF lines are 1:4:6:4:1 for any ion. It is seen that the SHF splitting for ion III is a bit smaller. The intensities of the lines for ion III are much weaker than those for ions I and II.

In Eq. (4.1), the successive terms represent the electronic Zeeman, the HF interaction, and the SHF interaction with the ligand protons, respectively.

B. Evaluation of the $\bar{g}^2$ and $\bar{A}^2$ tensors

The principal values and direction cosines of the $\bar{g}^2$ ($\equiv \bar{g}^T \cdot \bar{g}$) and $\bar{A}^2$ ($\equiv \bar{A}^T \cdot \bar{A}$) tensors at 295, 80, and 4.2 K were evaluated by the use of a least-squares fitting (LSF) procedure,[8–10] applicable to noncoincident principal axes of the $\bar{g}^2$ and $\bar{A}^2$ tensors. In this procedure all HF line positions observed for $\mathbf{B}$ in the Z-X, Z-Y, and X-Y planes are simultaneously fitted and the eigenvalues are calculated to second order in perturbation. The values so obtained for the VO^{2+} ions I and II at RT are listed in Table I. The absolute signs of the principal values of the matrix $\bar{A}$ have been assumed to be negative in accordance with those determined by Muncaster and Parke.[11] The present values of the spin-Hamiltonian parameters are temperature independent to within 1% for $\bar{g}$ principal values and to within 3% for $\bar{A}$ principal values. This temperature independence is typical of vanadyl complexes, whose EPR spectra are characterized by an axial symmetry of the ligand field with small distortion, as revealed by the slightly unequal principal values A_x- and A_y- of the hyperfine-interaction matrix $\bar{A}$ (Table I).

C. The "in-plane anisotropy" controversy

It is seen from Table I that the principal axes of the $\bar{g}^2$ and $\bar{A}^2$ tensors are almost coincident; in particular, no significant "in-plane anisotropy" exists. This is consistent with the results of Strach *et al.*,[5] and in disagreement with those of Borcherts *et al.*[1]

V. SUPERHYPERFINE INTERACTION

The maxima of the principal values of the SHF coupling tensor, $\bar{A}^L$, for the interaction of the VO^{2+} ion

TABLE I. Principal values and direction cosines of the $\bar{g}$ and $\bar{A}$ matrices of VO^{2+}-doped ZASH single crystal for ions I and II at room temperature. (The corresponding values at 80 and 4.2 K differ only within 1% and 3% for the principal values of $\bar{g}$ and $\bar{A}$ matrices, respectively.) The principal values of $\bar{g}$ are dimensionless, while those of $\bar{A}$ are expressed in GHz. The direction cosines of the $\bar{g}^2$ tensor (X',Y',Z') are given with respect to the X, Y, and Z axes (laboratory frame), defined in Sec. III, while those of the $\bar{A}^2$ tensor (X'', Y'',Z'') are expressed relative to (X', Y',Z'), the principal axes of the $\bar{g}^2$ tensor.

Ion	Principal values	Direction cosines Z/Z'	X/X'	Y/Y'
I	$g_z = 1.9384 \pm 0.0020$	0.4582	0.8011	0.3852
	$g_x = 1.9854 \pm 0.0020$	−0.8107	0.5543	0.1884
	$g_y = 1.9742 \pm 0.0020$	0.3644	0.2260	0.9034
	$A_z = -0.5648 \pm 0.0050$	−0.9974	0.0248	0.0677
	$A_x = -0.2881 \pm 0.0050$	−0.0406	0.9692	0.2429
	$A_y = -0.1724 \pm 0.0050$	0.0596	−0.2450	0.9677
II	$g_z = 1.9315 \pm 0.0020$	0.5298	0.2297	0.8164
	$g_x = 1.9821 \pm 0.0020$	−0.7609	−0.2964	0.5773
	$g_y = 1.9884 \pm 0.0020$	0.3745	−0.9271	0.0177
	$A_z = -0.5343 \pm 0.0050$	0.9948	0.1234	0.1221
	$A_x = -0.2588 \pm 0.0050$	−0.1423	0.9767	0.1608
	$A_y = -0.1676 \pm 0.0050$	0.0993	0.1758	−0.9794

with the protons of the nearest-neighbor water molecules in the ZASH lattice, for the VO^{2+} ions I, II, and III, were evaluated, from the respective maximum SHF splittings, to be 14.6, 14.6, and 12.9 MHz, using the following expression:

$$A^L = (\tfrac{1}{2})\mu_B g_L (B^- - B^-)\,, \tag{5.1}$$

where $(B^- - B^-)$ is the overall SHF splitting. For ion I of ZASH, since the SHF splittings of the lines for B along the two principal directions of the SHF tensor $\bar{A}^L$, other than that along which the maximum VO^{2+} SHF splitting occurred, were not clearly observed, it was concluded that the two other principal values of $\bar{A}^L$ for ion I were almost zero. Similar considerations are applicable to ions II and III.

It is noted here that the nearest-neighbor ligands of VO^{2+} ions I and II, for the two physically equivalent sites, responsible predominantly for the SHF splittings, are the four protons of the two $H_2O(9)$ molecules, which are the closest to the VO^{2+} sites. The resulting EPR spectra should, thus, consist of five SHF lines, due to the combined spin $I_L = 2$ of the four protons of nuclear spins $\frac{1}{2}$ each, with the intensity ratios 1:4:6:4:1;[1] this is in agreement with the present observations. Further, the SHF splitting is expected to possess axial symmetry about the bond axis,[12] i.e., the straight line drawn though the position of the magnetic electron of the VO^{2+} ion (I or II) and the center of the four protons of the two $H_2O(9)$ molecules (a Zn^{2+} site), for the two sites. Accordingly, the combined effect of the four protons results in the experimental maximum SHF splitting to occur along the Zn^{2+}-$H_2O(7)$ direction for ion I, and along the Zn^{2+}-$H_2O(8)$ direction for ion II, as deduced using the crystallographic data. There is a similar mechanism responsible for the SHF splitting of ion III, except that here the four protons responsible for this splitting belong either to the two $H_2O(7)$, or the two $H_2O(8)$, molecules. Since the distances between the VO^{2+} ion and the ligand protons of the two $H_2O(7)$, or the two $H_2O(8)$, molecules are a little longer than that of $H_2O(9)$ molecules from the VO^{2+} ion, the resulting SHF interaction is a bit weaker than that of ions I and II, as confirmed presently. (For more details, see Misra and Sun.[13])

VI. DENSITY OF THE UNPAIRED ELECTRON OF VO^{2+}

The density of the unpaired electron, f_L, at the site of ligand protons can be estimated from the values of the SHF interaction,[14] determined in Sec. V. The final expression, applicable presently, is

$$f_L = A_L^L / (1.3 A_L^0)\,. \tag{6.1}$$

where A_L^0 is the Fermi-contact interaction (reported to be 1420 MHz for Tutton salts[15]) and A^L is the largest SHF principal value. In deducing Eq. (6.1), the fact that two principal values of $\bar{A}^L$ are zero has been taken into account. Finally, f_L is estimated to be 0.34% for each of the ions I and II, and 0.30% for ion III.

VII. CONCLUDING REMARKS

The salient features of the present study are as follows.

(i) The principal values and orientations of the principal axes of the $\bar{g}$ and $\bar{A}$ matrices for VO^{2+} in ZASH have been determined at 295, 80, and 4.2 K. In particular, low temperature values have been determined for the first time; these indicate that there is *no* significant variation in the $\bar{g}$ and $\bar{A}$ matrices at low temperatures.

(ii) The SHF splitting for the three magnetically inequivalent VO^{2+} ions have been clearly observed, and interpreted. The principal values and orientations of the SHF tensors for the three VO^{2+} ions have been determined. The SHF interaction constants have been found to be temperature independent.

(iii) The densities of the unpaired electron of VO^{2+} at ligand protons have been estimated for the three magnetically inequivalent VO^{2+} ions.

(iv) The present study has resolved the "in-plane anisotropy" controversy, in that the principal axes of the $\bar{g}$ and $\bar{A}$ matrices in the X-Y plane are determined to be coincident.

ACKNOWLEDGMENTS

The authors are grateful to the Natural Sciences and Engineering Research Council (NSERC) of Canada for financial support (Grant No. OGP0004485), and to the Concordia University Computer Center for providing access to their facilities to analyze the data.

*On leave of absence from the Center of Materials Analysis, Nanjing University, Nanjing 210008, Jiangsu, the People's Republic of China.

[1] R. H. Borcherts and C. Kikuchi, J. Chem. Phys. 40, 2270 (1964).
[2] J. Strach and R. Bramley, Chem. Phys. Lett. 109, 361 (1984).
[3] R. W. G. Wyckoff, *Crystal Structures* (Interscience, New York, 1963), Vol. 3.
[4] M. Montgomery and E. C. Lingafelter, Acta Crystallogr. 20, 725 (1966).
[5] T. N. Margulis and D. H. Templeton, Z. Kristallogr. 117, 344 (1962).
[6] S. K. Misra and S. Z. Kurczak, Phys. Rev. B 34, 3080 (1986).
[7] S. K. Misra and C. Wang, Physica B (Amsterdam) 159, 321 (1989).
[8] S. K. Misra, Physica B+C (Amsterdam) 124B, 53 (1984); for application see S. K. Misra, G. Bandet, G. Bacquet, and T. E. McEnally, Phys. Status Solidi A 80, 581 (1983).
[9] S. K. Misra, Physica B (Amsterdam) 151, 433 (1988).
[10] S. K. Misra, Arab. J. Sci. Eng. 13, 255 (1988).
[11] R. Muncaster and S. Parke, J. Non-Cryst. Solids 24, 309 (1977).
[12] A. Abragam and B. Bleaney, *Electron Paramagnetic Resonance of Transition Ions* (Clarendon, Oxford, 1970).
[13] S. K. Misra and J. Sun, Physica B (Amsterdam) 162, 331 (1990).
[14] F. J. Owens, Rep. Prog. Phys. 29, 675 (1966).
[15] B. Jayaram and J. Sobhanadri, Cryst. Latt. Defects Amorph. Mater. 10, 47 (1983).

Physica B 162 (1990) 331–343
North-Holland

EPR OF VO^{2+} IN $Cd(NH_4)_2(SO_4)_2 \cdot 6H_2O$ AND $Mg(NH_4)_2(SO_4)_2 \cdot 6H_2O$ SINGLE CRYSTALS

LIGAND SUPERHYPERFINE INTERACTION AND BONDING COEFFICIENTS

Sushil K. MISRA and Jiansheng SUN[1]

Physics Department, Concordia University, 1455 de Maisonneuve Boulevard West, Montreal, Quebec H3G 1M8, Canada

Received 3 January 1990

Detailed X-band electron paramagnetic resonance (EPR) studies of the VO^{2+} ion have been carried out in the single crystals of Tutton salts $Cd(NH_4)_2(SO_4)_2 \cdot 6H_2O$ (CASH) and $Mg(NH_4)_2(SO_4)_2 \cdot 6H_2O$ (MASH) at 295, 80 and 4.2 K. For both samples the data are indicative of the presence of two magnetically inequivalent, but physically equivalent, VO^{2+} sites in the unit cell, each consisting of three magnetically inequivalent VO^{2+} ions, with one of them being present with a very small probability. Each vanadyl hyperfine line is characterized by an anisotropic quintet superhyperfine (SHF) splitting, with the intensity ratios 1:4:6:4:1. For any of the two samples investigated, the maximum separations of the SHF splitting for the two largely populated magnetically inequivalent VO^{2+} ions, corresponding to any one site, are observed when the orientations of the external magnetic field ($\boldsymbol{B}$) are along the M^{2+}–$H_2O(7)$, and the M^{2+}–$H_2O(8)$ directions (M^{2+} = divalent metal ion, Cd^{2+} or Mg^{2+}). The temperature dependence of the SHF splitting was found to be different for the two samples. The principal values and direction cosines of the principal axes of the $\tilde{g}^{2+}$ and $\tilde{A}^{2+}$ tensors are evaluated from a simultaneous fitting of the various EPR line positions, using a least-squares fitting program. The following details apply to both the samples: an impurity model of the vanadyl ion, described by the $[VO(H_2O)_4]^{2+}$ complex, is found to explain the data adequately. The orientations of the V^{4+}–O^{2-} bonds have been deduced to lie close to either the M^{2+}–$H_2O(7)$ and M^{2+}–$H_2O(8)$ directions. The SHF structure is explained to be due to the interaction of the unpaired electron of the VO^{2+} ion with the four protons of its two nearest-neighbor $H_2O(9)$ molecules. The principal values and orientations of the principal axes of the SHF interaction tensor have been estimated. Using the reported optical absorption- and the present EPR data, the bonding coefficients of the $[VO(H_2O)_4]^{2+}$ complex have been estimated

1. Introduction

The vanadyl ion (VO^{2+}) is the most stable cation, among the few molecular paramagnetic transition-metal ions, which can exist in a variety of ligand-field environments. The VO^{2+} EPR spectrum is very sensitive to the crystalline-field environment [1, 2]. Superhyperfine (SHF) structure of the EPR spectra, due to the interaction of the unpaired electron of the vanadyl ion with its ligands has been observed in single crystals of $(NH_4)_2Mg_2(SO_4)_3$ [3], $(NH_4)_2Zn_2(SO_4)_3$ [4], $Cd(COO)_2 \cdot 3H_2O$ [5] and $Zn(NH_4)_2(SO_4)_2 \cdot 6H_2O$ [6]. The SHF structure can be used to determine the locations of the VO^{2+} ions in the unit cell; this is because the maximum superhyperfine (SHF) separation occurs when the direction of the external magnetic field is parallel to the bond axis between the paramagnetic ion and the closest ligand ion [7]. The local symmetry of the VO^{2+} ion has been, generally, found to be rather high [6, 8].

Room temperature (RT) EPR of a VO^{2+}-doped $Cd(NH_4)_2(SO_4)_2 \cdot 6H_2O$ (CASH, hereafter) single crystal have been previously reported by Jain et al. [9]; two magnetically inequivalent VO^{2+} ions were observed at RT. The spin-Hamiltonian parameters and their direction cosines suggested a correlation between the V^{4+}–O^{2-} bonds and the Cd–H_2O directions. Satyanarayana et al. [10] reported more detailed VO^{2+} EPR data on CASH; the SHF structure for both the ions were observed and was explained using the model of $[VO(H_2O)_4]^{2+}$ complex. Salagram et al. [11] reported the EPR data

[1] On leave of absence from the Center of Materials Analysis, Nanjing University, Nanjing, Jiangsu, PR China.

0921-4526/90/$03.50

on a powder CASH sample, and calculated the molecular-orbital coefficients. As for the EPR study of VO^{2+}-doped $Mg(NH_4)_2(SO_4)_2 \cdot 6H_2O$ crystal (MASH, hereafter), Narayana et al. [12] found all VO^{2+} ions in the unit cell to be magnetically equivalent at RT, and estimated the principal values of the $\tilde{g}$ and $\tilde{A}$ matrices. Jayaram et al. [13] observed two magnetically inequivalent VO^{2+} ions in MASH at RT and evaluated the principal values and direction cosines of the principal axes of the $\tilde{g}$ and $\tilde{A}$ matrices for both the single crystal and powder samples. They also observed the SHF structure. Agarwal et al. [14] made EPR measurements on a powder MASH sample at RT and estimated the molecular-orbital coefficients.

Thus far, no EPR studies on VO^{2+}-doped MASH and CASH single crystals have been reported below RT. The interpretations of previously reported RT-EPR data have not been very consistent. As an attempt to study systematically VO^{2+}-doped Tutton salts, the present paper reports extensive X-band EPR studies on VO^{2+}-doped CASH and MASH single crystals at 295, 80 and 4.2 K. The particular motivations of the present studies are: (i) to determine the orientations of the V^{4+}–O^{2-} bond axes in CASH and MASH from the orientations of the principal axis of the $\tilde{g}^2$ tensor, (ii) to evaluate the spin-Hamiltonian parameters of the VO^{2+} ion in CASH and MASH using a least-squares fitting procedure, (iii) to investigate the interaction of the paramagnetic ion, VO^{2+}, with the protons of the ligand water molecules from the SHF splittings of the VO^{2+} hyperfine (HF) lines, (iv) to estimate the bonding coefficients of the $[VO(H_2O)_4]^{2+}$ complex using the present EPR and previously reported optical absorption data, (v) to compare the VO^{2+} EPR data of CASH and MASH crystals, and (vi) to study the temperature dependence of the SHF interaction.

2. Sample preparation and crystal structure

Single crystals of CASH and MASH, doped with VO^{2+}, were grown at room temperature by slow evaporation from saturated aqueous solutions, containing stoichiometric amounts of $3CdSO_4 \cdot 8H_2O$ or $MgSO_4 \cdot 7H_2O$ and $(NH_4)_2SO_4$, to which a small quantity of $VOSO_4 \cdot 2H_2O$ powder was added, so that there was one VO^{2+} ion for 100 Cd^{2+} (or Mg^{2+}) ions in the solutions. Crystals, suitable for EPR measurements, grew in about two weeks; those of size $3.0 \times 2.5 \times 1.0\ mm^3$ were chosen for the present measurements. CASH crystals were stored in oil to avoid dehydration.

CASH and MASH crystals, being Tutton salts, are characterized by monoclinic symmetry, with the space group $P2_1/a$ [15–17]. The unit-cell dimensions are: for MASH, $a = 9.32$ Å, $b = 12.60$ Å, $c = 6.21$ Å and $\beta = 107.14°$, and for CASH, $a = 9.43$ Å, $b = 12.82$ Å, $c = 6.29$ Å and $\beta = 106.87°$. The unit-cell of a Tutton salt contains two divalent metal ions, each of which is surrounded by six water molecules, forming almost an octahedron. The octahedron at the site $(0, \frac{1}{2}, \frac{1}{2})$ is derived from that at $(0, 0, 0)$ by a translation to $(0, \frac{1}{2}, \frac{1}{2})$ followed by a reflection in the a^*c plane ($a^* = a \sin\beta$). The six water mole-

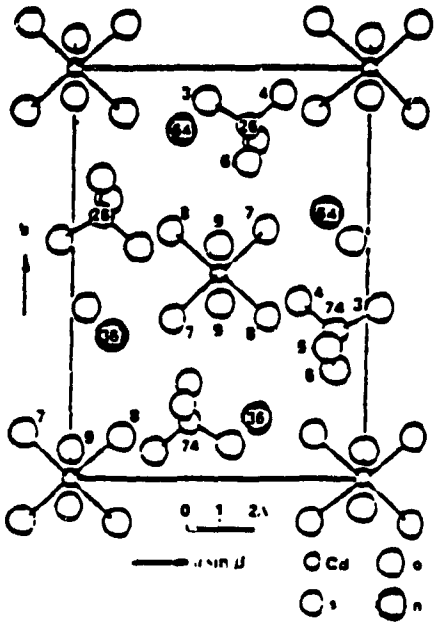

Fig. 1. The structure of CASH and MASH crystals as projected onto the a^*b plane [10].

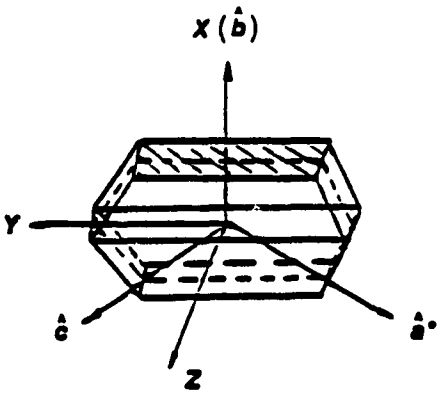

Fig. 2. Crystal-growth habits of CASH and MASH single crystals used for the present EPR measurements. The orientations of the laboratory axes *X*, *Y* and *Z* with respect to the crystal faces have been indicated. The (0 1 0) plane has been shaded.

cules surrounding a divalent metal ion are labelled, as seen in fig. 1, as $H_2O(7)$, $H_2O(8)$ and $H_2O(9)$ in pairs, each H_2O of a pair has the same distance from the metal ion. M^{2+}–$H_2O(7)$ (M = Cd or Mg) distance is the longest, while M^{2+}–$H_2O(9)$ distance is the shortest [16, 17]. Some relevant distances are Cd–O(7) = 2.298 Å, Cd–O(8) = 2.297 Å and Cd–O(9) = 2.241 Å; Mg–O(7) = 2.08 Å, Mg–O(8) = 2.07 Å and Mg–O(9) = 2.05 Å.

The crystals of CASH and MASH have similar growth habits. Figure 2 shows the crystal-growth habit of CASH. Since the (0 1 0) plane of the CASH crystals is well developed, the b axis is easy to identify (b is perpendicular to the (0 1 0) plane, which contains the a^* and c axes) [18]. For MASH crystals, the (0 1 0) plane is not well developed; however, b is parallel to the large flat surface [18].

3. Experimental arrangement and details of the spectra

The experimental arrangement is described elsewhere [5]. In order to observe the temperature dependence of the SHF structure, a cavity of higher Q was employed, in which the temperature at the sample was varied by blowing either cold nitrogen gas, or by using a heater coil, to vary the temperature from 123 to 398 K.

EPR spectra were recorded, for both the samples, at 295, 80 and 4.2 K for the orientation of the Zeeman field, B, in three mutually perpendicular planes, defined by the X, Y and Z axes. For CASH, the X axis was chosen to be parallel to the crystallographic b axis; the Y and Z axes were chosen to lie in the (0 1 0) plane of the crystal, as exhibited in fig. 2. For MASH, a similar coordinate system was chosen. EPR spectra were recorded by varying the orientation of the external magnetic field in each plane (ZX, ZY, XY) at 5° intervals. For both the CASH and MASH crystals, there were observed four sets of eight VO^{2+} allowed hyperfine lines ($\Delta M = \pm 1$, $\Delta m = 0$; M and m are the electronic and nuclear magnetic quantum numbers, respectively, for VO^{2+} electronic spin $S = \frac{1}{2}$ and nuclear spin $I = \frac{7}{2}$) at all temperatures, and at general orientations of the external magnetic field. These four sets of HF lines can be divided into two groups which are related to each other by symmetry. In the ZY [a^*c or (0 1 0)] plane, they merge to form two sets of eight HF lines. For $B \| X(b)$ axis, there were observed only two sets of eight HF lines, consistent with the fact that there are two formula units in the unit-cell and the two M^{2+} sites are symmetrically situated with respect to the b axis. This implies that there are two magnetically inequivalent VO^{2+} ions present at each of the two sites responsible for the four sets of spectra for an arbitrary orientation of B. The VO^{2+} ions, which are located at the two M^{2+} sites, are physically equivalent but magnetically inequivalent, being situated symmetrically about the a^*c plane. In addition, some very weak lines were also observed, which could be from a third possible magnetically inequivalent VO^{2+} ion, which also occupies a M^{2+} site. These lines will not be studied presently due to their much weaker intensity. Hereafter, the VO^{2+} ions I and II refer to those magnetically inequivalent VO^{2+} ions, which are located at the same M^{2+} site in the unit cell with large populations [10, 13]. Specifically, the V^{4+}–O^{2-} orientations of VO^{2+} ions I and II are along the M^{2+}–$H_2O(7)$ and M^{2+}–$H_2O(8)$ directions, respective-

ly (see section 4 for more details). For both the samples, the ratio of intensities of the VO^{2+} EPR lines corresponding to the ions I and II was found to be about 2:1, which is somewhat different from that reported previously, especially for CASH [10]. When the VO^{2+} ion replaces a M^{2+} ion, the V^{4+}–O^{2-} bonds orient themselves along the M^{2+}–$H_2O(7)$, M^{2+}–$H_2O(8)$, or M^{2+}–$H_2O(9)$ direction. These orientations are occupied with different populations, one of them being very small, while the other two being in the ratio 2:1. This is in agreement with the EPR results for VO^{2+}-doped $Zn(NH_4)_2(SO_4)_2 \cdot 6H_2O$ [6].

3.1. Room-temperature EPR spectra

The angular variation of the EPR spectra for VO^{2+}-doped CASH, which is similar to that for VO^{2+}-doped MASH, for B in the ZY [a^*c or (0 1 0)] plane at RT is displayed in fig. 3. Spectra from two magnetically inequivalent VO^{2+} ions corresponding to each site are clearly seen. The symmetry of the hyperfine line positions about the Z axis for B in the ZY plane is consistent with the crystallographic symmetry. It is seen from fig. 3 that the separations of the adjacent hyperfine lines for ion I are almost equal to each other for $B \| Y$, which is close to the direction of the maximum hyperfine splitting for ion I. They become more unequal, the farther the orientation of B deviates from the Y axis. VO^{2+} EPR spectra for ion II, for B in the ZY plane, exhibited the same features as those for ion I for B in the ZY plane except that the maximum HF splitting for ion II occurred for the orientation of B at 90° from that at which the maximum splitting of the HF lines occurs for VO^{2+} ion I. Also, the greater the separation of the adjacent hyperfine lines, the higher the external magnetic field value at which they occur for both the ions. Angular variation of the EPR spectra recorded for the orientation of B in the ZX and XY planes also confirmed the existence of two magnetically inequivalent VO^{2+} ions for each site.

The following features are common to both the CASH and MASH hosts. Anisotropic quintet SHF splitting for both the ions (I and II) was observed for B in the ZX and XY planes; no significant SHF splitting was observed for B in the ZY plane. The maximum SHF splitting, for ion I, was found to occur for B in the XY plane.

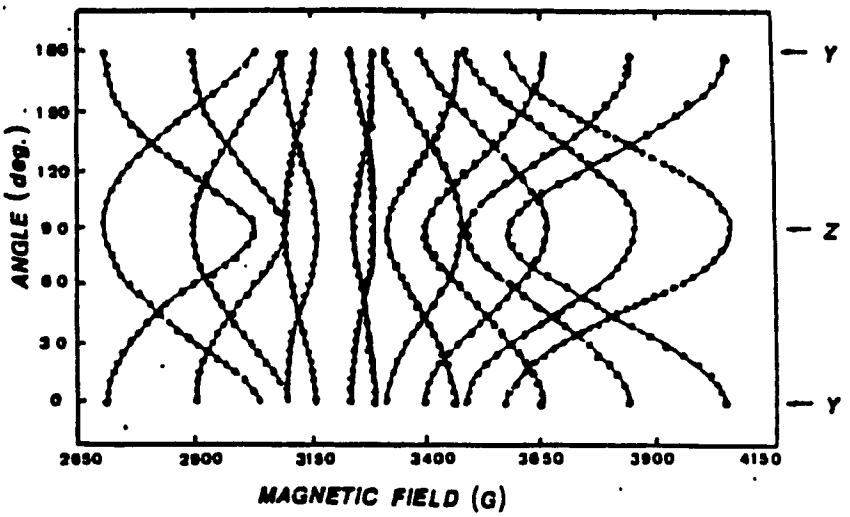

Fig. 3. Angular variation of the EPR line positions observed at room temperature for B in the ZY plane for VO^{2+}-doped CASH crystal. The empty and solid circles represent the experimental line positions corresponding to VO^{2+} ions I and II, respectively; the continuous lines are smooth curves that connect the data points belonging to the same transition. The SHF splitting has been suppressed, only the center of each SHF quintet is shown.

at an angle of 45° with the X axis (referred to as the X_A axis); this direction is very close to the M^{2+}–$H_2O(7)$ direction. The SHF splitting for ion I is symmetric about the X_A axis for B in the XY plane. The EPR spectra for this orientation of B are shown in fig. 4 for both the CASH and MASH hosts, exhibiting clearly that each HF line for ion I splits into five with intensity ratios of about 1:4:6:4:1. The farther B from the X_A axis in the XY plane, the smaller the observed SHF splitting for ion I. Finally, when B deviates from the X_A axis by more than 35°, the SHF splitting for ion I is no longer resolved, the five SHF lines merge to form a single HF line. Further, the HF lines for ion I become narrower as B deviates farther from the X_A axis in the XY plane, while their peak-to-peak heights increase. The minimum width of the HF lines for ion I was attained when B was perpendicular to the X_A axis in the XY plane. In the ZX plane the SHF splitting is the largest for $B \| X$, it decreases as B moves away from the X axis, being unresolved for $B \| Z$. For ion II, the maximum SHF splittings occurred for B in the XY plane, 90° away from, and very close to, the M^{2+}–$H_2O(8)$ direction (the X_B axis). The features of the SHF splitting for B in the XY plane for ion II were found to be the same as those for ion I, except that here the symmetry is about the X_B axis, which lies at 90° from the X_A axis.

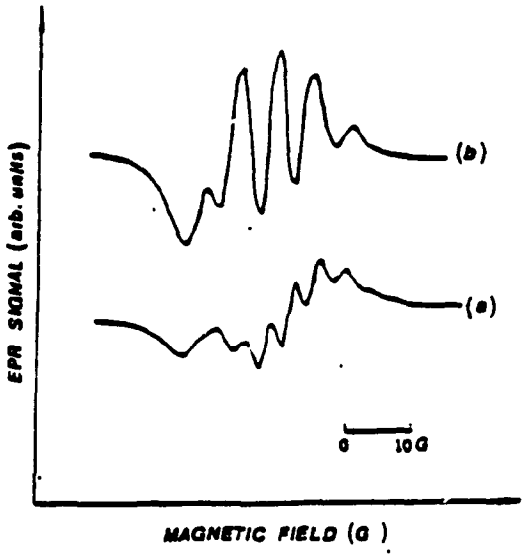

Fig. 4. First derivative EPR spectra, exhibiting the SHF structure for VO^{2+}-doped CASH and MASH single crystals, indicated by (a) and (b) respectively, at room temperature for the orientation of B for which maximum SHF splitting was observed. The intensity ratios of the five SHF lines are clearly seen to be about 1:4:6:4:1. Each of the magnetically inequivalent VO^{2+} ions I and II, exhibit this type of spectrum; however, the orientations of B for which the maximum SHF splitting are observed, are perpendicular to each other for the two ions.

3.2. EPR spectra at lower temperatures

At lower temperatures (below 123 K), it was not possible to observe well-resolved SHF splitting because of the use of a cavity with a lower Q. The other features of the spectra remained the same as those at room temperature. At liquid helium temperature, it was necessary to reduce the microwave power considerably in order that the EPR lines do not broaden due to saturation, and remain resolved, because of the long spin–lattice relaxation time of the VO^{2+} ion [5].

3.3. Temperature dependence of SHF splitting

The crystals of VO^{2+}-doped CASH and MASH were oriented so that B was along the direction for which the maximum SHF splitting for one of the two VO^{2+} ions occurs, using the cavity with the higher Q, and varying the temperature in the range 123–398 K. It is seen from fig. 4 that at room temperature the VO^{2+} SHF splitting is larger in MASH than in CASH. The SHF splitting for MASH was almost temperature independent. As for CASH, as the temperature was decreased, the resolution of the SHF splitting became worse (fig. 5). Below 186 K, the five SHF lines merged to form a single HF line. This is due either to an increase in the linewidth of the individual SHF lines, or, to a decrease in the SHF interaction. Above 350 K, the CASH crystal was destroyed due to dehydration.

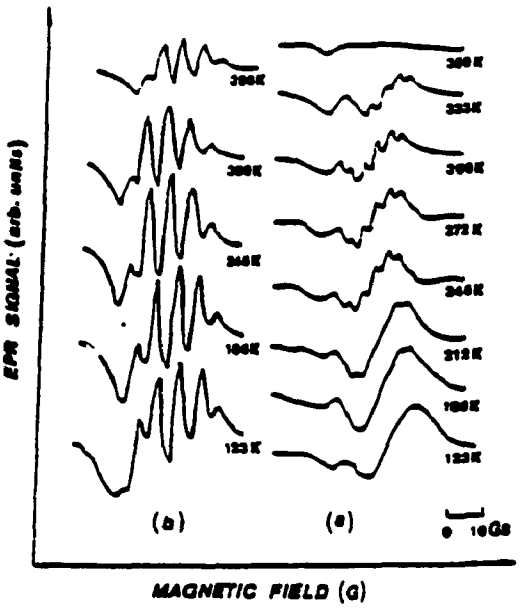

Fig. 5. EPR spectra exhibiting the temperature dependence of the maximum SHF splitting for CASH and MASH, as indicated by (a) and (b), respectively.

4. Spin Hamiltonian and evaluation of $\tilde{g}^2$ and $\tilde{A}^2$ tensors

4.1. Spin Hamiltonian

For VO^{2+} ion the effective electronic spin $S = \frac{1}{2}$ and its nuclear spin $I = \frac{7}{2}$. The spin Hamiltonian characterizing the VO^{2+} ion can be expressed as [5]

$$\mathcal{H} = \mu_B S \cdot \tilde{g} \cdot B + S \cdot \tilde{A} \cdot I + S \cdot \tilde{A}^L \cdot I_L . \qquad (4.1)$$

In eq. (4.1) the successive terms represent electronic Zeeman, HF and SHF interactions with the ligand protons, respectively, while μ_B, $\tilde{A}$, $\tilde{A}^L$ and I_L are the Bohr magneton, the hyperfine-interaction matrix, the SHF matrix and the resultant spin (= 2) of the four ligand protons, respectively.

4.2. Evaluation of the $\tilde{g}^2$ and $\tilde{A}^2$ tensors

The principal values of the $\tilde{g}^2$ ($= \tilde{g}^T \cdot \tilde{g}$; T denotes transpose of a matrix) and $\tilde{A}^2$ ($= \tilde{A}^T \cdot \tilde{A}$) tensors were evaluated by the use of a least-squares fitting (LSF) procedure [19, 20], applicable to the cases with non-coincident $\tilde{g}^2$ and $\tilde{A}^2$ tensors. In summary, a total of 384 allowed HF line positions (averaged over SHF splitting), observed for the VO^{2+} complex for any magnetically inequivalent VO^{2+} ion, were fitted simultaneously to evaluate the principal values of the $\tilde{g}$ and $\tilde{A}$ matrices and their direction cosines (eigenvectors). The values so obtained, for the two VO^{2+} ions, are listed in tables 1 and 2 for CASH and MASH, respectively. The absolute signs of the principal values of $\tilde{A}$ have been assumed to be negative in accordance with those determined by Muncaster and Parke [21]. At lower temperatures, the SHF splitting was not observed; thus no averaging of line positions was necessary in order to estimate $\tilde{g}$ and $\tilde{A}$. It is seen from tables 1 and 2 that the principal axes of the $\tilde{g}^2$ and $\tilde{A}^2$ tensors are almost coincident, for both the samples. These values of the parameters, listed in tables 1 and 2, are typical of vanadyl complexes characterized by the axial symmetry of the ligand field. The previously reported parameters for CASH by Satyanarayana et al. [10] and for MASH by Jayaram et al. [13], determined at room temperature only, are also included in tables 1 and 2 for comparison.

5. Superhyperfine interaction and the density of unpaired electrons

The maximum principal values of the SHF coupling tensor, $\tilde{A}_L$, for the interaction of VO^{2+} ion with the protons of the nearest-neighbor water molecule in CASH and MASH lattices, for both the VO^{2+} ions, were evaluated, from the respective maximum SHF splittings, to be 12.3 and 14.6 MHz, respectively, using the expression derived by Misra and Wang [5], modified to take into account quintet splitting:

$$A_\parallel^L = \tfrac{1}{4}\mu_B g\,(B_\parallel - B_\parallel^*) . \qquad (5.1)$$

where $(B_\parallel - B_\parallel^*)$ is the overall SHF splitting. For

Table 1
Principal values and direction cosines (eigenvectors) of the $\bar{g}$ and $\bar{A}$ matrices of VO^{2+}-doped CASH single crystal. The principal values of $\bar{g}$ are dimensionless, while those of $\bar{A}$ are expressed in GHz. The indicated errors are those estimated by the use of a statistical method [33]. The direction cosines of the $\bar{g}^2$ tensor (X', Y', Z') are given with respect to the X, Y and Z axes (laboratory frame), defined in section 3, and depicted in fig. 1, while those of the $\bar{A}^2$ tensor (X'', Y'', Z'') are expressed relative to (X', Y', Z'), the principal axes of the $\bar{g}^2$ tensor. The numbers in brackets are those reported by Satyanarayana et al. [10].

T	Ion	Principal values	Direction cosines		
			Z/Z'	X/X'	Y/Y'
295 K	I	$g_{z'} = 1.9363 \pm 0.0020$ (1.947)	0.7399	−0.6500	−0.1734
		$g_{x'} = 1.9810 \pm 0.0020$ (1.999)	−0.6550	0.7548	0.0348
		$g_{y'} = 1.9847 \pm 0.0020$ (1.992)	0.1535	0.0879	0.9842
		$A_{z'} = -0.5343 \pm 0.0050$ (0.5178)	0.9973	0.0421	0.0595
		$A_{x'} = -0.2159 \pm 0.0050$ (0.2068)	−0.0538	0.9761	0.2106
		$A_{y'} = -0.1997 \pm 0.0050$ (0.2007)	0.0493	0.2132	−0.9758
	II	$g_{z'} = 1.9242 \pm 0.0020$ (1.945)	0.2660	0.6560	−0.6941
		$g_{x'} = 1.9800 \pm 0.0020$ (1.998)	−0.3179	0.7674	0.4829
		$g_{y'} = 1.9846 \pm 0.0020$ (1.993)	0.9101	−0.0924	0.4034
		$A_{z'} = -0.5358 \pm 0.0050$ (0.5172)	0.9962	0.0448	−0.0742
		$A_{x'} = -0.2189 \pm 0.0050$ (0.2069)	−0.0356	0.9920	0.1214
		$A_{y'} = -0.2028 \pm 0.0050$ (0.2008)	0.0790	−0.1183	0.9898
80 K	I	$g_{z'} = 1.9481 \pm 0.0020$	0.7405	−0.6200	−0.2771
		$g_{x'} = 1.9961 \pm 0.0020$	−0.6669	0.7574	0.0530
		$g_{y'} = 1.9944 \pm 0.0020$	0.0668	0.2741	0.9594
		$A_{z'} = -0.5328 \pm 0.0050$	0.9988	−0.0046	0.0484
		$A_{x'} = -0.2224 \pm 0.0050$	−0.0162	0.9698	0.2432
		$A_{y'} = -0.2021 \pm 0.0050$	0.0458	0.2437	−0.9688
	II	$g_{z'} = 1.9488 \pm 0.0020$	0.3373	0.6427	−0.6879
		$g_{x'} = 1.9948 \pm 0.0020$	−0.3441	0.7868	0.4124
		$g_{y'} = 1.9940 \pm 0.0020$	0.9303	−0.3394	0.1390
		$A_{z'} = -0.5607 \pm 0.0050$	0.9863	0.1632	−0.0233
		$A_{x'} = -0.2191 \pm 0.0050$	−0.0763	0.9774	0.1129
		$A_{y'} = -0.1983 \pm 0.0050$	0.1461	−0.1000	0.9820
4.2 K	I	$g_{z'} = 1.9384 \pm 0.0020$	0.6851	−0.6838	−0.2511
		$g_{x'} = 1.9993 \pm 0.0020$	−0.7282	0.6344	0.2592
		$g_{y'} = 1.9894 \pm 0.0020$	0.0179	0.3604	0.9326
		$A_{z'} = -0.5514 \pm 0.0050$	0.9975	0.0431	0.0556
		$A_{x'} = -0.2337 \pm 0.0050$	−0.0480	0.9948	0.0903
		$A_{y'} = -0.1935 \pm 0.0050$	0.0514	0.0927	−0.9948
	II	$g_{z'} = 1.9418 \pm 0.0020$	0.3869	0.6238	−0.6821
		$g_{x'} = 1.9902 \pm 0.0020$	−0.2186	0.7756	0.4180
		$g_{y'} = 1.9918 \pm 0.0020$	0.9377	−0.2181	0.1875
		$A_{z'} = -0.5585 \pm 0.0050$	0.9829	0.1836	−0.0109
		$A_{x'} = -0.2397 \pm 0.0050$	−0.0109	0.9763	0.2235
		$A_{y'} = -0.1949 \pm 0.0050$	0.1812	−0.2286	0.9380

ion I of CASH or MASH, the maximum VO^{2+} SHF splitting occurred for B at 45° from the X axis in the XY plane. Since the lines corresponding to the SHF splittings for B along two orthogonal directions to this, i.e., at 135° from the X axis in the XY plane and along the Z axis, were not resolved, being too small, it was concluded that two principal values of $\bar{A}^2$ for the two ions of CASH and MASH were almost zero. Thus, the two principal directions of the SHF tensor,

Table 2
Principal values and direction cosines of the $\tilde{g}$ and $\tilde{A}$ matrices of VO^{2+}-doped MASH single crystal. The numbers in brackets are those reported by Jayaram et al. [13]. For other details see the caption of table 1.

T	Ion	Principal values	Direction cosines		
			$Z\,Z'$	X/X'	$Y\,Y''$
295 K	I	g_z = 1.9424 ± 0.0020 (1.9420)	0.8666	0.4906	−0.0909
		g_x = 1.9826 ± 0.0020 (2.0062)	−0.4940	0.8182	0.2940
		g_y = 1.9859 ± 0.0020 (1.9875)	0.0698	0.2997	0.9515
		A_z = −0.5226 ± 0.0050 (0.562)	0.9954	−0.0209	0.0935
		A_x = −0.2216 ± 0.0050 (0.220)	−0.0593	0.9724	0.1724
		A_y = −0.2072 ± 0.0050 (0.225)	0.0753	0.1744	−0.9783
	II	g_z = 1.9384 ± 0.0020 (1.9372)	0.1647	0.5420	−0.8241
		g_x = 1.9827 ± 0.0020 (2.0025)	0.2389	0.7888	0.5665
		g_y = 1.9862 ± 0.0020 (1.9972)	0.9570	−0.2902	0.0004
		A_z = −0.5319 ± 0.0050 (0.554)	0.9989	0.0420	−0.0224
		A_x = −0.2229 ± 0.0050 (0.221)	−0.0421	0.9991	0.0051
		A_y = −0.1942 ± 0.0050 (0.248)	−0.0223	−0.0061	0.9997
80 K	I	g_z = 1.9510 ± 0.0020	0.9190	0.3496	−0.1823
		g_x = 1.9958 ± 0.0020	−0.3513	0.9360	0.0242
		g_y = 1.9943 ± 0.0020	0.1791	0.0418	0.9830
		A_z = −0.5220 ± 0.0050	0.9942	−0.1197	0.0344
		A_x = −0.2588 ± 0.0050	−0.0056	0.9835	0.1466
		A_y = −0.1812 ± 0.0050	0.0760	0.1424	−0.9875
	II	g_z = 1.9507 ± 0.0020	0.0888	0.2905	−0.9527
		g_x = 1.9940 ± 0.0020	0.3384	0.8908	0.3032
		g_y = 1.9938 ± 0.0020	0.9368	−0.3493	0.0192
		A_z = −0.5360 ± 0.0050	0.9994	0.0325	−0.0144
		A_x = −0.2345 ± 0.0050	−0.0141	0.9333	0.2798
		A_y = −0.1830 ± 0.0050	−0.0327	−0.2792	0.9833
4.2 K	I	g_z = 1.9393 ± 0.0020	0.9492	0.2890	−0.1246
		g_x = 1.9921 ± 0.0020	−0.2603	0.9435	0.2053
		g_y = 1.9866 ± 0.0020	0.1769	0.1624	0.9707
		A_z = −0.5234 ± 0.0050	0.9999	−0.0008	0.0124
		A_x = −0.2612 ± 0.0050	−0.0026	0.9897	0.1431
		A_y = −0.1863 ± 0.0050	0.0121	0.1431	−0.9896
	II	g_z = 1.9470 ± 0.0020	0.1563	0.5063	−0.8481
		g_x = 1.9920 ± 0.0020	0.4227	0.7417	0.5208
		g_y = 1.9875 ± 0.0020	0.8927	−0.4399	0.0980
		A_z = −0.5534 ± 0.0050	0.9988	0.0008	−0.0479
		A_x = −0.2346 ± 0.0050	−0.0082	0.9325	0.3612
		A_y = −0.1965 ± 0.0050	−0.0482	−0.3612	0.9313

$\tilde{A}^L$, for ion I of CASH (or MASH) are very close to 45° and 135° from the X axis in the XY plane, while the third principal direction is along the Z axis; the corresponding principal values of $\tilde{A}^L$ are 12.3, 0 and 0 MHz, respectively. For ion II, the principal direction of the SHF tensor corresponding to the largest principal value is perpendicular to that for ion I in the XY plane, with the same principal values as those for ion I. The other two principal values are zero, the corresponding principal axes being very close to 90° from the principal direction corresponding to the maximum principal value in the XY plane and very close to the Z axis. The maximum principal value of the SHF interaction, i.e., 12.3 MHz for CASH, as found presently, is 25% lower than

that reported previously by Satyanarayana et al. [10] (16.8 MHz). For MASH, the present value (14.6 MHz) is almost the same as that reported by Jayaram et al. [13] (14.0 MHz). However, the minimum principal value of the SHF interaction for MASH, $A_{\perp}$, is found to be almost zero, which is different from that reported by Jayaram et al. [13] (8.3 MHz). The present maximum values of the SHF interaction for CASH and MASH are comparable to 13.8 MHz, as reported by Misra and Wang for VO^{2+}-doped $Cd(COO)_2 \cdot 3H_2O$ crystal [5].

The interaction between the magnetic electron of VO^{2+} ion, which is localized on the central magnetic ion, and the ligand nuclei, i.e., the protons of the neighboring H_2O, is dipolar [7]. There is a non-zero probability that this unpaired electron is localized on the ligand ions. (See section 7 below for more details). The combined effect of the dipolar and Fermi-contact interactions is responsible for the SHF splitting in the present case. It should be noted that the nearest-neighbor ligands to a VO^{2+} ion for both the sites are four protons of the two $H_2O(9)$ molecules, which determine predominantly the SHF splitting, as will be discussed below in section 6. The resulting EPR spectra should, then, consist of five SHF lines, due to the combined spin $I_L = 2$ of the four protons of nuclear spin $\frac{1}{2}$ each, with the intensity ratios of 1:4:6:4:1 [6]; this is in accordance with the present data. Further, the SHF splitting should possess axial symmetry about the bond axis [7], i.e., the line through the center of magnetic electron of the VO^{2+} ion (a M^{2+} site, M = Cd or Mg) and the center of four protons of two $H_2O(9)$ molecules, for the two sites. The combined effect of the four protons results in the experimental maximum SHF splitting to occur along the M^{2+}–$H_2O(7)$ direction for ion I, and along the M^{2+}–$H_2O(8)$ direction for ion II, as verified from the crystallographic data. For ion I this axis lies in the XY plane, at about 45° from the X axis (i.e., the X_{η} axis). This has been supported by the present EPR data, confirming that the VO^{2+} ion, indeed, substitutes for a M^{2+} ion in CASH or MASH. Satyanarayana et al. [10] also concluded that the orientations of the maximum SHF splitting were along M^{2+}–$H_2O(7)$ and M^{2+}–$H_2O(8)$ directions for CASH, but they did not specify which four protons were responsible for the observed SHF interaction. Although, Jayaram et al. [13] did point out that the four protons of $H_2O(9)$ were the origin of the SHF interaction, they did not report the orientations of the maximum SHF splitting. All the features of the SHF interaction have been well explained in the present study, for both the samples and for both the ions.

The density of the unpaired electron, f_s, at the site of ligand protons has been estimated from the SHF interaction, using the procedure described in the appendix, to be 0.28% for CASH and 0.34% for MASH. For comparison, Jayaram et al. [13] reported that $f_s = 0.8\%$ for MASH.

6. Positions of the vanadyl ions in CASH and MASH lattices

From the crystal structure of CASH and MASH, it appears that the site of a M^{2+} ion is the most probable site for substitution by the VO^{2+} ion. The orientation of the principal Z axis of the $\tilde{g}^2$ tensor, for any VO^{2+} complex, is expected to be along the V^{4+}–O^{2-} bond [6, 22]. From the present EPR data, the orientation of the principal Z axis of the $\tilde{g}^2$ tensor has been determined to be almost parallel to the M^{2+}–$H_2O(7)$ direction for ion I, and to the M^{2+}–$H_2O(8)$ direction for ion II, as seen from fig. 6, taking into account the direction cosines of the principal Z axes for the two ions [10, 13]. When the VO^{2+} ion enters the CASH-, or MASH-lattice it substitutes for a M^{2+} ion, expelling one of the two $H_2O(7)$ or $H_2O(8)$ molecules, and arranges itself in such a way that the geometrical axis of the VO^{2+} ion, i.e., the line joining the V^{4+} and O^{2-} ions, orients itself along the direction previously formed by M^{2+}–$H_2O(7)$ for ion I and by M^{2+}–$H_2O(8)$ for ion II. The orientations of $\boldsymbol{B}$, for which the maximum SHF splitting occurs, i.e., X_{η} and $X_{\parallel}$, also support this contention, as discussed in section 5 above. Using the model of $[VO(H_2O)_4]^{2+}$ complex, described below, all the features of the EPR spectra for VO^{2+}-doped CASH and MASH crystals can be

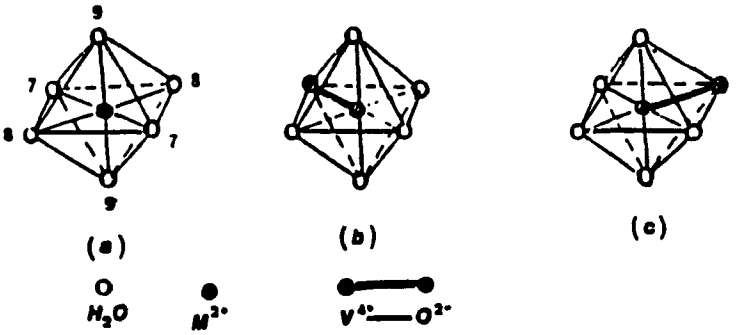

Fig. 6. Orientations of the VO^{2+} ions, and the $[VO(H_2O)_5]^{2+}$ complexes, in the CASH and MASH lattices. (a) octahedral coordination of water molecules around M^{2+} ion (M = Cd or Mg). (b) V^{4+}–O^{2-} bond orientation for ion I, and (c) V^{4+}–O^{2-} bond orientation for ion II. (It is noted that the maximum SHF splitting occurs when B is along the V^{4+}–O^{2-} bond.)

well interpreted. The two observed groups of symmetry related EPR lines are due to two symmetrically oriented $[VO(H_2O)_5]^{2+}$ complexes.

The distance between M^{2+} and $H_2O(9)$ is the smallest of the three M^{2+} and H_2O distances. There is a finite, although small, probability for the VO^{2+} ion to orient itself along the M^{2+}–$H_2O(9)$ direction, as exhibited by the set of very weak HF lines observed for MASH. Jayaram et al. [13] suggested, for MASH, that the axis of the VO^{2+} ion II was along the Mg–$H_2O(9)$ direction, which is, obviously, incorrect.

7. VO^{2+} energy levels and bonding coefficients

The VO^{2+} ion enters the lattice to substitute for an M^{2+} ion (M = Cd or Mg) and to form a $(VO(H_2O)_4)^{2+}$ complex with its nearest-neighbors (fig. 6), which possesses a tetragonally-distorted octahedral symmetry. The description of the molecular vanadyl ion, VO^{2+}, based on LCAO-MO [23] calculations of the $(VO(H_2O)_4)^{2+}$ complex, indicates that the ground state of the vanadyl ion is $3d^1$ ($^2D_{3/2}$). In an octahedral crystalline field, the d^1 electron occupies the lowest-lying orbital $^2T_{2g}$, the next-excited state being $^2E_{2g}$. The tetragonal component of the crystalline field splits the $^2T_{2g}$ and $^2E_{2g}$ levels into ($^2B_{2g}$, $^2E_{2g}$) and ($^2B_{1g}$, $^2A_{1g}$) levels respectively.

The predicted transitions are [24]:

$$\Delta_{\perp} = {}^2B_{2g} \rightarrow {}^2E_{2g}\,. \tag{7.1}$$

$$\Delta_{\parallel} = {}^2B_{2g} \rightarrow {}^2B_{1g}\,. \tag{7.2}$$

$$\Delta = {}^2B_{2g} \rightarrow {}^2A_{1g}\,. \tag{7.3}$$

in order of increasing energy. These transitions have been observed experimentally in the optical absorption spectra of the vanadyl ion in CASH and MASH lattices, recorded at room and liquid nitrogen temperatures [24].

Since the EPR and the optical absorption data suggest a nearly tetragonal vanadyl complex, which implies that $g_{xx} \cong g_{yy}$ and $A_{xx} \cong A_{yy}$, the bonding parameters for this complex can be estimated by using the following relations [23, 25–27]

$$g_{\parallel} - g_e = \frac{4g_e\lambda\beta_1^2\beta_2^2}{\Delta_{\parallel}}\,, \tag{7.4}$$

$$g_{\perp} - g_e = \frac{g_e\lambda\gamma^2\beta_2^2}{\Delta_{\perp}}\,. \tag{7.5}$$

$$A_{\parallel} = -PK - (\tfrac{4}{7}\beta_2^2)P - \left\{\frac{4g_e\lambda\beta_1^2\beta_2^2}{\Delta_{\parallel}}\right\}P - \frac{3}{7}\left\{\frac{g_e\lambda\gamma^2\beta_2^2}{\Delta_{\perp}}\right\}P\,. \tag{7.6}$$

and

$$A_{\parallel} = -PK + (\tfrac{4}{7}\beta_{\parallel}^2)P - \frac{11}{14}\left[\frac{g_{\parallel}\lambda\gamma_{\parallel}^2\beta_{\parallel}^2}{\Delta_{\parallel}}\right]P. \tag{7.7}$$

In eqs. (7.4)–(7.7), P is the direct dipolar term (dipole–dipole interaction of the electron and nuclear spins). K is the Fermi-contact term, proportional to the amount of the unpaired electron density at the vanadium nucleus, and λ is the spin–orbit coupling constant for the vanadium ion. The energy differences, as obtained from the optical data of VO^{2+} are for CASH: $\Delta_{\perp} = 14\,035$, $\Delta_{\parallel} = 16\,000$ and $\Delta = 23\,529\,cm^{-1}$ [10], and for MASH: $\Delta_{\perp} = 13\,000$, $\Delta_{\parallel} = 16\,100$ and $\Delta = 30\,000\,cm^{-1}$ [14]. Using $g_e = 2.0023$, $\lambda = 170\,cm^{-1}$ [22] and assuming $\beta_{\parallel}^2 = 1.00$ for the present case, since the orbital of the ground state is strictly non-(in-plane)-bonding, as predicted by Ballhausen and Gray [23] and accepted by others [28–30]. The estimated values of the bonding parameters, using eqs. (7.4)–(7.7), are listed in table 3. The values of $(1-\beta_{\perp}^2)$ and $(1-\gamma^2)$ are measures of covalency [29]. The former gives an indication of the influence of the σ-bonding between the atom and the equatorial ligands, i.e., the bonding between the VO^{2+} ion and $H_2O(9)$ molecules in the present case, while the latter indicates the π-bonding with the vanadyl oxygen.

Table 3 shows that the values of $(1-\beta_{\perp}^2)$ and $(1-\gamma^2)$ for CASH and MASH are comparable to each other, being different from those for the alums $KAl(SO_4)_2\cdot 12H_2O$ and $NH_4Al(SO_4)_2\cdot 12H_2O$ [32], for which the covalency due to σ-bonding is much greater than that due to π-bonding. However, the present values are comparable to those reported by Misra and Wang [5] for VO^{2+}-doped $Cd(COO)_2\cdot 3H_2O$. MASH has higher values of bonding parameters than those for CASH, due to the shorter distances between the M^{2+} ion and the neighbor H_2O molecules in CASH as compared to that in MASH. This explains why the VO^{2+} ion in MASH exhibits larger SHF splitting than that in CASH.

8. Concluding remarks

The following are the main findings of the present EPR study of VO^{2+}-doped CASH and MASH crystals.

(i) The principal values of the $\bar{g}$ and $\bar{A}$ matrices, and those of the SHF interaction ($\bar{A}^L$) matrix, as well as their direction cosines, have been evaluated from the positions of the allowed HF lines.

(ii) It is concluded that the VO^{2+} ion substitutes for a M^{2+} ion (M = Cd or Mg) upon entering the CASH- or MASH-lattice. The V^{4+}–O^{2-} orientations of two VO^{2+} ions I and II are deduced to be along the M^{2+}–$H_2O(7)$ and M^{2+}–$H_2O(8)$ directions, respectively; these are magnetically inequivalent.

(iii) The SHF splitting originates as a result of the interaction between the VO^{2+} ion and the

Table 3
Bonding parameters for VO^{2+}-doped CASH and MASH crystals, as calculated assuming $\beta_{\parallel}^2 = 1.00$. The units for P and K are GHz, while the other parameters are dimensionless. The numbers in brackets are those reported by Salagram et al. [11] and by Agarwal et al. [14] for CASH and MASH, respectively, who considered only one VO^{2+} ion.

Sample	Ion	$\beta_{\perp}^2$	γ^2	P	K	β_s^2
CASH	I	0.78	0.80	0.36	0.85	1.00
				(0.37)	(0.81)	(0.94)
	II	0.74	0.82	0.35	0.85	1.00
MASH	I	0.69	0.74	0.35	0.85	1.00
		(0.77)	(0.55)	(0.38)	(0.85)	
	II	0.71	0.71	0.35	0.85	1.00

four protons of its nearest-neighbor pair of water molecules, $H_2O(9)$, for both the samples and for both ions.

(iv) The bonding parameters of the complex $[VO(H_2O)_4]^{2+}$ have been estimated from the reported optical absorption and the present EPR data on CASH and MASH crystals. The density of the unpaired electron at the site of ligand protons has also been estimated.

(v) VO^{2+}-doped CASH and MASH crystals show different SHF splittings and temperature dependences, as well as different bonding coefficients. However, the principal values of their $\tilde{g}$ and $\tilde{A}$ matrices are comparable.

Acknowledgements

The authors are grateful to the Natural Sciences and Engineering Research Council of Canada for financial support (Grant no. A4485) and to the Concordia University Computer Center for providing their facilities to analyze the data.

Appendix

The procedure to estimate the value of f_s, the probability density of the unpaired electron of VO^{2+} at the ligand site, is described in this appendix. The SHF interaction with axial symmetry,

$$\mathcal{H}_{SHF} = S \cdot \tilde{A}^L \cdot I^L = A_\parallel^L S_z I_z^L + A_\perp^L (S_x I_x^L + S_y I_y^L) \quad (A.1)$$

can be rewritten as

$$\mathcal{H}_{SHF} = [A_s S^L \cdot I^L] + [2A_p S_z I_z^L - A_p (S_x I_x^L + S_y I_y^L)] . \quad (A.2)$$

with

$$A_\parallel^L = A_s + 2A_p . \quad (A.3)$$

and

$$A_\perp^L = A_s - A_p . \quad (A.4)$$

In eq. (A.2), the first term represents the isotropic interaction between the ligand ions and the unpaired electron, whose wave function contains an admixture of s and p states, while the second term represents the sum of the anisotropic interaction and the dipole–dipole interactions [31] of ligand ions with the unpaired electron being in the p state.

The density f_s of the unpaired electron at the ligand ions is related to A_s as follows [31]:

$$A_s = A_s^0 f_s , \quad (A.5)$$

where

$$A_s^0 = \frac{8\pi}{3} g_e \beta_e g_N \beta_N |\Psi(0)|_s^2 . \quad (A.6)$$

A_s^0 is the Fermi contact energy, which has been reported to be 1420 MHz for both CASH and MASH for protons [13].

From eqs. (A.3)–(A.5), one obtains

$$f_s = (A_\parallel^L + 2A_\perp^L)/(3A_s^0) , \quad (A.7)$$

which can be estimated using the values of $A_\parallel^L$ and $A_\perp^L$, as determined from the present EPR data.

References

[1] R.P. Kohin, Mag. Reson. Rev. 5 (1979) 75.
[2] P. Chand, V.K. Jain and G.C. Upreti, Mag. Reson. Rev. 14 (1988) 39.
[3] B.V.R. Chowdari, J. Phys. Soc. Jpn. 29 (1970) 105.
[4] B.V.R. Chowdari, J. Phys. Soc. Jpn. 27 (1969) 1135.
[5] S.K. Misra and C. Wang, Physica B 159 (1989) 105.
[6] R.H. Borcherts and C. Kikuchi, J. Chem. Phys. 40 (1964) 2270.
[7] A. Abragam and B. Bleaney, Electron Paramagnetic Resonance of Transition Ions (Clarendon, Oxford, 1970).
[8] S. Radhakrishna, M. Salagram, Solid State Commun. 47 (1983) 77.
[9] V.K. Jain and D. Saran, Ind. J. Phys. A 55 (1981) 285.
[10] N. Satyanarayana and S. Radhadrishna, J. Chem. Phys. 83 (1985) 529.
[11] M. Salagram, N. Satyanarayana and S. Radhakrishna, Polyhedron 5 (1986) 1171.

[12] M. Narayana, N. Satyanarayana and G.S. Sastry, Molec. Phys. 31 (1976) 203.
[13] B. Jayaram and J. Sobhanadri, Cryst. Latt. Def. Amorph. Mat. 10 (1983) 47.
[14] O.P. Agarwal and P. Chand, Z. Naturforsch. (a) 40 (1965) 1164.
[15] R.W.G. Wyckoff, Crystal Structures, Vol. 3 (Interscience, New York, 1963).
[16] M. Montgomery and E.C. Lingafelter, Acta Cryst. 20 (1966) 728.
[17] T.N. Margulis and D.H. Templeton, Z. Kristallogr. 117 (1962) 344.
[18] S.K. Misra and S.Z. Korczak, Phys. Rev. B 34 (1986) 3086.
[19] S.K. Misra, Physica B 124 (1983) 53.
For application, see: S.K. Misra, G. Bandet, G. Bacquet and T.E. McEnally, Phys. Stat. Sol. (a) 80 (1983) 581.
[20] S.K. Misra, Physica B 151 (1988) 433.
S.K. Misra, Arab. J. Sci. & Eng. 13 (1988) 255.
[21] R. Muncaster and S. Parke, J. Non-cryst. Solids 24 (1977) 399.
[22] V.K. Jain, Phys. Stat. Sol. (b) 97 (1980) 337.
[23] C.J. Ballhausen and H.B. Gray, Inorg. Chem. 1 (1962) 111.
[24] N. Satyanarayana and S. Radhakrishna, Cryst. Latt. Def Amorph. Mat. 97 (1984) 337.
[25] D. Kivelson and S. Lee, J. Chem. Phys. 41 (1964) 1896.
[26] K. DeArmond, B.B. Garrett and H.S. Gutowsky, J. Chem. Phys. 42 (1965) 1019.
[27] L.J. Boucher, E.C. Tynan and T.F. Yen, Electron Spin Resonance of Metal Complexes, T.F. Yen, ed. (Plenum, New York, 1969).
[28] A.K. Viswanath, J. Chem. Phys. 67 (1977) 3744.
[29] V.P. Seth, V.K. Jain, A. Yadav and R.S. Bansal, Phys. Stat. Sol. (b) 132 (1985) K139.
[30] V.K. Jain, J. Phys. Soc. Jpn. 46 (1979) 1250.
[31] F.J. Owens, Rep. Prog. Phys. 29 (1966) 675.
[32] K.V.S. Rao, M.D. Sastry and P. Venkateswarlu, J. Chem. Phys. 49 (1969) 4984.
[33] S.K. Misra and S. Subramanian, J. Phys. C 15 (1982) 7159.

phys. stat. sol. (b) 162, 585 (1990)

Subject classification: 76.30; S11

Department of Physics, Concordia University, Montreal[1])

EPR of a VO^{2+}-Doped $Fe(NH_4)_2(SO_4)_2 \cdot 6H_2O$ Single Crystal

VO^{2+}–Fe^{2+} Exchange Interaction and Spin–Lattice Relaxation Time of Host Fe^{2+} Ions

By

SUSHIL K. MISRA, JIANSHENG SUN[2]), and U. ORHUN

X-band (≈9.5 GHz) electron paramagnetic resonance (EPR) studies of the VO^{2+} ion are carried out on a single crystal of the Tutton salt $Fe(NH_4)_2(SO_4)_2 \cdot 6H_2O$ (FASH) at 295, 80, and 4.2 K. The data indicate two physically-equivalent VO^{2+} sites in the unit cell, each consisting of three magnetically-inequivalent VO^{2+} ions. The principal values and direction cosines of the principal axes of the $\mathbf{g}^2$ and $\mathbf{A}^2$ tensors are evaluated, using a least-squares-fitting program. An impurity $[VO(H_2O)_5]^{2+}$ complex model of the vanadyl ion is found to explain the data well. The V^{4+}–O^{2-} bond directions for the VO^{2+} ions are deduced. The VO^{2+}–Fe^{2+} exchange-interaction constant in FASH is estimated. The host-ion (Fe^{2+}) spin–lattice relaxation time is estimated from VO^{2+} EPR linewidth.

On a mesuré le RPE à bande-X sur un monocristal du sel Tutton, $Fe(NH_4)_2(SO_4)_2 \cdot 6H_2O$ (FASH), à 295, à 80, et à 4,2 K. Les données indiquent deux sites physiquement équivalents de VO^{2+} dans l'unité de cellule, chacun contient trois ions de VO^{2+}, non-équivalents magnétiquement. Les valeurs principaux et les cosinus des directions des axes principaux des tenseurs $\mathbf{g}^2$ et $\mathbf{A}^2$ ont été évalués, en utilisant un programme d'adaptation aux moindres carrés à l'ordinateur. Un modèle d'impureté, décrit par le complexe $[VO(H_2O_5]^{2+}$, explique bien les données. On a déduit les liens V^{4+}–O^{2-} pour les ions de VO^{2+}. Le constant d'intéraction d'échange VO^{2+}–Fe^{2+} a été estimé. Le temps de relaxation spin–réseau des ions hôtes (Fe^{2+}) a été estimé, en utilisant les largeurs RPE de l'ion d'impureté VO^{2+}.

1. Introduction

When a paramagnetic impurity ion is introduced in a paramagnetic host lattice, it experiences a g-shift from that in an isostructural diamagnetic host [1] at low temperatures due to the exchange interaction between the impurity and host paramagnetic ions, in addition to that due to the shape of the paramagnetic host crystal [2]. Using this technique, Misra et al. [3 to 6] estimated Mn^{2+}-Ni^{2+}, Mn^{2+}-Fe^{2+}, Co^{2+}-Ni^{2+}, and Gd^{3+}-Yb^{3+} exchange-interaction constants from their EPR measurements. No report has, so far, been published on the estimate of exchange interaction between the molecular paramagnetic impurity ion, VO^{2+}, and host paramagnetic ions. Neither has any study been published on the estimate of host spin–lattice relaxation time (τ) of the paramagnetic host ion Fe^{2+}, using EPR linewidths of impurity ions, in particular, that of the VO^{2+} ion [7]. Further, in the previously-made estimates of τ of host ions using the VO^{2+} ion as impurity an incorrect expression was used [7, 8], which is only applicable to the case, where there is present only one kind of paramagnetic spin in the system, thus neglecting the important dipolar and exchange

[1]) 1455 de Maisonneuve Boulevard West, Montreal, Quebec H3G 1M8, Canada.

[2]) Permanent address: Center of Materials Analysis, Nanjing University, Nanjing, Jiangsu, 210008, People's Republic of China.

interactions between the impurity and host ions. Misra and Orhun [8] derived the correct expression for τ, valid for a typical EPR situation, where there are present two different kinds of magnetic spins in the system, e.g., VO^{2+} and Fe^{2+} in the VO^{2+}-doped $Fe(NH_4)_2(SO_4)_2 \cdot 6H_2O$ (FASH, hereafter) lattice.

EPR of VO^{2+}-doped FASH single crystals has been previously reported by Upreti and Saraswat [9]; however, these studies were confined to room temperature (RT). Two magnetically-inequality VO^{2+} ions were observed. The spin-Hamiltonian parameters and their direction cosines, calculated using a first-order perturbation approximation, suggested a correlation between the $V^{4+}-O^{2-}$ bonds and the $Fe^{2+}-H_2O$ directions. The spin-Hamiltonian was assumed to have axial, rather than orthorhombic, symmetry, and the principal axes of g^2 and A^2 were assumed to be coincident; no estimate of $VO^{2+}-Fe^{2+}$ exchange interaction, or that of τ of the host Fe^{2+} ions, was made.

In an attempt to study systematically VO^{2+}-doped Tutton salts [10, 11], the present paper reports an extensive X-band EPR study on VO^{2+}-doped FASH single crystal at 295, 80, and 4.2 K. The particular motivations of the present studies are: (i) to evaluate accurately the spin-Hamiltonian parameters of the VO^{2+} ion in FASH, at room, liquid-nitrogen, and liquid-helium temperatures without the assumptions of axial symmetry and coincidence of the principal axes of g^2 and A^2 tensors, using eigenvalues calculated to second order in perturbation; (ii) to determine the orientations of the $V^{4+}-O^{2-}$ bond axes in FASH from a knowledge of the orientations of the principal axes of the g^2 tensor; (iii) to estimate the $VO^{2+}-Fe^{2+}$ exchange-interaction constant in FASH, using the g-shift of VO^{2+} in the paramagnetic FASH host lattice from that in the isostructural diamagnetic $Zn(NH_4)_2(SO_4)_2 \cdot \cdot 6H_2O$ (ZASH), $Mg(NH_4)_2(SO_4)_2 \cdot 6H_2O$ (MASH), and $Cd(NH_4)_2(SO_4)_2 \cdot 6H_2O$ (CASH) lattices [10, 11]; and (iv) to estimate the spin–lattice relaxation time of the host Fe^{2+} ions in FASH from VO^{2+} EPR linewidths, using the correct expression [8].

2. Sample Preparation and Crystal Structure

Single crystals of VO^{2+}-doped FASH were grown at room temperature by slow evaporation of a saturated aqueous solution, containing stoichiometric amounts of $FeSO_4$ and $(NH_4)_2SO_4$, to which a small quantity of $VOSO_4 \cdot 2H_2O$ powder was added, so that there was one VO^{2+} ion per 100 Fe^{2+} ions in the solution. Crystals, suitable for EPR measurements, grew in about two weeks; a crystal of size $3.0 \times 3.0 \times 1.0\ mm^3$ was chosen for the present measurements.

FASH crystal, being a Tutton salt, is characterized by monoclinic symmetry (space group $P2_1/a$) [12, 13]. The unit-cell dimensions are: $a = 0.932$ nm, $b = 1.265$ nm, $c = 0.624$ nm, and $\beta = 106.8°$. The unit cell of a Tutton salt contains two divalent metal ions, each of which is surrounded by six water molecules, forming closely an octahedron. The octahedron of water molecules about the site (1/2, 1/2, 0) is derived from that at (0, 0, 0) by a translation to (1/2, 1/2, 0) followed by a reflection in the a^*c plane ($a^* = a \sin \beta$). The six water molecules surrounding a divalent metal ion are labelled as $H_2O(7)$, $H_2O(8)$, and $H_2O(9)$ in pairs; each H_2O of a pair has the same distance from the metal ion; the distances of the oxygens belonging to the various water molecules from the metal ion are: Fe–O(7) = 0.216 nm, Fe–O(8) = 0.214 nm, and Fe–O(9) = 0.209 nm [13].

The growth habit of a FASH crystal, as depicted in Fig. 1, is similar to that of the other Tutton salts [4, 10, 11]. Since the (0 1 0) plane of the FASH crystal is well developed as a rectangular flat surface, the b-axis, which is perpendicular to the (0 1 0) plane containing the a^*- and c-axes [4, 10, 11], is easy to identify.

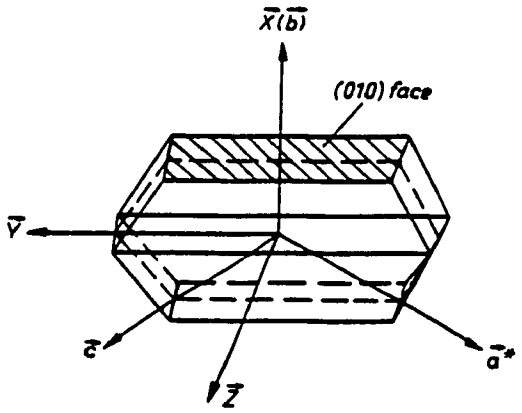

Fig. 1. Crystal-growth habit of the FASH single crystal used for the present EPR measurements. The orientations of the laboratory axes X, Y, and Z with respect to the crystal faces have been indicated

3. EPR Spectra

The experimental arrangement is described elsewhere [14, 15]. EPR spectra were recorded at 295, 80, and 4.2 K for the orientation of the Zeeman field, B, in three mutually perpendicular planes, ZX, ZY, and XY, at every 5° interval. The X-axis was chosen to be parallel to the crystallographic b-axis, while the Y- and Z-axes were chosen to lie in the (0 1 0) plane of the crystal with the Z-axis being perpendicular to the largest flat crystal surface, which defines the XY plane [4, 10, 11]; this is indicated in Fig. 1. At a general orientation of B, there were observed four intense distinct sets of eight VO^{2+} allowed hyperfine (HF) lines ($\Delta M = \pm 1$, $\Delta m = 0$; where M and m are, respectively, the electronic and nuclear magnetic quantum numbers; for VO^{2+} electronic spin $S = 1/2$ and nuclear spin $I = 7/2$) each, at any temperature. These four sets of HF lines can be divided into two groups which can be obtained from each other by symmetry operations, i.e., these two groups are physically equivalent to each other. For B in the ZY plane, as well as for $B \parallel X$, only two distinct sets of eight HF lines each were observed, consistent with the physical symmetry. Thus, there were present four magnetically-inequivalent, i.e., distingushable by B, VO^{2+} molecular ions in the unit cell of FASH with intense EPR spectra for an arbitrary orientation of B. These correspond to two pairs of physically-equivalent VO^{2+} molecular ions in the unit cell, referred to as I and II. In addition, some weak lines were also observed, which were presumably due to a third possible pair of physically-equivalent VO^{2+} molecular ions, referred to as III, with different orientation of its axis, also occupying a Fe^{2+} site. In conclusion, each of the two Fe^{2+} sites in the unit cell of FASH is occupied by VO^{2+} ions with three different orientations of their molecular axes. The group of the three VO^{2+} ions occupying a Fe^{2+} site is physically equivalent to that occupying the other Fe^{2+} site in the unit cell of FASH (for more details see Section 5). The lines corresponding to the third ion were not studied in detail, due to their much weaker intensities. A typical EPR spectrum, for B in the ZY plane, showing the presence of the various kinds of VO^{2+} ions is exhibited in Fig. 2. The angular variation of EPR spectra for B in the ZY plane at room temperature is displayed in Fig. 3. The ratios of the intensities of the VO^{2+} EPR lines corresponding to the VO^{2+} complexes I, II, and III were found to be about 10:6:1. According to the model of the $[VO(H_2O)_5]^{2+}$ complex (Section 5), when a VO^{2+} ion replaces a Fe^{2+} ion in FASH the V^{4+}–O^{2-} bonds orient themselves along the Fe^{2+}–$H_2O(7)$, Fe^{2+}–$H_2O(8)$, or Fe^{2+}–$H_2O(9)$ directions. In the

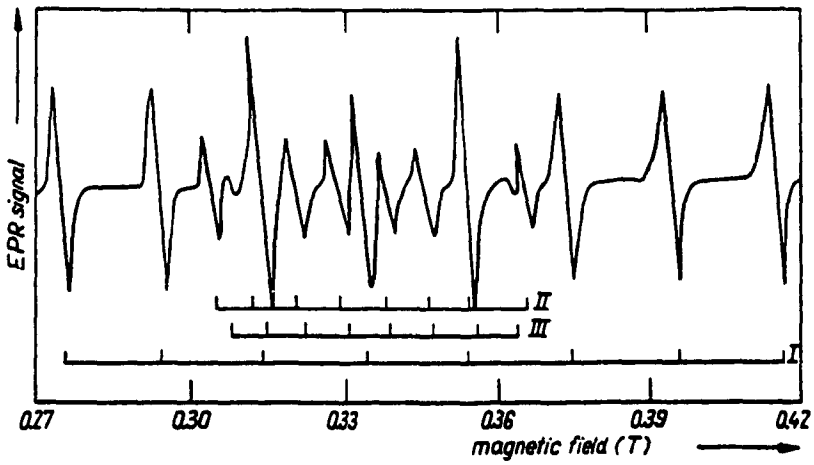

Fig. 2. First-derivative room-temperature VO^{2+} EPR spectrum in FASH, recorded for B in the ZY plane, at 25° from the Z-axis. Due to inversion symmetry, only two distinct sets of VO^{2+} hyperfine lines were observed in this plane; the lines for each of the two physically-equivalent VO^{2+} pairs merged into each other for the orientation of B in the ZY plane. There were four sets of lines at an arbitrary orientation of B, see Section 3. The line positions for the two largely-populated physically-equivalent pairs VO^{2+} ions (I and II) are indicated. The much weaker lines are due to the third pair of physically-equivalent VO^{2+} ion III (Section 3)

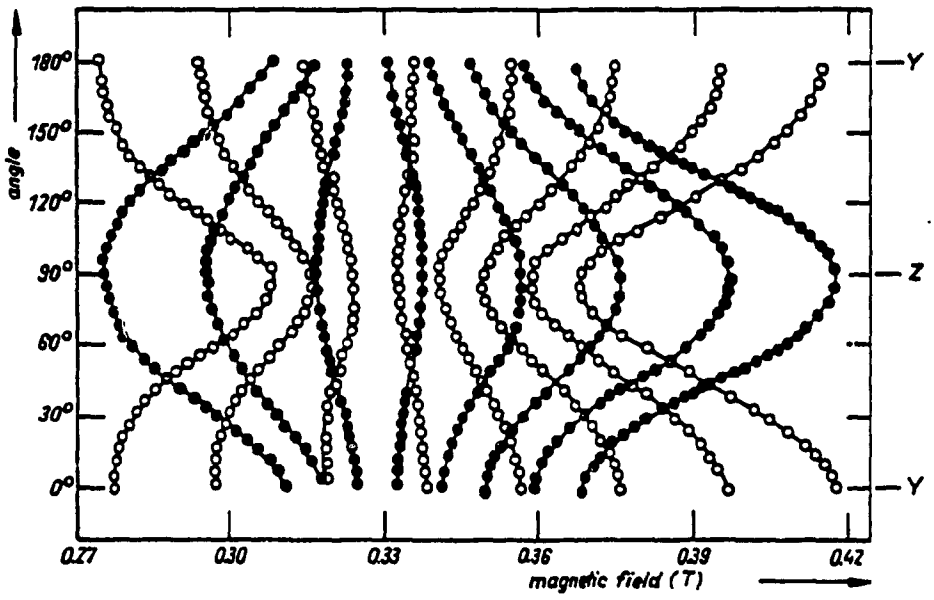

Fig. 3. Angular variation of EPR line positions observed at room temperature for B in the ZY plane for VO^{2+}-doped FASH crystal. The empty and solid circles represent experimental line positions corresponding to VO^{2+} ions I and II, respectively; the continuous lines are smooth curves that connect data points belonging to the same transition

present case, the ions belonging to these orientations are present with different probabilities, one of them (ion III) being very small.

The EPR linewidths of VO^{2+} in FASH were found independent of temperature in the range 4.2 to 393 K, being 1.4 ± 0.1 mT for the two VO^{2+} ions I and II, for any transition. These VO^{2+} EPR linewidths in the paramagnetic FASH host are found to be twice those in the diamagnetic ZASH, MASH, and CASH hosts [10, 11]. Because of narrower linewidth, the ligand superhyperfine (SHF) structure was well resolved in the diamagnetic hosts; however, SHF for the VO^{2+} ion in FASH was not resolved due to increased linewidth.

4. Spin-Hamiltonian and Evaluation of $\mathbf{g}^2$ and $\mathbf{A}^2$ Tensors

The spin-Hamiltonian, without the assumption of axial symmetry, or coincidences of the principal axes of the $\mathbf{g}^2$ and $\mathbf{A}^2$ tensors, describing the interactions of the VO^{2+} ion, responsible for the observed EPR transitions, can be expressed as [14]

$$\mathcal{H} = \mu_B S \cdot \mathbf{g} \cdot B + S \cdot \mathbf{A} \cdot I. \tag{1}$$

In (1), the two terms represent the electronic Zeeman and the HF interactions, with $S = 1/2$ and $I = 7/2$, respectively. Here μ_B, $\mathbf{g}$, and $\mathbf{A}$ are, respectively, the Bohr magneton, the matrix for $\mathbf{g}$ and the hyperfine-interaction matrix. In (1) the quadruple-interaction term has been omitted, as it has negligible effect [14].

The principal values and direction cosines of the $\mathbf{g}^2$ ($\equiv \mathbf{g}^T \cdot \mathbf{g}$; T denotes the transposed matrix) and $\mathbf{A}^2$ ($\equiv \mathbf{A}^T \cdot \mathbf{A}$) tensors were evaluated by the use of a least-squares fitting (LSF) procedure [16 to 18], using eigenvalues calculated to second order in perturbation, applicable to non-coincident principal axes of the $\mathbf{g}^2$ and $\mathbf{A}^2$ tensors. In summary, a total of 384 allowed HF line positions observed for the VO^{2+} complex for B in the ZX, ZY, XY planes in FASH, for any magnetically-inequivalent VO^{2+} ion, were fitted simultaneously in the LSF procedure. The results for the VO^{2+} ions I and II are listed in Table 1. The absolute signs of the principal values of A have been assumed to be negative in accordance with those determined by Muncaster and Parke [19]. Table 1 reveals that the principal axes of the $\mathbf{g}^2$ and $\mathbf{A}^2$ tensors are almost coincident. As well, the values of g_x and g_y are somewhat different from each other; this is also true for A_x and A_y. This implies a small departure from axial symmetry. The present values of the spin-Hamiltonian parameters are typical of vanadyl complexes, characterized by axial symmetry of ligand field with small distortion, especially in so far as the hyperfine parameters are concerned. The previously-reported room-temperature parameters [9] have also been included in Table 1 for comparison.

5. Positions of the Vanadyl Ions in FASH Lattice

Similar to the situations in VO^{2+}-doped ZASH, MASH, and CASH [10, 11], the site of the metallic host ion (Fe^{2+} ion in the present case) is the most probable site for substitution by the VO^{2+} ion, both being doubly ionized. The orientation of the principal Z-axis of the $\mathbf{g}^2$ tensor, for any VO^{2+} complex, is expected to be along the V^{4+}–O^{2-} bond [20, 21]. Using the direction cosines (Table 1) and crystal-structure data, the principal Z-axes of the $\mathbf{g}^2$ tensor are found to be almost parallel to the Fe^{2+}-$H_2O(7)$ direction for ion I, and to the Fe^{2+}–$H_2O(8)$ direction for ion II. When the VO^{2+} ion substitutes for a Fe^{2+} ion in the FASH lattice, it expels one of the $H_2O(7)$, $H_2O(8)$, or $H_2O(9)$ molecules, forming the so-called $[VO(H_2O)_5]^{2+}$ complex [20], whose geometrical axis, i.e., the line joining the V^{4+}

Table 1
Principal values and direction cosines of the g and A matrices of VO^{2+} in FASH single crystal for the ions I and II. The principal values of g are dimensionless, while those of A are expressed in GHz. The indicated errors have been estimated by the use of a statistical method [26]. The direction cosines of the principal axes of the g^2 tensor (X', Y', Z') are given with respect to the laboratory frame (X, Y, Z), defined in Section 3, while those of the A^2 tensor (X'', Y'', Z'') are expressed relative to (X', Y', Z'). The numbers in brackets for the principal values are those reported by Upreti and Saraswat [9], who assumed $g_{x'} = g_{y'} = g_\perp$ and $A_{x'} = A_{y'} = A_\perp$ (room temperature)

temperature	ion	principal values	direction cosines		
			Z/Z'	X/X'	Y/Y'
295 K	I	$g_{z'} = 1.9364 \pm 0.0020$ (1.941)	0.7400	0.6499	−0.1734
		$g_{x'} = 1.9809 \pm 0.0020$ (1.990)	−0.6550	0.7549	0.0345
		$g_{y'} = 1.9846 \pm 0.0020$ (1.990)	0.1534	0.0880	0.9843
		$A_{z'} = -0.5344 \pm 0.0050$ (0.540)	−0.9919	0.1124	0.0593
		$A_{x'} = -0.2136 \pm 0.0050$ (0.220)	0.1098	0.9930	−0.0446
		$A_{y'} = -0.1813 \pm 0.0050$ (0.220)	0.0639	0.0378	0.9972
	II	$g_{z'} = 1.9371 \pm 0.0020$ (1.941)	0.0408	0.7407	−0.6707
		$g_{x'} = 1.9801 \pm 0.0020$ (1.990)	−0.3309	0.6343	0.6904
		$g_{y'} = 1.9741 \pm 0.0020$ (1.990)	0.9428	0.1938	0.6904
		$A_{z'} = -0.5412 \pm 0.0050$ (0.522)	0.9909	−0.0041	0.1347
		$A_{x'} = -0.2578 \pm 0.0050$ (0.220)	0.0157	0.9963	−0.0850
		$A_{y'} = -0.1776 \pm 0.0050$ (0.220)	0.1339	−0.0864	−0.9872
80 K	I	$g_{z'} = 1.9363 \pm 0.0020$	0.7452	0.6466	−0.1630
		$g_{x'} = 1.9907 \pm 0.0020$	−0.6514	0.7582	0.0292
		$g_{y'} = 1.9868 \pm 0.0020$	0.1425	0.0844	0.9862
		$A_{z'} = -0.5318 \pm 0.0050$	−0.9512	−0.2967	0.0856
		$A_{x'} = -0.2174 \pm 0.0050$	−0.2983	0.9545	−0.0063
		$A_{y'} = -0.1835 \pm 0.0050$	0.0793	0.0314	0.9964
	II	$g_{z'} = 1.9401 \pm 0.0020$	0.0388	0.7407	−0.6707
		$g_{x'} = 1.9827 \pm 0.0020$	−0.3319	0.6426	0.6906
		$g_{y'} = 1.9661 \pm 0.0020$	0.9425	0.1958	0.2708
		$A_{z'} = -0.5633 \pm 0.0050$	0.9972	−0.0058	0.0742
		$A_{x'} = -0.2567 \pm 0.0050$	0.0155	0.9912	−0.1312
		$A_{y'} = -0.2008 \pm 0.0050$	0.0728	−0.1320	−0.9886
4.2 K	I	$g_{z'} = 1.9364 \pm 0.0020$	0.7400	0.6499	−0.1734
		$g_{x'} = 1.9809 \pm 0.0020$	−0.6550	0.7549	0.0345
		$g_{y'} = 1.9846 \pm 0.0020$	0.1534	0.0880	0.9843
		$A_{z'} = -0.5344 \pm 0.0050$	−0.9972	0.0378	0.0639
		$A_{x'} = -0.2136 \pm 0.0050$	0.0446	0.9930	−0.1098
		$A_{y'} = -0.1813 \pm 0.0050$	0.0593	0.1124	0.9919
	II	$g_{z'} = 1.9237 \pm 0.0020$	0.0398	0.7413	−0.6699
		$g_{x'} = 1.9769 \pm 0.0020$	−0.3310	0.6423	0.6913
		$g_{y'} = 1.9749 \pm 0.0020$	0.9428	0.1942	0.2710
		$A_{z'} = -0.5238 \pm 0.0050$	0.9915	−0.0027	0.1303
		$A_{x'} = -0.2373 \pm 0.0050$	0.0010	0.9999	0.0129
		$A_{y'} = -0.1570 \pm 0.0050$	0.1303	0.0127	−0.9914

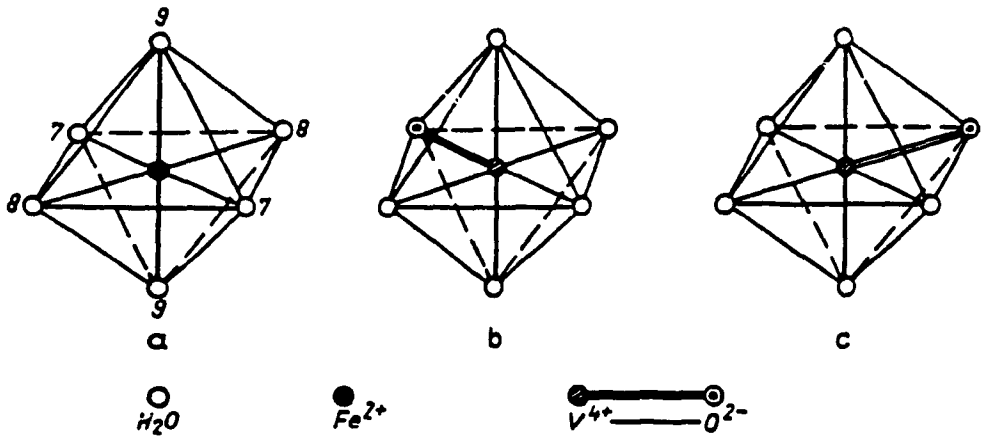

Fig. 4. Orientations of the VO^{2+} ions, and the $[VO(H_2O)_5]^{2+}$ complex, in FASH lattice. a) Octahedral coordination of water molecules around Fe^{2+} ion, b) V^{4+}–O^{2-} bond orientation for ion I, and c) V^{4+}–O^{2-} bond orientation for ion II

and O^{2-} ions, is oriented along the direction previously formed by Fe^{2+}–$H_2O(7)$ for ion I, and by Fe^{2+}–$H_2O(8)$ for ion II, as shown in Fig. 4. There is a finite, though small, probability, in agreement with experimental data, for the VO^{2+} ion to orient itself along the Fe^{2+}–$H_2O(9)$ direction, because the Fe^{2+}–$H_2O(9)$ distance is the smallest of the three Fe^{2+}–$H_2O(i)$, i = 7, 8, 9, distances. Thus, the model of the $[VO(H_2O)_5]^{2+}$ complex (Fig. 4) explains well the features of the EPR spectra for VO^{2+}-doped FASH crystal. The two observed groups of symmetry-related intense EPR spectra are due to the two symmetrically-oriented $[VO(H_2O)_5]^{2+}$ complexes. The same conclusion applies to VO^{2+} EPR spectra in other VO^{2+}-doped Tutton salts [10, 11].

6. g-Shift and VO^{2+}–Fe^{2+} Exchange Interaction

6.1 Shape effect

At low temperatures, the magnetization of paramagnetic FASH crystal causes a shift of the g-value of the VO^{2+} impurity ion, which depends (i) on the shape of the crystal [2] and (ii) on the exchange interaction with the host Fe^{2+} ion, as described in Section 6.2.

In general, it is difficult to estimate the shape-dependent g-shift for an arbitrary orientation of $\boldsymbol{B}$, and for an arbitrary crystal shape [3 to 6]. However, for special orientations of $\boldsymbol{B}$, and for particular crystal shapes, there exist simple expressions to calculate the g-shift theoretically, e.g., when $\boldsymbol{B}$ is along one of the susceptibility axes. For FASH, one of the principal axes of magnetic susceptibility has been reported to be parallel to the crystal b-axis, for which the susceptibility is $\chi_3 = 0.79$ e.m.u./mol at 4.2 K [4, 22]. For external magnetic field $\boldsymbol{B} \parallel \boldsymbol{b}$, the magnetization (in e.m.u.) is $M = \chi_3 Bd/A$, where d (= 1.864 g/cm^3) is the density of FASH crystal and A (= 394.14) is its gram-molecular weight [4]. For the presently-used thin disk-shaped FASH crystal the demagnetization factor, N, for $\boldsymbol{B}$ along $\boldsymbol{b}$ is approximately zero [4, 10, 11]. Thus, the shape-dependent g-shift for $\boldsymbol{B} \parallel \boldsymbol{b}$ is estimated, according to Kittel [2], to be $\Delta g = 3M[(4\pi/3) - N]\,2B = 2\pi\chi_3 d/A = 0.0023$.

6.2 Exchange interaction

At liquid-helium temperature, the exchange interaction of the VO^{2+} ion with the host Fe^{2+} ions is equivalent to the presence of an internal magnetic field at the VO^{2+} site, since magnetic moments are induced on the paramagnetic host ions (Fe^{2+}) due to the polarization effect of the external magnetic field. This results in a shift of the resonant-field value in the paramagnetic host from that in an isostructural host lattice consisting of diamagnetic ions. This g-shift can be estimated by taking into account the effect of the VO^{2+}–Fe^{2+} exchange interaction in a perturbation calculation.

Assume a pairwise exchange interaction between a VO^{2+} ion with a neighbor Fe^{2+} ion. The total spin-Hamiltonian for the pair can be expressed as

$$\mathcal{H}_t = \mathcal{H} + \mathcal{H}' + \mathcal{H}_p , \tag{2}$$

where $\mathcal{H} = g_d \mu_B S \cdot B$ is the spin-Hamiltonian of the VO^{2+} ion neglecting the HF term, g_d is the effective g-factor of VO^{2+} in an isostructural diamagnetic host, and

$$\mathcal{H}' = g'_{\parallel} \mu_B B_z S'_z + \Delta_x S'^2_x + \Delta_y S'^2_y , \tag{3}$$

is the spin-Hamiltonian of the non-Kramer's ion Fe^{2+}, where the effective spin $S' = 1/2$, and $\Delta = (\Delta_x^2 + \Delta_y^2)^{1/2}$ represents the small zero-field splitting due to local distortion [1, 23, 24]. The third term in (2),

$$\mathcal{H}_p = J_p S \cdot S' , \tag{4}$$

exhibits the VO^{2+}–Fe^{2+} exchange interaction, where J_p is the exchange-interaction constant.

The wave functions of the total system can be expressed as product wave functions $\psi_1(M)\psi_2(M')$, where the values of the magnetic quantum numbers are $M = \pm 1/2$, and $M' = \pm 1/2$ for the VO^{2+} and Fe^{2+} ions, respectively. Thus, the spin-Hamiltonian of the pair system is a 4×4 matrix. The following expressions are derived for the energy levels $E(M, M')$, using perturbation theory, for B parallel to the principal axis of the g^2 tensor of the Fe^{2+} ion, for the Fe^{2+} energy level ($M' = -1/2$), which lies lowest at liquid-helium temperature.

$$E(+1/2, -1/2) = \mu_B g_d B/2 - (1/2)[(g'_{\parallel}\mu_B B)^2 + \Delta^2]^{1/2} - J_p/4 , \tag{5}$$

$$E(-1/2, -1/2) = -\mu_B g_d B/2 - (1/2)[(g'_{\parallel}\mu_B B)^2 + \Delta^2]^{1/2} + J_p/4 . \tag{6}$$

Using these energy levels, the resonance condition (for the transition $1/2, -1/2 \leftrightarrow -1/2, -1/2$) $\Delta E = h\nu = g_p \mu_B B$, where g_p is the impurity-ion g-value in the paramagnetic host, and taking into account the nearest and next-nearest neighbor Fe^{2+} ions to a VO^{2+} ion, one obtains for the exchange constant J_p, considering only the nearest- and next-nearest neighbors,

$$J_p = 2\mu_B B(g_d - g_p)/n' , \tag{7}$$

where $\Delta g = g_p - g_d$ is the shift in the g-value of the VO^{2+} ion in FASH paramagnetic host from that in an isostructural diamagnetic host, ZASH, CASH, or MASH; it can be determined experimentally. In (7), $n' = 6$ is the number of nearest and next-nearest neighbors to a VO^{2+} ion in FASH. To estimate J_p from (7), B can be chosen to be 0.34 T, being close to the central magnetic field used in the present EPR measurements.

6.3 Estimation of J_p

For the effective g-factor for VO^{2+} in the orientation $B \parallel X$, which is one of the principal axes of magnetic susceptibility for FASH [4, 22], one has

$$g_X = [g_{Z'}^2 \cdot \cos^2(Z', X) + g_{X'}^2 \cdot \cos^2(X', X) + g_{Y'}^2 \cdot \cos^2(Y', X)]^{1/2}. \tag{8}$$

where Z', X', Y' are the directions of the principal axes of the g matrix, $(g_{Z'}, g_{X'}, g_{Y'})$ are the principal values of the g matrix of the VO^{2+} ion in FASH, (Z', X), etc. represent the angle between the Z' and X axes, etc. which can be calculated using the values given in Table 1.

Finally, for $B \parallel X$,

$$J_p = (2\mu_B B/n')(g_{dx} - g_{px} + 2\pi\chi_3 d/A). \tag{9}$$

For diamagnetic ZASH, MASH, and CASH, the average $g_{dx} = 1.9945$ [10, 11], while for paramagnetic FASH $g_{px} = 1.9622$ averaged over VO^{2+} ions I and II, as determined presently. Then, the VO^{2+}–Fe^{2+} exchange-interaction constant, J_p, averaged over the nearest and the next-nearest neighbors is estimated presently to be 0.07 GHz in FASH. For comparison, Mn^{2+}–Fe^{2+} exchange interaction constant was reported to be −0.006 GHz [3, 4].

7. Spin–Lattice Relaxation Time (τ) of Host Fe^{2+} Ions

For a correct estimate of τ in doped crystals, where there are present two different kinds of paramagnetic ions, one has to use the appropriate second moment, described by Van Vleck [25]. Misra and Orhun [8] showed that for the case when the distances between the impurity ions are sufficiently large and when the number of neighbors considered is confined to N, the correct second moment can be reduced to

$$\langle \Delta\nu^2 \rangle_{II} = \tfrac{1}{3} S'(S'+1) h^{-2} \left[N J_p^2 + (gg')\mu_B^4 \mu_0^2 \sum_{k'}^{N} (1 - 3\gamma_{jk'}^2)^2 r_{jk'}^{-6} + 2J_p gg' \mu_B^2 \mu_0 \sum_{k'}^{N} (1 - 3\gamma_{jk'}^2) r_{jk'}^{-3} \right]. \tag{10}$$

In (10), J_p is the average host-impurity pair-exchange constant and μ_0 is the permeability constant, required for the purpose of calculations in SI units, the summation is over the host ions surrounding the impurity ion: r_{jk} and γ_{jk} represent the length of the straight line joining the j and k ions and the direction cosines of r_{jk} with the external field, respectively; the primed quantities describe the host ions, while the unprimed ones the impurity ion. Finally, τ of the host paramagnetic ions in doped crystals, at temperature around or higher than the room temperature, can be estimated, using the contribution to the EPR linewidth of the impurity ion due to the paramagnetism of the host ions ΔB_{imp}, from the following expression [8]:

$$\tau = (3\Delta B_{imp} g^2 \mu_B)/(110 h g' \langle \Delta\nu^2 \rangle_{II}). \tag{11}$$

In order to estimate ΔB_{imp}, one should subtract, from the observed impurity-ion linewidth (1.4 mT) the linewidth of the impurity ion in an isostructural diamagnetic host, as well as the linewidth due to the inhomogeneous broadening, caused by the unresolved super-hyperfine structure, i.e. a total of 0.7 mT [10, 11]. Finally, ΔB_{imp} is estimated to be 0.7 mT at room temperature.

A computer program was used to generate the FASH lattice in order to calculate the required distances between the impurity ion (VO^{2+}) and the neighbor host Fe^{2+} ions and the direction cosines (γ_μ) of the external field, relative to the position vectors of the various ions. For the calculation of the second moment, it was found sufficient to consider only up to the fifth-nearest neighbors, i.e., a total of 20 Fe^{2+} ions ($N = 20$), the contributions of the farther-lying neighbors were found to be negligible.

In the estimation of τ, the values of all the parameters required, except for S' and g', have been determined presently. For the values of S' and g' the following considerations were made. For Fe^{2+}, which is a non-Kramer's ion, its spin-Hamiltonian for the case of lower symmetry (equivalent to the presence of local distortions superimposed on higher symmetry due to Jahn-Teller effect), as described by Abragam and Bleaney [1], is given by (3), wherein Δ_x, Δ_y represent the distortion: and $g'_\mu = 2\langle\xi_0| S'_\mu |\xi_0\rangle$ where $|\xi_0\rangle$ is one of the time-conjugate states for the ground state of Fe^{2+}, and $g'_\perp = 0$. $g'_\parallel$ value has been reported to be 8.989 for FASH [23, 24]. In the numerical estimates, made presently for τ, the direction of external field was assumed to be along the Z (or parallel) magnetic axis of the VO^{2+} ion. However, the parallel (Z') magnetic axis for the host ion is not necessarily along the respective parallel axes of the impurity VO^{2+} ion. Thus, the average of $g'_\parallel$ and $g'_\perp$ values (= 4.49) for the host ion was chosen for estimating τ. This does not lead to any significant error in the calculated values of τ, because of the uncertainty in other factors. Finally, the value of τ was estimated to be 7.20×10^{-15} s at room temperature.

The temperature independence of the VO^{2+} EPR linewidth in FASH (Section 3) does not necessarily imply that τ does not vary with temperature. It is well known that all processes of spin–lattice relaxation do depend on temperature [27]. Usually, the EPR linewidth decreases as temperature increases due to host–ion spin–lattice relaxation. Thus, there must exist compensating processes which cause increase in EPR linewidth as temperature increases. Upreti and Saraswat [9] suggested that this compensating process might be the spin-quenching process, but they could not provide an appropriate justification. The population fluctuation of the crystal field levels of Fe^{2+} may cause the impurity-ion linewidth to decrease with decreasing temperature which could be the compensating process, similar to those for Tm^{3+}, Pr^{3+}, and Tb^{3+} [28 to 30]. Further, it may be suggested here that the ordering of the host Fe^{2+} ions at low temperatures may also play this compensating role [31].

8. Concluding Remarks

The main results of the present EPR study on VO^{2+}-doped FASH are as follows:

(i) The principal values of the **g** and **A** matrices, without the assumption of axial symmetry, as well as their direction cosines, have been evaluated at 295, 80, and 4.2 K, from the present EPR data. The results indicate some distortion from axial symmetry. The model of the $[VO(H_2O)_5]^{2+}$ complex is found to explain the data adequately.

(ii) The VO^{2+}–Fe^{2+} exchange-interaction constant has been estimated to be 0.07 GHz in the paramagnetic host FASH, using the g-shift in the paramagnetic host from that in the isostructural diamagnetic hosts $M(NH_4)_2(SO_4)_2 \cdot 6H_2O$ (M = Zn, Mg, Cd).

(iii) The host ion (Fe^{2+}) spin–lattice relaxation time has been estimated to be 7.20×10^{-15} s at room temperature in the FASH crystal lattice, using an appropriate expression taking into account the presence of two kinds of paramagnetic ions from VO^{2+}-impurity ion EPR linewidths.

Acknowledgements

The authors are grateful to the Natural Sciences and Engineering Research Council of Canada for financial support (grant no. OGP0004485), and to the Concordia University Computer Center for providing their facilities to analyze the data.

References

[1] A. ABRAGAM and B. BLEANEY, Electron Paramagnetic Resonance of Transition Ions, Clarendon Press, Oxford 1970.
[2] C. KITTEL, Phys. Rev. 73, 155 (1948).
[3] S. K. MISRA and S. Z. KORCZAK, Phys. Rev. B 35, 4625 (1987).
[4] S. K. MISRA and S. Z. KORCZAK, Phys. Rev. B 34, 3086 (1986).
[5] S. K. MISRA, C. WANG, S. HAN, and S. Z. KORCZAK, Phys. Rev. B 36, 3542 (1987).
[6] S. K. MISRA, M. KAHRIZI, P. MIKOLAJCZAK, and L. MISIAK, Phys. Rev. B 32, 4738 (1985).
[7] P. CHAND, V. K. JAIN, and G. C. UPRETI, Magnetic Resonance Rev. 14, 49 (1988).
[8] S. K. MISRA and U. ORHUN, Phys. Rev. B 39, 2856 (1989).
[9] G. C. UPRETI and R. S. SARASWAT, phys. stat. sol. (b) 122, K169 (1984).
[10] S. K. MISRA and J. SUN, Phys. Rev. B 42 (1990).
[11] S. K. MISRA and J. SUN, Physica B 162, 331 (1990).
[12] R. W. G. WYCKOFF, Crystal Structures, Vol. 3, Interscience Publishers, New York 1963.
[13] H. MONTGOMERY, R. V. CHASTAIN, J. J. NATT, A. M. WITKOWSKA, and E. C. LINGAFELTER, Acta cryst. 22, 775 (1967).
[14] S. K. MISRA and C. WANG, Physica 159B, 321 (1989).
[15] S. K. MISRA, J. SUN, and S. JERZAK, Phys. Rev. B 40, 74 (1989).
[16] S. K. MISRA, Physica 124B, 53 (1984).
For application see S. K. MISRA, J. BANDET, G. BACQUET, and T. E. MCENALLY, phys. stat. sol. (a) 80, 581 (1983).
[17] S. K. MISRA, Physica 151B, 433 (1988).
[18] S. K. MISRA, Arab. J. Sci. Engng. 13, 255 (1988).
[19] R. MUNCASTER and S. PARKE, J. non-crystall. Solids 24, 399 (1977).
[20] R. H. BORCHERTS and C. KIKUCHI, J. chem. Phys. 40, 2270 (1964).
[21] V. K. JAIN, phys. stat. sol. (b) 97, 337 (1980).
[22] J. C. GILL and P. A. IVEY, J. Phys. C 7, 1536 (1974).
[23] S. A. ALTSHULER and B. M. KOZYREV, Electron Paramagnetic Resonance in Compounds of Transition Elements, Keter, Jerusalem 1974.
[24] A. BOSE, A. S. CHAKRAVARTY, and R. CHATTERJEE, Proc. Roy. Soc. London. A261, 207 (1961).
[25] J. H. VAN VLECK, Phys. Rev. 74, 1168 (1948).
[26] S. K. MISRA and S. SUBRAMANIAN, J. Phys. C 15, 7199 (1982).
[27] K. N. SHRIVASTAVA, phys. stat. sol. (b) 117, 437 (1983).
[28] K. SUGAWARA, C. Y. HUANG, and B. R. COOPER, Phys. Rev. B 11, 4455 (1975).
[29] K. SUGAWARA, C. Y. HUANG, and B. R. COOPER, Phys. Rev. B 28, 4955 (1983).
[30] B. R. COOPER, R. C. FEDDER, and D. P. SCHUMACHER, Phys. Rev. 163, 506 (1967).
[31] S. K. MISRA, U. ORHUN, and J. SUN, Solid State Commun., to be published.

(Received May 15, 1990; in revised form September 4, 1990)

phys. stat. sol. (b) 162, 265 (1990)

Subject classification: 76.30, S11

Physics Department, Concordia University, Montreal[1])

EPR of a Gd^{3+}-Doped $NH_4Pr(SO_4)_2 \cdot 4\,H_2O$ Single Crystal

Study of Phase Transition and Superposition Model Calculation of Zero-Field Splitting Parameters

By

S. K. MISRA and JIANSHENG SUN[2])

X-band EPR spectra of a single crystal of Gd^{3+}-doped $NH_4Pr(SO_4)_2 \cdot 4\,H_2O$ (APST) are recorded in the temperature range 4.2 to 410 K. The angular variation of the EPR line positions indicates the presence of two magnetically-inequivalent Gd^{3+} ions. The orientations of their principal axes are determined. The Gd^{3+} spin-Hamiltonian parameters are evaluated using a rigorous least-squares-fitting procedure. The superposition model is applied to calculate the values of the zero-field splitting parameters b_2^0, b_4^0 of Gd^{3+}, and those of the intrinsic parameters $\bar{b}_2$ and $\bar{b}_4$. The temperature variation of the EPR spectra reveals the occurrences of two first-order phase transitions in APST crystal at 266 and 155 K.

On a enregistré les spectres de la RPE à bande-X sur un monocristal de $NH_4Pr(SO_4)_2 \cdot 4\,H_2O$, dopé par l'ion Gd^{3+}, dans l'intervalle de températures 4.2 à 410 K. La variation angulaire des positions des raies de la RPE indique le présence de deux centres non-équivalent magnétiquement de l'ion Gd^{3+}. Leurs axes principaux ont été déterminés. Les paramètres du spin hamiltonien du Gd^{3+} ont été évalués par une méthode rigoureuse d'adaptation aux moindres carrés. Le modèle de superposition a été utilisé, pour calculer les valeurs des paramètres b_2^0, b_4^0 du clivage dans un champ nul du Gd^{3+} dans le cristal, ainsi que les valeurs des paramètres intrinsèques $\bar{b}_2$, $\bar{b}_4$. Les variations des spectres de la RPE indiquent l'occurrence de deux transitions de phase dans ce cristal, à 266 et à 155 K.

1. Introduction

The $NH_4Pr(SO_4)_2 \cdot 4\,H_2O$ crystal (hereafter, APST) belongs to the series of isostructural crystals of the double sulfates $NH_4R(SO_4)_2 \cdot 4\,H_2O$ (R = rare earth) [1], which are of analytical significance, because they can be used to separate the light and heavy lanthanides [2]. These crystals are interesting for EPR studies, since they exhibit a series of phase transitions below room temperature [3 to 6]. Infrared (IR) studies on these crystals have been reported [1, 5].

EPR studies on Gd^{3+}-doped $NH_4Nd(SO_4)_2 \cdot 4\,H_2O$ (ANST), $NH_4Sm(SO_4)_2 \cdot 4\,H_2O$ (ASST), and $NH_4Ce(SO_4)_2 \cdot 4\,H_2O$ (ACST) have been reported by Buckmaster, Malhotra, and Bist [3 to 5]. The room-temperature (RT) values of the spin-Hamiltonian parameters (SHP) of Gd^{3+} in these crystals were evaluated, assuming an orthorhombic site symmetry. Three phase transitions were deduced to occur in the 97 to 304 K temperature range. So far, no EPR studies above RT, as well as below 97 K, have been reported on ANST, ASST, and ACST. Further, there exist some discrepancies in the interpretation of the previously-

[1]) 1455 de Maisonneuve Boulevard West, Montreal, Quebec H3G 1M8, Canada.

[2]) Permanent address: Center of Materials Analysis, Nanjing University, Nanjing, Jiangsu, People's Republic of China.

reported EPR studies 3 to 5]: (i) an incorrect formula was used in the estimation of τ the spin–lattice relaxation time, as pointed out by Misra et al. [7]; (ii) a spin-Hamiltonian appropriate to a monoclinic site symmetry should have been used, in accordance with the crystal structure [1], instead of the orthorhombic site symmetry used in [3 to 5]; and (iii) there was no explanation provided as to why the value of the parameter b_2^0 of Gd^{3+} was unusually small in the ANST, ASST, and ACST hosts, as compared to that found usually in other host crystals.

As for APST, no EPR studies have so far been reported. Jasty et al. [6] studied the phase transitions in APST using Fourier-transform infrared (FTIR) and differential scanning calorimetry (DSC) techniques in the 100 to 300 K temperature range, and detected two phase transitions, occurring at about 230 and 150 K. The present paper reports an extensive X-band EPR study of a Gd^{3+}-doped APST crystal in the 4.2 to 410 K temperature range, with particular emphasis on the explanation of the values of SHP of Gd^{3+} in this crystal, as well as on the detection of the phase transitions experienced by the APST lattice.

2. Sample Preparation and Crystal Structure

The experimental arrangement has been described elsewhere [8, 9].

APST crystals doped with Gd^{3+} were grown by slow evaporation at RT of an aqueous solution, containing $Pr_2(SO_4)_3 \cdot 8\,H_2O$ and $(NH_4)_2SO_4$ mixed in the molar ratio of 1:4, to which a small quantity of $Gd_2(SO_4)_3 \cdot 8\,H_2O$ powder was added, so that there was one Gd^{3+} ion for every 100 Pr^{3+} ions in the solution. An amount greater than the stoichiometric amount of $(NH_4)_2SO_4$ was used, since it has a strong tendency to creep out of the container [4, 5]. Also, some dilute H_2SO_4 was added to the solution in order to prevent hydrolysis. Prismatic crystals, with the green characteristic color of Pr^{3+} ions, were obtained in about three weeks; one of size $3.0 \times 2.0 \times 1.0\ mm^3$ was chosen for the present measurements. The crystals were stored in oil to avoid dehydration.

At room temperature, an APST crystal is monoclinic, characterized by the space group C_{2h}^5, containing four formula units per unit cell [1]; the unit-cell parameters are: a

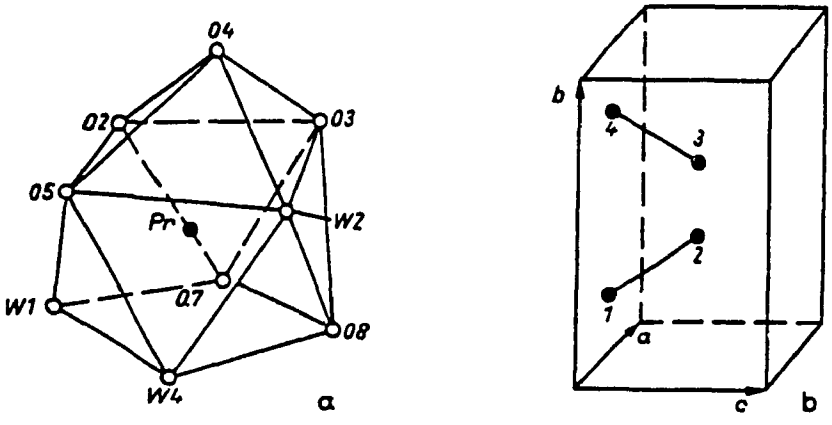

Fig. 1. Crystal structure of APST at room temperature. a) The coordination polyhedron about a Pr^{3+} ion for APST: a monocapped square antiprism. Wn indicates an oxygen ion belonging to a water molecule, while On an oxygen ion belonging to a sulfate ion, as displayed in [1]. Only the oxygen ions nearest to the rare-earth ion have been shown. b) Positions of the four Pr^{3+} ions in the unit cell of APST

= 0.6444 nm, b = 1.8963 nm, c = 0.8798 nm, and β = 97.18°. The Pr^{3+} ion is coordinated to nine oxygen ions as shown in Fig. 1a, of which six belong to sulfate ions and three to three water molecules. The fourth water molecule is held between the sulfate layers by hydrogen bonding. The polyhedron of the nine-coordinated oxygens can be considered to be equivalent to a distorted monocapped square antiprism (approximately C_{4v} symmetry). The Pr^{3+} ions are located in the unit cell at (0.5, 0.1321, 0.0), (0.5, 0.3677, 0.5), (0.5, 0.6323, 0.5), and (0.5, 0.8678, 0.0) [7], labelled as 1, 2, 3, and 4, respectively, as depicted in Fig. 1b. The Pr^{3+} ions 1 and 2 belong to a pair, having parallel orientations of the respective C_{4v} axes, which is the Pr^{3+}–O(4) bond axis, making angles of about (51°, 45°, 72°) relative to the (a, b, c) axes. The pair of ions 1, 2 is symmetrically related to the other pair (ions 3, 4) by the ac inversion plane. So far, no information about the crystal-growth habit for APST is available. As well, no crystal-structure data have been reported for the phases different from the RT phase.

3. RT EPR Spectra and Orientations of the Principal Axes

EPR spectra were recorded at RT for the orientations of the external magnetic field ($\boldsymbol{B}$) in the principal ZX and ZY planes of the zero-field splitting tensor b_2^m of one of the magnetically inequivalent Gd^{3+} ions in the unit cell. (The principal axes (X, Y, Z) are defined to be those directions of the external magnetic field ($\boldsymbol{B}$) for which the extrema of overall splittings occur [10, 11], with the splittings being successively greater for $\boldsymbol{B} \parallel X, Y, Z$.) The spectra revealed the presence of two magnetically-inequivalent Gd^{3+} ions. Each ion exhibited seven allowed transitions ($\Delta M = \pm 1$; here M is the electronic magnetic quantum number), corresponding to the electronic spin $S = 7/2$ of Gd^{3+}. The Gd^{3+} ions substitute with equal preference at the two magnetically-inquivalent Pr^{3+} sites in the unit cell, because the intensities of the EPR spectra for $\boldsymbol{B}$ parallel to their respective Z-axes are equal.

The EPR spectrum, for $\boldsymbol{B} \parallel Z$, of one of the magnetically-inequivalent Gd^{3+} ion is shown in Fig. 2, while Fig. 3a and b exhibit the angular variations of the EPR lines for the same Gd^{3+} ion for $\boldsymbol{B}$ in its ZX and XY planes, respectively. The four Pr^{3+} ions in the unit cell of APST, having the same nine-fold coordinations as the ligand ions, were found to be physically-equivalent, as revealed by the EPR spectra. For each of the two magnetically-inequivalent Gd^{3+} ions, the splittings for $\boldsymbol{B}$ along its X and Y-axes were found to be about the same. The Z-axis for one pair was found to be parallel to the X-axis for the other pair,

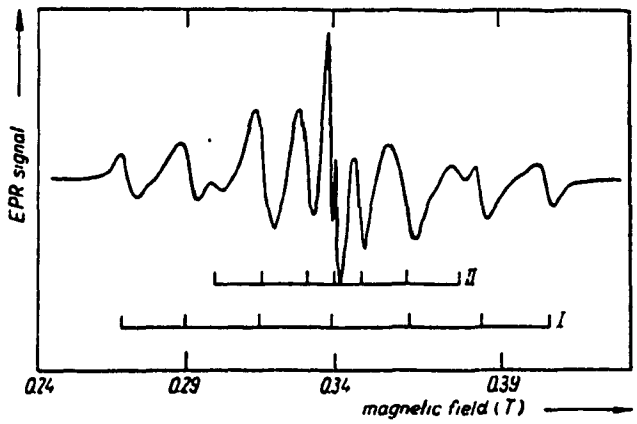

Fig. 2. First-derivative EPR spectrum of Gd^{3+} in APST for $\boldsymbol{B} \parallel Z$ for one of the magnetically-inequivalent Gd^{3+} ions (I), and $\boldsymbol{B} \parallel X$ for the other magnetically-inequivalent Gd^{3+} ion (II) at room temperature

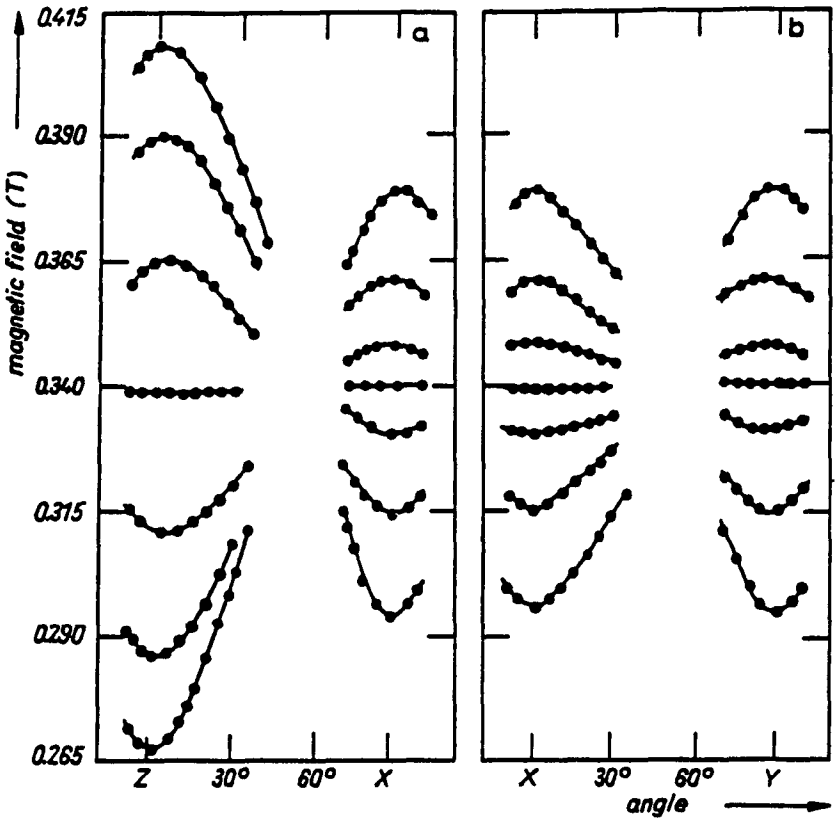

Fig. 3. Angular variation of EPR line positions for one of the magnetically-inequivalent Gd^{3+} ions at room temperature for B a) in its ZX plane and b) in its XY plane.

and vice versa; the Y-axes for the two pairs, lying in the ac plane were observed to be parallel to each other, at 64° from the a-axis. Buckmaster and coworkers [3 to 5] also made the same observations in the isostructural ANST, ASST, and ACST crystals. However, they did not relate the magnetic axes (Z, X, Y) to the crystal axes.

4. RT Spin-Hamiltonian Parameters

A spin-Hamiltonian (SH) $\mathscr{H}$ appropriate to monoclinic symmetry, with the two-fold axis $C_2 \parallel Z$, was chosen to fit the EPR line positions of Gd^{3+} in APST. This is consistent with the site symmetry, since the Z-axis, as discussed in Section 3, lies along the local C_{4v} axis, which is oriented very close to the crystal C_2 axis (b-axis). Accordingly [10, 11],

$$\mathscr{H} = \mu_B[g_\parallel B_z S_z + g_\perp (B_x S_x + B_y S_y)] + \sum_{m=0,\pm 2} (1/3)\, b_2^m O_2^m + \\ + \sum_{m=0,\pm 2,\pm 4} (1/60)\, b_4^m O_4^m + \sum_{m=0,\pm 2,\pm 4,\pm 6} (1/1260)\, b_6^m O_6^m . \qquad (4.1)$$

where μ_B is the Bohr magneton and O_i^m are spin operators, as defined by Abragam and Bleaney [11]. In (4.1), $g_\parallel$, $g_\perp$, and b_i^m are the spin-Hamiltonian parameters (SHP). (The monoclinic spin-Hamiltonians appropriate to $C_2 \parallel X$ and $C_2 \parallel Y$ [10], as well as a

spin-Hamiltonian for orthorhombic symmetry, were also used to fit the EPR line positions; however, they gave much larger least-squares χ^2 values, and thus were excluded.)

A rigorous least-squares fitting (LSF) procedure [12], utilizing numerical diagonalization of the SH matrix on a digital computer, in which all clearly-resolved Gd^{3+} allowed line positions, observed for several orientations of B in the ZX and XY planes, were simultaneously fitted to evaluate the 17 SHP's, $g_{\parallel}$, $g_{\perp}$, and b_l^m. The errors of the parameters were estimated by the use of a statistical method [13]. Finally, a total of 154 line positions were used to evaluate the 17 SHP; they are listed in Table 1. As for the absolute signs of the parameters, they could not be determined from the present data, since no relative-intensity data are available at liquid-helium temperature (LHT); because at LHT, the crystal is in a different phase (Section 5). The sign of b_2^0 was then assumed to be positive, which is consistent with the results of the superposition-model calculation (Section 5). The signs of the other fine-structure parameters (b_l^m), relative to that of b_2^0, as yielded by the LSF procedure, are, of course, correct.

It was not possible to evaluate the SHP below the phase-transition temperature 266 K, since the orientations of the magnetic axes changed below 266 K, and the magnetic field orientation could no longer be varied in the magnetic ZX, XY planes, required for the evaluation of SHP.

5. Superposition Model Calculation of RT SHP (b_l^m)

It is noted that the value of the parameter b_2^0 of Gd^{3+} in APST ($\approx$0.35 GHz), which is about the same as those in the isostructural ANST, ASST, and ACST [3 to 5], is much smaller compared to those in other host crystals, e.g., $|b_2^0| = 2.4$ to 2.6 GHz in $LiYb_xY_{1-x}F_4$ ($x = 0$ to 1) [14] and $|b_2^0| = 0.7$ to 0.8 GHz in RF_3 (R = La, Ce, Pr, Nd) [15]. Buckmaster and coworkers [3 to 5] suggested that a lower symmetry would lead to a larger value of b_2^0, which is in disagreement with the present case of a local symmetry lower than C_{4v} at the Gd^{3+} ion, for which the value of b_2^0 is rather small.

Table 1

Room-temperature Gd^{3+} spin-Hamiltonian parameters in the $NH_4Pr(SO_4)_2 \cdot 4H_2O$ single crystal

parameter	value	parameter	value
$g_{\parallel}$	1.9950 ± 0.0004	b_6^0	0.0006 ± 0.0005
$g_{\perp}$	1.9948 ± 0.0004	b_6^2	0.0001 ± 0.0034
b_2^0	0.3469 ± 0.0009	b_6^4	−0.0215 ± 0.0060
b_2^2	−0.0003 ± 0.0013	b_6^6	0.0075 ± 0.0054
b_2^{-2}	0.0914 ± 0.0041	b_6^{-2}	−0.0796 ± 0.0043
b_4^0	−0.0087 ± 0.0004	b_6^{-4}	−0.0085 ± 0.0001
b_4^2	−0.0002 ± 0.0020	b_6^{-6}	0.0176 ± 0.069
b_4^4	−0.0284 ± 0.0022	n	154
b_4^{-2}	0.0328 ± 0.0049	χ^2/n	0.0037
b_4^{-4}	0.0014 ± 0.0032		

The unit for the values of b_l^m is GHz, while it is GHz^2 for $\chi^2 \left(\equiv \sum_j (|\Delta E_j| - h\nu_j)^2 \right)$; here ΔE_j is the calculated energy difference between the pair of levels participating in resonance for the j-th line position, ν_j the corresponding klystron frequency, and h Planck's constant), n is the number of lines fitted simultaneously.

The presently-estimated small value of b_2^0 can be well explained by the superposition model of Newman [15, 16]. In the superposition model, the SHP (b_l^m) can be expressed as linear combinations of single-ligand contributions via the intrinsic parameters $\bar{b}_l(R_0)$, as follows:

$$b_l^m = \sum_i \bar{b}_l(R_i)\, K_l^m(\theta_i, \varphi_i)\,, \tag{5.1}$$

where

$$\bar{b}_l(R_i) = \bar{b}_l(R_0)\,(R_0/R_i)^n\,. \tag{5.2}$$

In (5.1) and (5.2), $(R_i, \theta_i, \varphi_i)$ are the coordinates of ligand i, and R_0 is a particular reference bond length, which has been presently chosen to be 0.2499 nm, namely, the length of the Pr^{3+}–O(2) bond. The $K_l^m(\theta, \varphi)$ are angular functions. Specifically [16],

$$K_2^0(\theta, \varphi) = (3\cos^2\theta - 1)/2\,,$$
$$K_4^0(\theta, \varphi) = (35\cos^4\theta - 30\cos^2\theta + 3)/8\,,$$
$$K_4^4(\theta, \varphi) = (35\sin^4\theta\cos 4\varphi)/8\,.$$

In the APST crystal, one takes into account the nine ligand-oxygen ions, forming a distortedmonocapped square antiprism (Section 2), being the nearest neighbors to the Gd^{3+} ion, which substitutes for a Pr^{3+} ion (Fig. 1a). In the absence of crystal-structure data for APST, the values of $(R_i, \theta_i, \varphi_i)$ for APST can be calculated from the reported crystal-structure data for the isostructural ASST [1], by the use of Vegard's law [17]. Finally

$$\bar{b}_l(R_0) = b_l^m/[\sum_i (R_0/R_i)^n\, K_l^m(\theta_i, \varphi_i)]\,. \tag{5.3}$$

The intrinsic parameter $\bar{b}_2$ and value of t_2 can now be determined, following the procedure described by Misra et al. [15], to be

$$\bar{b}_2 = -4.85\,\text{GHz} \quad \text{and} \quad t_2 = 9.5 \pm 1.0\,.$$

The intrinsic parameter $\bar{b}_2$ calculated here for Gd^{3+} in APST is very close to those calculated for Gd^{3+} in $LiYb_xY_{1-x}F_4$ ($x = 0$ to 1) [14] and RF_3 (R = La, Ce, Pr, Nd) [15]. The t_2 value determined here is close to that found for RF_3 ($t_2 = 9$) [15]. It is to be noted here, in particular, that the sign of the presently-calculated value of $\bar{b}_2$ is negative, the same as those in some other hosts, for which the sign of the resulting b_2^0 has been determined to be positive from relative-intensity data [14, 15] at LHT. This fact supports the present assumption of a positive absolute sign for b_2^0 (Section 4) [16].

As for the value of the intrinsic parameter $\bar{b}_4$ (= 0.020 GHz), it was estimated using only the value of b_4^0 (= −0.0087 GHz), since the use of b_4^m with $m \neq 0$ requires the exact values of φ_i, which are not available. $\bar{b}_4$ was found to increase slowly with the increase in the value of t_4. The corresponding value of t_4 was found to be 27 ± 1, which is much larger than 14, calculated for RF_3 [15] and in the range 5 to 8 for MeF_2 (Me = Cd, Ca, Sr, Pb, Ba) [18]. This value of t_4 for APST was, however, calculated without considering any distortions of the positions of the ligand oxygen ions, which are likely to be caused when a Gd^{3+} ion substitutes for a Pr^{3+} ion, the two ions possessing different ionic radii. In the absence of any knowledge of what these distortions are, some simple distortions were considered in order to see the effect on t_4. For example, rather small but equal increases by $\Delta\theta$ of each of the nine angles θ_i for the oxygen ions, yield the t_4 values to be 15, 11, and

2 for $\Delta\theta$ equal to 1.5°, 2° and 5°, respectively. This means that the same small increase in the values of all θ_i by $\Delta\theta = 1.7°$ yields $t_4 = 14$ which is consistent with those for RF_3 and MeF_2 hosts.

Finally, a small value of b_2^0 is quite plausible, if one realizes that the different angular factors $K_i^m(\theta_i, \varphi_i)$ in (5.1) for various oxygen ligands partially cancel each other for the nine-fold coordinated Gd^{3+} ion in APST. The same considerations should apply to the isostructural Gd^{3+}-doped ANST, ASST, and ACST host crystals.

6. Temperature Variation of EPR Spectra and Phase Transitions

EPR spectra were recorded, for B parallel to the RT Z-axis of one of the magnetically-inequivalent Gd^{3+} ions, in the 4.2 to 410 K temperature range. (Above 410 K the crystal is destroyed due to dehydration.) Fig. 4a and b display, respectively, the temperature variations of the overall splitting and linewidth of EPR spectra.

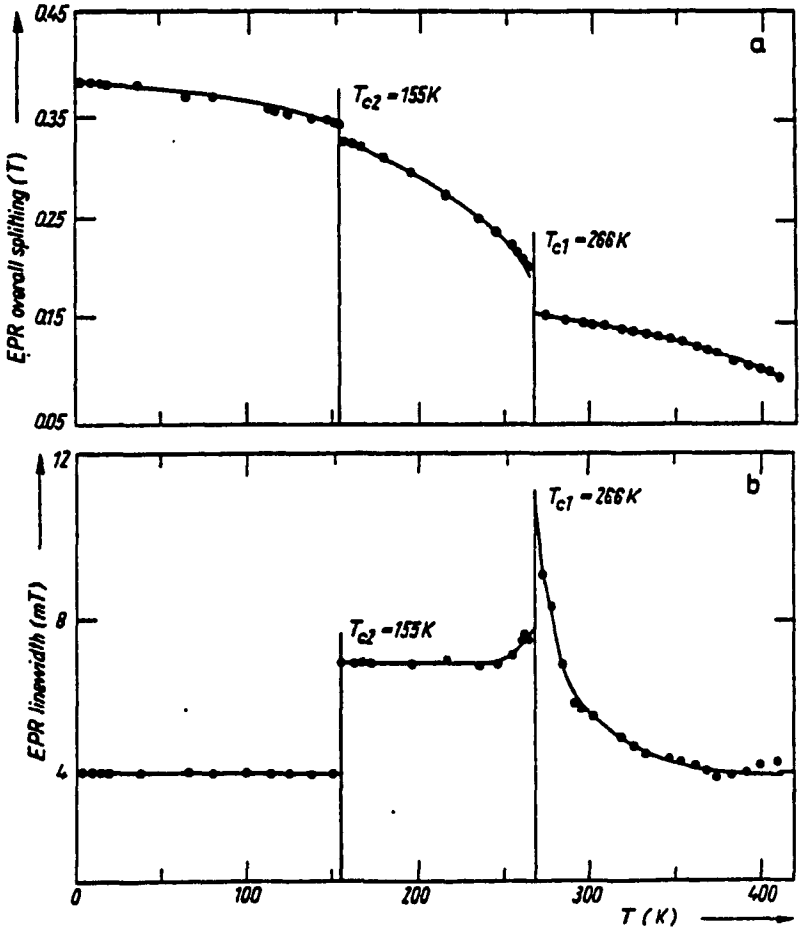

Fig. 4. Temperature variation of a) the overall splittings of the EPR spectra and b) the EPR linewidth for B along the room-temperature Z-axis of one of the magnetically-inequivalent Gd^{3+} ions. The two phase transitions, occurring at $T_{c1} = 266$ K and $T_{c2} = 155$ K, are clearly seen

6.1. EPR spectra above RT

As seen from Fig. 4a and b, the main features of the EPR spectra remain the same at temperatures higher than RT as those at RT. However, at higher temperatures, the overall splitting decreases significantly, implying that the zero-field splitting parameter, b_2^0, decreases as the temperature increases. For example, at 374 K, b_2^0 was estimated to be (0.297 ± 0.002) GHz using the EPR line positions for $B \parallel Z$ and $B \parallel X$, being 14.2% less than the RT value. This behavior is similar to that for Gd^{3+}-doped $LiYb_xY_{1-x}F_4$ ($x = 0$ to 1) crystals [14], where the temperature dependence of b_2^0 has been accounted for by the spin–phonon interaction and thermal expansion. Further, the EPR linewidth decreases as the temperature is increased, indicating a decrease in the spin–lattice relaxation time τ [7].

6.2. EPR spectra and phase transitions below RT

As the temperature was decreased below RT, the overall splitting of the spectrum for $B \parallel Z$ increased, associated with an increase in the linewidths of each of the 14 allowed lines corresponding to the two magnetically-inequivalent Gd^{3+} ions. The linewidths for all the lines were the same at any temperature. At (267 ± 0.5) K, only seven broad lines could be observed. A new spectrum with 14 lines, characterized by a much larger overall splitting, appeared below T_{c1} = (266 ± 0.5) K, indicating that a phase transition had occurred at T_{c1}. Below T_{c1}, the EPR spectra were much better resolved than those observed between RT and 267 K. The Z-axis of one of the magnetically-inequivalent Gd^{3+} ions had about the same orientation as that in the RT phase. However, the Z-axes corresponding to the two magnetically-inequivalent Gd^{3+} ions were no longer perpendicular to each other, as was the case at RT, perhaps due to the disappearance of the inversion plane that existed in the RT phase. No significant change in the spectra was observed in the temperature range 266 to 156 K, except that the overall splitting continued to increase monotonically as the temperature was lowered. At T_{c2} = (155 ± 0.5) K another phase transition occurred, since the spectrum showed a drastic change, as revealed by the appearance of a well-resolved spectrum, with very narrow linewidths, below T_{c2}. The EPR line intensities increased abruptly as the temperature was lowered below T_{c2}; a total of 56 lines corresponding to eight magnetically-inequivalent Gd^{3+} ions were observed. Below T_{c2}, as B was rotated in the ZX plane of the RT phase, eight maxima of overall splitting were observed. Below T_{c2}, the overall splitting of the EPR spectra increased; however, no further drastic changes were found down to 4.2 K.

The abrupt changes of overall splittings and linewidths exhibited in Fig. 4a and b indicate that the two phase transitions, occurring at T_{c1} and T_{c2}, are each of first order.

As the temperature was increased from 4.2 K to RT, all the spectra and the phase transitions as observed with the lowering of temperature were found to repeat themselves, except that T_{c1}, T_{c2} were found to be about 2 K higher than those determined when decreasing the temperature.

6.3. Comparison with previously-reported data on the phase transitions in the other isostructural ASST and ACST crystals

Buckmaster and coworkers [4, 5] reported the occurrence of three phase transitions in the 97 to 304 K temperature range for the ASST and ACST crystals. For the APST crystal, the present EPR study revealed only the existence of two phase transitions in this temperature range with different values of T_{c1} and T_{c2} from those for ASST and ACST. However, the

present results are in agreement with those found by the FTIR and DSC measurements for the APST crystal, which also yielded two transitions although they occurred at lower temperatures, T_{c1} and T_{c2} being 36 and 5 K lower, respectively [6].

7. Discussion

Some conclusions regarding the nature and physical mechanisms of the phase transition, can be made for APST, based on the present and previously-reported EPR data on the isostructural ANST, ACST, and ASST [3 to 5], in conjunction with the crystal structure and IR data on APST. These are described as follows:

(i) Between T_{c1} and T_{c2}, the Z-axes of the two magnetically-inequivalent Gd^{3+} centres were no longer observed to be perpendicular to each other, implying the disappearance of the inversion plane that existed at RT.

(ii) Below T_{c2}, there were observed eight magnetically-inequivalent Gd^{3+} ions, implying the breakdown of the Pr^{3+} pairs that existed above T_{c2}, and the appearance of a doubled unit cell, wherein one of the three unit cell parameters (a, b, c) becomes doubled, forming the so-called "superstructure".

(iii) At temperatures just above T_{c1} (266 K), the broadening of EPR lines is similar to that observed for the Cr^{3+} impurity ion in the $(NH_4)Al(SO_4)_2 \cdot 12\,H_2O$ alum, reported by Owens [19], attributed to the fluctuations in the fine-structure tensor due to the H_2O dipoles. Further, the behaviors of the H_2O molecules and the NH_4^+, SO_4^{2-} ions change at low temperatures, thereby affecting the EPR spectra. As revealed by IR studies [1, 5], the NH_4^+ ions rotate freely in the RT phase, but not below T_{c1}. Below T_{c2}, new bands in the IR spectra, due to the H_2O molecules and the SO_4^{2-} ions, were observed [5], as compared to that at RT.

(iv) The sudden increase in the intensity of the EPR lines below T_{c2} is due to a decrease in the dielectric constant of the sample [20], since a sudden decrease in the leakage current of the microwave power reflected from the EPR cavity was observed upon cooling the sample below T_{c2}.

8. Concluding Remarks

The main results of the present EPR studies on Gd^{3+}-doped APST are as follows:

(i) The orientations of the principal axes for the two magnetically-inequivalent Gd^{3+} ions, as well as the SHP of a monoclinic spin-Hamiltonian for Gd^{3+}, have been determined for Gd^{3+} in APST at RT.

(ii) The superposition model has been satisfactorily exploited to explain the observed small values of b_2^0 in this crystal. Similar application should explain the small observed values of b_2^0 in the isostructural crystals ACST, ASST, and ANST.

(iii) Two first-order phase transitions have been deduced to occur at 266 and 155 K.

Acknowledgements

The authors are grateful to the Natural Sciences and Engineering Research Council of Canada for financial support (grant No. OGP0004485). The facilities of the Concordia University Computer Center were used to evaluate the spin-Hamiltonian parameters.

References

[1] B. ERIKSSON, L. O. LARSSON, L. NIINISTO, and U. SKOGLUND, Inorg. Chem. **13**, 290 (1974).
[2] R. J. CALLOW, The Industrial Chemistry of the Lanthanides: Yttrium, Thorium and Uranium, Pergamon Press, Oxford 1967.
[3] V. M. MALHOTRA, H. D. BIST, and G. C. UPRETI, Chem. Phys. Letters **28**, 390 (1974).
[4] H. A. BUCKMASTER, V. M. MALHOTRA, and H. D. BIST, Canad. J. Phys. **59**, 596 (1981).
[5] V. M. MALHOTRA, H. A. BUCKMASTER and H. D. BIST, Canad. J. Phys. **58**, 1667 (1980).
[6] S. G. JASTY and V. M. MALHOTRA, EPR Symp., Rocky Mountain Conf., Denver (Colorado) 1988.
[7] S. K. MISRA, U. ORHUN, and J. SUN, Solid State Commun., to be published.
[8] S. K. MISRA and C. WANG, Physica (Utrecht) **B159**, 321 (1989).
[9] S. K. MISRA, J. SUN, and S. JERZAK, Phys. Rev. B **40**, 74 (1989).
[10] S. K. MISRA and C. RUDOWICZ, phys. stat. sol. (b) **147**, 677 (1988).
[11] A. ABRAGAM and B. BLEANEY, Electron Paramagnetic Resonance of Transition Ions, Clarendon Press, Oxford 1970.
[12] S. K. MISRA, J. magnetic Resonance **23**, 403 (1976).
[13] S. K. MISRA and S. SUBRAMANIAN, J. Phys. C **15**, 7199 (1982).
[14] L. E. MISIAK, S. K. MISRA, and P. MIKOLAJCZAK, Phys. Rev. B **38**, 8673 (1988).
[15] S. K. MISRA, P. MIKOLAJCZAK, and N. R. LEWIS, Phys. Rev. B **24**, 3729 (1981).
[16] D. J. NEWMAN and W. URBAN, Adv. Phys. **24**, 793 (1975).
[17] L. VEGARD, Z. Krist. **67**, 239 (1928).
[18] J. KURIATA and W. PASTUSIAK, Acta Phys. Polon. **A66**, 627 (1984).
[19] F. J. OWENS, phys. stat. sol. (b) **79**, 623 (1977).
[20] F. J. OWENS, in: Magnetic Resonance and Phase Transitions, Ed. F. J. OWENS, C. P. POOLE, JR., and H. A. FARACH, Academic Press, New York 1979 (p. 303).

(Received April 11, 1990; in revised form August 1, 1990)

Solid State Communications, Vol. 76, No. 7, pp. 949–954, 1990.
Printed in Great Britain.

0038-1098/90 $3.00 + .00
Pergamon Press plc

DETERMINATION OF HOST-ION SPIN-LATTICE RELAXATION TIMES FROM Gd^{3+} EPR LINEWIDTHS IN $NH_4R(SO_4)_2 \cdot 4H_2O$ (R = Pr, Sm, Ce, Nd) SINGLE CRYSTALS

Sushil K. Misra, Ufuk Orhun and Jiansheng Sun*

Physics Department, Concordia University, 1455 de Maisonneuve Blvd. West, Montreal, Quebec, Canada H3G 1M8

(*Received* 15 *June* 1990 *by P. Burlet*)

Spin-lattice relaxation times (τ) for the host rare-earth ions R^{3+} (R = Sm, Ce, Nd) in $NH_4R(SO_4)_2 \cdot 4H_2O$ crystal lattices have been estimated at room-temperature from X-band EPR linewidths of Gd^{3+} impurity ion, using an appropriate expression based on the second moment for crystals consisting of two different kinds of paramagnetic spins. In addition, the τ values for Pr^{3+} ions in $NH_4Pr(SO_4)_2 \cdot 4H_2O$ lattice have been estimated in the 266–410 K temperature range from EPR linewidths of the impurity ion Gd^{3+}. The values of τ for Pr^{3+} indicate that τ^{-1} varies as T^7 (T = temperature) in the 266–296 K range, and as T^2 in the range 296–410 K. It is concluded that the T^7 behaviour is predominantly due to the sum process, while the T^2 behaviour is predominantly due to the Raman process.

1. INTRODUCTION

$NH_4R(SO_4)_2 \cdot 4H_2O$ (R = rare-earth) compounds, forming a series of isostructural crystals [1], are interesting because they exhibit multiple phase transitions below room-temperature (RT) as revealed by EPR, infrared [2–5], and differential scanning calorimetry (DSC) [6] studies. As for EPR, temperature variation of EPR linewidth (ΔB) of the impurity ion, e.g. Gd^{3+}, in these host crystals, being sensitive to temperature variation of the host crystal lattices [7], has been exploited to study phase transitions.

The impurity ion linewidths can also be used to estimate spin-lattice relaxation times (τ) of the host paramagnetic ions [8]. For the $NH_4R(SO_4)_2 \cdot 6H_2O$ hosts, characterized by R = Sm, Ce and Nd, estimates of spin-lattice relaxation times have been reported by Malhotra *et al.* [2] and by Buckmaster *et al.* [3], using Gd^{3+} EPR linewidths. However, in their calculations, they employed a frequently-used erroneous expression, applicable to the presence of only one kind of magnetic spin in the system, valid only for a simple cubic lattice [9]. Misra and Orhun [8] derived the correct expression for τ, for the presence of two different kinds of magnetic spins in the system, typical of the EPR situation wherein the host ions are paramagnetic. The purpose of the present paper is to estimate τ of the host ions R^{3+} in the $NH_4R(SO_4)_2 \cdot 4H_2O$ crystals, for R = Sm, Ce, Nd at room temperature, and for R = Pr in the temperature range 266–296 K, by the use of the correct expression [8], employing experimentally observed Gd^{3+} impurity-ion EPR linewidths. The power-law temperature dependence of the values of τ for Pr^{3+} will be used to discern the spin-lattice relaxation processes governing the host Pr^{3+} ions in the $NH_4Pr(SO_4)_2 \cdot 4H_2O$ lattice. To this end, the X-band data of Misra and Sun [4] for Gd^{3+} EPR linewidths in the $NH_4Pr(SO_4)_2 \cdot 4H_2O$ crystal will be used.

2. CRYSTAL STRUCTURE

$NH_4R(SO_4)_2 \cdot 4H_2O$ crystals are monoclinic, characterized by the space group C_{2h}^5, containing four formula units per unit cell [1]. The unit-cell parameters for crystals, where R = Nd, Ce, Sm and Pr, are listed in Table 1. In the absence of reported experimental data for the positions of the four R^{3+} ions in the unit cell, required to estimate the spin-lattice relaxation time (τ) of the host ions, the R^{3+} positions have been presently deduced, using the information provided in the literature [1, 3] to be (0.5, 0.1321, 0.0), (0.5, 0.3677, 0.5), (0.5, 0.6323, 0.5) and (0.5, 0.8678, 0.0), as shown in Fig. 1; they are labeled as 1, 2, 3 and 4, respectively. The R^{3+} ions 1 and 2 form a pair, being related by symmetry to the other pair, formed by the ions 3 and 4, through an inversion plane.

* On leave of absence from the Center of Materials Analysis, Nanjing University, Nanjing, Jiangsu, The People's Republic of China.

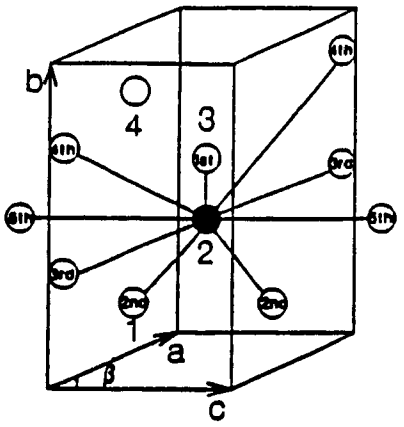

Fig. 1. Positions of the four R^{3+} ions in the unit cell of the $NH_4R(SO_4)_2 \cdot 4H_2O$ hosts. They are marked as 1, 2, 3 and 4, respectively. The positions of the nine R^{3+} ions (one 1st, two 2nd, two 3rd, two 4th and two 5th nearest neighbors) surrounding the impurity Gd^{3+} ion, substituting for the R^{3+} ion 2, are also exhibited. Similar considerations apply when the Gd^{3+} ion replaces any one of the R^{3+} ions 1, 3 or 4.

3. ESTIMATE OF τ

3.1. Theoretical expression

τ of the host paramagnetic ions in doped crystals can be estimated from impurity ion EPR linewidth (ΔB), using the expression [8]

$$\tau = (3\Delta B g^2 \mu_B)/(110 h g' \langle \Delta\nu^2 \rangle). \quad (1)$$

where μ_B, h, g, and g' are respectively Bohr's magneton, Planck's constant, the impurity-ion Lande's factor, and the host-ion Lande's factor. In equation (1) $\langle \Delta\nu^2 \rangle$ is the second moment for the impurity ion. Misra and Orhun [8] showed that $\langle \Delta\nu^2 \rangle$ for crystals containing two different species of magnetic ions, for the case when the distances between the impurity ions are sufficiently large, and when the number of host-ion neighbors considered is limited to N, can be expressed as [8]

$$\langle \Delta\nu^2 \rangle = \tfrac{1}{5} S'(S'+1)\hbar^2 \left[N J_p^2 + (gg')^2 \mu_B^4 \mu_0^4 \times \sum_k^N (1 - 3\gamma_{jk}^2)^2 r_{jk}^{-6} + 2 J_p g g' \mu_B^2 \mu_0^2 \sum_k^N (1 - 3\gamma_{jk}^2) r_{jk}^{-3} \right]. \quad (2)$$

In equation (2) S', J_p, μ_0, r_{jk}, and γ_{jk} are the effective spin of the host-ion, the average impurity-host ion-pair exchange constant, the permeability constant, the distance between j and k' ions and the direction cosines of r_{jk} with the external Zeeman field, respectively. (The primed quantities refer to the host ions while the unprimed ones to the impurity ions.)

3.2. Numerical estimates

In order to compute τ, using equations (1) and (2), one first needs to know the values of the various quantities appearing therein. A computer programme was used to generate the various $NH_4R(SO_4)_2 \cdot 4H_2O$ (R = Nd, Ce, Sm, and Pr) lattices required to calculate the distances r_{jk} and the corresponding direction cosines (γ_{jk}) of the external field. For the calculation of the second moment, $\langle \Delta\nu^2 \rangle$, using equation (2), it was found sufficient to consider only up to the fifth-nearest neighbors ($N = 9$), the contributions of the farther-lying neighbors were found to be negligible. Table 2 lists the calculated distances for these neighbors of an impurity Gd^{3+} ion, while their positions are shown in Fig. 1. As for the values of S', g' and J_p, the following considerations were made. The effective spin of each of the Kramer's ions Ce^{3+}, Nd^{3+}, and Sm^{3+}, as well as that of the non-Kramer's ion Pr^{3+}, is $S' = 1/2$ [7, 10]. ($S' = 1/2$ for Pr^{3+} is true for the case of lower symmetry, being equivalent to the presence of local distortions superimposed on higher symmetry due to Jahn–Teller effect). Further, for Pr^{3+}, $g'_z = 2\langle \xi_n | S'_z | \xi_n \rangle$, where $|\xi_n\rangle$ is one of the time-conjugate states for the ground state of Pr^{3+}, and $g'_x = 0$ [7]. No experimental g' values have been reported for the host

Table 1. Unit-cell parameters of $NH_4R(SO_4)_2 \cdot 4H_2O$ single crystals (R = Nd, Ce, Sm and Pr) [1]

R	a(Å)	b(Å)	c(Å)	β
Nd	6.625	18.928	8.789	97.06°
Ce	6.676	19.005	8.821	97.28°
Sm	6.582	18.886	8.736	96.88°
Pr	6.644	18.963	8.798	97.18°

Table 2. Distances (in Å) between Gd^{3+} and the neighbor R^{3+} ions. There are one 1st-, two 2nd-, two 3rd-, two 4th- and two 5th-nearest neighbors (nn)

R	1st *nn*	2nd *nn*	3rd *nn*	4th *nn*	5th *nn*
Pr	5.02	6.27	6.44	8.17	8.80
Sm	5.00	6.24	6.58	8.26	8.74
Nd	5.01	6.26	6.62	8.31	8.79
Ce	5.03	6.28	6.68	8.36	8.82

ions in the presently considered crystals. However, the coordinations around a R^{3+} ion in $NH_4R(SO_4)_2 \cdot 4H_2O$ lattice are the same as that of a R^{3+} ion in the $Y(C_2H_5SO_4)_3 \cdot 9H_2O$ lattice, so that the g' values for R^{3+} ions in the two lattices are about the same [12]. A theoretical calculation yields $g'_\parallel = 3.81$, $g'_\perp = 0.20$ for Ce^{3+} in $Y(C_2H_5SO_4)_3 \cdot 9H_2O$ [11]. Similarly, one has for the Pr^{3+}, Nd^{3+} and Sm^{3+} ions $(g'_\parallel, g'_\perp) =$ (1.6, 0.0), (3.65, 1.98), and (0.73, 0.40), respectively [12, 13]. In the numerical estimates made presently for τ, the direction of the external field has been assumed to be along the principal Z magnetic axis, i.e. the principal axis of the b_2^0 tensor, of the Gd^{3+} ion [2–4]; the Z axis for the Gd^{3+} ion in $NH_4Pr(SO_4)_2 \cdot 4H_2O$ has been determined by Misra and Sun [4] to be along the 4-fold axis of a distorted-monocapped-square antiprism, making approximately the angles (51°, 45°, 72°) relative to the (a, b, c) axes. However, the principal magnetic axes (Z') for the host R^{3+} ions are not necessarily parallel to the respective principal Z axes of the impurity Gd^{3+} ion. In this case, the averages of $g'_\parallel$ and $g'_\perp$ values, listed in Table 3, for the host ions were chosen for g' in equations (1) and (2) for estimating τ. This does not lead to any significant error in the calculated values of τ, because of some uncertainty in other factors. The required g values of the Gd^{3+} ion have been reported previously [2–5], and are listed in Table 3. As for the values of J_p, they have not been determined experimentally for the Gd^{3+}–Nd^{3+}, Gd^{3+}–Pr^{3+}, Gd^{3+}–Sm^{3+}, and Gd^{3+}–Ce^{3+} pairs. The present calculations of τ have been made for $J_p = 0.1$, 1.0, 5.0, 10.0 GHz values, which cover the possible range of values.

The room-temperature τ values for Sm^{3+}, Ce^{3+}, and Nd^{3+} were estimated from equations (1) and (2), using the reported experimental Gd^{3+} EPR linewidths in the $NH_4R(SO_4)_2 \cdot 4H_2O$, R = Sm, Ce, and Nd hosts [2, 3, 5]. As for the estimate of τ for the Pr^{3+} ion, the Gd^{3+} EPR linewidths, as reported by Misra and Sun [4], in the 266–410 K temperature range, in the $NH_4Pr(SO_4)_2 \cdot 4H_2O$ host, were used. No estimates were made for τ for Pr^{3+} in $NH_4Pr(SO_4)_2 \cdot 4H_2O$ host crystal at temperature above 410 K, or below 266 K, because of the unavailability of ΔB values. This is because below 266 K the crystal underwent a phase transition, while above 410 K the crystal deteriorated due to dehydration [4].

The τ values estimated at room temperature for Sm^{3+}, Ce^{3+}, Pr^{3+} and Nd^{3+}, are listed in Table 3, along with the previously reported values of τ by Malhotra *et al.* [2] and Buckmaster *et al.* [3], estimated using the incorrect expression, for comparison purposes.

As for Pr^{3+}, Fig. 2 exhibits the log–log plot of τ^{-1} vs. temperature in the 266–410 K range for $J_p = 5$ GHz; the calculated τ values being listed in Table 4 along with the required experimental linewidths at different temperatures.

3.3. *Discussion of τ values*

As seen from Table 3, the τ values for Sm^{3+}, Ce^{3+}, Pr^{3+} and Nd^{3+}, computed using the correct expression, equation (1), for various values of J_p, are quite different, by up to an order of 3, from those calculated using the incorrect expression. The large differences arise because of the inclusion of dipolar interactions, along with exchange interactions, between two different kinds of ions (host and impurity) in $\langle \Delta v^2 \rangle$,

Table 3. Calculated room-temperature spin-lattice relaxation times (τ) for Sm^{3+}, Ce^{3+}, Nd^{3+} and Pr^{3+} ions in $NH_4R(SO_4)_2 \cdot 4H_2O$ lattices. The values of S', g, g', J_p, and the impurity-ion (Gd^{3+}) linewidth (ΔB), used in the present calculations, are also listed. τ values are expressed in seconds, while the figures inside the round brackets following τ are J_p values in GHz

R	Sm	Nd	Pr	Ce
S'	1/2	1/2	1/2	1/2
g	1.9922	1.9830	1.9949	1.9930
g'	0.57	2.82	0.80	2.01
ΔB (Gs)	44	64	53	51
τ (0.1)[a]	3.09×10^{-11}	3.76×10^{-11}	1.35×10^{-11}	8.54×10^{-13}
τ (1.0)[a]	5.04×10^{-12}	3.45×10^{-11}	3.95×10^{-12}	6.70×10^{-13}
τ (5.0)[a]	2.12×10^{-13}	5.91×10^{-14}	1.84×10^{-13}	6.95×10^{-14}
τ (10.0)[a]	5.26×10^{-14}	1.56×10^{-14}	4.55×10^{-14}	1.76×10^{-14}
τ[b]	2.10×10^{-10}	2.10×10^{-12}	-	1.00×10^{-11}

[a]Calculated presently.
[b]Reported in [2] and [3].

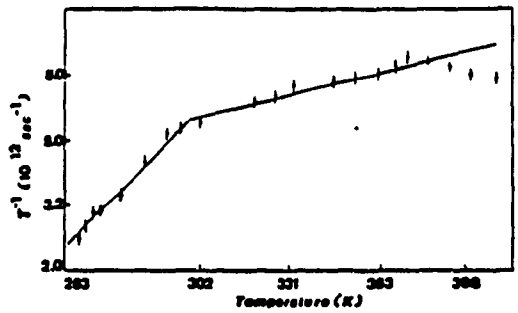

Fig. 2. A log-log plot of the inverse of spin-lattice relation time (τ^{-1}) versus the temperature (T), in the 266–410 K range, for the host paramagnetic ion Pr^{3+} in the $NH_4Pr(SO_4)_2 \cdot 4H_2O$ crystal for J_p = 5.0 GHz. (The values of the slopes do not change for different values of J_p, as seen from equations (1) and (2).)

given by equation (2). It is also seen from Table 3, for Pr^{3+} and Sm^{3+} ions, that their τ values fluctuate by three orders of magnitude, while this fluctuation is only by one order of magnitude for Nd^{3+} and Ce^{3+} ions, for J_p values ranging from 0.1 to 10 GHz. However, as seen from equations (1) and (2), the T power-law dependence of τ^{-1}, which enables one to discern the spin-lattice relaxation process in effect, is independent of a particular J_p value. For Pr^{3+} host ions in $NH_4Pr(SO_4)_2 \cdot 4H_2O$, a T^7 dependence of τ is found in the temperature range 266–296 K, while a T^2 dependence in the temperature interval 296–410 K.

4. SPIN-LATTICE RELAXATION MECHANISM FOR Pr^{3+} IN $NH_4Pr(SO_4)_2 \cdot 4H_2O$

A least-squares fitting of τ to temperature indicates that the τ values of Pr^{3+} in $NH_4Pr(SO_4)_2 \cdot 4H_2O$, as calculated presently for J_p = 5.0 GHz, can be fitted well to $\tau = BT^{-7}$ with $B = 3.79 \times 10^{4}$ s. K^{7} in the temperature range 266–296 K, and to $\tau = CT^{-2}$ with $C = 1.61 \times 10^{-4}$ s. K^{2} in the temperature range 296–410 K. It is now possible, from these T^7 and T^2 temperature dependences of τ^{-1}, to deduce as to which mechanisms are responsible for SLR in the two temperature regions. Surveys of the various SLR mechanisms have been provided by Abragam and Bleaney [7], and by Shrivastava [14].

As for the T^7 dependence of τ^{-1} for a non-Kramers ion, such as Pr^{3+}, it is caused by the following processes: (i) at *low* temperature, by Raman processes, specifically Raman spin-one phonon interaction in second order, Raman spin-two-phonon interaction, and Raman process effected by short wave-length phonons. (ii) At *low* temperatures, by a process involving three phonons, described by Le Naour [15], in which first the small wave-vector approximation is used to obtain a transition from an upper level E_b to another upper level E_c by the emission of two phonons, and integration is made over all the phonons from 0 to Δ_c ($= E_c - E_a$, where E_a is the ground state). This is followed by the calculation of a Raman process using phonons from Δ_c to Debye cutoff, thus making full use of the Debye spectrum. (iii) At *intermediate* temperatures, by the "sum" process [16, 17], in which a spin transition is achieved by means of emission or absorption of two phonons; the range of temperature being centered at about 0.14 Δ_c [17], depending very sensitively on the structure of levels in the host crystal [16, 17]. From the temperature ranges over which the processes (i), (ii) and (iii) are applicable, it appears that the presently-observed T^7 behaviour of τ^{-1} in the range 266–296 K may be explained to be due predominantly to the sum process, since this tempera-

Table 4. The calculated spin-lattice relaxation times (τ) of the Pr^{3+} ion and the observed Gd^{3+} EPR linewidths (ΔB) in the $NH_4Pr(SO_4)_2 \cdot 6H_2O$ host at various temperatures (T) for J_p = 5 GHz. The error for ΔB is ± 3 Gs

T (K)	ΔB (Gs)	τ (s)	T (K)	ΔB (Gs)	τ (s)
266	116	4.03×10^{-11}	333	39	1.35×10^{-12}
269	106	3.68×10^{-11}	347	38	1.32×10^{-12}
271	96	3.33×10^{-11}	354	37	1.28×10^{-12}
273	95	3.30×10^{-11}	362	36	1.25×10^{-12}
278	85	2.95×10^{-11}	369	34	1.18×10^{-12}
285	67	2.33×10^{-11}	374	32	1.11×10^{-12}
292	55	1.91×10^{-11}	383	33	1.15×10^{-12}
296	53	1.84×10^{-11}	392	34	1.18×10^{-12}
303	51	1.77×10^{-11}	400	36	1.25×10^{-12}
319	44	1.53×10^{-11}	410	37	1.28×10^{-12}
326	42	1.46×10^{-11}			

ture range is more appropriately "intermediate", rather than "low".

As for the T^2 behavior of τ^{-1} in the range 296–410 K, it can be explained to be due to any one of the various Raman processes, described above, as well as due to the sum process, all of which predict T^2 dependence of τ^{-1} at high temperatures. However, the sum process has *negligible* contribution compared to that of the usual Raman process, particularly because in the sum process only the lowest-energy phonons are required, whose number diminishes considerably at *high* temperatures: in addition, the value of the integral required in the expression for τ^{-1} for the sum process becomes quite small at elevated temperatures [16, 17]. To explain further, at elevated temperatures, the number of phonons for which $\omega_1 - \omega_2 = \omega$, required for the usual Raman process, is extemely large compared to that for which $\omega_1 + \omega_2 = \omega$ required for the sum process. (Here $\hbar\omega$ is the difference in the two levels of the spin system and ω_1, ω_2 are the frequencies of the phonons involved in the Raman, or sum, processes.) This is because the energy density of phonons depends on temperature as $x^2/(e^x - 1)$, where $x = \hbar\omega/k_B T$, which tends to zero as T approaches zero; or infinity, from an intermediate value [7]. Thus, the number of phonons required for the sum process, which come from the lowest part of the phonon spectrum because $\omega = \omega_1 + \omega_2$, is negligible at high temperatures, while the number of phonons required for the Raman process is large, because they can belong to any part of the phonon spectrum, including those belonging to the highest phonon density, as long as $\omega = \omega_1 - \omega_2$. Thus, the Raman process is the predominant mechanism for SLR of host Pr^{3+} ions in $NH_4Pr(SO_4)_2 \cdot 4H_2O$ in the 296–410 K temperature range.

Finally, as seen from Fig. 2, the τ^{-1} values for Pr^{3+} in $NH_4Pr(SO_4)_2 \cdot 4H_2O$ exhibit a sudden transition from T^7 to T^2 behavior at 296 K as the temperature is increased. If only one of the above-mentioned processes, which is capable of exhibiting both T^7 and T^2 dependence of τ^{-1} as one goes from low to high temperature, were operative over the entire temperature range 266–410 K, a gradual, and not sudden, transition from the T^7 to T^2 behavior for τ^{-1} would be observed. The sudden transition of the T dependence of τ^{-1} is, most likely, due to the *simultaneous* presence of a number of competing SLR mechanisms which are in force at the transition temperature 296 K, depending on the Pr^{3+} energy levels in a complex manner. Such a sudden transition, from T^{n1} to T^{n2} behaviour of τ^{-1}, is in conformity with the various experimental data exhibited in [7] and [14].

5. CONCLUDING REMARKS

The main results of the present numerical computations of τ are as follows:

(i) The correct expression, equations (1) and (2), yields much shorter τ values for the host R^{3+} ions in the $NH_4R(SO_4)_2 \cdot 4H_2O$ crystals, where R = Ce, Nd and Sm, than those estimated using the incorrect expression.

(ii) The power-law dependence on temperature of τ^{-1} values of the Pr^{3+} ion, which is independent of J_z, suggests the dominance of the sum relaxation process in $NH_4Pr(SO_4)_2 \cdot 4H_2O$ crystal in the temperature range 266–296 K (T^7 dependence of τ^{-1}), and that of the Raman process in the 296–410 K range (T^2 dependence of τ^{-1}). For $NH_4R(SO_4)_2 \cdot 4H_2O$ (R = Sm, Ce and Nd) Malhotra *et al.* [2] and Buckmaster *et al.* [3] predicted an Orbach process. However, this conclusion was only guessed by comparison with other systems and not arrived at by a study of temperature variation of τ, as only room-temperature values of τ were estimated.

Acknowledgement – The authors are grateful to the Natural Sciences and Engineering Research Council of Canada for partial financial support (grant No. OGP0004485).

REFERENCES

1. E. Eriksson, L.O. Larsson, L. Niinisto & U. Skoglund, *Inorg. Chem.* **13**, 290 (1974).
2. V.M. Malhotra, H.A. Buckmaster & H.D. Bist, *Can. J. Phys.* **58**, 1667 (1980).
3. H.A. Buckmaster, V.M. Malhotra & H.D. Bist, *Can. J. Phys.* **59**, 596 (1981).
4. S.K. Misra & J. Sun, *Phys. Status Solidi (b)*, to be published.
5. V.M. Malhotra, H.D. Bist & G.C. Upreti, *Chem. Phys. Lett.* **28**, 390 (1974).
6. S.G. Jasty & V.M. Malhotra, *EPR Symposium, Rocky Mountain Conference*, 1988.
7. A. Abragam & B. Bleaney, *Electron Paramagnetic Resonance of Transition Ions*, Clarendon, Oxford (1970).
8. S.K. Misra & U. Orhun, *Phys. Rev.* **B39**, 2856 (1989).
9. P.W. Anderson & P.R. Weiss, *Rev. Mod. Phys.* **25**, 269 (1953).
10. S.A. Al'tshuler & B.M. Kozyrev, *Electron Paramagnetic Resonance*, Academic Press, New York (1964).
11. G.H. Larson & C.D. Jeffries, *Phys. Rev.* **141**, 461 (1966).
12. S.A. Al'tshuler & B.M. Kozyrev, *Electron Paramagnetic Resonance in Compounds of Transition Elements*, Keter, Jerusalem (1974).

13. W.T. Gray IV & H.J. Stapleton, *Phys. Rev.* **B9**, 2863 (1974).
14. K.N. Shrivastava, *Phys. Status Solidi (b)* **117**, 437 (1983).
15. R. Le Naour, *Phys. Rev.* **B1**, 2007 (1970).
16. K.N. Shrivastava, *Phys. Status Solidi* **42**, K177 (1970).
17. K.N. Shrivastava, *Phys. Status Solidi (b)* **92**, K19 (1979).

APPENDIX II

COMPUTER PROGRAMS

This appendix contains the computer programmes for the evaluation of (i) the values of $g_{\|}$, $g_{\perp}$, b_{ℓ}^{m}, A and B for the Mn^{2+} ion from the hyperfine line positions (programme MN), (ii) the values of g_x, g_y, g_z and b_{ℓ}^{m} of the Gd^{3+} ion from the fine-structure line positions (programme GD), (iii) the principal values and direction cosines of the $\tilde{g}^2$ and $\tilde{A}^2$ tensors of the VO^{2+} ion from the hyperfine line positions (programme VO), and (iv) the principal values and direction cosines of the $\tilde{g}^2$ and $\tilde{A}^2$ tensors of the Cu^{2+} ion from the hyperfine line positions (programme CU).

The four programs have similar structures. Each contains a main program which inputs (i) the experimental data, e.g., EPR line positions as required for different orientations of $\vec{B}$ and the microwave frequency; (ii) the initial values of the spin-Hamiltonian parameters as required in the least-squares fitting procedure. The main program calls the subroutine CURFIT, which in return calls the subroutines FUNC, EXAM, MATINV and JACOBI. The subroutines CURFIT and FUNC are the key parts of each program, apart from the main programme. The subroutine CURFIT does the least-squares fitting, utilizing the procedure described in Chapter IV, using the energy levels corresponding to the various resonant-field values, as calculated in the subroutine FUNC. The other subroutines are

used to handle the calculations involving the various matrices: subroutine JACOBI is used to diagolize the spin-Hamiltonian matrix in order to find its eigenvalues and eigenvectors (direction cosines), while the subroutine MATINV is used to invert a matrix.

The programmes VO and CU are almost the same, except for a little difference in the respective subroutines FUNC due to the difference in the nuclear spin (I) for the VO^{2+} and Cu^{2+} ions. The main program of each programme calls the subroutine EULER, which calculates the Euler angles required to rotate the laboratory axes to coincide with principal axes of the $\tilde{g}^2$ tensor. The subroutines JACOBI3 and JACOBI4 are used in the programmes VO and CU to diagolize the matrices of different dimensions.

The programmes MN and GD are similar to each other; the difference lies in the subroutine FUNC due to the different electronic spins, 5/2 and 7/2 for Mn^{2+} and Gd^{3+} ions, respectively. In addition the Mn^{2+} ion is characterized by the nuclear spin 5/2. The subroutines EXAM and MATINV in these two programmes are almost the same as those in the programmes VO and CU, except for differences in the matrix dimensions. For the diagolization of the matrices, instead of JACOBI3 and JACOBI4, the library-subroutines EIGRS, HTRIDI and HTRIBK are used, from the computation-package IMSLIB4 and EISPACK. Therefore, when executing the programmes MN and GD on the computer, one has

to use appropriate commands to avail the usage of these library-subroutines.

Full programme listing for the evaluation of spin-Hamiltonian parameters of the VO^{2+} ion (programme VO) is listed. While for those of Mn^{2+}, Gd^{3+} and Cu^{2+} ions (programmes MN, GD and CU), respectively, in order to avoid repetitions of listings, only the main programs, the subroutines CURFIT and FUNC, and the beginning parts of the other subroutines, indicating the dimensions of the matrices, are listed. The subroutines in the programs for the Mn^{2+}, Gd^{3+} and Cu^{2+} ions are very similar to those listed for the VO^{2+} ion, except for the possible differences in the dimensions of the matrices required. One can reconstruct the subroutines, other than the subroutines CURFIT and FUNC, for programmes MN, GD and CU from those for programme VO, by appropriately changing the beginning part of respective subroutines.

```
      PROGRAM MN (INPUT,OUTPUT,TAPE5=INPUT,TAPE6=OUTPUT)
C     NO = THE NO. OF FIRST MAG FIELD IN DATA INCLUDED IN
C          FITTING
C     M  = NO. OF PARAMETERS
C     L4 = NO. OF ITERATIONS ALLOWED
C     Q1 = MIN. VALUE OF SUM OF SQUARES FOR FITS (CHI-SQUARE
C          TOLERANCE)
C     Z(I) = MAGNETIC FIELD VALUES FOR FITS
C     B  = PARAMETER MATRIX
C     N  = NO. OF  DATA POINTS USED IN LEAST-SQARES FITTING
C     Q1 = N/10
C     Q2 = TOLERANCE ON GRAD(CHI**2) = APPROX .01
C     FM(I) = MEASURED VALUES
C     FC(I) = CALCULATED VALUES
C     ERR(I) = STANDARD DEVIATION ON FM(I) = SQRT(FM(I))
C     ENTER THETA IN DEGREES
C     DIMENSIONS OF Q,V IN JACOBI1 SHOULD  BE  THE  SAME  AS
C     THOSE OF B3,B2 RESPECTIVELY IN CURFIT
C     NUMBER = INDEX THAT CHANGES WITH EACH NEW CASE
C     NCASES = NO. OF CASES CONSIDERED. ITS VALUE SHOULD  BE
C              ENTERED.
C      IBB(II,1)  AND  IBB(II,2)  INDICATE  THE  EIGENVALUES
C      INVOLVED IN RESONANCE FOR THE NO. II MAG FIELD VALUE
C      B = G = GPARRALEL,  GPERPENDICULAR,  B20,  B22,  B40,
C              B42, B44, A, B.
      DIMENSION Z(350), FM(350), FC(350), DF(350), ERR(350),
     1B(12), B1(12), B2(12,12), DC(5000), ABC(2), Y(4),
     2ZZ(350,4), G(12,20), THETA(350), GG(12,4),
     3IBB(350,2), DELHH(350,4), DELH(350)
      DIMENSION TEETA(350,4), FREQ(20), FACTOR(20),  NN(20),
     1HN(20), Z1(350,4), ADD(20), Z2(350), IAB(30,2),
     2ICC(30,2), DDF(350,4), SMDD(4), JJII(10,2),
     3IA1(350,4), IA2(350,4), SSS(350)
      COMMON/DATA1/ABC,Y
```

```
 COMMON/DATA2/DC
 COMMON/DATA3/DELH
 EQUIVALENCE (Z,DC), (FM,DC(501)), (FC,DC(1001)),
1(DF,DC(1501)), (ERR,DC(2001)), (B,DC(2989)),
2(B1,DC(3013)), (B2,DC(3025)), (N,DC(3169)),
3(L4,DC(3170)), (Q1,DC(3171)), (Q2,DC(3172)),
4(M,DC(3173)), (SSMD,DC(3178)),  (IBB,DC(4000)),
5(THETA,DC(3500)), (I,DC(3174)), (L,DC(3175)),
6(BO,DC(3176)), (SMD,DC(3177)), (HN,DC(3179)),
7(NUMBER,DC(4999))
 DATA(ABC=2HNO,3HYES),(Y=1H ,1HC,1H*,1HM)
 DATA(ZZ(J,1),J=1,204)/
1 28.5,41.,54.,66.,78.5,91.5,103.5,116.,128.5,141.,
2 154.,167.,248.,260.5,274.,287.5,301.,315.5,322.5,
4 335.,348.,363.,377.5,392.5,29.,41.5,54.5,66.5,79.,
5 91.5,103.5,116.,128.5,141.,154.167.,248.5,261.,
6 274.5,287.5,301.5,316.,321.5,334.5,347.5,362.5,
7 377.,392.,31.,43.5,56.,69.,81.5,94.,105.5,117.5,
8 130.,142.5,155.5,168.5,248.,260.5,274.,287.,301.,
9 315.,317.,330.,343.,358.,372.5,388.,35.,48.,60.5,73.,
1 85.5,98.5,109.,121.,133.,145.5,158.5,171.5,245.5,
2 258.5,271.5,285.,298.5,312., 307.,320.,333.5,347.5,
3 362.5,378.,42.,54.,67.,79.5,92.,105.,114.,125.5,138.,
8 150.5,163.5,176.,348.,363.5,61.,74.,86.5,99.5,112.5,
9 125.5,130.,140.5,153.,165.,177.,190.,236.5, 249.,
1 260.5,274.,287.,300.,253.,266.5,280.,294.5,309.5,
2 330.,104.5,118.5,132.,146.5,159.,172.,218.,231.5,
3 244.,257.,270.5,284.,88.,101.5,115.5,129.5,144.5,
4 158.5,217.,268.,279.,292.,305.,319.,83.,96.,110.,
5 124.,138.5,154.,128.,140.5,154.,167.5, 244.,257.,
6 271.,284.5,80.5,94.,108.,122.,136.,324.5,338.,80.,
7 93.,107.,121.,135.5,151.,125.,138.,151.5,275.5,
2 287.,299.5,312.,325.5, 340./
 DATA(TEETA(J,1),J=1,204)/
1 24*0.,24*2.0,24*4.0,24*6.0,24*8.0,24*10.0,
```

```
     2 12*82.,12*84.,12*86.,12*88.,12*90./
      DATA(G(J,1),J=1,9)/
     1 2*2.,.7,-.2,.001,-.02,-.035,-.26,-.26/
C     HERE ONE DEFINES THE QUANTUM NUMBERS FOR VARIOUS LINES
      DATA(IAB(J,1),J=1,30)/
     130,29,28,27,26,25,24,23,22,21,20,19,13,14,15,16,17,18,
     27,8,9,10,11,12,1,2,3,4,5,6/
      DATA(IAB(J,2),J=1,30)/
     136,35,34,33,32,31,30,29,28,27,26,25,24,23,22,21,20,19,
     213,14,15,16,17,18,7,8,9,10,11,12/
      DATA(ICC(J,1),J=1,30)/
     1 1,2,3,4,5,6,7,8,9,10,11,12,13,14,15,16,17,18,
     2 24,23,22,21,20,19,30,29,28,27,26,25/
      DATA(ICC(J,2),J=1,30)/
     1 7,8,9,10,11,12,13,14,15,16,17,18,24,23,22,21,20,19,
     2 30,29,28,27,26,25,36,35,34,33,32,31/
C      JJII(,1),(,2) TELL GROUPS OF 30 LINES WHICH ARE
C       BETWEEN 0 AND 25 DEG. AND BETWEEN 75 AND 90 DEG.
C       RESPECTTIVELY.
      DATA(JJII(J,1),J=1,3)/6,6,7/
      DATA(JJII(J,2),J=1,3)/5,5,4/
      DATA(FREQ(J),J=1,3)/9.412,9.435,9.447/
      DATA(FACTOR(J),J=1,3)/6.8004,6.7537,12.205/
      DATA(ADD(J),J=1,3)/281.1490,223.5594,115.088/
      DATA(NN(J),J=1,3)/204,330,330/
      DO 331 JJ=1,3
      NNJJ=NN(JJ)
      DO 331 J=1,NNJJ
      DELHH(J,JJ)=FACTOR(JJ)*2
  331 CONTINUE
      NZERO=1
      NUMBER=NZERO
      NCASES=2
    1 CONTINUE
C*****DEFINE HERE QUANTUM NOS. FOR VARIOUS LINES
```

```
C      FACTOR CONVERTS MMS ON GRAPH TO GAUSS
  188 FORMAT(1H1)
    8 FORMAT(1X,4HQ1 = ,E13.5,5X,4HQ2 = ,E13.5)
  137 FORMAT (3X,I2,5X,E16.6/)
  136 FORMAT(10X,19H INITIAL
     1PARAMETERS//3X,1HJ,10X,4HB(J)//)
  135 FORMAT(1X,11H PARAMETERS//
     13X,1HJ,10X,4HB(J),27X,6HERRORS//)
    9 FORMAT(2X,4H HN= ,F9.4)
  140 FORMAT(3X,I2,5X,E16.6,15X,E16.6/)
  138 FORMAT(5X,14H CASE NUMBER =,I2//)
  141 FORMAT(10X,6H SMD =,E13.5//)
  235 FORMAT (15X,5(E13.5,8X)/)
  144 FORMAT(2X,*LINE NUMBER*,2X,*LINE POSITION*,2X,*ANGLE*,
     1 2X,*LINE NUMBER*,2X,*LINE POSITION*,2X,*ANGLE*,/)
  145 FORMAT(3X,I3,6X,F10.1,6X,F8.2,3X,I3,6X,F10.1,6X,F8.2)
      M=11
      MM=M
      L4=1
      Q1=1.E-8
      Q2=1.E-40
C      BO CONVERTS GAUSS TO GHZ
      BO=92.732/(6.6252*10000.)
      IG=1
  958 CONTINUE
      WRITE (6,188)
      N=NN(NUMBER)
      HN(NUMBER)=FREQ(NUMBER)
      N1=N
C     THE FOLLOWING FOR MEASURING MAGNETIC  FIELD  FROM  THE
C     GRAPH WITH A LINEAR FACTOR
      DO 16 IJK=1,N1
      THETA(IJK)=TEETA(IJK,NUMBER)
      Z1(IJK,NUMBER)=(ZZ(IJK,NUMBER)+ADD(NUMBER))*
     1FACTOR(NUMBER)
```

```
      IF (ZZ(IJK,NUMBER).EQ.(0.)) Z1(IJK,NUMBER)=0.
C     FOLLOWING PUTS SELECTED LINES EQUAL TO 0
      THI=THETA(IJK)
      IF (THI.LT.(0.)) Z1(IJK,NUMBER)=0.
      IF (THI.GT.(90.)) Z1(IJK,NUMBER)=0.
   16 CONTINUE
      DO 806 IJK=1,N1
      IF (THETA(IJK).GT.(25.)) GO TO807
      JYJ=JJII(NUMBER,1)
      DO 340 II=1,30
      DO 340 JJ=1,JYJ
      JJ1=(JJ-1)
      IIJJ=II+JJ1*30
      IBB(IIJJ,1)=IAB(II,1)
      IA1(IIJJ,NUMBER)=IBB(IIJJ,1)
      IBB(IIJJ,2)=IAB(II,2)
      IA2(IIJJ,NUMBER)=IBB(IIJJ,2)
  340 CONTINUE
      GO TO 342
  807 CONTINUE
      JXJ=JJII(NUMBER,2)
      DO343 II=1,30
      DO 343 JJ=1,JXJ
      JJ1=(JJ-1)
      IIJJ=II+JJ1*30+JJII(NUMBER,1)*30
      IBB(IIJJ,1)=ICC(II,1)
      IA1(IIJJ,NUMBER)=IBB(IIJJ,1)
      IBB(IIJJ,2)=ICC(II,2)
      IA2(IIJJ,NUMBER)=IBB(IIJJ,2)
  343 CONTINUE
  342 CONTINUE
  806 CONTINUE
      DO 210 LL=1,MM
  210 B(LL)=G(LL,NUMBER)
      WRITE (6,138) NUMBER
```

```
      WRITE (6,136)
      WRITE (6,137) (J,B(J),J=1,M)
      DO 3 IJK = 1,N1
      DELH(IJK)=DELHH(IJK,NUMBER)
    3 Z(IJK) = Z1(IJK,NUMBER)
      IF (NUMBER.NE.1) GO TO 20
   21 CONTINUE
      IF(NUMBER.NE.3) GO TO 22
   22 CONTINUE
      WRITE(6,144)
      DO 146 IJK=1,N1
  146 IF(Z(IJK).NE.(0.)) WRITE (6,145) IJK,Z(IJK),THETA(IJK)
      IF(Z(IJK).NE.0.)WRITE(7,145)IJK,Z(IJK),THETA(IJK)
      WRITE(6,8)Q1,Q2
      WRITE(6,9) HN(NUMBER)
      DO 201 II=1,N1
  201 FM(II)=HN(NUMBER)
      CALL CURFIT
      DO 202 II=1,N1
  202 DDF(II,NUMBER)=DF(II)
      SMDD(NUMBER) = SSMD
      WRITE(6,188)
      WRITE(6,135)
      DO 220 LL=1,M
  220 GG(LL,NUMBER) = B(LL)
      WRITE(6,140)(J,B(J),B1(J),J=1,M)
      WRITE(6,188)
      NUMBER = NUMBER + 1
      IF ( NUMBER - NCASES) 1,1,2
    2 CONTINUE
      DO 230 LL=NZERO,NCASES
      N=NN(LL)
      IF (LL.GT.NZERO) WRITE(6,188)
      WRITE (6,138) LL
      WRITE (6,141) SMDD(LL)
```

```
      WRITE(6,302)
  302 FORMAT(5X,* IDENTIFICATION OF LINES*)
      DO 300 II=1,N
      IF(Z1(II,LL))563,562,563
  563 CONTINUE
  562 CONTINUE
  300 CONTINUE
      WRITE(6,301)((II,IA1(II,LL),IA2(II,LL)),II=1,N)
      WRITE (6,658)
  658 FORMAT(//)
C      SSS1 IS SMD(1),THAT IS WHEN ALL(LINES)SIGMA=1
      SSS1=0.
      NEFF=0
      DO 555 ID=1,N
      IF(ZZ(ID,LL))561,560,561
  561 CONTINUE
      NEFF=NEFF+1
      SSS(ID)=DDF(ID,LL)**2
      SSS1=SSS(ID)+SSS1
  560 CONTINUE
  555  CONTINUE
      WRITE(6,656)((ID,SSS(ID)),ID=1,N)
      ANEFF=FLOAT(NEFF)
      SSSAV5=SSS1*5./ANEFF
      WRITE(6,658)
      WRITE (6,657)SSS1,SSSAV5
  657 FORMAT (10X,*SMD(1)=*,E13.5,5X,*SSSAV5=*,E13.5,//)
  656 FORMAT(2X,*LINE NO.=*,I3,3X,*SMD=*,E13.5,2X,*LINE
     1NO.=*,I3,3X,*SMD=*,E13.5)
  301 FORMAT(2X,*FIELD NO.=*,I3,3X,*E-VAL1=*,I3,3X,
     1*E-VAL2=*,I3,2X,*FIELD
     2NO.=*,I3,3X,*E-VAL1=*,I3,3X,*E-VAL2=*,I3)
  230 WRITE (6,235) (GG(LM,LL),LM=1,11)
  708 CONTINUE
      STOP
```

```
      END

      SUBROUTINE CURFIT
C     EXAM HANDLES ALL MATRICES OF DIMENSIONS UPTO THE
C     DIMS.MM OF A,B,C THAT IS M IS LESS THAN OR EQUAL TO MM
C     (SAME IS TRUE OF MATINV AND JACOBI)
C      IN EQUIVALENCEGRAD SHOULD BE PLACED IMMEDIATELY AFTER
C       B SINCE IN FUNC B(12,2)=BB(12),GRAD(12) IN CURFIT
C     DIMENSION OF B3 SHOULD BE M*(M+1)/2
      DIMENSION Z(350),FM(350),FC(350),DF(350),
     1ERR(350),B(12),B1(12), B2(12,12),B4(12,12),HN(10),
     2DC(5000),ABC(2),Y(4),X(350),GRAD(12),D1(12),
     3D2(12,12),B3(66),IBB(350,2),THETA(350)
      COMMON/DATA1/ABC,Y
      COMMON/DATA2/DC
      EQUIVALENCE (Z,DC),(FM,DC(501)),(FC,DC(1001)),
     1(DF,DC(1501)),(ERR,DC(2001)),(B,DC(2989)),
     2(GRAD,DC(3001)),(B1,DC(3013)),(B2,DC(3025)),
     3(N,DC(3169)),(L4,DC(3170)),(Q1,DC(3171)),
     4(Q2,DC(3172)),(M,DC(3173)),(I,DC(3174)),
     6(L,DC(3175)),(D1,DC(2501)),(D2,DC(2513)),
     7(BO,DC(3176)),(SMD,DC(3177)),(SSMD,DC(3178)),
     9(IBB,DC(4000)),(THETA,DC(3500)),(HN,DC(3179)),
     1(S,DC(2901)),(SA,DC(2902)),(BMOD,DC(2903)),
     2(PROD,DC(2904)),
     3(GMOD,DC(2905)),(LE,DC(2906)),(LLX,DC(4998))
      DATA(ABC=2HNO,3HYES),(Y=1H ,1HC,1H*,1HM)
      MM=M
      NN=N
      L1 = 0
      SA = 0.0
C      SA1 IS SA WITH SIGMA (ALL LINES)=1.
      SA1=0.
      DO 1000 J=1,MM
      B1(J)=0.0
```

```
      DO 1000 K=1,MM
 1000 B2(J,K)=0.0
      WRITE(6,901)
C      LLX=0 ALLOWS WRITING E.VALUES IN FUNC
      LLX=0
      DO 100 II = 1, NN
      I=II
      L=1
      CALL FUNC(2)
      X(II)=ERR(II)**2
 901  FORMAT(5X,10H FUNC2,210  )
      DF(II) =FM(II) - FC(II)
      DO 101 J=1,MM
      B1(J)=B1(J)-(2.0*DF(II)*D1(J))/X(II)
      DO 101 K=1,MM
  101 B2(J,K)=
     1B2(J,K)-(2.0*(DF(II)*D2(J,K)-D1(J)*D1(K)))/X(II)
      SA1=SA1+DF(II)**2
  100 SA = SA + DF(II)**2/X(II)
C      LLX=1 OMITS WRITING E.VALUES IN FUNC
      LLX=1
C      EQZERO TELLS IF ELEMENTS OF B2,B1 ARE ZERO
      CALL EQZERO(B2,B1,M,IC1,IC2,IC3)
      WRITE(6,901)
      LM=1
      WRITE(6,5)CPU,LM
    5 FORMAT(5X,*CPU=*,F8.2,*LM=*,I2)
      GMOD=0.0
      DO 102 J=1,M
  102 GMOD=GMOD+B1(J)**2
      WRITE(6,243)SA,GMOD
  243 FORMAT (1X,26H*INITIAL VALUE SUM OF
     1SQ.=E13.5,20X,17H*SQ MOD OF GRAD =E13.5)
      WRITE(6,244) SA1
  244 FORMAT(5X,*INITIAL VALUE SUM OF SQ.(ALL SIGMA
```

```
     1 =1)=*,E13.5,//)
       WRITE(6,1751)
 1751 FORMAT(14H0 DERIVATIVES-)
       WRITE(6,240)(B1(J),J=1,M)
  240 FORMAT (15X,5(E13.5,8X)/)
       LLJJ=0
C***** FOLLOWING FOR CALCULATING INITIAL VALUES ONLY
C       LLJJ=1
       IF(LLJJ.NE.0) GOTO 559
       IF (SA - Q1) 110, 110, 200
  110 LE = 1
       GO TO 600
  200 S = 0.0
       GMOD = 0.0
       BMOD = 0.0
       PROD = 0.0
       A2=ABC(1)
       DO 210 J = 1, MM
       B1(J) = 0.0
       DO 210 K = 1, MM
  210 B2(J,K) = 0.0
       WRITE(6,902)
       DO 220 II = 1, NN
       I=II
       L=1
       CALL FUNC(2)
       X(II)=ERR(II)**2
 902   FORMAT(5X,10H FUNC2,210  )
       DF(II) = FM(II) - FC(II)
       DO 220 J = 1, MM
       B1(J) = B1(J) - (2.0*DF(II)*D1(J))/X(II)
       DO 220 K = 1, MM
  220 B2(J,K) = B2(J,K) - (2.0*(DF(II)*D2(J,K)
      1-D1(J)*D1(K)))/X(II)
       CALL EQZERO(B2,B1,M,IC1,IC2,IC3)
```

```
      WRITE(6,902)
      LM=2
      WRITE(6,5)CPU,LM
       DO 230 J = 1, MM
  230 GRAD(J) = B1(J)
      L1 = L1 + 1
      WRITE(6,903)
      CALL EXAM (B2,B1,M,LF)
      WRITE(6,903)
  903 FORMAT(5X,9H EXAM,230  )
      IF (LF)  250, 250, 305
  250 DO 231 II=1,M
      DO 231 JJ=1,II
      KK=II*(II-1)/2+JJ
  231 B3(KK)=B2(II,JJ)
      WRITE(6,904)
      CALL EIGRS(B3,M,1,B1,B2,M,B4,NR)
      IF(NR.EQ.0) GO TO 387
      WRITE(6,386)NR
  386 FORMAT(5X,*NR=*,2X,I5)
  387 CONTINUE
      WRITE(6,904)
  904 FORMAT(5X,12H EIGRS,231  )
      WRITE(6,240)B1
      DO 389 I5=1,MM
      AB1=ABS(B1(I5))
      IF((AB1).GT.(1.E-10)) GO TO 388
      B1(I5)=0.
  388 CONTINUE
  389 CONTINUE
      I4=5
      IF (I4.EQ.1) GO TO 912
      A2=ABC(2)
      DO 260 J = 1, MM
  260 D1(J) = 0.0
```

```
      DO 270 J = 1, MM
      DO 270 K = 1, MM
  270 D1(K) = D1(K) + B2(J,K) *GRAD(J)
      DO 275 J = 1, MM
      IF (B1(J))  280, 290, 285
  280 B1(J) = - B1(J)
  285 D1(J) = D1(J)/B1(J)
      GO TO 275
  290 D1(J) = 0.0
  275 CONTINUE
      DO 295 J = 1, MM
  295 B1(J) = 0.0
      DO 300 J = 1, MM
      DO 300 K = 1, MM
  300 B1(J) = B1(J) + B2(J,K)*D1(K)
  305 DO 310 J=1,MM
      GMOD = GMOD + GRAD(J)**2
      BMOD = BMOD + B1(J)**2
  310 PROD = PROD + GRAD(J)*B1(J)
      IF (GMOD - Q2)  315, 315, 320
  315 LE = 2
      WRITE(6,1761) GMOD
 1761 FORMAT(5X,7H GMOD =,E13.5//)
      GO TO 600
  320 C=PROD/SQRT(BMOD*GMOD)
      IF (C) 335, 335, 400
  335 LE = 4
      GO TO 600
  400 LD = 0
      L3 = 0
      DO 410 J = 1, MM
  410 GRAD(J) = B(J) - B1(J)
      WRITE(6,905)
  450 DO 420 II = 1, NN
      I=II
```

```
      L=2
      CALL FUNC(1)
      X(II)=ERR(II)**2
  905 FORMAT(5X,10H FUNC1,450  )
      DF(II) = FM(II) - FC(II)
  420 S = S + DF(II)**2/X(II)
      LM=3
      WRITE(6,5)CPU,LM
      WRITE(6,905)
      IF (SA - S) 435, 500, 500
  435 LD = LD + 1
      WRITE(6,906)
  430 DO440 J = 1, MM
      B1(J) = B1(J)/2.0
  906 FORMAT(5X,16H BINARY CHOP,430  )
  440 GRAD(J) = B(J) - B1(J)
      WRITE(6,906)
      S = 0.0
      L3 = L3 + 1
      IF(L3-3)450,460,460
  460 LE = 5
      GO TO 600
  500 IF (LD) 505, 505, 506
  506 LD = 0
      GO TO 430
  505 DO 510 J = 1, MM
  510 B(J) = GRAD(J)
      SA = S
      IF (SA - Q1) 507, 507, 530
  507 LE = 1
      GO TO 600
  530 IF (L4) 200, 200, 900
  900 WRITE(6,920)L1,A2,L3,S,GMOD,(B(J),J=1,M)
  920 FORMAT(//,15H ITERATION NO.=I5,10X,43H
     1TRANSFORMATION MADE TO PRINCIPAL AXES = A4,10X,   18H
```

```
     2BINARY CHOP USED=I3,6H TIMES/1X,27H WEIGHTED SUM OF
     3SQUARES = E14.7,25X,32H   SQUARE MODULUS OF GRADIENT =
     4E14.7/20H   PARAMETERS B(J) -/(6E17.8)/)
      IF (L1 - L4) 200, 910, 910
  910 LE = 6
      GO TO 600
  600 DO 710 J=1,MM
      B1(J) = 0.0
      DO 710 K=1,MM
  710 B2(J,K) = 0.0
      L=1
  907 FORMAT(5X,*FUNC(2) AT 720*,/)
C*****FOLLOWING FOR INITIAL VALUES ONLY
  559 CONTINUE
      WRITE(6,907)
      DO 720 II = 1, NN
      I=II
      CALL FUNC(2)
      X(II)=ERR(II)**2
      DF(II) = FM(II) - FC(II)
      DO 720 J = 1, MM
      B1(J) = B1(J) - (2.0*DF(II)*D1(J))/X(II)
      DO 720 K = 1, MM
  720 B2(J,K) = B2(J,K) - ((DF(II)*D2(J,K)
     1-D1(J)*D1(K)))/X(II)
      CALL EQZERO(B2,B1,M,IC1,IC2,IC3)
      LM=4
      WRITE(6,5)CPU,LM
      WRITE (6,3029)
 3029 FORMAT(* I AM LOST IN MATINV*)
 3030 FORMAT(*   I AM OUT OF MATINV*)
      CALL MATINV(B2,M,B1,1,DETERM)
      WRITE (6,3030)
      DO 730 J=1,MM
      IF (B2(J,J)) 2001,2002,2002
```

```
2001  B1(J) = -SQRT(-B2(J,J))
      GO TO 730
2002  B1(J)= SQRT(B2(J,J))
  730 CONTINUE
      DO 740 J=1,MM
      DO 740 K=1,MM
  740 B2(J,K)=B2(J,K)/(B1(J)*B1(K))
      WRITE(6,551)LE,SA
  551 FORMAT(//,13H EXIT NUMBER=I3,20X,25H WEIGHTED SUM OF
     1SQUARES=E15.8//)
      SSMD = SA
  912 CONTINUE
      RETURN
      END

      SUBROUTINE FUNC(LX)
C     SUBROUTINE FUNC
      DIMENSION SZ(6,6),SX(6,6),S20(6,6),S40(6,6),
     1S42(6,6),SU(6,6),AR(6,6),SY(6,6),S22(6,6),
     2SPX(6),S44(6,6),HN(10)
      DIMENSION DC(5000),B(12,2),D1(12),D2(12,12),
     1FC(350),Z(350),SIGN(350),SP(8,12),IBB(350,2),
     2THETA(350),W(36),ZR(36,36),SR(36,36),SI(36,36),
     3CC(36,36),A(666),ERR(350),DELH(350)
      COMMON/DATA2/DC
      COMMON/DATA3/DELH
      EQUIVALENCE (Z,DC),(B,DC(2989)),(D1,DC(2501)),
     1(D2,DC(2513)),(M,DC(3173)),(L,DC(3175)),
     2(I,DC(3174)),(BO,DC(3176)),(HN,DC(3179)),
     3(IBB,DC(4000)),(THETA,DC(3500)),(FC,DC(1001)),
     4(LLX,DC(4998)),(NUMBER,DC(4999)),(ERR,DC(2001))
C B(I,L) ARE THE LITTLE B(I,L) AS IN THE SPIN HAMILTONIAN
C  FOR RELATION TO CAP.B(I,L) SEE ABRAGAM AND BLEANEY
      DATA(SP(J,1),J=1,6)/2.5,1.5,.5,-.5,-1.5,-2.5/
      DATA(SPX(J),J=1,6)/10.,-2.,-8.,-8.,-2.,10./
```

```
      DATA(SP(J,5),J=1,6)/1.,-3.,2.,2.,-3.,1./
C    ****TO BE REMOVED LATER
      DO 91 JIJ=1,6
   91 SP(JIJ,3)=SPX(JIJ)/3.
      R2=SQRT(2.0)
      R3=SQRT(3.0)
      R5=SQRT(5.0)
      R7=SQRT(7.0)
      R10=SQRT(10.0)
      SP(1,4)=R10/3.
      SP(2,4)=R2
      SP(3,4)=R2
      SP(4,4)=R10/3.
      SP(1,6)=3.*R10/20.
      SP(2,6)=-5.*R2/20.
      SP(3,6)=-5.*R2/20.
      SP(4,6)=3.*R10/20.
      SP(1,7)=1./R5
      SP(2,7)=1./R5
      SP(1,2)=R5/2.
      SP(2,2)=R2
      SP(3,2)=1.5
      SP(4,2)=R2
      SP(5,2)=R5/2.
      IF (Z(I)) 18,21,18
   18 CONTINUE
C          PBBZ,  PBBX,  PBBY  ARE  COEFFS.  MULTIPLYING  S(Z),
C  S(X),S(Y) SPIN COMPONENTS
      DO 500 IX=1,6
      DO 500 JX=1,6
      SZ(IX,JX) = 0.
      SX(IX,JX) = 0.
      SY(IX,JX) = 0.
      S20(IX,JX) = 0.
      S22(IX,JX) = 0.
```

```
      S40(IX,JX) = 0.
      S42(IX,JX)=0.
      S44(IX,JX) = 0.
      AR(IX,JX) = 0.
      SU(IX,JX) = 0.
  500 CONTINUE
      DO 605 IX=1,36
      W(IX) = 0.
      DO 605 JX=1,36
      SR(IX,JX)=0.
      ZR(IX,JX)=0.
      SI(IX,JX)=0.
  605 CC(IX,JX)=0.
      DO 505 IX=1,6
      SZ(IX,IX) = SP(IX,1)
      S20(IX,IX) = SP(IX,3)
      S40(IX,IX) = SP(IX,5)
      SU(IX,IX) = 1.
  505 CONTINUE
      DO 510 IX=1,4
      IX2 = IX + 2
      S22(IX,IX2) = SP(IX,4)
      S22(IX2,IX) = SP(IX,4)
  510 CONTINUE
      DO 515 IX=1,5
      IX1=IX+1
      SX(IX,IX1) = SP(IX,2)
      SX(IX1,IX) = SP(IX,2)
  515 CONTINUE
      S42(1,3)=9.*R10/60.
      S42(2,4)=-15.*R2/60.
      S42(3,5)=S42(2,4)
      S42(4,6)=S42(1,3)
      S42(3,1)=S42(1,3)
      S42(4,2)=S42(2,4)
```

```
      S42(5,3)=S42(3,5)
      S42(6,4)=S42(4,6)
      S44(1,5)=12.*R5/60.
      S44(2,6)=S44(1,5)
      S44(5,1)=S44(1,5)
      S44(6,2)=S44(2,6)
      TH = THETA(I)*3.14159264/180.
      CSTH =(COS(TH))
      SNTH =(SIN(TH))
      PBBZ = B(1,L)*BO*Z(I)*CSTH
C***  NEXT TWO LINES CHANGE FROM GXX INDEPENDENT TO GXX=GZZ
      PBBX = B(2,L)*BO*Z(I)*SNTH
C      PBBX=B(1,L)*BO*Z(I)*SNTH
      PBBY = 1.
      AR(1,1)=2.5*PBBZ+10.*B(3,L)/3.+B(5,L)
      AR(2,2)=1.5*PBBZ-2.*B(3,L)/3.-3.*B(5,L)
      AR(3,3)=.5*PBBZ-8.*B(3,L)/3.+2.*B(5,L)
      AR(4,4)=AR(3,3)-PBBZ
      AR(5,5)=AR(2,2)-3.*PBBZ
      AR(6,6)=AR(1,1)-5.*PBBZ
      AR(1,3)=B(4,L)*R10/3.+B(6,L)*9.*R10/60.
      AR(2,4)=B(4,L)*3.*R2/3.-B(6,L)*15.*R2/60.
      AR(3,5)=AR(2,4)
      AR(4,6)=AR(1,3)
      AR(3,1)=AR(1,3)
      AR(4,2)=AR(2,4)
      AR(5,3)=AR(3,5)
      AR(6,4)=AR(4,6)
      AR(1,5)=B(7,L)*R5*12./60.
      AR(2,6)=AR(1,5)
      AR(5,1)=AR(1,5)
      AR(6,2)=AR(2,6)
      AR(1,2)=R5*PBBX/2.
      AR(2,1)=AR(1,2)
      AR(2,3)=R2*PBBX
```

```
      AR(3,2)=AR(2,3)
      AR(3,4)=1.5*PBBX
      AR(4,3)=AR(3,4)
      AR(4,5)=R2*PBBX
      AR(5,4)=AR(4,5)
      AR(5,6)=R5*PBBX/2.
      AR(6,5)=AR(5,6)
      SY(1,2)=-R5*PBBY/2.
      SY(2,1)=-SY(1,2)
      SY(2,3)=-R2*PBBY
      SY(3,2)=-SY(2,3)
      SY(3,4)=-1.5*PBBY
      SY(4,3)=-SY(3,4)
      SY(4,5)=-R2*PBBY
      SY(5,4)=-SY(4,5)
      SY(5,6)=-R5*PBBY/2.
      SY(6,5)=-SY(5,6)
      DO 520 IY=1,6
      DO 520 JY =1,6
      DO 520 IZ=1,6
      DO 520 JZ=1,6
      IX=(IY-1)*6+IZ
      JX=(JY-1)*6+JZ
      SR(IX,JX)=AR(IY,JY)*SU(IZ,JZ)+
     1 SU(IY,JY)*(S20(IZ,JZ)*B(8,L)+S22(IZ,JZ)*B(9,L))+
     2B(10,L)*SZ(IY,JY)*SZ(IZ,JZ)+B(11,L)*(SX(IY,JY)*
     3SX(IZ,JZ -SY(IY,JY)*SY(IZ,JZ))
520   CONTINUE
      DO 999 II=1,36
      DO 999 JJ=1,II
      KK=II*(II-1)/2 + JJ
999   A(KK)=SR(II,JJ)
      CALL EIGRS(A,36,1,W,ZR,36,SI,IER)
      IF(IER)997,996,997
997   CONTINUE
```

```
      WRITE (6,998) IER
  996 CONTINUE
  998 FORMAT(5X,*IER=*,I3)
C     ** TO BE REMOVED LATER(LLX IS DEFINED IN FUNC)
      IF(LLX)992,993,992
  993 CONTINUE
      WRITE(6,995)I
  995 FORMAT(5X,*I=*,I3)
      WRITE(6,994)W
  994 FORMAT(2X,6E12.4)
  992 CONTINUE
C DEFINE HERE THE LINES WHOSE QUANTUM NOS. NOT DEFINED ABOVE
      I6=I
      IF(NUMBER.NE.1) GO TO 1814
      I1=IBB(I6,1) $ I2=IBB(I6,2)
      GO TO 803
 1814 CONTINUE
      IF(NUMBER.NE.2) GO TO 815
      I1=IBB(I6,1) $ I2=IBB(I6,2)
      GO TO 803
  815 CONTINUE
      IF(NUMBER.NE.3) GO TO 816
      I1=IBB(I6,1) $ I2=IBB(I6,2)
      GO TO 803
  816 CONTINUE
      IF (NUMBER.NE.4) GO TO 817
      I1=IBB(I6,1) $ I2=IBB(I6,2)
      GO TO 803
  817 CONTINUE
C  DEFINE ABOVE THE LINES WHOSE QUANTUM NOS. NOT DEFINED
C ABOVE
  802 CONTINUE
      I1=1
      I2=2
      DELMIN=ABS(ABS(W(1)-W(2))-HN(NUMBER))
```

```
      DO 85 IX=1,35
      IX1=IX+1
      DO 81 JX=IX1,36
      DELI=ABS(ABS(W(IX)-W(JX))-HN(NUMBER))
      IF(DELI-DELMIN)84,84,86
   84 DELMIN=DELI
      I1=IX
      I2=JX
      IBB(I,1)=I1
      IBB(I,2)=I2
   86 CONTINUE
   81 CONTINUE
   85 CONTINUE
  803 CONTINUE
      FC(I)=ABS(W(I1)-W(I2))
      SIGN(I)=(W(I1)-W(I2))/FC(I)
      DO 301 IY=1,6
      DO 301 JY=1,6
      DO 301 IZ=1,6
      DO 301 JZ=1,6
      IX=(IY-1)*6+IZ
      JX=(JY-1)*6+JZ
      CC(IX,JX)=BO*DELH(I)*(B(1,L)*CSTH*SZ(IY,JY)*SU(IZ,JZ)+
     1 B(2,L)*SNTH*SX(IY,JY)*SU(IZ,JZ))
  301 CONTINUE
      ERR(I)=0.
      DO 814 IX=1,36
      DO 814JX=1,36
      ERR(I)=ERR(I)+CC(IX,JX)*(ZR(JX,I1)*ZR(IX,I1)
     1 -ZR(JX,I2)*ZR(IX,I2))
  814 CONTINUE
      GO TO 17
   21 CONTINUE
      FC(I)=HN(NUMBER)
      ERR(I)=1.
```

```
      SIGN(I) =1.
   17 CONTINUE
      IF(LX-1)110,110,120
  120 CONTINUE
      DO 235 IZ=1,12
      D1(IZ) = 0.0
      DO 235 JZ=1,12
  235 D2(IZ,JZ) =0.0
      IF (Z(I)) 418,217,418
  418 CONTINUE
      DO 237 KX=1,11
      DO 236 IY=1,6
      DO 236 JY=1,6
      DO 236 IZ=1,6
      DO 236 JZ=1,6
      IX=(IY-1)*6 + IZ
      JX=(JY-1)*6 + JZ
      GO TO (705,706,707,708,709,710,711,712,713,714,715),KX
  705 CC(IX,JX)=SZ(IY,JY)*SU(IZ,JZ)
      ALPHA=BO*Z(I)*CSTH
      GO TO 720
  706 CC(IX,JX)=SX(IY,JY)*SU(IZ,JZ)
      ALPHA=BO*Z(I)*SNTH
      GO TO 720
  707 CC(IX,JX)=S20(IY,JY)*SU(IZ,JZ)
      ALPHA=1.
      GO TO 720
  709 CC(IX,JX)=S40(IY,JY)*SU(IZ,JZ)
      ALPHA=1.
      GO TO 720
  714 CC(IX,JX)=SZ(IY,JY)*SZ(IZ,JZ)
      ALPHA=1.
      GO TO 720
  712 CC(IX,JX)=SU(IY,JY)*S20(IZ,JZ)
      ALPHA=1.
```

```
      GO TO 720
  710 CC(IX,JX)=S42(IY,JY)*SU(IZ,JZ)
      ALPHA=1.
      GO TO 720
  711 CC(IX,JX)=S44(IY,JY)*SU(IZ,JZ)
      ALPHA=1.
      GO TO 720
  708 CC(IX,JX)=S22(IY,JY)*SU(IZ,JZ)
      ALPHA=1.
      GO TO 720
  713 CC(IX,JX)=SU(IY,JY)*S22(IZ,JZ)
      ALPHA=1.
      GO TO 720
  715 CC(IX,JX)=SX(IY,JY)*SX(IZ,JZ)
     2 -SY(IY,JY)*SY(IZ,JZ)
      ALPHA=1.
  720 CONTINUE
      SR(JX,IX)=(ZR(JX,I1)*ZR(IX,I1)-ZR(JX,I2)*ZR(IX,I2))*
     1 SIGN(I)
C FOLLOWING TWO LINES CHANGE FROM GXX INDEPENDENT TO GXX=GZZ
      KX1=KX
C      IF(KX.EQ.2) KX1=1
  236 D1(KX1)=D1(KX1)+CC(IX,JX)*SR(JX,IX)*ALPHA
C      FOLLOWING LINE CHANGES GXX INDEP. TO GXX=GZZ
C      D1(2)=0.
  237 CONTINUE
  217 CONTINUE
  110 CONTINUE
      RETURN
      END


      SUBROUTINE EXAM(A,B,M,LF)
C     SUBROUTINE EXAM
      DIMENSION A(12,12),B(12),C(12)
```

```
      SUBROUTINE MATINV(A,N,B,M,DETERM)
C     SUBROUTINE MATINV
C     MATRIX INVERSION WITH ACCOMPANYING SOLUTION OF  LINEAR
C     EQUATIONS
      DIMENSION IPIVOT(12),A(12,12),B(12,1),
     1INDEX(12,2),PIVOT(12)
      EQUIVALENCE (IROW,JROW),(ICOLUM,JCOLUM),(AMAX,T,SWAP)

      SUBROUTINE EQZERO(A,B,M,IC1,IC2,IC3)
      DIMENSION A(12,12),B(12)
      IC1=0
      IC2=0
      IC3=0
      DO 5 J3=1,M
      IF((ABS(B(J3))).GT.(1.E-20)) GO TO 10
      B(J3)=0.
      IC1=J3
      WRITE(6,100) IC1
   10 CONTINUE
      DO 5 J4=1,M
      IF((ABS(A(J3,J4))).GT.(1.E-10)) GO TO 15
      A(J3,J4)=0.
      IC2=J3
      IC3=J4
      WRITE(6,101) IC2,IC3
   15 CONTINUE
    5 CONTINUE
  100 FORMAT(5X, I3)
  101 FORMAT(5X,2I3)
      RETURN
      END
```

```
      PROGRAM GD(INPUT,OUTPUT=121B,TAPE5=INPUT,TAPE6=OUTPUT)
C     ANGLES IN XY PLANE ARE ENTERED TO BE  BETWEEN  -1  AND
C     -360 DEG. (0 DEG.= -360 DEG.)
C     NO =THE NO. OF FIRST MAG FIELD  IN  DATA  INCLUDED  IN
C     FITTING
C     M  =NO. OF PARAMETERS
C     L4 =NO. OF ITERATIONS ALLOWED
C     Q1 =MIN. VALUE OF SUM OF SQUARES FOR FITS (CHI-SQUARE
C         TOLERANCE)
C     Z(I) = MAGNETIC FIELD VALUES FOR FITS
C     B = PARAMETER MATRIX
C     B=GZZ,B20,B22,B2-2,(OR B21,OR B2-1),B40,B42,B44,B4-2
C     (OR B41,OR B4-1),B4-4 (OR B43, OR
C     B4-3),GXX,GYY,GXY(ORGZX,OR GZY),
C         B60,B62,B64,B66,B6-2,B6-4,B6-6.
C     N  =NO. OF  DATA POINTS USED IN LEAST-SQARES FITTING
C     Q1 =N/10
C     Q2 =TOLERANCE ON GRAD(CHI**2) =APPROX .01
C     FM(I) = MEASURED VALUES
C     FC(I) = CALCULATED VALUES
C     ERR(I)= STANDARD DEVIATION ON FM(I) = SQRT(FM(I))
C      DIMENSIONS OF A,B  IN  EXAM  AND  MATINV  SUBROUTINES
C      SHOULD BE THE SAME AS THOSE OF B2,B1 RESPECTIVELY  IN
C      THE MAIN PROOGRAM AND IN CURFIT
C      DIMENSIONS OF Q,V IN JACOBI1 SHOULD  BE  THE  SAME AS
C     THOSE OF B3,B2 RESPECTIVELY IN CURFIT
C     NUMBER=INDEX THAT CHANGES WITH EACH NEW CASE
C     NCASES=NO. OF CASES CONSIDERED. ITS  VALUE  SHOULD  BE
C     ENTERED.
C     NN(J)=NO. OF LINES IN ZX PLANE FOR JTH CASE
C     NM(J)=NO. OF LINES IN XY PLANE FOR JTH CASE
C     NMAG(2,20),FOR 20 CASES,REPRESENTS A NUMBER THAT TELLS
C     WHETHER THE MAG.FIELD DATA IS RECORDED  IN  KHZ,MM  OR
C     GAUSS (FOR N= 0,2,4 RESPECIVELY)
```

```
 DIMENSION Z(400),FM(400),FC(400),DF(400),ERR(400),
1B(16),B1(16),B2(16,16),DC(4500),ABC(2),
3Y(4),THETA(400),HN(400),ZZ(325,10),HHDPPH(325,10),
4NN(25), GG(16,10),SMD(10),IBB(400,2),
3SSMD(400),TEETA(325,10),G(16,10),ADD(2,20),NMAG(2,20)
 DIMENSION FREQ(2,20),FACTOR(2,20),NM(25),N11(25)
 COMMON/DATA1/ABC,Y
 COMMON/DATA2/DC
 COMMON/DATA3/NN,NM
 EQUIVALENCE(Z,DC),(FM,DC(801)),(DF,DC(401)),
1(FC,DC(1201)),(ERR,DC(1601)),(THETA,DC(2001)),
1(HN,DC(2401)),(B,DC(4000)),(B2,DC(4049)),
2(N,DC(3675)),(L4,DC(3676)),(Q1,DC(3677)),
3(Q2,DC(3678)),(M,DC(3679)),(I,DC(3680)),(L,DC(3681)),
4 (B1,DC(4032)),(IBB,DC(2801)),(SMD,DC(3683)),
5(NUMBER,DC(3682))
 DATA(ABC=2HNO,3HYES),(Y=1H ,1HC,1H*,1HM)
 DATA(G(J,1),J=1,16)/
1 1.9869,1.8518,-1.054,-.0329,-.03312,.
2 03175,-.005,-.001877, -.02389,7*0.0/
 DATA(ZZ(J,1),J=1,147)/
1 10.5,42.0,70.5,98.0,128.0,157.5,211.0,10.0,40.0,70.0,
2 97.5,129.0,158.5,214.0,10.0,69.0,97.0,129.0,
3 159.0,214.0,245.0,10.0,41.0,71.0,98.0,127.5,
4 158.0,210.0,10.0,42.0,71.5,98.0,127.0,155.0,208.0,
4 12.0,45.0,73.0,98.0,125.0,150.5,175.0,208.0,13.5,
5 75.0,98.0,123.0,147.0,199.0,17.0,52.0,76.5,97.5,
6 120.0,141.0,197.0,18.0,38.0,53.5,77.0,96.0,116.5,
7 136.5,185.0,24.0,58.5,79.0,95.0,113.0,131.0,152.0,
8 178.0,27.5,61.0,79.0,92.5,109.5,126.5,172.0,35.5,
9 65.5, 80.5,91.5,106.0,121.5,166.0,69.0,
2 80.0,89.0,103.5,118.0,162.0,52.5,72.5,80.0,88.0,
3 100.0,145.5,158.0,60.0,74.0,79.0,85.5,97.5,111.0,
4 153.5,69.0,76.0,78.5,84.0,96.0,109.0,150.0,77.0,
5 78.0,82.0,93.0,105.5,146.0,76.5,78.0,81.5,86.0,92.5,
```

```
     6 105.0,144.5,76.0,77.5,81.0,87.5,92.0,105.0,
     7 144.5,76.5,77.5,81.5,86.0,93.0,105.0,145.5,77.0,
     8 78.0,82.0,83.0,93.0,105.5,146.0/
      DATA(TEETA(J,1),J=1,147)/
     1 7*-350.,7*-360.,7*-5.,7*-10.,7*-15.,7*-20.,7*-25.,
     2 7*-30.,7*-35.,7*-40.,7*-45.,7*-50.,7*-55.,7*-60.,
     3 7*-65.,7*-70.,7*-80.,7*-85.,7*-90.,7*-95.,7*-100./
      DATA(NN(J),J=1,10)/
     1 147,90,97,64,56,81,64,84,72,57/
      DATA(NM(J),J=1,10)/
     1 147,70,155,133,142,154,142,70,158,139/
      DATA(ADD(1,J),J=1,10)/7*0.,453.2,0.0,0.0/
      DATA(FACTOR(1,J),J=1,10)/7*0.,5.291,0.0,0.0/
      DATA(FREQ(1,J),J=1,10)/7*0.,9.534,0.0,0.0/
  188 FORMAT(1H1)
    8 FORMAT(1X,4HQ1 = ,E13.5,5X,4HQ2 = ,E13.5)
  137 FORMAT (3X,I2,5X,E16.6/)
  136 FORMAT(10X,19H INITIAL
     1 PARAMETERS//3X,1HJ,10X,4HB(J)//)
  135 FORMAT(1X,11H
     1 PARAMETERS//3X,1HJ,10X,4HB(J),27X,6HERRORS//)
    9 FORMAT(2X,*HN=*,10(F9.4,4X))
  140 FORMAT(3X,I2,5X,E16.6,15X,E16.6/)
  138 FORMAT(5X,14H CASE NUMBER =,I2//)
  141 FORMAT(10X,6H SMD =,E13.5//)
  235 FORMAT (15X,5(E13.5,8X)/)
      NUMBER=1
      NCASES=1
      NUMBII=NUMBER
      M=12
      MM=M
      L4=5
      Q1 =1.E-8
      Q2 =1.E-40
      WRITE (6,188)
```

```
    1 CONTINUE
      N=NN(NUMBER) + NM(NUMBER)
      N11(NUMBER)=NN(NUMBER)+1
      DO 210 LL=1,16
  210 B(LL)=0.
      DO 211 LL=1,MM
  211 B(LL)=G(LL,NUMBER)
      WRITE (6,138) NUMBER
      WRITE (6,136)
      WRITE (6,137) (J,B(J),J=1,M)
      N1=N
      DO 3 IJK = 1,N1
      ID=1
      IF(IJK.GT.NN(NUMBER))  ID=2
      IF(IJK.LT.NN(NUMBER).OR.IJK.EQ.NN(NUMBER))
      NNMAG=NMAG(1,NUMBER)
      IF(IJK.GT.NN(NUMBER))  NNMAG=NMAG(2,NUMBER)
      IF(NNMAG.EQ.(-9)) GO TO 620
      IF(NNMAG-2)605,610,615
  605 CONTINUE
C     FOLLOWING FOR LINE POSITION FREQUENCY(KHZ) MEASURED BY
C     FLUXMETER
      HN(IJK)=HHDPPH(IJK,NUMBER)*
     1 (92.732/66252.)*2.0037*.23487
      THETA(IJK) =  TEETA(IJK,NUMBER)
      IF(NUMBER.GT.1.AND.IJK.LT.N11(NUMBER))
      THETA(IJK)=90.-THETA(IJK)
      Z(IJK)=ZZ(IJK,NUMBER)*.23487
      GO TO 620
  610 CONTINUE
C     FOLLOWING FOR MEASURING MAG.FIELD FROM GRAPH IN MM
      HN(IJK)=FREQ(ID,NUMBER)
      THETA(IJK)=TEETA(IJK,NUMBER)
      IF(NUMBER.GT.1.AND.IJK.LT.N11(NUMBER))
      THETA(IJK)=90.-THETA(IJK)
```

```
      Z(IJK)=(ZZ(IJK,NUMBER) +
     1 ADD(ID,NUMBER))*FACTOR(ID,NUMBER)
      GO TO 620
  615 CONTINUE
C FOLLOWING FOR DPPH AND LINE POSITIONS RECORDED IN GAUSS
      HN(IJK)=HHDPPH(IJK,NUMBER)*2.0037*(92.732/66252.)
      Z(IJK)=ZZ(IJK,NUMBER)
      THETA(IJK)=TEETA(IJK,NUMBER)
      IF(NUMBER.GT.1.AND.IJK.LT.N11(NUMBER))
      THETA(IJK)=90.-THETA(IJK)
  620 CONTINUE
    3 CONTINUE
      WRITE(6,8)Q1,Q2
      WRITE(6,9) (HN(J),J=1,N1)
      WRITE(6,726)(Z(J),J=1,N1)
  726 FORMAT(2X,*Z=*,10(F7.1,2X))
      DO 201 J = 1,N1
      ERR(J)=1.
  201 FM(J)=HN(J)
      CALL CURFIT
      WRITE(6,188)
      WRITE(6,135)
      DO 220 LL=1,M
  220 GG(LL,NUMBER) = B(LL)
      WRITE(6,140)(J,B(J),B1(J),J=1,M)
      DO 300 II=1,N
  300 WRITE(6,301) II,IBB(II,1),IBB(II,2)
      SSS=0.
      DO 555 ID=1,N
      SSS=DF(ID)**2
      WRITE(6,656) ID,SSS
  555  CONTINUE
  656 FORMAT(10X,*LINE NUMBER = *,I3,5X,*SMD = *,E13.5)
  301 FORMAT(10X,*LINE NO. = *,I3,5X,*EIGENVALUE1 =*,I3,5X,
     1* EIGENVALUE 2 =*,I3)
```

```
      WRITE(6,188)
      NUMBER = NUMBER + 1
      IF ( NUMBER - NCASES) 1,1,2
    2 CONTINUE
      DO 230 LL=NUMBII,NCASES
      WRITE (6,138) LL
      WRITE (6,141) SMD(LL)
  230 WRITE (6,235) (GG(LM,LL),LM=1,M)
      STOP
      END

      SUBROUTINE CURFIT
C     EXAM HANDLES ALL MATRICES OF DIMENSIONS UPTO THE
C     DIMS.MM OF A,B,C THAT IS M IS LESS THAN OR EQUAL TO
C     MM (SAME IS TRUE OF MATINV AND JACOBI)
      DIMENSION Z(400),FM(400),FC(400),DF(400),ERR(400),
     1B(16),B1(16),DC(4500),ABC(2),Y(4),X(400),GRAD(16),
     2D1(16),D2(16,16),SMD(10),B3(16,16),B2(16,16)
      DIMENSION AI(16,16),W(16),ZR(16,16),ZI(16,16),FV1(16),
     2FM1(2,16)
      COMMON/DATA1/ABC,Y
      COMMON/DATA2/DC
      EQUIVALENCE (Z,DC),(FM,DC(801)),(DF,DC(401)),
     1(FC,DC(1201)),(ERR,DC(1601)),(B,DC(4000)),
     1(GRAD,DC(4016)),(B2,DC(4049)),(N,DC(3675)),
     2(L4,DC(3676)),(Q1,DC(3677)),(Q2,DC(3678)),
     3(M,DC(3679)),(I,DC(3680)),(L,DC(3681)),(D1,DC(3700)),
     4(D2,DC(3720)),(SMD,DC(3683)),(NUMBER,DC(3682))
      EQUIVALENCE(B1,DC(4032)),(NZ,DC(3694))
      DATA(ABC=2HNO,3HYES),(Y=1H ,1HC,1H*,1HM)
      L1 = 0
      SA = 0.0
      MM = M
      DO 1000 J =1,MM
      B1(J)=0.0
```

```
      DO 1000 K = 1,MM
 1000 B2(J,K)=0.0
      WRITE(6,901)
      NN = N
      DO 100 I8 = 1,NN
      X(I8) = ERR(I8)**2
      L=1
      I=I8
      CALL FUNC(2)
 901  FORMAT(5X,10H FUNC2,210  )
      DF(I8) =FM(I8) - FC(I8)
      DO 101 J=1,MM
      B1(J)=B1(J)-(2.0*DF(I8)*D1(J))/X(I8)
      DO 101 K=1,MM
  101 B2(J,K)=B2(J,K)-(2.0*(DF(I8)*D2(J,K)-
     1D1(J)*D1(K)))/X(I8)
  100 SA = SA + DF(I8)**2/X(I8)
      WRITE(6,901)
      GMOD=0.0
      DO 102 J=1,MM
  102 GMOD=GMOD+B1(J)**2
      WRITE(6,243)SA,GMOD
  243 FORMAT (1X,26H*INITIAL VALUE SUM
     1OF SQ.=E13.5,20X,17H*SQ MOD OF GRAD =E13.5)
      WRITE(6,1751)
 1751 FORMAT(14H0 DERIVATIVES-)
      WRITE(6,240)(B1(J),J=1,MM)
  240 FORMAT (15X,5(E13.5,8X)/)
      IF (SA - Q1) 110, 110, 200
  110 LE = 1
      GO TO 600
  200 S = 0.0
      GMOD = 0.0
      BMOD = 0.0
      PROD = 0.0
```

```
      A2=ABC(1)
      DO 210 J =1,MM
      B1(J) = 0.0
      DO 210 K=1,MM
  210 B2(J,K) = 0.0
      WRITE(6,902)
      DO 220 I8=1,NN
      L=1
      I=I8
      CALL FUNC(2)
  902 FORMAT(5X,10H FUNC2,210  )
      DF(I8) = FM(I8) - FC(I8)
      DO 220 J=1,MM
      B1(J) = B1(J) - (2.0*DF(I8)*D1(J))/X(I8)
      DO 220 K =1,MM
  220 B2(J,K) = B2(J,K) - (2.0*(DF(I8)*D2(J,K)
     1-D1(J)*D1(K)))/X(I8)
      WRITE(6,902)
      DO 230 J=1,MM
  230 GRAD(J) = B1(J)
      L1 = L1 + 1
      WRITE(6,903)
      CALL EXAM (B2,B1,MM,LF)
      WRITE(6,903)
  903 FORMAT(5X,9H EXAM,230  )
      IF (LF)  250, 250, 305
  250 DO 231 II=1,MM
      DO 231 JJ=1,MM
      AI(II,JJ)=0.
  231 B3(II,JJ)=B2(II,JJ)
      WRITE(6,904)
      CALL HTRIDI(MM,MM,B3,AI,W,FV1,FV1,FM1)
      DO 1001 IR=1,MM
      DO 5000 JR=1,MM
      ZR(IR,JR)=0.
```

```
5000 CONTINUE
     ZR(IR,IR)=1.
1001 CONTINUE
     CALL TQL2(MM,MM,W,FV1,ZR,IERR)
     CALL HTRIBK(MM,MM,B3,AI,FM1,MM,ZR,ZI)
     DO 5005 IR=1,MM
     B3(IR,IR)=W(IR)
     DO 5005 JR=1,MM
5005 B2(IR,JR)=ZR(JR,JR)
     WRITE(6,904)
904  FORMAT(5X,12H JACOBI1,231  )
     DO 235 K =1,MM
 235 B1(K)=B3(K,K)
     A2=ABC(2)
     DO 260 J=1,MM
 260 D1(J) = 0.0
     DO 270 J=1,MM
     DO 270 K=1,MM
 270 D1(K) = D1(K) + B2(J,K) *GRAD(J)
     DO 275 J = 1, MM
     IF (B1(J))  280, 290, 285
 280 B1(J) = - B1(J)
 285 D1(J) = D1(J)/B1(J)
     GO TO 275
 290 D1(J) = 0.0
 275 CONTINUE
     DO 295 J=1,MM
 295 B1(J) = 0.0
     DO 300 J=1,MM
     DO 300 K=1,MM
 300 B1(J) = B1(J) + B2(J,K)*D1(K)
 305 DO 310 J=1,MM
     GMOD = GMOD + GRAD(J)**2
     BMOD = BMOD + B1(J)**2
 310 PROD = PROD + GRAD(J)*B1(J)
```

```
      IF (GMOD - Q2)  315, 315, 320
  315 LE = 2
      WRITE(6,1761) GMOD
 1761 FORMAT(5X,7H GMOD =,E13.5//)
      GO TO 600
  320 C=PROD/SQRT(BMOD*GMOD)
      IF (C) 335, 335, 400
  335 LE = 4
      GO TO 600
  400 LD = 0
      L3 = 0
      DO 410 J=1,MM
  410 GRAD(J) = B(J) - B1(J)
      WRITE(6,905)
  450 DO 420 I8=1,NN
      L=2
      I=I8
      CALL FUNC (1)
  905 FORMAT(5X,10H FUNC1,450  )
      DF(I8) = FM(I8) - FC(I8)
  420 S = S + DF(I8)**2/X(I8)
      WRITE(6,905)
      IF (SA - S) 435, 500, 500
  435 LD = LD + 1
      WRITE(6,906)
  430 DO 440 J=1,MM
      B1(J) = B1(J)/2.0
  906 FORMAT(5X,16H BINARY CHOP,430  )
  440 GRAD(J) = B(J) - B1(J)
      WRITE(6,906)
      S = 0.0
      L3 = L3 + 1
      IF (L3-4  )450,460,460
  460 LE = 5
      GO TO 600
```

```
500 IF (LD) 505, 505, 506
506 LD = 0
    GO TO 430
505 DO 510 J=1,MM
510 B(J) = GRAD(J)
    SA = S
    IF (SA - Q1) 507, 507, 530
507 LE = 1
    GO TO 600
530 IF (L4) 200, 200, 900
900 WRITE(6,920)L1,A2,L3,S,GMOD,(B(J),J=1,MM)
920 FORMAT(//,15H ITERATION NO.=I5,10X,43H
   1TRANSFORMATION MADE TO PRINCIPAL AXES = A4,10X, 18H
   2BINARY CHOP USED=I3,6H TIMES/1X,27H WEIGHTED SUM OF
   3SQUARES = E14.7,25X,32H SQUARE MODULUS OF GRADIENT =
   4E14.7/20H PARAMETERS B(J) -/(6E17.8)/)
    IF (L1 - L4) 200, 910, 910
910 LE = 6
    GO TO 600
600 DO 710 J=1,MM
    B1(J) = 0.0
    DO 710 K=1,MM
710 B2(J,K) = 0.0
    L=1
    DO 720 I8=1,NN
    I=I8
    CALL FUNC(2)
    DF(I8) = FM(I8) - FC(I8)
    DO 720 J=1,MM
    B1(J) = B1(J) - (2.0*DF(I8)*D1(J))/X(I8)
    DO 720 K=1,MM
720 B2(J,K) = B2(J,K) - (2.0*(DF(I8)*D2(J,K)
   1-D1(J)*D1(K)))/X(I8)
    CALL MATINV(B2,MM,B1,1,DETERM)
    DO 730 J=1,MM
```

```
      IF (B2(J,J)) 2001,2001,2002
 2001 B1(J) = -SQRT(-B2(J,J))
      GO TO 730
 2002 B1(J) = SQRT(B2(J,J))
  730 CONTINUE
      DO 740 J=1,MM
      DO 740 K=1,MM
  740 B2(J,K)=B2(J,K)/(B1(J)*B1(K))
      WRITE(6,551)LE,SA
  551 FORMAT(//,13H EXIT NUMBER=I3,20X,25H WEIGHTED  SUM  OF
     1SQUARES=E15.8//)
      SMD(NUMBER)=SA
      RETURN
      END

      SUBROUTINE FUNC(LX)
C     SUBROUTINE FUNC
      DIMENSION DC(4500),B(16,2),D1(16),
     1FC(400),Z(400),HN(400),S(8,8),R(8,8),SIGN(400),
     2THETA(400),IBB(400,2),SP(8,17),D2(16,16)
      DIMENSION AR(8,8),AI(8,8),W(8),
     1ZR(8,8),ZI(8,8),FV1(8),FM1(2,8)
      DIMENSION NN(25),NM(25)
      COMMON/DATA2/DC
      COMMON/DATA3/NN,NM
      EQUIVALENCE (Z,DC),(FC,DC(1201)),(THETA,DC(2001)),
     1(B,DC(4000)),(D1,DC(3700)),(D2,DC(3720)),
     2(M,DC(3679)),(I,DC(3680)),(L,DC(3681)),(HN,DC(2401)),
     3(IBB,DC(2801)),(N,DC(3675)),(NZ,DC(3694)),(NUMBER,
     4DC(3682))
      DATA(SP(J,1),J=1,8)/3.5,2.5,1.5,.5,-.5,-1.5,-2.5,-3.5/
      DATA(SP(J,3),J=1,8)/7.,1.,-3.,-5.,-5.,-3.,1.,7./
      DATA(SP(J,5),J=1,8)/7.,-13.,-3.,9.,9.,-3.,-13.,7./
      DATA(SP(J,8),J=1,8)/1.,-5.,9.,-5.,-5.,9.,-5.,1./
      FACTOR=92.732/66252.
```

```
      RD=3.14159264/180.
      R2=SQRT(2.0)
      R3=SQRT(3.0)
      R5=SQRT(5.0)
      R7=SQRT(7.0)
      AA1=1.
      AA2=0.
      AA3=0.
C     (AA1,AA2,AA3)=(1,0,0) CONSIDERS B2-2, =(0,1,0)
C  CONSIDERS B21, =(0,0,1) CONSIDERS B2-1
      SP(1,4)=R7/R3
      SP(2,4)=R5
      SP(3,4)=2.*R5/R3
      SP(4,4)=2.*R5/R3
      SP(5,4)=R5
      SP(6,4)=R7/R3
      SP(1,6)=R7*R3/2.
      SP(2,6)=1./(2.*R5)
      SP(3,6)=-2.*R3/R5
      SP(4,6)=-2.*R3/R5
      SP(5,6)=1./(2.*R5)
      SP(6,6)=R7*R3/2.
      SP(1,9)=2./(R7*R3)
      SP(2,9)=-2./R5
      SP(3,9)=2./(R3*R5)
      SP(4,9)=2./(R3*R5)
      SP(5,9)=-2./R5
      SP(6,9)=2./(R7*R3)
      SP(1,7)=R7/R5
      SP(2,7)=R3
      SP(3,7)=R3
      SP(4,7)=R7/R5
      SP(1,10)=R5/R7
      SP(2,10)=-1./R3
      SP(3,10)=-1./R3
```

```
      SP(4,10)=R5/R7
      SP(1,11)=2./R7
      SP(2,11)=2./R7
      SP(1,2)=R7/2.
      SP(2,2)=R3
      SP(3,2)=R3*R5/2.
      SP(4,2)=2.
      SP(5,2)=R3*R5/2.
      SP(6,2)=R3
      SP(7,2)=R7/2.
C  FOLLOWING IS MATRIX FOR O21 OPERATOR(REPLACES O2-2)
      SP(1,12)=1.5*R7
      SP(2,12)=2.*R3
      SP(3,12)=R3*R5/2.
      SP(4,12)=0.
      SP(5,12)= -SP(3,12)
      SP(6,12)= -SP(2,12)
      SP(7,12)= -SP(1,12)
C FOLLOWING IS THE MATRIX FOR O41 OPERATOR (REPLACES O4-2)
      SP(1,13) = R7*30.
      SP(2,13) = -R3*30.
      SP(3,13) = -R3*R5*18.
      SP(4,13) = 0.
      SP(5,13) = -SP(3,13)
      SP(6,13) = -SP(2,13)
      SP(7,13) = -SP(1,13)
C FOLLOWING IS MATRIX FOR O43 OPERATOR (REPLACES O4-4)
      SP(1,14)= R7*R5*6.
      SP(2,14)= R5*12.
      SP(3,14)= 0.
      SP(4,14)= -SP(2,14)
      SP(5,14)= -SP(1,14)
      DO 100 IX=1,8
      DO 100 JX=1,8
      AI(IX,JX)=0.
```

```
      S(IX,JX) = 0.0
  100 R(IX,JX) = 0.0
      IF(I.GT.NN(NUMBER)) GO TO 97
      TH=THETA(I)*3.14159264/180.
      ACOSTH=COS(TH)
      ASINTH=SIN(TH)
C     PBB IS COEFFT. OF SZ
      PBB=B(1,L)*Z(I)*ACOSTH+B(12,L)*Z(I)*ASINTH*AA2
      PBB = PBB*92.732/66252.
C     PAA IS COFFT. OF SX
      PAA = B(10,L)*Z(I)*ASINTH+B(12,L)*Z(I)*ACOSTH*AA2
      PAA = PAA*92.732/66252.
      PAD=Z(I)*ASINTH
      PBD=Z(I)*ACOSTH
      PBAD=Z(I)*ASINTH*AA2
      PABD=Z(I)*ACOSTH*AA2
      PACD=0.*AA1
      PCAD=Z(I)*ASINTH*AA1
      PBCD=AA3*0.
      PCBD=Z(I)*ACOSTH*AA3
C  PCCIS COEFFICIENT OF SY
      PCC=AA1*B(12,L)*Z(I)*ASINTH*92.732/66252.
     1 +AA3*B(12,L)*Z(I)*ACOSTH*92.732/66252.
      PCD=0.
      GO TO 98
   97 CONTINUE
      TH=-THETA(I)*RD
      ACOSTH=COS(TH)
      ASINTH=SIN(TH)
      PBB=B(12,L)*Z(I)*ACOSTH*FACTOR*AA2+
     1B(12,L)*Z(I)*ASINTH*FACTOR*AA3
      PBD=0.
      PAA=B(10,L)*Z(I)*ACOSTH*FACTOR+
     1B(12,L)*Z(I)*ASINTH*FACTOR*AA1+AA3*0.
      PAD=Z(I)*ACOSTH
```

```
      PBAD=Z(I)*ACOSTH*AA2
      PABD=0.*AA2
      PACD=Z(I)*ASINTH*AA1
      PCAD=Z(I)*ACOSTH*AA1
      PCBD=0.*AA3
      PBCD=Z(I)*ASINTH*AA3
      PCC=B(11,L)*Z(I)*ASINTH*FACTOR+
     1B(12,L)*Z(I)*ACOSTH*FACTOR*AA1
      PCD=Z(I)*ASINTH
   98 CONTINUE
      S(1,1)=3.5*PBB  +7.*B(2,L) +7.*B(5,L) + B(13,L)
      S(2,2)=2.5*PBB  +B(2,L) -13.*B(5,L) - 5.*B(13,L)
      S(3,3)=1.5*PBB -3.*B(2,L) -3.*B(5,L) +9.*B(13,L)
      S(4,4)=.5*PBB -5.*B(2,L) +9.*B(5,L) -5.*B(13,L)
      S(5,5)=S(4,4) -PBB
      S(6,6)=S(3,3) -3.*PBB
      S(7,7) =S(2,2)-5.*PBB
      S(8,8) =S(1,1)-7.*PBB
      S(1,3) =R7*B(3,L)/R3 + R7*R3*B(6,L)/2. +
     1 2.*B(14,L)/(R7*R3)
C  IN FOLLOWING LINE 16,L SHOULD BE CHANGED  TO  17,L  AFTER
C  INCREASING DIM. OF B
      AI(1,3)=(-R7*B(4,L)/R3-R7*R3*B(8,L)/2.
     1-2.*B(16,L)/(R7*3.))*AA1
      S(1,5) = R7*B(7,L)/R5 + R5*B(15,L)/R7
      AI(1,5)=(-R7*B(9,L)/R5 - R5*B(16,L)/R7)*AA1
C IN LINE ABOVE CHANGE 16,L TO 18,L AFTER CHANGING DIM. OF B
      S(1,7) = 2.*B(16,L)/R7
C IN LINE BELOW CHANGE 16,L TO 19,L AFTER CHANGING DIM. OF B
      AI(1,7)=(-2.*B(16,L)/R7)*AA1
      S(2,4) = R5*B(3,L)+B(6,L)/(R5*2.) - 2.*B(14,L)/R5
C IN LINE BELOW CHANGE 16,L TO 17,L AFTER CHANGING DIM. OF B
      AI(2,4)=(-B(8,L)/(R5*2.)-R5*B(4,L)+2.*B(16,L)/R5)*AA1
      S(2,6) = R3*B(7,L) - B(15,L)/R3
C IN LINE BELOW CHANGE 16,L TO 18,L AFTER CHANGING DIM. OF B
```

```
      AI(2,6)=(-R3*B(9,L) +B(16,L)/R3)*AA1
      S(3,5)=2.*R5*B(3,L)/R3-2.*B(6,L)*R3/R5+
     1 2.*B(14,L)/(R5*R3)
C IN LINE BELOW CHANGE 16,L TO 17,L AFTER CHANGING DIM. OF B
      AI(3,5)=(2.*B(8,L)*R3/R5-2.*R5*B(4,L)-
     1 2.*B(16,L)/(R5*R3))*AA1
      DO 901 I4=1,6
      II4=I4+1
      II5=8-I4
      AI(II4,8)=AI(1,II5)
  901 S(II4,8)=S(1,II5)
      DO 902 I5=1,4
      II6=I5+2
      II7=7-I5
      AI(II6,7)=AI(2,II7)
  902 S(II6,7)=S(2,II7)
      DO 903 I6=1,2
      II8=I6+3
      II9=6-I6
      AI(II8,6)=AI(3,II9)
  903 S(II8,6)=S(3,II9)
      S(1,2)=PAA*R7/2. +AA2*(3.*(R7/2.)
     1 *B(4,L)+30.*R7*B(8,L))
      S(2,3)=PAA*R3+AA2*(2.*R3*B(4,L)-30.*R3*B(8,L))
      S(3,4)=PAA*R3*(R5/2.)+AA2*(R3*(R5/2.)
     1 *B(4,L)-18.*R3*R5*B(8,L))
      S(4,5)=PAA*2.
      S(5,6)=S(3,4)-2.*AA2*(R3*(R5/2.)
     1 *B(4,L)-18.*R3*R5*B(8,L))
      S(6,7)=S(2,3)-2.*AA2*(2.*R3*B(4,L)-30.*R3*B(8,L))
      S(7,8)=S(1,2) -2.*AA2*(3.*(R7/2.)
     1 *B(4,L)+30.*R7*B(8,L))
      S(1,4)=AA2*R7*R5*6.*B(9,L)
      S(2,5)=AA2*R5*12.*B(9,L)
      S(3,6)=0.
```

```
      S(4,7)=-S(2,5)
      S(5,8)=-S(1,4)
      AI(1,2)=-PCC*R7/2.
     1 +AA3*(-3.*B(4,L)*R7/2.-30.*R7*B(8,L))
      AI(2,3)=-PCC*R3+AA3*(-2.*R3*B(4,L)+30.*R3*B(8,L))
      AI(3,4)=-PCC*R3*R5/2.
     1 +AA3*(-R3*R5*B(4,L)/2.+18.*R3*R5*B(8,L))
      AI(4,5)=-PCC*2.
      AI(5,6)=-AI(3,4)-PCC*R3*R5
      AI(6,7)=-AI(2,3)-2.*R3*PCC
      AI(7,8)=-AI(1,2)-PCC*R7
      AI(1,4)=-AA3*R7*R5*6.*B(9,L)
      AI(2,5)=-AA3*R5*12.*B(9,L)
      AI(3,6)=0.
      AI(4,7)=-AI(2,5)
      AI(5,8)=-AI(1,4)
      DO 207 IY=1,8
      DO 207 JY=1,8
      IF(IY-JY) 205,205,206
  206 S(IY,JY) =S(JY,IY)
      AI(IY,JY)=-AI(JY,IY)
  205 CONTINUE
  207 CONTINUE
      DO 5006 IR=1,8
      DO 5006 JR=1,8
 5006 AR(IR,JR)=S(IR,JR)
      CALL HTRIDI(8,8,AR,AI,W,FV1,FV1,FM1)
      DO 1000 IR=1,8
      DO 5000 JR=1,8
      ZR(IR,JR)=0.
 5000 CONTINUE
      ZR(IR,IR)=1.
 1000 CONTINUE
      CALL TQL2(8,8,W,FV1,ZR,IERR)
      CALL HTRIBK(8,8,AR,AI,FM1,8,ZR,ZI)
```

```
      DO 5005 IR=1,8
      S(IR,IR) = W(IR)
      DO 5005 JR=1,8
5005  R(IR,JR)=ZR(IR,JR)
      CBA=ABS(ABS(S(1,1)-S(2,2))-HN(I))
      IBB(I,1)=1
      IBB(I,2)=2
      I6 = 1
      I7 = 2
      DO 20 I8 = 1,7
      IZ = I8 + 1
      DO 20 I9 = IZ,8
      S1=ABS(ABS(S(I8,I8)-S(I9,I9))-HN(I))
      IF (CBA-S1)21,22,22
   22 CBA=S1
      IBB(I,1)=I8
      IBB(I,2)=I9
      I6=I8
      I7=I9
   21 CONTINUE
   20 CONTINUE
      FC(I)=ABS(S(I6,I6)-S(I7,I7))
      SIGN(I)=(S(I6,I6)-S(I7,I7))/FC(I)
      IF(LX-1)110,110,121
  121 CONTINUE
      DO 235 IZ=1,16
      D1(IZ) = 0.0
      DO 235 JZ=1,16
  235 D2(IZ,JZ) =0.0
      DO 236 IT=1,8
      RR1=(R(IT,I6)**2-R(IT,I7)**2)*SIGN(I)
     1+(ZI(IT,I6)**2 - ZI(IT,I7)**2)*SIGN(I)
      D1(1) = D1(1) + SP(IT,1)*RR1*PBD*FACTOR
      D1(2) = SP(IT,3)*RR1 +D1(2)
      D1(5) = SP(IT,5)*RR1 +D1(5)
```

```
      D1(13)=SP(IT,8)*RR1+D1(13)
      D1(12)=D1(12)+SP(IT,1)*RR1*(PBAD+PBCD)*FACTOR
  236 CONTINUE
      DO 237 IT=1,6
      IT2 =IT + 2
      RR2=2.*(R(IT,I6)*R(IT2,I6)-R(IT,I7)*R(IT2,I7))*SIGN(I)
     1 +2.*(ZI(IT,I6)*ZI(IT2,I6)
     1 -ZI(IT,I7)*ZI(IT2,I7))*SIGN(I)
      RR3=-2.*(-ZR(IT,I6)*ZI(IT2,I6)+ZI(IT,I6)*ZR(IT2,I6)
     1+ZR(IT,I7)*ZI(IT2,I7)-ZI(IT,I7)*ZR(IT2,I7))*SIGN(I)
      D1(3) = SP(IT,4)*RR2 +D1(3)
      D1(6) = SP(IT,6)*RR2 +D1(6)
      D1(14)=SP(IT,9)*RR2+D1(14)
      D1(8)=SP(IT,6)*RR3*AA1+D1(8)
      D1(4)=SP(IT,4)*RR3*AA1+D1(4)
C IN FOLLOWING LINE CHANGE D1(16) TO D1(17)  AFTER  CHANGING
C  DIM. OF B
      D1(16)=SP(IT,9)*RR3+D1(16)
  237 CONTINUE
      DO 238 IT=1,4
      IT4 = IT + 4
      RR4=2.*(R(IT,I6)*R(IT4,I6)-R(IT,I7)*R(IT4,I7))*SIGN(I)
     1+2.*(ZI(IT,I6)*ZI(IT4,I6)
     1-ZI(IT,I7)*ZI(IT4,I7))*SIGN(I)
      RR5=-2.*(-ZR(IT,I6)*ZI(IT4,I6)+ZI(IT,I6)*ZR(IT4,I6)
     1+ZR(IT,I7)*ZI(IT4,I7)-ZI(IT,I7)*ZR(IT4,I7))*SIGN(I)
      D1(7) =SP(IT,7)*RR4 +D1(7)
      D1(9)=SP(IT,7)*RR5*AA1+D1(9)
      D1(15)=SP(IT,10)*RR4+D1(15)
C IN LINE BELOW CHANGE D1(16) TO D1(18) AFTER CHANGING  DIM.
C  OF B
      D1(16)=SP(IT,10)*RR5+D1(16)
  238 CONTINUE
      DO 239 IT=1,2
      IT6=IT+6
```

```
      RR6=2.*(R(IT,I6)*R(IT6,I6)-R(IT,I7)*R(IT6,I7))*SIGN(I)
     1+2.*(ZI(IT,I6)*ZI(IT6,I6)
     1-ZI(IT,I7)*ZI(IT6,I7))*SIGN(I)
      RR7=-2.*(-ZR(IT,I6)*ZI(IT6,I6)+ZI(IT,I6)*ZR(IT6,I6)
     1+ZR(IT,I7)*ZI(IT6,I7)-ZI(IT,I7)*ZR(IT6,I7))*SIGN(I)
      D1(16)=SP(IT,11)*RR6+D1(16)
C IN LINE BELOW CHANGE D1(16) TO D1(19) AFTER CHANGING  DIM.
C OF B
  239 D1(16)=SP(IT,11)*RR7+D1(16)
      DO 401 IT=1,7
      IT1=IT+1
      RR2=2.*(R(IT,I6)*R(IT1,I6)-R(IT,I7)*R(IT1,I7))*SIGN(I)
     1+2.*(ZI(IT,I6)*ZI(IT1,I6)
     2-ZI(IT,I7)*ZI(IT1,I7))*SIGN(I)
      RR3=-2.*(-ZR(IT,I6)*ZI(IT1,I6)+ZI(IT,I6)*ZR(IT1,I6)
     1 +ZR(IT,I7)*ZI(IT1,I7)-ZI(IT,I7)*ZR(IT1,I7))*SIGN(I)
      D1(4)=D1(4) + AA2*SP(IT,12)*RR2
      D1(4)=D1(4)-AA3*SP(IT,12)*RR3
      D1(8)=D1(8)+AA2*SP(IT,13)*RR2
      D1(8)=D1(8)-AA3*SP(IT,13)*RR3
      D1(10)=D1(10)+SP(IT,2)*RR2*PAD*FACTOR
      D1(12)=D1(12)+SP(IT,2)*
     1(RR2*(PABD+PACD)+RR3*(PCAD+PCBD))*FACTOR
  401 D1(11)=D1(11)+SP(IT,2)*RR3*PCD*FACTOR
      DO 402 IT=1,5
      IT3=IT+3
      RR2=2.*(R(IT,I6)*R(IT3,I6)-R(IT,I7)*R(IT3,I7))*SIGN(I)
     1  +2.*(ZI(IT,I6)*ZI(IT3,I6)
     1 -ZI(IT,I7)*ZI(IT3,I7))*SIGN(I)
      RR3=-2.*(ZR(IT,I6)*ZI(IT3,I6)+ZI(IT,I6)*ZR(IT3,I6)
     1 +ZR(IT,I7)*ZI(IT3,I7)-ZI(IT,I7)*ZR(IT3,I7))*SIGN(I)
      D1(9)=D1(9)-AA3*SP(IT,14)*RR3
  402  D1(9)=D1(9)+AA2*SP(IT,14)*RR2
  110 CONTINUE
      RETURN
```

```
      END

      SUBROUTINE EXAM(A,B,M,LF)
C     SUBROUTINE EXAM
      DIMENSION A(16,16),B(16),C(16)

      SUBROUTINE MATINV(A,N,B,M,DETERM)
C     SUBROUTINE MATINV
C     MATRIX INVERSION WITH ACCOMPANYING SOLUTION OF LINEAR
C     EQUATIONS
      DIMENSION IPIVOT(16),A(16,16),
     1B(16,1),INDEX(16,2),PIVOT(16)
      EQUIVALENCE (IROW,JROW),(ICOLUM,JCOLUM),(AMAX,T,SWAP)
```

```
      PROGRAM VO (INPUT,OUTPUT,TAPE5=INPUT,TAPE58=OUTPUT)
C     THIS PROGRAM ANALYSES EPR DATA FROM HYPERFINE LINES
C     WITH ELECTRON SPIN S=1/2 AND NUCLEAR SPIN I=7/2 FOR
C     VO2+. IT FITS BOTH G-SQUARE AND A-SQUARE
C     TENSOR (12 PARAMETERS)-SECOND ORDER PERTURB.
C     M =NO. OF PARAMETERS; L4 =NO. OF ITERATIONS ALLOWED
C     Q1 =MIN. VALUE OF SUM OF SQUARES FOR FITS (CHI-SQUARE
C     TOLERANCE)
C     Z(I)=MAGNETIC FIELD VALUES FOR FITS; B =PARAMETER
C     MATRIX
C     N =NO. OF DATA POINTS USED IN LEAST-SQARES FITTING
C     Q1 =N/10; Q2 =TOLERANCE ON GRAD(CHI**2) =APPROX .01
C     FM(I) = MEASURED VALUES; FC(I) = CALCULATED VALUES
C     ERR(I)= STANDARD DEVIATION ON FM(I) = SQRT(FM(I))
C     DIMENSIONS OF A,B IN EXAM AND MATINV SUBROUTINES
C     SHOULD BE THE SAME AS THOSE OF B2,B1 RESPECTIVELY IN
C     THE MAIN PROOGRAM AND IN CURFIT.
C     ENTER TEETA IN DEGREES
C     DIMENSIONS OF Q,V IN JACOBI1 SHOULD BE THE SAME AS
C     THOSE OF B3,B2 RESPECTIVELY IN CURFIT
C     PARAMETERS=I.GT IS G**2-TENSOR
C     (G**2ZZ,G**2ZX,G**2XX,G**2ZY,G**2YY,G**2XY)
C     GGT(J,NUMBER) REPRESENTS G-SQUARE TENSOR.
C     II. (B(I),I=1,6)=AZZ,AZX,AXX,AZY,AYY,AXY
C     A=A-SQUARE TENSOR ABOVE ENTER A WITH POSITIVE SIGN
C     DELANG(I,J),J=1,2,3 ARE ANGLE CORRECTIONS FOR ZX,ZY,XY
C     PLANES AS DETERMINED BY "KRDBLT" FOR VARIOUS CASES.
C     NUMBER=INDEX THAT CHANGES WITH EACH NEW CASE
C     ITS VALUE SHOULD BE THAT OF THE FIRST CASE CONSIDERED.
C     NCASES=NO. OF LAST CASE CONSIDERED. ITS VALUE SHOULD
C     BE ENTERED.
C     N1(J1,NUMBER)=NO.OF LINES(FOR VARIOUS ORIENTATIONS)
C     FOR J1 HYPERFINE LINE OF CASE NO.=NUMBER
C     ZZ(J,K,L)=LINE POSITIONS,J=WHICH ONE OF K=HYPERFINE
```

```
C      LINE OF CASE NO.=L
       DIMENSION Z(400),FM(400),FC(400),DF(400),ERR(400),
      1B(12),B1(12),B2(12,12),DC(5000),ABC(2),Y(4),
      3HN(400),G(8,12),GG(6,8),SMD(9),AAA(3,3),QQQ(3,3),
      4AAV(3,3),QQV(3,3),IBB(400,2),THETA(400), D1(12),
      4D2(12,12),HHN(3,8),AADD(3,8),FFACTR(3,8),
      5TEETA(50,8,8),ZZ(50,8,8),NN(8),N1(8,8),ACOSZ(400),
      6ACOSX(400),ACOSY(400),DELANG(8,3), AJ1(400),GGT(3,3),
      7GGTT(8,3,3),DELHH(400,8),DELH(400),A4(3)
       COMMON/DATA1/ABC,Y
       COMMON/DATA2/DC,ACOSZ,ACOSX,ACOSY,AJ1
       COMMON/DATA3/DELH
       EQUIVALENCE (Z,DC),(FM,DC(401)),(FC,DC(801)),
      1 (DF,DC(1201)), (ERR,DC(1601)),(HN,DC(2001)),
      3 (THETA,DC(2401)),(IBB,DC(2801)),(B,DC(4101)),
      4 (B1,DC(4125)),(B2,DC(4137)),(N,DC(4301)),
      6 (L4,DC(4302)),(Q1,DC(4303)),(Q2,DC(4304)),
      7 (M,DC(4305)),(I,DC(4306)),(L,DC(4307)),
      9 (BO,DC(4308)),(SMD,DC(4309)),(SSMD,DC(4320)),
      1 (D1,DC(4321)),(D2,DC(4333)),
      2 (NUMBER,DC(4100)),(GT,DC(4093))
        DATA(HHN(J,1),J=1,3)/9.5280,9.5255,9.5260/
        DATA(FFACTR(J,1),J=1,3)/5.236,5.281,5.236/
        DATA(AADD(J,1),J=1,3)/468.95,463.27,468.88/
        DATA(G(1,J),J=1,3)/3.91900,3.94790,3.77984/
        DATA(G(1,J),J=7,12)/
      1 0.0285,-0.0020471,0.014641,0.0260,0.203,-0.002/
        DATA(DELANG(1,J),J=1,3)/0.0, 0.0,0.0/
        DATA(GGTT(1,1,J),J=1,3)/0.2094,-0.9762,-0.05568/
        DATA(GGTT(1,2,J),J=1,3)/0.5473,0.16425,-0.8205/
        DATA(GGTT(1,3,J),J=1,3)/0.8102,0.1413,0.5687/
        DATA(N1(J,1),J=1,8)/8*48/
        DATA(DELHH(J,1),J=1,384)/384*2.0/
        DATA(ZZ(J,1,1),J=1,16)/
      1  99.3, 99.5,100.1,101.4,105.0,107.2,110.0,113.4,
```

```
     2 120.9,125.5,129.5,133.6,142.4,145.5,148.5,149.4/
       DATA(ZZ(J,2,1),J=1,16)/
     1 126.7,127.2,127.4,128.0,130.4,131.7,133.7,136.5,
     2 141.0,144.4,146.5,149.4,154.3,156.0,157.3,157.5/
       DATA(ZZ(J,3,1),J=1,16)/
     1 154.2,154.3,154.4,154.5,155.5,156.3,157.2,158.5,
     2 160.5,162.3,163.5,164.4,166.0,166.5,166.6,166.7/
       DATA(ZZ(J,4,1),J=1,16)/
     1 180.9,180.8,180.6,180.5,180.3,180.2,180.1,180.0,
     2 179.8,179.7,179.5,179.2,178.1,177.5,177.1,177.0/
       DATA(ZZ(J,5,1),J=1,16)/
     1 207.4,207.1,206.5,206.0,204.4,203.2,202.3,201.3,
     2 198.3,197.2,195.4,193.5,190.4,188.8,188.1,188.0/
       DATA(ZZ(J,6,1),J=1,16)/
     1 233.3,233.1,232.4,231.3,228.0,226.1,224.1,221.6,
     2 216.4,214.0,210.6,207.7,202.7,201.0,199.9,199.4/
       DATA(ZZ(J,7,1),J=1,16)/
     1 259.3,259.2,258.0,256.3,251.6,248.7,245.5,242.1,
     2 234.4,230.3,225.4,222.4,215.7,213.5,212.3,211.5/
       DATA(ZZ(J,8,1),J=1,16)/
     1 285.4,285.2,283.6,281.5,275.4,271.6,267.1,262.5,
     2 252.4,247.4,242.1,236.9,229.4,226.5,225.0,224.4/
       DATA(TEETA(J,1,1),J=1,16)/
     1   0.,  5., 10., 15., 25., 30., 35., 40.,
     2  50., 55., 60., 65., 75., 80., 85., 90./
       DATA(ZZ(J,1,1),J=17,32)/
     1  99.4, 96.4, 93.6, 91.5, 89.0, 88.0, 87.6, 88.0,
     2  90.2, 91.9, 94.0, 97.4,105.0,108.6,113.8,119.0/
       DATA(ZZ(J,2,1),J=17,32)/
     1 126.9,124.9,123.1,121.6,119.9,119.4,119.3,119.4,
     2 121.0,122.0,123.4,125.4,130.5,132.7,136.5,139.6/
       DATA(ZZ(J,3,1),J=17,32)/
     1 153.7,153.0,152.4,151.8,151.3,150.8,150.5,150.9,
     2 151.4,152.0,152.6,153.0,155.5,156.4,158.4,159.6/
       DATA(ZZ(J,4,1),J=17,32)/
```

```
     1 180.4,180.7,181.5,182.1,182.5,182.5,182.5,182.4,
     2 182.2,182.0,181.5,181.0,180.3,180.1,179.8,179.5/
       DATA(ZZ(J,5,1),J=17,32)/
     1 206.5,208.5,210.0,211.5,213.3,213.7,214.0,213.8,
     2 212.4,211.0,209.6,208.3,204.7,202.2,200.2,197.5/
       DATA(ZZ(J,6,1),J=17,32)/
     1 232.4,235.7,238.6,241.4,244.8,245.4,245.7,245.3,
     2 242.6,240.5,238.4,235.3,228.5,224.3,220.5,216.0/
       DATA(ZZ(J,7,1),J=17,32)/
     1 258.5,263.6,267.6,271.4,276.5,277.4,277.7,277.4,
     2 273.6,270.6,266.6,262.4,252.4,246.2,240.3,233.5/
       DATA(ZZ(J,8,1),J=17,32)/
     1 284.3,291.4,296.4,301.5,308.4,309.5,310.1,309.4,
     2 304.5,300.5,295.4,289.4,276.0,268.0,260.0,251.5/
       DATA(TEETA(J,1,1),J=17,32)/
     1 -360.,-5.,-10.,-15.,-25.,-30.,-35.,-40.,
     2 -50.,-55.,-60.,-65.,-75.,-80.,-85.,-90./
       DATA(ZZ(J,1,1),J=33,48)/
     1 149.5,149.0,147.6,145.7,140.7,138.5,135.7,133.2,
     2 128.5,126.5,124.5,122.8,120.7,119.7,119.0,118.7/
       DATA(ZZ(J,2,1),J=33,48)/
     1 157.5,157.3,156.7,156.0,153.6,152.1,150.6,149.0,
     2 146.0,144.7,143.5,142.2,140.8,140.3,139.9,139.6/
       DATA(ZZ(J,3,1),J=33,48)/
     1 166.6,166.6,166.5,166.4,165.8,165.4,164.9,164.4,
     2 162.9,162.2,161.6,161.0,160.2,160.0,159.8,159.7/
       DATA(ZZ(J,4,1),J=33,48)/
     1 177.0,177.0,177.2,177.4,177.8,178.5,178.8,179.0,
     2 179.1,179.2,179.2,179.3,179.4,179.4,179.5,179.5/
       DATA(ZZ(J,5,1),J=33,48)/
     1 188.0,188.0,188.1,188.7,190.4,191.4,192.3,193.2,
     2 194.8,195.4,195.9,196.5,197.4,197.5,197.7,197.7/
       DATA(ZZ(J,6,1),J=33,48)/
     1 199.4,199.5,200.0,200.6,203.0,204.6,206.0,207.4,
     2 210.2,211.6,212.7,213.6,215.0,215.4,215.7,215.9/
```

```
      DATA(ZZ(J,7,1),J=33,48)/
     1 211.5,212.0,212.4,213.2,216.2,218.0,219.7,221.5,
     2 225.4,227.1,228.6,230.1,232.3,233.0,233.5,233.6/
      DATA(ZZ(J,8,1),J=33,48)/
     1 224.6,225.0,225.5,226.4,229.8,231.9,233.8,235.8,
     2 240.5,242.8,244.8,246.7,249.5,250.4,251.0,251.3/
      DATA(TEETA(J,1,1),J=33,48)/
     1 9000.,9005.,9010.,9015.,9025.,9030.,9035.,9040.,
     2 9050.,9055.,9060.,9065.,9075.,9080.,9085.,9090./
     2 9050.,9055.,9060.,9065.,9075.,9080.,9085.,9090./
  188 FORMAT(1H1)
    8 FORMAT(1X,4HQ1 = ,E13.5,5X,4HQ2 = ,E13.5)
  137 FORMAT (3X,I2,5X,E16.6/)
  136 FORMAT(10X,18HINITIAL PARAMETERS/3X,1HJ,10X,4HB(J)/)
  135 FORMAT(1X,9HPARAMETER/3X,1HJ,10X,4HB(J),27X,6HERRORS/)
    9 FORMAT(2X,4H HN= ,F9.4)
  140 FORMAT(3X,I2,5X,E16.6,15X,E16.6/)
  138 FORMAT(5X,14H CASE NUMBER =,I2//)
  141 FORMAT(10X,6H SMD =,E13.5//)
  235 FORMAT (15X,5(E13.5,8X)/)
  236 FORMAT(15X,3(E13.5,8X)///)
 7237 FORMAT(15X,*DIAGONAL ELEMENTS OF G-SQUARE TENSOR
     1ARE=*,///)
  237  FORMAT(15X,*DIAGONAL ELEMENTS OF A-SQUARE TENSOR
     1ARE=*,///)
  238 FORMAT(15X,*"G" DIR. COS.(ROWS) ACC. TO E.VALS. ABOVE=
     1*,///)
 7238 FORMAT(15X,*"A" DIR. COS.(ROWS) ACC. TO E.VALS. ABOVE=
     1*,///)
      PI2=2.*3.1415926
      RD=PI2/360.
      NZERO=1
      NUMBER=NZERO
      NCASES=1
      M=12
```

```
      L4=7
      Q1=1.E-8
      Q2=1.E-20
      MM=M
      WRITE(58,188)
    1 CONTINUE
      N11=N1(1,NUMBER)
      DO 1188 J=1,8
      DO 1188 J1=1,N11
 1188 TEETA(J1,J,NUMBER)=TEETA(J1,1,NUMBER)
      DO 300 IA=1,3
      DO 300 JA=1,3
  300 GGT(IA,JA)=GGTT(NUMBER,IA,JA)
      WRITE(58,121)
      DO 122 IA=1,3
  122 WRITE(58,123) (GGT(IA,JA),JA=1,3)
  121 FORMAT(5X,*ELEMENTS OF INITIAL GGT MATRIX AS THE
     1MATRIX OF DIR. COSINES OF G-SQUARE TENSOR ARE=*,//)
  123 FORMAT(5X,3(F10.6,2X),/)
      CALL EULER(GGT,THITA,PHI,PSI)
      B(4)=THITA
      B(5)=PHI
      B(6)=PSI
      LINE=0
      DO 150 J1=1,8
      NN1=N1(J1,NUMBER)
      DO 150 I1=1,NN1
      LINE=LINE+1
      AJ1(LINE)=J1
      THETA(LINE)=TEETA(I1,J1,NUMBER)
      IF(THETA(LINE).GT.8000.) GO TO 155
      IF(THETA(LINE).LT.0.) GO TO 160
      TH=THETA(LINE)*RD+DELANG(NUMBER,1)*RD
      ACOSZ(LINE)=COS(TH)
      ACOSX(LINE)=SIN(TH)
```

```
      ACOSY(LINE)=0.
      HN(LINE)=HHN(1,NUMBER)
      Z(LINE)=(ZZ(I1,J1,NUMBER)
     1 +AADD(1,NUMBER))*FFACTR(1,NUMBER)
      IF(ZZ(I1,J1,NUMBER).EQ.0.) Z(LINE)=0.
 9160 FORMAT(5X,*ACOSZ ETC=*,3E12.5)
      GO TO 165
  160 TH=-THETA(LINE)*RD + DELANG(NUMBER,2)*RD
      ACOSZ(LINE)=COS(TH)
      ACOSY(LINE)=SIN(TH)
      ACOSX(LINE)=0.
      HN(LINE)=HHN(2,NUMBER)
Z(LINE)=(ZZ(I1,J1,NUMBER)+AADD(2,NUMBER))*FFACTR(2,NUMBER)
      IF(ZZ(I1,J1,NUMBER).EQ.0.) Z(LINE)=0.
      GO TO 165
  155 TH=THETA(LINE)*RD+DELANG(NUMBER,3)*RD
      ACOSZ(LINE)=0.
      ACOSX(LINE)=COS(TH)
      ACOSY(LINE)=SIN(TH)
      HN(LINE)=HHN(3,NUMBER)
      Z(LINE)=(ZZ(I1,J1,NUMBER)
     1 +AADD(3,NUMBER))*FFACTR(3,NUMBER)
      IF(ZZ(I1,J1,NUMBER).EQ.0.) Z(LINE)=0.
  165 CONTINUE
  150 CONTINUE
      NN(NUMBER)=LINE
      N=NN(NUMBER)
      N9=N
      DO 210 LL=1,MM
      IF (LL.GT.3.AND.LL.LT.7) GO TO 210
      B(LL)=G(NUMBER,LL)
  210 CONTINUE
      WRITE(58,138) NUMBER
      WRITE(58,136)
      WRITE(58,137) (J,B(J),J=1,M)
```

```
      WRITE(58,6659)
      WRITE(58,6657) (Z(J),J=1,N)
      WRITE(58,6660)
      WRITE(58,6657) (HN(J),J=1,N)
 6660 FORMAT(5X,*FREQUENCY-KLYSTRON ARE=*,/)
 6659 FORMAT(5X,*MAG. FIELD VALUES ARE=*,/)
 6657 FORMAT(5X,8(E12.5,2X))
      DO 201 II=1,N9
      DELH(II)=DELHH(II,NUMBER)
  201 FM(II) = HN(II)
      CALL CURFIT
      SMD(NUMBER) = SSMD
      WRITE(58,188)
      WRITE(58,135)
      DO 220 LL=1,M
  220 GG(LL,NUMBER) = B(LL)
      WRITE(58,140)(J,B(J),B1(J),J=1,M)
      WRITE(58,188)
    3 CONTINUE
      SSS=0.
      SSS1=0.
      DO 555 ID=1,N
      SSS=DF(ID)**2
      SSS1=SSS1+SSS
      WRITE(58,656) ID,SSS
  555 CONTINUE
      WRITE(58,6656) SSS1
 6656 FORMAT(/,10X,*CHI-SQUARE=*,E13.5,/)
  656 FORMAT(10X,*LINE NUMBER = *,I3,5X,*SMD = *,E13.5)
      WRITE (58,7237)
      WRITE(58,236) (B(J1),J1 = 1,3)
      WRITE (58,238)
      SB4L=SIN(B(4))
      CB4L=COS(B(4))
      SB5L=SIN(B(5))
```

```
      CB5L=COS(B(5))
      SB6L=SIN(B(6))
      CB6L=COS(B(6))
      GGT(1,1)=CB4L
      GGT(1,2)=SB4L*SB5L
      GGT(1,3)=-SB4L*CB5L
      GGT(2,1)=SB6L*SB4L
      GGT(2,2)=CB6L*CB5L-CB4L*SB5L*SB6L
      GGT(2,3)=CB6L*SB5L+CB4L*CB5L*SB6L
      GGT(3,1)=CB6L*SB4L
      GGT(3,2)=-SB6L*CB5L-CB4L*SB5L*CB6L
      GGT(3,3)=-SB6L*SB5L+CB4L*CB5L*CB6L
      DO 25 J1 = 1,3
      WRITE (58,236) (GGT(J1,J2),J2 = 1,3)
   25 CONTINUE
      DO 245 J=1,3
  245 A4(J)=SQRT(B(J))
      WRITE (58,246)
      WRITE(58,236)(A4(J),J=1,3)
  246 FORMAT(5X,*PRINCIPAL VALUES OF G-TENSOR ARE=*,/)
      AAA(1,1)=B(7)
      AAA(1,2)=B(8)
      AAA(2,2)=B(9)
      AAA(1,3)=B(10)
      AAA(3,3)=B(11)
      AAA(2,3)=B(12)
      DO 720 J1=1,2
      J4=J1+1
      DO 720 J2=J4,3
      AAA(J2,J1)=AAA(J1,J2)
  720 CONTINUE
      CALL JACOBI3(3,AAA,1,NR,AAV)
      WRITE (58,237)
      WRITE (58,236) (AAA(J1,J1),J1=1,3)
      WRITE (58,7238)
```

```
      DO 725 J1=1,3
      WRITE (58,236) (AAV(J2,J1),J2=1,3)
  725 CONTINUE
      DO 7245 J=1,3
      IF (AAA(J,J) .LT. 1.0E-4) AAA(J,J)=0
 7245 A4(J)=SQRT(AAA(J,J))
      WRITE (58,7246)
      WRITE (58,236) (A4(J),J=1,3)
 7246 FORMAT(5X,*PRINCIPAL VALUES OF A-TENSOR ARE=*,/)
      NUMBER=NUMBER+1
      IF(NUMBER-NCASES) 1,1,2
    2 CONTINUE
      DO 230 LL=NZERO,NCASES
      WRITE(58,138) LL
      WRITE(58,141) SMD(LL)
  230 WRITE (58,235) (GG(LM,LL),LM=1,MM)
      STOP
      END

      SUBROUTINE CURFIT
C     EXAM HANDLES ALL MATRICES OF DIMENSIONS UPTO THE
C     DIMS.MM OF A,B,C, THAT IS M IS LESS THAN OR EQUAL TO
C     MM (SAME IS TRUE OF MATINV AND JACOBI)
C     EQUIVALENCE OF GRAD BEGINS AT DIMENSION OF B AFTER THE
C     EQUIV. OF B
      DIMENSION Z(400),FM(400),FC(400),
     1DF(400),ERR(400),B(12),B1(12),
     2B2(12,12),DC(5000),ABC(2),Y(4),
     3X(400),GRAD(12),D1(12),D2(12,12),
     4B3(12,12),SMD(9),HN(400),
     5ACOSZ(400),ACOSX(400),ACOSY(400)
      DIMENSION IBB(400,2),THETA(400),GT(6)
      DIMENSION AJ1(400),GGTL(8,3),GGTM(8,3),GGTN(8,3)
      COMMON/DATA1/ABC,Y
      COMMON/DATA2/DC,ACOSZ,ACOSX,ACOSY,AJ1
```

```
      EQUIVALENCE (Z,DC),(FM,DC(401)),(FC,DC(801)),
     1 (DF,DC(1201)),(ERR,DC(1601)),(HN,DC(2001)),
     3 (THETA,DC(2401)),(IBB,DC(2801)),(B,DC(4101)),
     4 (B1,DC(4125)),(B2,DC(4137)),(N,DC(4301)),
     6 (L4,DC(4302)),(Q1,DC(4303)),(Q2,DC(4304)),
     7 (M,DC(4305)),(I,DC(4306)),(L,DC(4307)),
     9 (BO,DC(4308)),(SMD,DC(4309)),(SSMD,DC(4320)),
     1 (D1,DC(4321)),(D2,DC(4333)),(GRAD,DC(4113)),
     3 (NUMBER,DC(4100)),(GT,DC(4093))
      ABC(1)="NO"
      ABC(2)="YES"
      L1 = 0
      SA = 0.0
      MM=M
      I6=I
      NN=N
      DO 1000 J=1,MM
      B1(J)=0.0
      DO 1000 K=1,MM
1000  B2(J,K)=0.0
      DO 100 I6 = 1, NN
      L=1
      I=I6
      CALL FUNC(2)
      X(I6)=ERR(I6)**2
901   FORMAT(5X,10H FUNC2,210  )
      DF(I6) =FM(I6) - FC(I6)
      DO 101 J=1,MM
      B1(J)=B1(J)-(2.0*DF(I6)*D1(J))/X(I6)
      DO 101 K=1,MM
 101  B2(J,K)=B2(J,K)-(2.0*(DF(I6)*D2(J,K)-
     1D1(J)*D1(K)))/X(I6)
 100  SA = SA + DF(I6)**2/X(I6)
      GMOD=0.0
      DO 102 J=1,M
```

```
  102 GMOD=GMOD+B1(J)**2
      WRITE(58,243)SA,GMOD
  243 FORMAT (1X,26H*INITIAL VALUE SUM OF
     1SQ.=E13.5,20X,17H*SQ MOD OF GRAD =E13.5)
      WRITE(58,1751)
 1751 FORMAT(14H0 DERIVATIVES-)
      WRITE(58,240)(B1(J),J=1,M)
  240 FORMAT (15X,5(E13.5,8X)/)
      IF (SA - Q1) 110, 110, 200
  110 LE = 1
      GO TO 600
  200 S = 0.0
      GMOD = 0.0
      BMOD = 0.0
      PROD = 0.0
      A2=ABC(1)
      DO 210 J = 1, MM
      B1(J) = 0.0
      DO 210 K = 1, MM
  210 B2(J,K) = 0.0
      WRITE(58,902)
      DO 220 I6 = 1, NN
      L=1
      I=I6
      CALL FUNC(2)
      X(I6)=ERR(I6)**2
  902 FORMAT(5X,10H FUNC2,210  )
      DF(I6) = FM(I6) - FC(I6)
      DO 220 J = 1, MM
      B1(J) = B1(J) - (2.0*DF(I6)*D1(J))/X(I6)
      DO 220 K = 1, MM
  220 B2(J,K) = B2(J,K) - (2.0*(DF(I6)*D2(J,K)
     1-D1(J)*D1(K)))/X(I6)
      DO 230 J = 1, MM
  230 GRAD(J) = B1(J)
```

```
      L1 = L1 + 1
      CALL EXAM (B2,B1,M,LF)
      WRITE(58,903)
  903 FORMAT(5X,9H EXAM,230  )
      WRITE (58,914) LF
  914 FORMAT (5X,I3)
      IF (LF)  250, 250, 305
  250 DO 231 II=1,M
      DO 231 JJ=1,M
  231 B3(II,JJ)=B2(II,JJ)
      WRITE (58,904)
      CALL JACOBI4(M,B3,4,NR,B2)
  904 FORMAT(5X,12H JACOBI1,231  )
      WRITE(58,904)
      DO 235 I6=1,MM
  235 B1(I6)=B3(I6,I6)
      A2=ABC(2)
      DO 260 J = 1, MM
  260 D1(J) = 0.0
      DO 270 J = 1, MM
      DO 270 K = 1, MM
  270 D1(K) = D1(K) + B2(J,K) *GRAD(J)
      DO 275 J = 1, MM
      IF (B1(J))  280, 290, 285
  280 B1(J) = - B1(J)
  285 D1(J) = D1(J)/B1(J)
      GO TO 275
  290 D1(J) = 0.0
  275 CONTINUE
      DO 295 J = 1, MM
  295 B1(J) = 0.0
      DO 300 J = 1, MM
      DO 300 K = 1, MM
  300 B1(J) = B1(J) + B2(J,K)*D1(K)
  305 DO 310 J=1,MM
```

```
      GMOD = GMOD + GRAD(J)**2
      BMOD = BMOD + B1(J)**2
  310 PROD = PROD + GRAD(J)*B1(J)
      IF (GMOD - Q2)  315, 315, 320
  315 LE = 2
      WRITE(58,1761) GMOD
 1761 FORMAT(5X,7H GMOD =,E13.5//)
      GO TO 600
  320 C=PROD/SQRT(BMOD*GMOD)
      IF (C) 335, 335, 400
  335 LE = 4
      GO TO 600
  400 LD = 0
      L3 = 0
      DO 410 J = 1, MM
  410 GRAD(J) = B(J) - B1(J)
  450 DO 420 I6 = 1, NN
      L=2
      I=I6
      CALL FUNC (1)
      X(I6)=ERR(I6)**2
  905  FORMAT(5X,10H FUNC1,450  )
      DF(I6) = FM(I6) - FC(I6)
  420 S = S + DF(I6)**2/X(I6)
      WRITE(58,905)
      IF (SA - S) 435, 500, 500
  435 LD = LD + 1
  430 DO440 J = 1, MM
      B1(J) = B1(J)/2.0
  906 FORMAT(5X,16H BINARY CHOP,430  )
  440 GRAD(J) = B(J) - B1(J)
      WRITE(58,906)
      S = 0.0
      L3 = L3 + 1
      IF(L3-5)450,460,460
```

```
460 LE = 5
    GO TO 600
500 IF (LD) 505, 505, 506
506 LD = 0
    GO TO 430
505 DO 510 J = 1, MM
510 B(J) = GRAD(J)
    SA = S
    IF (SA - Q1) 507, 507, 530
507 LE = 1
    GO TO 600
530 IF (L4) 200, 200, 900
900 WRITE(58,920)L1,A2,L3,S,GMOD,(B(J),J=1,M)
920 FORMAT(//,15H ITERATION NO.=I5,10X,43H
   1TRANSFORMATION MADE TO PRINCIPAL AXES = A4,10X, 18H
   2BINARY CHOP USED=I3,6H TIMES/1X,27H WEIGHTED SUM OF
   3SQUARES = E14.7,25X,32H   SQUARE MODULUS OF GRADIENT =
   4E14.7/20H   PARAMETERS B(J) -/(6E17.8)/)
    IF (L1 - L4) 200, 910, 910
910 LE = 6
    GO TO 600
600 DO 710 J=1,MM
    B1(J) = 0.0
    DO 710 K=1,MM
710 B2(J,K) = 0.0
    L=1
    WRITE(58,907)
907 FORMAT(5X,* FUNC(2),720 *)
    DO 720 I6 = 1, NN
    I=I6
    CALL FUNC(2)
    X(I6)=ERR(I6)**2
    DF(I6) = FM(I6) - FC(I6)
    DO 720 J = 1, MM
    B1(J) = B1(J) - (2.0*DF(I6)*D1(J))/X(I6)
```

```
      DO 720 K = 1, MM
  720 B2(J,K) = B2(J,K) - ((DF(I6)*D2(J,K)
     1-D1(J)*D1(K)))/X(I6)
      WRITE (58,3029)
 3029 FORMAT(* I AM LOST IN MANTINV*)
      CALL MATINV(B2,M,B1,1,DETERM)
      WRITE (58,3029)
      DO 730 J=1,MM
      IF (B2(J,J)) 2001,2001,2002
2001  B1(J) = -SQRT(-B2(J,J))
      GO TO 730
2002  B1(J)= SQRT(B2(J,J))
  730 CONTINUE
      DO 740 J=1,MM
      DO 740 K=1,MM
  740 B2(J,K)=B2(J,K)/(B1(J)*B1(K))
      WRITE(58,551)LE,SA
  551 FORMAT(//,13H EXIT NUMBER=I3,20X,25H WEIGHTED  SUM  OF
     1SQUARES=E15.8//)
      SSMD = SA
 9999 CONTINUE
      RETURN
      END
      SUBROUTINE FUNC(LX)
C     SUBROUTINE FUNC
      DIMENSION DC(5000),B(12,2),D1(12),
     1 D2(12,12),FC(400),Z(400),S(4,4),SIGN(400), HN(400),
     3 ST(4,4,16),FM(400),DF(400),DELH(400),ERR(400),B1(12),
     4 B2(12,12),SMD(9),ACOSZ(400),ACOSX(400),ACOSY(400),
     6 IBB(400,2),THETA(400),DD(16),GT(6),AJ1(400),
     7 AL(400),AM(400),AN(400),GGT(3,3),C1(12),
     9 AZ(6),AX(6),AY(6),GB(6),F2(6),C2(12),C3(12),CK(12),
     1 F4(12),CC(12),AK2(6),BB(6)
      COMMON/DATA2/DC,ACOSZ,ACOSX,ACOSY,AJ1
      COMMON/DATA3/DELH
```

```
      EQUIVALENCE (Z,DC),(FM,DC(401)),(FC,DC(801)),
     1 (DF,DC(1201)),(ERR,DC(1601)),(HN,DC(2001)),
     3 (THETA,DC(2401)),(IBB,DC(2801)),(B,DC(4101)),
     4 (B1,DC(4125)),(B2,DC(4137)),(N,DC(4301)),
     6 (L4,DC(4302)),(Q1,DC(4303)),(Q2,DC(4304)),
     7 (M,DC(4305)),(I,DC(4306)),(L,DC(4307)),
     9 (BO,DC(4308)),(SMD,DC(4309)),(SSMD,DC(4320)),
     1 (D1,DC(4321)),(D2,DC(4333)),
     2 (NUMBER,DC(4100)),(GT,DC(4093))
      IF(Z(I).EQ.0.) GO TO 135
      BETA=92.732/66252.
      BETAN=.00054464*BETA
      RD=3.1415926/180.
      FACTOR=92.732/66252.
      SB4L=SIN(B(4,L))
      CB4L=COS(B(4,L))
      SB5L=SIN(B(5,L))
      CB5L=COS(B(5,L))
      SB6L=SIN(B(6,L))
      CB6L=COS(B(6,L))
      GGT(1,1)=CB4L
      GGT(1,2)=SB4L*SB5L
      GGT(1,3)=-SB4L*CB5L
      GGT(2,1)=SB6L*SB4L
      GGT(2,2)=CB6L*CB5L-CB4L*SB5L*SB6L
      GGT(2,3)=CB6L*SB5L+CB4L*CB5L*SB6L
      GGT(3,1)=CB6L*SB4L
      GGT(3,2)=-SB6L*CB5L-CB4L*SB5L*CB6L
      GGT(3,3)=-SB6L*SB5L+CB4L*CB5L*CB6L
      IF (I.GT.1) GO TO 119
      WRITE(58,118)
      DO 117 IA=1,3
  117 WRITE(58,116) (GGT(IA,IB),IB=1,3)
  116 FORMAT(5X,3(F10.6,3X),/)
  118 FORMAT(5X,*ELEMENTS OF COMPUTED GGT MATRIX FROM  EULER
```

```
     1 ANGLES ARE=*,//)
  119 CONTINUE
      AL(I)=ACOSZ(I)*GGT(1,1)+
     1ACOSX(I)*GGT(1,2)+ACOSY(I)*GGT(1,3)
      AM(I)=ACOSZ(I)*GGT(2,1)+
     1ACOSX(I)*GGT(2,2)+ACOSY(I)*GGT(2,3)
      AN(I)=ACOSZ(I)*GGT(3,1)+
     1ACOSX(I)*GGT(3,2)+ACOSY(I)*GGT(3,3)
      FCI=B(1,L)*AL(I)**2+B(2,L)*AM(I)**2+B(3,L)*AN(I)**2
      ENELSP=Z(I)*BETA*SQRT(FCI)
      BB(1)=B(1,L)*AL(I)**2
      BB(3)=B(2,L)*AM(I)**2
      BB(5)=B(3,L)*AN(I)**2
      BB(2)=2.*SQRT(B(1,L)*B(2,L))*AL(I)*AM(I)
      BB(4)=2.*SQRT(B(1,L)*B(3,L))*AL(I)*AN(I)
      BB(6)=2.*SQRT(B(2,L)*B(3,L))*AM(I)*AN(I)
      AEFF2=B(7,L)*BB(1)+B(9,L)*BB(3)+B(11,L)*BB(5)+
     1B(8,L)*BB(2)+B(10,L)*BB(4)+B(12,L)*BB(6)
      AMI=4.5-AJ1(I)
      IF(AEFF2.LT.(0.)) GO TO 109
      AEFF=SQRT(AEFF2/FCI)
      HYPFEN=AEFF*AMI
      CC(7)=B(7,L)**2+B(8,L)**2+B(10,L)**2
      CC(8)=B(7,L)*B(8,L)+B(8,L)*B(9,L)+B(10,L)*B(12,L)
      CC(9)=B(8,L)**2+B(9,L)**2+B(12,L)**2
      CC(10)=B(7,L)*B(10,L)+B(8,L)*B(12,L)+B(10,L)*B(11,L)
      CC(11)=B(10,L)**2+B(12,L)**2+B(11,L)**2
      CC(12)=B(8,L)*B(10,L)+B(9,L)*B(12,L)+B(11,L)*B(12,L)
      CKK=CC(7)*BB(1)+CC(9)*BB(3)+CC(11)*BB(5)+CC(8)*BB(2)+
     1CC(10)*BB(4)+CC(12)*BB(6)
      AKK=SQRT(CKK/AEFF2)
      AI=3.5
      AI1=AI*(AI+1.)
      DELE3=(0.5*(B(7,L)+B(9,L)+B(11,L))*(AI1-AMI**2)-
     1AKK**2*(AI1-3.*AMI**2)/2.-HYPFEN**2)/(2.*ENELSP)
```

```
      FC(I)=ENELSP+HYPFEN+DELE3
      ERR(I)=SQRT(FCI)*DELH(I)*FACTOR
      ERR(I)=1.
      GO TO 136
  135 CONTINUE
      FC(I)=HN(I)
      ERR(I)=1.
  136 CONTINUE
      IF(LX-1)110,110,120
  120 CONTINUE
      DO  235 IZ = 1,12
      D1(IZ) = 0.0
      DO  235 JZ = 1,12
  235 D2(IZ,JZ) =0.0
      IF(Z(I).EQ.0.) GO TO 110
      DDD=.5*AMI/(FCI*AEFF)
      C2(7)=DDD*BB(1)
      C2(8)=DDD*BB(2)
      C2(9)=DDD*BB(3)
      C2(10)=DDD*BB(4)
      C2(11)=DDD*BB(5)
      C2(12)=DDD*BB(6)
      BETAB=BETA*Z(I)
      GZ=SQRT(B(1,L))
      GX=SQRT(B(2,L))
      GY=SQRT(B(3,L))
      AZZ=SQRT(BB(1))
      AXX=SQRT(BB(3))
      AYY=SQRT(BB(5))
      AZ(1)=0.5*AL(I)/GZ
      AZ(2)=AZ(3)=0.
      AX(2)=0.5*AM(I)/GX
      AX(1)=AX(3)=0.
      AY(3)=0.5*AN(I)/GY
      AY(1)=AY(2)=0.
```

```
      ALL=ACOSX(I)
      AMM=ACOSY(I)
      ANN=ACOSZ(I)
      AZ(4)=GZ*(ALL*CB4L*SB5L-AMM*CB4L*CB5L-ANN*SB4L)
      AZ(5)=GZ*(ALL*SB4L*CB5L+AMM*SB4L*SB5L)
      AZ(6)=0.
      AX(4)=GX*(ALL*SB4L*SB5L*SB6L-
     1AMM*SB4L*CB5L*SB6L+ANN*CB4L*SB6L)
      AX(5)=GX*(ALL*(-CB6L*SB5L-CB4L*CB5L*SB6L)+
     1AMM*(CB6L*CB5L-1CB4L*SB5L*SB6L))
      AX(6)=GX*(ALL*(-SB6L*CB5L-CB4L*SB5L*CB6L)+
     1AMM*(-SB6L*SB5L+CB4L*CB5L*CB6L)+ANN*CB6L*SB4L)
      AY(4)=GY*(ALL*SB4L*SB5L*CB6L-
     1AMM*SB4L*CB5L*CB6L+ANN*CB6L*CB5L)
      AY(5)=GY*(ALL*(SB6L*SB5L-CB4L*CB5L*CB6L)+
     1AMM*(-SB6L*CB5L-1CB4L*SB5L*CB6L))
      AY(6)=GY*(ALL*(-CB6L*CB5L+CB4L*SB5L*SB6L)+
     1AMM*(-CB6L*SB5L-CB4L*CB5L*SB6L)-ANN*SB6L*SB4L)
      DO 910 IA=1,6
      GB(IA)=(AZZ*AZ(IA)+AXX*AX(IA)+AYY*AY(IA))*BETAB/ENELSP
      IA1=IA+6
      C1(IA1)=0.
  910 C1(IA)=BETAB*GB(IA)
C     C1(IA) ARE DERIVATIVES OF ENELSP
      AXX=SQRT(BB(3))
      AYY=SQRT(BB(5))
      AZZ=SQRT(BB(1))
      F2(1)=2.*AZ(1)*(AZZ*B(7,L)+AXX*B(8,L)+AYY*B(10,L))
      F2(2)=2.*AX(2)*(AZZ*B(8,L)+AXX*B(9,L)+AYY*B(12,L))
      F2(3)=2.*AY(3)*(AZZ*B(10,L)+AXX*B(12,L)+AYY*B(11,L))
      DO 915 IA=4,6
      F2(IA)=2.*(AXX*AX(IA)*B(9,L)+AYY*AY(IA)*B(11,L)+
     1AZZ*AZ(IA)*B(7,L)+(AXX*AY(IA)+AYY*AX(IA))*B(12,L)+
     2(AXX*AZ(IA)+AZZ*AX(IA))*B(8,L)+
     3(AYY*AZ(IA)+AZZ*AY(IA))*B(10,L))
```

```
  915 CONTINUE
      F4(1)=2.*AZ(1)*(AZZ*CC(7)+AXX*CC(8)+AYY*CC(10))
      F4(2)=2.*AX(2)*(AZZ*CC(8)+AXX*CC(9)+AYY*CC(12))
      F4(3)=2.*AY(3)*(AZZ*CC(10)+AXX*CC(12)+AYY*CC(11))
      DO 920 IA=4,6
      F4(IA)=2.*(AXX*AX(IA)*CC(9)+AYY*AY(IA)*CC(11)+
     1AZZ*AZ(IA)*CC(7)+
     2(AXX*AY(IA)+AYY*AX(IA))*CC(12)+
     3(AXX*AZ(IA)+AZZ*AX(IA))*CC(8)+
     4(AYY*AZ(IA)+AZZ*AY(IA))*CC(10))
  920 CONTINUE
      DO 925 IA=1,6
  925 C2(IA)=(-BETAB*HYPFEN*GB(IA)/ENELSP+
     1(BETAB**2)*F2(IA)/(2.*(ENELSP**2)*HYPFEN))*AMI
C     C2(IA) ARE DERIVATIVES OF HYPFEN
      DO 927 IA=1,6
      IA1=IA+1
  927 C2(IA1)=(AMI**2)*BB(IA)/(0.5*FCI*HYPFEN)
      DO 930 IA=1,6
  930 AK2(IA)=((BETAB*AMI/(ENELSP*HYPFEN))**2)*(F4(IA)-
     1(2.*CCK/(ENELSP*HYPFEN))*(C1(IA)*HYPFEN+
     2ENELSP*C2(IA)))
      DO 935 IA=1,6
  935 C3(IA)=(ENELSP*(-0.5*(AI1-3.*(AMI**2))*AK2(IA)-
     1 2.*HYPFEN*C2(IA))-
     2(0.5*(B(7,L)+B(9,L)+B(11,L))*(AI1-(AMI**2))-
     3 0.5*(AKK**2)*(AI1-3.*(AMI**2))-
     4 HYPFEN**2)*C1(IA))/(2.*(ENELSP**2))
C     C3(IA) ARE DERIVATIVES OF DELE3
      F4(7)=2.*BB(1)*B(7,L)+BB(2)*B(8,L)+BB(4)*B(10,L)
      F4(8)=2.*(BB(1)+BB(3))*B(8,L)+BB(2)*(B(7,L)+B(9,L))+
     1BB(4)*B(12,L)+BB(6)*B(10,L)
      F4(9)=2.*BB(3)*B(9,L)+BB(2)*B(8,L)+BB(6)*B(12,L)
      F4(10)=2.*(BB(1)+BB(5))*B(10,L)+
     1BB(4)*(B(7,L)+B(11,L))+
```

```
     2BB(2)*B(12,L)+BB(6)*B(8,L)
      F4(11)=2.*BB(5)*B(11,L)+BB(4)*B(10,L)+BB(6)*B(12,L)
      F4(12)=2.*(BB(3)+BB(5))*B(12,L)+
     1BB(6)*(B(9,L)+B(11,L))+
     2BB(2)*B(10,L)+BB(4)*B(8,L)
      DO 1237 IA=7,12
1237  CK(IA)=-AKK*C2(IA)/(AEFF*AMI)+
     1F4(IA)/(2.*FCI*(AEFF**2)*AKK)
      DO 1236 IA=7,12
      AIA=0.
      IF (IA.EQ.7.OR.IA.EQ.9.OR.IA.EQ.11) AIA=1.
1236  C3(IA)=(AKK*CK(IA)*(3.*AMI**2-
     1 AI1)+0.5*(AI1-AMI**2)*AIA-
     2 2.*HYPFEN*C2(IA))/(2.*ENELSP)
      DO 1235 IA=1,12
123   D1(IA)=C1(IA)+C2(IA)+C3(IA)
      GO TO 110
 109  WRITE(58,108) I
 108  FORMAT(5X,*NEG AEFF2 FOR I=*,I3)
      FC(I)=FM(I)
      DO 197 JJ=1,12
 197  D1(JJ)=0.
 110  CONTINUE
      RETURN
      END
C
      SUBROUTINE EULER(GGT,THETA,PHI,PSI)
C     SUBROUTINE EULER
C     THIS PROGRAMME CALCULATES THE EULER ANGLES THETA, PHI
C        AND PSI FROM THE DIRECTION COSINES OF G-SQUARE
C      DIAGONAL MATRIX.
      DIMENSION GGT(3,3),TPS(4,4,4),AMTRX(9),
     1 BMTRX(64,9),A(64),B(64),
     2 C(64),IA(64),IB(64),IC(64),ABSMT(9)
      AMTRX(1)=GGT(1,1)
```

```
      AMTRX(2)=GGT(1,2)
      AMTRX(3)=GGT(1,3)
      AMTRX(4)=GGT(2,1)
      AMTRX(5)=GGT(2,2)
      AMTRX(6)=GGT(2,3)
      AMTRX(7)=GGT(3,1)
      AMTRX(8)=GGT(3,2)
      AMTRX(9)=GGT(3,3)
      DO 50 I=1,9
   50 ABSMT(I)=AMTRX(I)/ABS(AMTRX(I))
      ATHETA=ACOS(ABS(AMTRX(1)))
      APHI=ATAN(ABS(AMTRX(2)/AMTRX(3)))
      APSI=ATAN(ABS(AMTRX(4)/AMTRX(7)))
      API=3.141592654
      DO 5 I1=1,4
      DO 5 I2=1,4
      DO 5 I3=1,4
      IJK=I3+(I2-1)*4+(I1-1)*16
      IF (I1.EQ.1.) THETA=ATHETA
      IF (I2.EQ.1.) PHI=APHI
      IF (I3.EQ.1.) PSI=APSI
      IF (I1.EQ.2) THETA=API-ATHETA
      IF (I1.EQ.3) THETA=API+ATHETA
      IF (I1.EQ.4) THETA=2.*API-ATHETA
      IF (I2.EQ.2) PHI=API-APHI
      IF (I2.EQ.3) PHI=API+APHI
      IF (I2.EQ.4) PHI=2.*API-APHI
      IF (I3.EQ.2) PSI=API-APSI
      IF (I3.EQ.3) PSI=API+APSI
      IF (I3.EQ.4) PSI=2.*API-APSI
      BMTRX(IJK,1)=COS(THETA)
      BMTRX(IJK,2)=SIN(THETA)*SIN(PHI)
      BMTRX(IJK,3)=-SIN(THETA)*COS(PHI)
      BMTRX(IJK,4)=SIN(THETA)*SIN(PSI)
      BMTRX(IJK,5)=COS(PHI)*COS(PSI)
```

```
     1-COS(THETA)*SIN(PHI)*SIN(PSI)
      BMTRX(IJK,6)=SIN(PHI)*COS(PSI)
     1+COS(THETA)*COS(PHI)*SIN(PSI)
      BMTRX(IJK,7)=SIN(THETA)*COS(PSI)
      BMTRX(IJK,8)=-COS(PHI)*SIN(PSI)
     1-COS(THETA)*SIN(PHI)*COS(PSI)
      BMTRX(IJK,9)=-SIN(PHI)*SIN(PSI)
     1+COS(THETA)*COS(PHI)*COS(PSI)
      DO 100 I=1,9
  100 BMTRX(IJK,I)=BMTRX(IJK,I)/ABS(BMTRX(IJK,I))
      IA(IJK)=I1
      IB(IJK)=I2
      IC(IJK)=I3
      WRITE(58,60) IJK,IA(IJK),IB(IJK),IC(IJK),BMTRX(IJK,1),
     1BMTRX(IJK,2),BMTRX(IJK,3),BMTRX(IJK,4),BMTRX(IJK,5),
     2BMTRX(IJK,6),BMTRX(IJK,7),BMTRX(IJK,8),BMTRX(IJK,9)
   60 FORMAT(5X,4(I3,2X),9(F8.2,1X),/)
    5 CONTINUE
      DO 25 IJK=1,64
      ACOS2=0.
      DO 10 II=1,9
   10 ACOS2=ACOS2+(BMTRX(IJK,II)-ABSMT(II))**2
      WRITE(58,55) ACOS2,IA(IJK),IB(IJK),IC(IJK)
   55 FORMAT(5X,*ACOS2=*,E10.4,3X,
     1*IA=*,I2,3X,*IB=*,I2,3X,*IC=*,I2,/)
      IF (ACOS2.GT.(0.01)) GO TO 15
      WRITE(58,35) IJK, IA(IJK),IB(IJK),IC(IJK)
      I1=IA(IJK)
      I2=IB(IJK)
      I3=IC(IJK)
      I4=IJK
   15 CONTINUE
   25 CONTINUE
   35 FORMAT(2X,*IJK=*,I4,2X,*IA=*,
     1I4,2X,*IB=*,I4,2X,*IC=*,I4,/)
```

```
   40 FORMAT(2X,*THETA=*,F10.4,2X,
     1*PHI=*,F10.4,2X,*PSI=*,F10.4,2X,
     2*DTAETA=*,F10.4,2X,*DPHI=*,F10.4,2X,*DPSI=*,F10.4)
      IF (I1.EQ.1) THETA=ATHETA
      IF (I2.EQ.1) PHI=APHI
      IF (I3.EQ.1) PSI=APSI
      IF (I1.EQ.2) THETA=API-ATHETA
      IF (I1.EQ.3) THETA=API+ATHETA
      IF (I1.EQ.4) THETA=2.*API-ATHETA
      IF (I2.EQ.2) PHI=API-APHI
      IF (I2.EQ.3) PHI=API+APHI
      IF (I2.EQ.4) PHI=2.*API-APHI
      IF (I3.EQ.2) PSI=API-APSI
      IF (I3.EQ.3) PSI=API+APSI
      IF (I3.EQ.4) PSI=2.*API-APSI
      DTHETA=180.*THETA/API
      DPHI=180.*PHI/API
      DPSI=180.*PSI/API
      WRITE(58,40) THETA,PHI,PSI,DTHETA,DPHI,DPSI
      RETURN
      END
C
      SUBROUTINE EXAM(A,B,M,LF)
C     SUBROUTINE EXAM
      DIMENSION A(12,12),B(12),C(12)
      DO 80 J=1,M
   80 C(J)=A(J,J)
      IF(A(1,1)) 60,200,70
   60 A(1,1) =-SQRT(-A(1,1))
      GO TO 300
   70 A(1,1) =SQRT(A(1,1))
      GO TO 100
  100 IF(M-1)400,400,110
  110 DO 115 K=2,M
  115 A(1,K)=A(1,K)/(A(1,1)
```

```
      DO 120 J=2,M
      J1=J-1
      S=A(J,J)
      DO 125 L=1,J1
  125 S=S-A(L,J)**2
      IF (S) 50,200,40
   50 A(J,J) =-SQRT(-S)
      GO TO 300
   40 A(J,J) =SQRT(S)
      GO TO 130
  130 IF(J-M)135,400,400
  135 J2=J+1
      DO 120 K=J2,M
      S=A(J,K)
      DO 145 L=1,J1
  145 S=S-A(L,J)*A(L,K)
  120 A(J,K)=S/A(J,J)
  400 B(1)=B(1)/A(1,1)
      IF(M-1)420,420,405
  405 DO 410 J=2,M
      S=B(J)
      J1=J-1
      DO 415 L=1,J1
  415 S=S-A(L,J)*B(L)
  410 B(J)=S/A(J,J)
  420 B(M)=B(M)/A(M,M)
      J=M-1
  435 IF(J)450,450,425
  425 S=B(J)
      J2=J+1
      DO 430 L=J2,M
  430 S=S-A(J,L)*B(L)
      B(J)=S/A(J,J)
      J=J-1
      GO TO 435
```

```
  450 LF=1
      GO TO 460
  200 LF=0
      GO TO 460
  300 LF=-1
  460 DO 465 J=1,M
      A(J,J)=C(J)
      IF(J-M)470,475,475
  470 J2=J+1
      DO 465 K=J2,M
  465 A(J,K)=A(K,J)
  475 RETURN
      END
C
      SUBROUTINE MATINV(A,N,B,M,DETERM)
C     SUBROUTINE MATINV
C     MATRIX INVERSION WITH ACCOMPANYING SOLUTION OF LINEAR
C     EQUATIONS
      DIMENSION IPIVOT(12),A(12,12),
     1B(12,1),INDEX(12,2),PIVOT(12)
      EQUIVALENCE (IROW,JROW),(ICOLUM,JCOLUM),(AMAX,T,SWAP)
      DETERM=1.0
      DO 20 J=1,N
   20 IPIVOT(J)=0
      DO 550 I=1,N
      AMAX=0.0
      DO 105 J=1,N
      IF(IPIVOT(J)-1)60,105,60
   60 DO 100 K=1,N
      IF(IPIVOT(K)-1)80,100,740
   80 IF(ABS(AMAX)-ABS(A(J,K)))85,100,100
   85 IROW=J
      ICOLUM=K
      AMAX=A(J,K)
  100 CONTINUE
```

```
105 CONTINUE
    IPIVOT(ICOLUM)=IPIVOT(ICOLUM)+1
    IF (IROW-ICOLUM)140,260,140
140 DETERM=-DETERM
    DO 200 L=1,N
    SWAP=A(IROW,L)
    A(IROW,L)=A(ICOLUM,L)
200 A(ICOLUM,L)=SWAP
    IF(M)260,260,210
210 DO 250 L=1,M
    SWAP=B(IROW,L)
    B(IROW,L)=B(ICOLUM,L)
250 B(ICOLUM,L)=SWAP
260 INDEX(I,1)=IROW
    INDEX(I,2)=ICOLUM
    PIVOT(I)=A(ICOLUM,ICOLUM)
    DETERM=DETERM*PIVOT(I)
    A(ICOLUM,ICOLUM)=1.0
    DO 350 L=1,N
350 A(ICOLUM,L)=A(ICOLUM,L)/PIVOT(I)
    IF(M)380,380,360
360 DO 370 L=1,M
370 B(ICOLUM,L)=B(ICOLUM,L)/PIVOT(I)
380 DO 550 L1=1,N
    IF (L1-ICOLUM)400,550,400
400 T=A(L1,ICOLUM)
    A(L1,ICOLUM)=0.0
    DO 450 L=1,N
450 A(L1,L)=A(L1,L)-A(ICOLUM,L)*T
    IF(M)550,550,460
460 DO 500 L=1,M
500 B(L1,L)=B(L1,L)-B(ICOLUM,L)*T
550 CONTINUE
    DO 710 I=1,N
    L=N+1-I
```

```
      IF(INDEX(L,1)-INDEX(L,2))630,710,630
  630 JROW=INDEX(L,1)
      JCOLUM=INDEX(L,2)
      DO 705 K=1,N
      SWAP=A(K,JROW)
      A(K,JROW)=A(K,JCOLUM)
      A(K,JCOLUM)=SWAP
  705 CONTINUE
  710 CONTINUE
  740 RETURN
      END
C
      SUBROUTINE JACOBI4(N,Q,JVEC,M,V)
C       SUBPROGRAM  FOR  DIAGONALIZATION  OF  MATRIX  Q  BY
C       SUCCESSIVE ROTATIONS
      DIMENSION Q(12,12),V(12,12),X(12),IH(12)
   13 FORMAT (2E15.5,//)
C NEXT 8 STATEMENTS FOR SETTING INITIAL VALUES OF MATRIX V
      IF(JVEC) 10,15,10
   10 DO 14 I=1,N
      DO 14 J=1,N
      IF(I-J) 12,11,12
   11 V(I,J)=1.0
      GO TO 14
   12 V(I,J)=0.
   14 CONTINUE
   15 M=0
C     NEXT 8 STATEMENTS SCAN FOR LARGEST OFF DIAG. ELEM.  IN
C     EACH ROW
C     X(I) CONTAINS LARGEST ELEMENT IN ITH ROW
C     IH(I) HOLDS  SECOND  SUBSCRIPT  DEFINING  POSITION  OF
C     ELEMENT
      MI=N-1
      DO 30 I=1,MI
      X(I)=0.
```

```
      MJ=I+1
      DO 30 J=MJ,N
      IF (X(I)-ABS (Q(I,J))) 20,20,30
   20 X(I)=ABS (Q(I,J))
      IH(I)=J
   30 CONTINUE
C     NEXT 7 STATEMENTS FIND FOR MAXIMUM OF X(I)S FOR  PIVOT
C     ELEMENT
   40 DO 70 I=1,MI
      IF(I-1) 60,60,45
   45 IF (XMAX-X(I)) 60,70,70
   60 XMAX=X(I)
      IP=I
      JP=IH(I)
   70 CONTINUE
C     NEXT 2 STATEMENTS TEST FOR XMAX,IF LESS THAN 10**-8,GO
C     TO 1000
      EPSI=1.E-12
      IF (XMAX-EPSI) 1000,1000,148
  148 M=M+1
C     NEXT 11 STATEMENTS FOR COMPUTING
C     TANG,SINE,COSN,Q(I,I),Q(J,J)
      IF (Q(IP,IP)-Q(JP,JP)) 150,151,151
  150 TANG =-2.*Q(IP,JP)/(ABS(Q(IP,IP)-
     1Q(JP,JP))+SQRT((Q(IP,IP)-Q(JP,JP)
     2)**2+4.*Q(IP,JP)**2))
      GO TO 160
  151 TANG =+2.*Q(IP,JP)/(ABS(Q(IP,IP)-
     1Q(JP,JP))+SQRT((Q(IP,IP)-Q(JP,JP)
     2)**2+4.*Q(IP,JP)**2))
  160 COSN=1.0/SQRT(1.0+TANG**2)
      SINE=TANG*COSN
      QII= Q(IP,IP)
      Q(IP,IP)=
     1COSN**2*(QII+TANG*(2.*Q(IP,JP)+TANG*Q(JP,JP)))
```

```
      Q(JP,JP)=
     1COSN**2*(Q(JP,JP)-TANG*(2.*Q(IP,JP)-TANG*QII))
      Q(IP,JP)=0.
C     NEXT 4 STATEMENTS FOR PSEUDO RANK OF THE E1GENVALUES
      IF (Q(IP,IP)-Q(JP,JP)) 152,153,153
  152 TEMP=Q(IP,IP)
      Q(IP,IP)=Q(JP,JP)
      Q(JP,JP)=TEMP
C     NEXT 6 STATEMENTS ADJUST SIN,COS FOR COMPUTATION OF
C     Q(I,K),V(I,K)
      IF(SINE) 154,155,155
  154 TEMP=+COSN
      GO TO 170
  155 TEMP=-COSN
  170 COSN=ABS(SINE)
      SINE=TEMP
C     NEXT 10 STATEMENTS FOR INSPECTING T8E IHS BETWEEN I+1
C     AND N-1 TO DETERMINE WHETHER A NEW MAXIMUM VALUE
C     SHOULD BE COMPUTED SINCE THE PRESENT MAXIMUM IS IN THE
C     I OR J ROW
  153 DO 350 I=1,MI
      IF (I-IP) 210,350,200
  200 IF (I-JP) 210,350,210
  210 IF (IH(I)-IP) 230,240,230
  230 IF (IH(I)-JP) 350,240,350
  240 K= IH(I)
      TEMP=Q(I,K)
      Q(I,K)=0.
      MJ=I+1
      X(I)=0.
C     NEXT 5 STATEMENTS SEARCH IN DEPLETED ROW FOR NEW
C     MAXIMUM
      DO 320 J=MJ,N
      IF (X(I)-ABS(Q(I,J))) 300,300,320
  300 X(I)=ABS(Q(I,J))
```

```
      IH(I)=J
  320 CONTINUE
      Q(I,K)=TEMP
  350 CONTINUE
      X(IP)=0.
      X(JP)=0.
C NEXT 30 STATEMENTS FOR CHANGING THE OTHER ELEMENTS  OF Q
      DO 530 I=1,N
      IF (I-IP) 370,530,420
  370 TEMP=Q(I,IP)
      Q(I,IP)=COSN*TEMP+SINE*Q(I,JP)
      IF (X(I)-ABS(Q(I,IP))) 380,390,390
  380 X(I)=ABS(Q(I,IP))
      IH(I)=IP
  390 Q(I,JP)=-SINE*TEMP+COSN*Q(I,JP)
      IF (X(I)-ABS(Q(I,JP))) 400,530,530
  400 X(I)=ABS(Q(I,JP))
      IH(I)=JP
      GO TO 530
  420 IF (I-JP) 430,530,480
  430 TEMP=Q(IP,I)
      Q(IP,I)=COSN*TEMP+SINE*Q(I,JP)
      IF (X(IP)-ABS(Q(IP,I))) 440,450,450
  440 X(IP)=ABS(Q(IP,I))
      IH(IP)=I
  450 Q(I,JP)=-SINE*TEMP+COSN*Q(I,JP)
      IF (X(I)-ABS(Q(I,JP))) 400,530,530
  480 TEMP=Q(IP,I)
      Q(IP,I)=COSN*TEMP+SINE*Q(JP,I)
      IF(X(IP)-ABS(Q(IP,I))) 490,500,500
  490 X(IP)=ABS(Q(IP,I))
      IH(IP)=I
  500 Q(JP,I)=-SINE*TEMP+COSN*Q(JP,I)
      IF (X(JP)-ABS(Q(JP,I))) 510,530,530
  510 X(JP)=ABS(Q(JP,I))
```

```
      IH(JP)=I
  530 CONTINUE
C     NEXT 6 STATEMENTS TEST FOR COMPUTATION OF E1GENVECTORS
      IF (JVEC) 540,40,540
  540 DO 550 I=1,N
      TEMP=V(I,IP)
      V(I,IP)= COSN*TEMP+SINE*V(I,JP)
  550 V(I,JP)=-SINE*TEMP+COSN*V(I,JP)
      GO TO 40
 1000 AAM=FLOAT(M)
      WRITE (58,13) EPSI,AAM
      RETURN
      END
C
      SUBROUTINE JACOBI3(N,Q,JVEC,M,V)
C      SUBPROGRAM  FOR  DIAGONALIZATION  OF  MATRIX  Q  BY
C      SUCCESSIVE ROTATIONS
      DIMENSION Q(3,3),V(3,3),X(3),IH(3)
   13 FORMAT (2E15.5)
C NEXT 8 STATEMENTS FOR SETTING INITIAL VALUES OF MATRIX V
      IF(JVEC) 10,15,10
   10 DO 14 I=1,N
      DO 14 J=1,N
      IF(I-J) 12,11,12
   11 V(I,J)=1.0
      GO TO 14
   12 V(I,J)=0.
   14 CONTINUE
   15 M=0
C     NEXT 8 STATEMENTS SCAN FOR LARGEST OFF DIAG. ELEM.  IN
C     EACH ROW X(I) CONTAINS  LARGEST  ELEMENT  IN  ITH  ROW
C     IH(I) HOLDS  SECOND  SUBSCRIPT  DEFINING  POSITION  OF
C     ELEMENT
      MI=N-1
      DO 30 I=1,MI
```

```
      X(I)=0.
      MJ=I+1
      DO 30 J=MJ,N
      IF (X(I)-ABS (Q(I,J))) 20,20,30
   20 X(I)=ABS (Q(I,J))
      IH(I)=J
   30 CONTINUE
C     NEXT 7 STATEMENTS FIND FOR MAXIMUM OF X(I)S FOR PIVOT
C     ELEMENT
   40 DO 70 I=1,MI
      IF(I-1) 60,60,45
   45 IF (XMAX-X(I)) 60,70,70
   60 XMAX=X(I)
      IP=I
      JP=IH(I)
   70 CONTINUE
C     NEXT 2 STATEMENTS TEST FOR XMAX,IF LESS THAN 10**-8,GO
C     TO 1000
      EPSI=1.E-12
      IF (XMAX-EPSI) 1000,1000,148
  148 M=M+1
C                NEXT   11   STATEMENTS   FOR   COMPUTING
C      TANG,SINE,COSN,Q(I,I),Q(J,J)
      IF (Q(IP,IP)-Q(JP,JP)) 150,151,151
  150 TANG =-2.*Q(IP,JP)/(ABS(Q(IP,IP)-Q(JP,JP))+
     1 SQRT((Q(IP,IP)-Q(JP,JP))**2+4.*Q(IP,JP)**2))
      GO TO 160
  151 TANG =+2.*Q(IP,JP)/(ABS(Q(IP,IP)-Q(JP,JP))+
     1SQRT((Q(IP,IP)-Q(JP,JP)
     1)**2+4.*Q(IP,JP)**2))
  160 COSN=1.0/SQRT(1.0+TANG**2)
      SINE=TANG*COSN
      QII= Q(IP,IP)
      Q(IP,IP)=
     1COSN**2*(QII+TANG*(2.*Q(IP,JP)+TANG*Q(JP,JP)))
```

```
      Q(JP,JP)=
     1COSN**2*(Q(JP,JP)-TANG*(2.*Q(IP,JP)-TANG*QII))
      Q(IP,JP)=0.
C     NEXT 4 STATEMENTS FOR PSEUDO RANK OF THE E1GENVALUES
      IF (Q(IP,IP)-Q(JP,JP)) 152,153,153
  152 TEMP=Q(IP,IP)
      Q(IP,IP)=Q(JP,JP)
      Q(JP,JP)=TEMP
C     NEXT 6 STATEMENTS ADJUST SIN,COS  FOR  COMPUTATION  OF
C     Q(I,K),V(I,K)
      IF(SINE) 154,155,155
  154 TEMP=+COSN
      GO TO 170
  155 TEMP=-COSN
  170 COSN=ABS(SINE)
      SINE=TEMP
C     NEXT 10 STATEMENTS FOR INSPECTING  T8E IHS BETWEEN I+1
C     AND N-1 TO  DETERMINE  WHETHER  A  NEW  MAXIMUM  VALUE
C     SHOULD BE COMPUTED SINCE THE PRESENT MAXIMUM IS IN THE
C     I OR J ROW
  153 DO 350 I=1,MI
      IF (I-IP) 210,350,200
  200 IF (I-JP) 210,350,210
  210 IF (IH(I)-IP) 230,240,230
  230 IF (IH(I)-JP) 350,240,350
  240 K= IH(I)
      TEMP=Q(I,K)
      Q(I,K)=0.
      MJ=I+1
      X(I)=0.
C     NEXT 5 STATEMENTS  SEARCH  IN  DEPLETED  ROW  FOR  NEW
C     MAXIMUM
      DO 320  J=MJ,N
      IF (X(I)-ABS(Q(I,J))) 300,300,320
  300 X(I)=ABS(Q(I,J))
```

```
      IH(I)=J
  320 CONTINUE
      Q(I,K)=TEMP
  350 CONTINUE
      X(IP)=0.
      X(JP)=0.
C  NEXT 30 STATEMENTS FOR CHANGING THE OTHER ELEMENTS OF Q
      DO 530 I=1,N
      IF (I-IP) 370,530,420
  370 TEMP=Q(I,IP)
      Q(I,IP)=COSN*TEMP+SINE*Q(I,JP)
      IF (X(I)-ABS(Q(I,IP))) 380,390,390
  380 X(I)=ABS(Q(I,IP))
      IH(I)=IP
  390 Q(I,JP)=-SINE*TEMP+COSN*Q(I,JP)
      IF (X(I)-ABS(Q(I,JP))) 400,530,530
  400 X(I)=ABS(Q(I,JP))
      IH(I)=JP
      GO TO 530
  420 IF (I-JP) 430,530,480
  430 TEMP=Q(IP,I)
      Q(IP,I)=COSN*TEMP+SINE*Q(I,JP)
      IF (X(IP)-ABS(Q(IP,I))) 440,450,450
  440 X(IP)=ABS(Q(IP,I))
      IH(IP)=I
  450 Q(I,JP)=-SINE*TEMP+COSN*Q(I,JP)
      IF (X(I)-ABS(Q(I,JP))) 400,530,530
  480 TEMP=Q(IP,I)
      Q(IP,I)=COSN*TEMP+SINE*Q(JP,I)
      IF(X(IP)-ABS(Q(IP,I))) 490,500,500
  490 X(IP)=ABS(Q(IP,I))
      IH(IP)=I
  500 Q(JP,I)=-SINE*TEMP+COSN*Q(JP,I)
      IF (X(JP)-ABS(Q(JP,I))) 510,530,530
  510 X(JP)=ABS(Q(JP,I))
```

```
      IH(JP)=I
  530 CONTINUE
C     NEXT 6 STATEMENTS TEST FOR COMPUTATION OF E1GENVECTORS
      IF (JVEC) 540,40,540
  540 DO 550 I=1,N
      TEMP=V(I,IP)
      V(I,IP)= COSN*TEMP+SINE*V(I,JP)
  550 V(I,JP)=-SINE*TEMP+COSN*V(I,JP)
      GO TO 40
 1000 AAM=FLOAT(M)
      WRITE (58,13) EPSI,AAM
      RETURN
      END
```

```
      PROGRAM CU (INPUT,OUTPUT,TAPE5=INPUT,TAPE58=OUTPUT)
C     THIS PROGRAM ANALYSES EPR DATA WITH NUCLEAR HYPERFINE
C     LINES WITH ELECTRON SPIN S=1/2 AND NUCLEAR SPIN I=3/2
C     FOR SIGLE CRYSTAL/CU2+. IT FITS BOTH G-SQUARE AND
C     A-SQUARE TENSOR ELEMENTS (12 PARAMETERS) - SECOND
C     ORDER PERTURBATION.
C     M  =NO. OF PARAMETERS
C     L4 =NO. OF ITERATIONS ALLOWED
C     Q1 =MIN. VALUE OF SUM OF SQUARES FOR FITS (CHI-SQUARE
C     TOLERANCE)
C     Z(I)=MAGNETIC FIELD VALUES FOR FITS
C     B  =PARAMETER MATRIX
C     N  =NO. OF  DATA POINTS USED IN LEAST-SQARES FITTING
C     Q1 =N/10
C     Q2 =TOLERANCE ON GRAD(CHI**2) =APPROX .01
C     FM(I) = MEASURED VALUES
C     FC(I) = CALCULATED VALUES
C     ERR(I)= STANDARD DEVIATION ON FM(I) = SQRT(FM(I))
C      DIMENSIONS OF A,B  IN  EXAM  AND  MATINV  SUBROUTINES
C      SHOULD BE THE SAME AS THOSE OF B2,B1 RESPECTIVELY  IN
C      THE MAIN PROOGRAM AND IN CURFIT
C     ENTER TEETA IN DEGREES
C     DIMENSIONS OF Q,V IN JACOBI1 SHOULD  BE  THE  SAME  AS
C     THOSE OF B3,B2 RESPECTIVELY IN CURFIT
C     PARAMETERS=I.GT IS G**2-TENSOR(G**2ZZ,
C     G**2ZX,G**2XX,G**2ZY,G**2YY,G**2XY)
C     GGT(J,NUMBER) REPRESENTS G-SQUARE TENSOR.
C     II. (B(I),I=1,6)=AZZ,AZX,AXX,AZY,AYY,AXY
C     A=A-SQUARE TENSOR ABOVE
C     DELANG(I,J),J=1,2,3 ARE ANGLE CORRECTIONS FOR ZX,ZY,XY
C     PLANES AS DETERMINED BY "KRDBLT" FOR VARIOUS CASES.
C     NUMBER=INDEX THAT CHANGES WITH EACH NEW CASE IS  VALUE
C     SHOULD BE THAT OF THE FIRST CASE CONSIDERED.
C     NCASES=NO. OF LAST CASE CONSIDERED. ITS  VALUE  SHOULD
```

```
C      BE ENTERED.
C      N1(J1,NUMBER)=NO.OF LINES(FOR VARIOUS ORIENTATIONS)
C      FOR J1 HYPERFINE LINE OF CASE NO.=NUMBER
C      ZZ(J,K,L)=LINE POSITIONS,J=WHICH  ONE  OF  K=HYPERFINE
C      LINE OF CASE NO.=L
       DIMENSION Z(400),FM(400),FC(400),DF(400),ERR(400),
      1B(12),B1(12),B2(12,12),DC(5000),ABC(2),Y(4),HN(400),
      2G(8,12),GG(6,8),SMD(9),AAA(3,3),QQQ(3,3),AAV(3,3),
      3QQV(3,3),IBB(400,2),THETA(400),D1(12),D2(12,12),
      4HHN(3,8),AADD(3,8),FFACTR(3,8),TEETA(100,4,8),
      5ZZ(100,4,8),NN(8),N1(4,8),ACOSZ(400),ACOSX(400),
      6ACOSY(400),DELANG(8,3),AJ1(400),GGT(3,3),
      7GGTT(8,3,3),DELHH(400,8),DELH(400),A4(3)
       COMMON/DATA1/ABC,Y
       COMMON/DATA2/DC,ACOSZ,ACOSX,ACOSY,AJ1
       COMMON/DATA3/DELH
       EQUIVALENCE (Z,DC),(FM,DC(401)),(FC,DC(801)),
      1(DF,DC(1201)),(ERR,DC(1601)),(HN,DC(2001)),
      1(THETA,DC(2401)),(IBB,DC(2801)),(B,DC(4101)),
      2(B1,DC(4125)),(B2,DC(4137)),(N,DC(4301)),
      3(L4,DC(4302)),(Q1,DC(4303)),(Q2,DC(4304)),
      4(M,DC(4305)),(I,DC(4306)),(L,DC(4307)),
      4(BO,DC(4308)),(SMD,DC(4309)),
      5 (SSMD,DC(4320)),(D1,DC(4321)),(D2,DC(4333)),
      6 (NUMBER,DC(4100)),(GT,DC(4093))
        DATA(HHN(J,1),J=1,3)/9.5325,9.5400,9.5400/
        DATA(FFACTR(J,1),J=1,3)/2.6328243,2.636795,2.636795/
        DATA(AADD(J,1),J=1,3)/2500.,2500.,2500./
        DATA(G(1,J),J=1,3)/5.72122,4.80753,4.00318/
        DATA(G(1,J),J=7,12)/ 0.1352,0.000589,0.0586,
      1 -0.00114844,-0.05544440,-0.00339278/
        DATA(DELANG(1,J),J=1,3)/0.5,2.4,0.0/
        DATA(GGTT(1,1,J),J=1,3)/0.451027,0.200998,0.869583/
        DATA(GGTT(1,2,J),J=1,3)/-0.648625,0.743082,0.164664/
        DATA(GGTT(1,3,J),J=1,3)/-0.613075,-0.638301,0.465522/
```

```
      DATA(N1(J,1),J=1,4)/4*45/
      DATA(DELHH(J,1),J=1,180)/180*5.0/
      DATA(ZZ(J,1,1),J=1,15)/
     1 200.5,202.5,205.5,208.0,211.0,
     2 214.0,220.0,227.0,234.0,240.5,
     3 248.5,255.0,261.5,268.0,282.5/
      DATA(ZZ(J,2,1),J=1,15)/
     1 227.5,229.5,232.0,234.0,236.5,
     2 239.0,243.0,249.0,254.5,257.0,
     3 263.0,269.0,275.0,281.0,282.0/
      DATA(ZZ(J,3,1),J=1,15)/
     1 253.5,255.0,257.0,258.5,260.5,
     2 262.0,265.5,269.5,273.0,276.0,
     3 280.0,282.5,286.5,291.0,290.0/
      DATA(ZZ(J,4,1),J=1,15)/
     1 278.5,279.5,281.0,282.0,283.0,
     2 283.5,285.0,287.5,289.5,290.0,
     3 293.0,293.0,293.5,291.0,290.0/
      DATA(TEETA(J,1,1),J=1,15)/
     1 354.,356.,358.,360., 2., 4., 8., 12.,16.,20.,
     2  24., 28., 32., 36., 40./
      DATA(ZZ(J,1,1),J=16,30)/
     1 213.5,207.0,199.0,185.5,172.0,
     2 159.0,145.5,133.5,118.5,111.5,
     3  96.5, 88.0, 82.5, 79.0, 76.5/
      DATA(ZZ(J,2,1),J=16,30)/
     1  238.5,232.5,226.0,214.5,203.0,
     2 190.5,181.5,169.5,158.5,149.0,
     3 135.0,127.0,124.5,120.0,117.5/
      DATA(ZZ(J,3,1),J=16,30)/
     1 262.0,257.5,252.5,242.5,233.0,
     2 223.0,213.5,203.5,197.0,187.5,
     3 173.0,168.5,165.0,161.5,160.5/
      DATA(ZZ(J,4,1),J=16,30)/
     1 284.0,281.0,278.0,271.5,262.5,
```

```
     2 254.5,246.5,238.5,231.0,224.5,
     3 214.0,208.0,204.5,201.5,198.0/
       DATA(TEETA(J,1,1),J=16,30)/
     1 -358.,-360.,-2.,-6.,-10.,-14.,-18.,-22.,-26.,-30.,
     2 -38.,-42.,-46.,-50.,-54./
       DATA(ZZ(J,1,1),J=31,45)/
     1 110.5,113.5,115.0,117.5,124.5,
     2 134.5,144.5,155.5,167.0,178.5,
     3 190.5,203.0,215.0,227.5,239.5/
       DATA(ZZ(J,2,1),J=31,45)/
     1 149.5,152.0,153.5,156.0,161.5,
     2 170.5,179.5,189.0,199.0,208.0,
     3 218.5,228.5,240.0,254.0,262.5/
       DATA(ZZ(J,3,1),J=31,45)/
     1 187.0,189.0,191.5,192.0,198.0,
     2 205.5,213.0,221.5,229.0,238.0,
     3 246.5,255.0,263.0,272.0,278.0/
       DATA(ZZ(J,4,1),J=31,45)/
     1 224.5,226.5,228.0,228.5,233.5,
     2 240.0,246.5,253.5,260.0,265.5,
     3 272.5,280.5,282.5,291.5,292.5/
       DATA(TEETA(J,1,1),J=31,45)/
     1 9267.,9269.,9270.,9271.,9275.,9279.,9283.,9287.,
     2 9291.,9295.,9299.,9303.,9307.,9311.,9315./
   188 FORMAT(1H1)
     8 FORMAT(1X,4HQ1 = ,E13.5,5X,4HQ2 = ,E13.5)
   137 FORMAT (3X,I2,5X,E16.6/)
   136 FORMAT(10X,19H INITIAL
      1PARAMETERS//3X,1HJ,10X,4HB(J)//)
   135 FORMAT(1X,11H PARAMETERS
      1//3X,1HJ,10X,4HB(J),27X,6HERRORS//)
     9 FORMAT(2X,4H HN= ,F9.4)
   140 FORMAT(3X,I2,5X,E16.6,15X,E16.6/)
   138 FORMAT(5X,14H CASE NUMBER =,I2//)
   141 FORMAT(10X,6H SMD =,E13.5//)
```

```
 235 FORMAT (15X,5(E13.5,8X)/)
 236 FORMAT(15X,3(E13.5,8X)///)
7237 FORMAT(15X,*DIAGONAL ELEMENTS OF G-SQUARE TENSOR
    1ARE=*,///)
 237 FORMAT(15X,*DIAGONAL ELEMENTS OF A-SQUARE TENSOR
    1ARE=*,///)
 238 FORMAT(15X,*"G" DIR. COS.(ROWS) ACC. TO E.VALS. ABOVE=
    1*,///)
7238 FORMAT(15X,*"A" DIR. COS.(ROWS) ACC. TO E.VALS. ABOVE=
    1*,///)
     PI2=2.*3.1415926
     RD=PI2/360.
     NZERO=1
     NUMBER=NZERO
     NCASES=1
     M=12
     L4=7
     Q1=1.E-8
     Q2=1.E-20
     MM=M
     WRITE(58,188)
   1 CONTINUE
      N11=N1(1,NUMBER)
      DO 1188 J=1,8
      DO 1188 J1=1,N11
1188 TEETA(J1,J,NUMBER)=TEETA(J1,1,NUMBER)
      DO 300 IA=1,3
      DO 300 JA=1,3
300   GGT(IA,JA)=GGTT(NUMBER,IA,JA)
     WRITE(58,121)
     DO 122 IA=1,3
 122 WRITE(58,123) (GGT(IA,JA),JA=1,3)
 121 FORMAT(5X,*ELEMENTS OF INITIAL GGT MATRIX AS THE
    1MATRIX OF DIR. COS-INES OF G-SQUARE TENSOR ARE=*,//)
 123 FORMAT(5X,3(F10.6,2X),/)
```

```
      CALL EULER(GGT,THITA,PHI,PSI)
      B(4)=THITA
      B(5)=PHI
      B(6)=PSI
      LINE=0
     DO 150 J1=1,8
     NN1=N1(J1,NUMBER)
     DO 150 I1=1,NN1
     LINE=LINE+1
     AJ1(LINE)=J1
     THETA(LINE)=TEETA(I1,J1,NUMBER)
     IF(THETA(LINE).GT.8000.) GO TO 155
     IF(THETA(LINE).LT.0.) GO TO 160
     TH=THETA(LINE)*RD+DELANG(NUMBER,1)*RD
     ACOSZ(LINE)=COS(TH)
     ACOSX(LINE)=SIN(TH)
     ACOSY(LINE)=0.
     HN(LINE)=HHN(1,NUMBER)
     Z(LINE)=(ZZ(I1,J1,NUMBER)
    1*FFACTR(1,NUMBER)+AADD(1,NUMBER))
     IF(ZZ(I1,J1,NUMBER).EQ.0.) Z(LINE)=0.
9160 FORMAT(5X,*ACOSZ ETC=*,3E12.5)
     GO TO 165
 160 TH=-THETA(LINE)*RD + DELANG(NUMBER,2)*RD
     ACOSZ(LINE)=COS(TH)
     ACOSY(LINE)=SIN(TH)
     ACOSX(LINE)=0.
     HN(LINE)=HHN(2,NUMBER)
     Z(LINE)=(ZZ(I1,J1,NUMBER)
    1*FFACTR(2,NUMBER)+AADD(2,NUMBER))
     IF(ZZ(I1,J1,NUMBER).EQ.0.) Z(LINE)=0.
     GO TO 165
 155 TH=THETA(LINE)*RD+DELANG(NUMBER,3)*RD
     ACOSZ(LINE)=0.
     ACOSX(LINE)=COS(TH)
```

```
      ACOSY(LINE)=SIN(TH)
      HN(LINE)=HHN(3,NUMBER)
      Z(LINE)=(ZZ(I1,J1,NUMBER)*
     1FFACTR(3,NUMBER)+AADD(3,NUMBER))
      IF(ZZ(I1,J1,NUMBER).EQ.0.) Z(LINE)=0.
  165 CONTINUE
  150 CONTINUE
  199 CONTINUE
      NN(NUMBER)=LINE
      N=NN(NUMBER)
      N9=N
      DO 210 LL=1,MM
      IF (LL.GT.3.AND.LL.LT.7) GO TO 210
      B(LL)=G(NUMBER,LL)
  210 CONTINUE
      WRITE(58,138) NUMBER
      WRITE(58,136)
      WRITE(58,137) (J,B(J),J=1,M)
      WRITE(58,6659)
      WRITE(58,6657) (Z(J),J=1,N)
      WRITE(58,6660)
      WRITE(58,6657) (HN(J),J=1,N)
 6660 FORMAT(5X,*FREQUENCY-KLYSTRON ARE=*,/)
 6659 FORMAT(5X,*MAG. FIELD VALUES ARE=*,/)
 6657 FORMAT(5X,8(E12.5,2X))
      DO 201 II=1,N9
      DELH(II)=DELHH(II,NUMBER)
  201 FM(II) = HN(II)
      CALL CURFIT
      SMD(NUMBER) = SSMD
      WRITE(58,188)
      WRITE(58,135)
      DO 220 LL=1,M
  220 GG(LL,NUMBER) = B(LL)
      WRITE(58,140)(J,B(J),B1(J),J=1,M)
```

```
      WRITE(58,188)
    3 CONTINUE
      SSS=0.
      SSS1=0.
      DO 555 ID=1,N
      SSS=DF(ID)**2
      SSS1=SSS1+SSS
      WRITE(58,656) ID,SSS
  555 CONTINUE
      WRITE(58,6656) SSS1
 6656 FORMAT(/,10X,*CHI-SQUARE=*,E13.5,/)
  656 FORMAT(10X,*LINE NUMBER = *,I3,5X,*SMD = *,E13.5)
      WRITE (58,7237)
      WRITE(58,236) (B(J1),J1 = 1,3)
      WRITE (58,238)
      SB4L=SIN(B(4))
      CB4L=COS(B(4))
      SB5L=SIN(B(5))
      CB5L=COS(B(5))
      SB6L=SIN(B(6))
      CB6L=COS(B(6))
      GGT(1,1)=CB4L
      GGT(1,2)=SB4L*SB5L
      GGT(1,3)=-SB4L*CB5L
      GGT(2,1)=SB6L*SB4L
      GGT(2,2)=CB6L*CB5L-CB4L*SB5L*SB6L
      GGT(2,3)=CB6L*SB5L+CB4L*CB5L*SB6L
      GGT(3,1)=CB6L*SB4L
      GGT(3,2)=-SB6L*CB5L-CB4L*SB5L*CB6L
      GGT(3,3)=-SB6L*SB5L+CB4L*CB5L*CB6L
      DO 25 J1 = 1,3
      WRITE (58,236) (GGT(J1,J2),J2 = 1,3)
   25 CONTINUE
      DO 245 J=1,3
  245 A4(J)=SQRT(B(J))
```

```
      WRITE (58,246)
      WRITE(58,236)(A4(J),J=1,3)
  246 FORMAT(5X,*PRINCIPAL VALUES OF G-TENSOR ARE=*,/)
      AAA(1,1)=B(7)
      AAA(1,2)=B(8)
      AAA(2,2)=B(9)
      AAA(1,3)=B(10)
      AAA(3,3)=B(11)
      AAA(2,3)=B(12)
      DO 720 J1=1,2
      J4=J1+1
      DO 720 J2=J4,3
      AAA(J2,J1)=AAA(J1,J2)
  720 CONTINUE
      CALL JACOBI3(3,AAA,1,NR,AAV)
      WRITE (58,237)
      WRITE (58,236) (AAA(J1,J1),J1=1,3)
      WRITE (58,7238)
      DO 725 J1=1,3
      WRITE (58,236) (AAV(J2,J1),J2=1,3)
  725 CONTINUE
      DO 7245 J=1,3
       IF (AAA(J,J) .LT. 1.0E-4) AAA(J,J)=0
 7245 A4(J)=SQRT(AAA(J,J))
      WRITE (58,7246)
      WRITE (58,236) (A4(J),J=1,3)
 7246 FORMAT(5X,*PRINCIPAL VALUES OF A-TENSOR ARE=*,/)
      NUMBER=NUMBER+1
      IF(NUMBER-NCASES) 1,1,2
    2 CONTINUE
      DO 230 LL=NZERO,NCASES
      WRITE(58,138) LL
      WRITE(58,141) SMD(LL)
  230 WRITE (58,235) (GG(LM,LL),LM=1,MM)
      STOP
```

```
      END

      SUBROUTINE CURFIT
C     EXAM  HANDLES ALL  MATRICES  OF  DIMENSIONS  UPTO  THE
C     DIMS.MM OF A,B,C THAT IS M IS LESS THAN OR EQUAL TO MM
C     EQUIVALENCE OF GRAD BEGINS AT DIMENSION OF B AFTER THE
C     EQUIV. OF B
      DIMENSION Z(400),FM(400),FC(400),DF(400),ERR(400),
     1B(12),B1(12),B2(12,12),DC(5000),ABC(2),Y(4),X(400),
     2GRAD(12),D1(12),D2(12,12),B3(12,12),SMD(9),HN(400),
     2ACOSZ(400),ACOSX(400),ACOSY(400)
      DIMENSION IBB(400,2),THETA(400),GT(6)
      DIMENSION AJ1(400),GGTL(8,3),GGTM(8,3),GGTN(8,3)
      COMMON/DATA1/ABC,Y
      COMMON/DATA2/DC,ACOSZ,ACOSX,ACOSY,AJ1
      EQUIVALENCE (Z,DC),(FM,DC(401)),(FC,DC(801)),
     1(DF,DC(1201)),(ERR,DC(1601)),(HN,DC(2001)),
     1 (THETA,DC(2401)),(IBB,DC(2801)),(B,DC(4101)),
     1 (B1,DC(4125)),(B2,DC(4137)),(N,DC(4301)),
     3 (L4,DC(4302)),(Q1,DC(4303)),(Q2,DC(4304)),
     3 (M,DC(4305)),(I,DC(4306)),(L,DC(4307)),
     4 (BO,DC(4308)),(SMD,DC(4309)),(SSMD,DC(4320)),
     4 (D1,DC(4321)),(D2,DC(4333)),(GRAD,DC(4113)),
     6 (NUMBER,DC(4100)),(GT,DC(4093))
C       DATA ABC/2HNO,3HYES/
C      DATA Y/1H ,1HC,1H*,1HM/
      ABC(1)="NO"
      ABC(2)="YES"
      L1 = 0
      SA = 0.0
      MM=M
      I6=I
      NN=N
      DO 1000 J=1,MM
      B1(J)=0.0
```

```
      DO 1000 K=1,MM
1000 B2(J,K)=0.0
      DO 100 I6 = 1, NN
      L=1
      I=I6
      CALL FUNC(2)
      X(I6)=ERR(I6)**2
901   FORMAT(5X,10H FUNC2,210  )
      DF(I6) =FM(I6) - FC(I6)
      DO 101 J=1,MM
      B1(J)=B1(J)-(2.0*DF(I6)*D1(J))/X(I6)
      DO 101 K=1,MM
 101 B2(J,K)=B2(J,K)-(2.0*(DF(I6)*D2(J,K)
     1-D1(J)*D1(K)))/X(I6)
 100 SA = SA + DF(I6)**2/X(I6)
      GMOD=0.0
      DO 102 J=1,M
 102 GMOD=GMOD+B1(J)**2
      WRITE(58,243)SA,GMOD
 243 FORMAT (1X,26H*INITIAL VALUE SUM OF
     1SQ.=E13.5,20X,17H*SQ MOD OF GRAD =E13.5)
      WRITE(58,1751)
1751 FORMAT(14H0 DERIVATIVES-)
      WRITE(58,240)(B1(J),J=1,M)
 240 FORMAT (15X,5(E13.5,8X)/)
      IF (SA - Q1) 110, 110, 200
 110 LE = 1
      GO TO 600
 200 S = 0.0
      GMOD = 0.0
      BMOD = 0.0
      PROD = 0.0
      DO 210 K = 1, MM
 210 B2(J,K) = 0.0
      WRITE(58,902)
```

```
      DO 220 I6 = 1, NN
      L=1
      I=I6
      CALL FUNC(2)
      X(I6)=ERR(I6)**2
902   FORMAT(5X,10H FUNC2,210  )
      DF(I6) = FM(I6) - FC(I6)
      DO 220 J = 1, MM
      B1(J) = B1(J) - (2.0*DF(I6)*D1(J))/X(I6)
      DO 220 K = 1, MM
 220  B2(J,K) = B2(J,K) - (2.0*(DF(I6)*D2(J,K)
     -D1(J)*D1(K)))/X(I6)
       DO 230 J = 1, MM
 230  GRAD(J) = B1(J)
      L1 = L1 + 1
      CALL EXAM (B2,B1,M,LF)
      WRITE(58,903)
903   FORMAT(5X,9H EXAM,230  )
      WRITE (58,914) LF
 914  FORMAT (5X,I3)
      IF (LF)  250, 250, 305
 250  DO 231 II=1,M
      DO 231 JJ=1,M
 231  B3(II,JJ)=B2(II,JJ)
      WRITE (58,904)
      CALL JACOBI4(M,B3,4,NR,B2)
904   FORMAT(5X,12H JACOBI1,231  )
      WRITE(58,904)
      DO 235 I6=1,MM
 235  B1(I6)=B3(I6,I6)
      A2=ABC(2)
      DO 260 J = 1, MM
 260  D1(J) = 0.0
      DO 270 J = 1, MM
      DO 270 K = 1, MM
```

```
270 D1(K) = D1(K) + B2(J,K) *GRAD(J)
    DO 275 J = 1, MM
    IF (B1(J))  280, 290, 285
280 B1(J) = - B1(J)
285 D1(J) = D1(J)/B1(J)
    GO TO 275
290 D1(J) = 0.0
275 CONTINUE
    DO 295 J = 1, MM
295 B1(J) = 0.0
    DO 300 J = 1, MM
    DO 300 K = 1, MM
300 B1(J) = B1(J) + B2(J,K)*D1(K)
305 DO 310 J=1,MM
    GMOD = GMOD + GRAD(J)**2
    BMOD = BMOD + B1(J)**2
310 PROD = PROD + GRAD(J)*B1(J)
    IF (GMOD - Q2)  315, 315, 320
315 LE = 2
    WRITE(58,1761) GMOD
1761 FORMAT(5X,7H GMOD =,E13.5//)
    GO TO 600
320 C=PROD/SQRT(BMOD*GMOD)
    IF (C) 335, 335, 400
335 LE = 4
    GO TO 600
400 LD = 0
    L3 = 0
    DO 410 J = 1, MM
410 GRAD(J) = B(J) - B1(J)
450 DO 420 I6 = 1, NN
    L=2
    I=I6
    CALL FUNC (1)
    X(I6)=ERR(I6)**2
```

```
905  FORMAT(5X,10H FUNC1,450  )
     DF(I6) = FM(I6) - FC(I6)
 420 S = S + DF(I6)**2/X(I6)
     WRITE(58,905)
     IF (SA - S) 435, 500, 500
 435 LD = LD + 1
 430 DO440 J = 1, MM
     B1(J) = B1(J)/2.0
906  FORMAT(5X,16H BINARY CHOP,430  )
 440 GRAD(J) = B(J) - B1(J)
     WRITE(58,906)
     S = 0.0
     L3 = L3 + 1
     IF(L3-5)450,460,460
 460 LE = 5
     GO TO 600
 500 IF (LD) 505, 505, 506
 506 LD = 0
     GO TO 430
 505 DO 510 J = 1, MM
 510 B(J) = GRAD(J)
     SA = S
     IF (SA - Q1) 507, 507, 530
 507 LE = 1
     GO TO 600
 530 IF (L4) 200, 200, 900
 900 WRITE(58,920)L1,A2,L3,S,GMOD,(B(J),J=1,M)
 920 FORMAT(//,15H ITERATION NO.=I5,10X,43H
    1TRANSFORMATION MADE TO PRINCIPAL AXES = A4,10X,   18H
    2BINARY CHOP USED=I3,6H TIMES/1X,27H WEIGHTED SUM OF
    3SQUARES = E14.7,25X,32H   SQUARE MODULUS OF GRADIENT =
    4E14.7/20H   PARAMETERS B(J) -/(6E17.8)/)
IF (L1 - L4) 200, 910, 910
910 LE = 6
     GO TO 600
```

```
  600 DO 710 J=1,MM
      B1(J) = 0.0
      DO 710 K=1,MM
  710 B2(J,K) = 0.0
      L=1
      WRITE(58,907)
  907 FORMAT(5X,* FUNC(2),720 *)
      DO 720 I6 = 1, NN
      I=I6
      CALL FUNC(2)
      X(I6)=ERR(I6)**2
      DF(I6) = FM(I6) - FC(I6)
      DO 720 J = 1, MM
      B1(J) = B1(J) - (2.0*DF(I6)*D1(J))/X(I6)
      DO 720 K = 1, MM
  720 B2(J,K) = B2(J,K) - ((DF(I6)*D2(J,K)
     1-D1(J)*D1(K)))/X(I6)
      WRITE (58,3029)
 3029 FORMAT(* I AM LOST IN MANTINV*)
      CALL MATINV(B2,M,B1,1,DETERM)
      WRITE (58,3029)
      DO 730 J=1,MM
      IF (B2(J,J)) 2001,2001,2002
2001  B1(J) = -SQRT(-B2(J,J))
      GO TO 730
2002  B1(J)= SQRT(B2(J,J))
  730 CONTINUE
      DO 740 J=1,MM
      DO 740 K=1,MM
  740 B2(J,K)=B2(J,K)/(B1(J)*B1(K))
      WRITE(58,551)LE,SA
  551 FORMAT(//,13H EXIT NUMBER=I3,20X,25H WEIGHTED SUM OF
     1SQUARES=E15.8//)
      SSMD = SA
9999  CONTINUE
```

```
      RETURN
      END

      SUBROUTINE FUNC(LX)
C     SUBROUTINE FUNC
      DIMENSION DC(5000),B(12,2),D1(12),D2(12,12),FC(400),
     1 Z(400),S(4,4),SIGN(400),HN(400),ST(4,4,16),FM(400),
     1 DF(400),DELH(400),ERR(400),B1(12),B2(12,12), SMD(9),
     2 ACOSZ(400),ACOSX(400),ACOSY(400),IBB(400,2),
     2 THETA(400),DD(16),GT(6),AJ1(400),AL(400),AM(400),
     4 AN(400),GGT(3,3),C1(12),AZ(6),AX(6),AY(6),GB(6),
     4F2(6),C2(12),C3(12),CK(12),F4(12),CC(12),AK2(6),BB(6)
      COMMON/DATA2/DC,ACOSZ,ACOSX,ACOSY,AJ1
      COMMON/DATA3/DELH
      EQUIVALENCE (Z,DC),(FM,DC(401)),(FC,DC(801)),
     1 (DF,DC(1201)),(ERR,DC(1601)),(HN,DC(2001)),
     1 (THETA,DC(2401)),(IBB,DC(2801)),(B,DC(4101)),
     2 (B1,DC(4125)),(B2,DC(4137)),(N,DC(4301)),
     3 (L4,DC(4302)),(Q1,DC(4303)),(Q2,DC(4304)),
     3 (M,DC(4305)),(I,DC(4306)),(L,DC(4307)),
     4 (BO,DC(4308)),(SMD,DC(4309)),(SSMD,DC(4320)),
     5 (D1,DC(4321)),(D2,DC(4333)),
     6 (NUMBER,DC(4100)),(GT,DC(4093))
      IF(Z(I).EQ.0.) GO TO 135
      BETA=92.732/66252.
      BETAN=.00054464*BETA
      RD=3.1415926/180.
      FACTOR=92.732/66252.
      SB4L=SIN(B(4,L))
      CB4L=COS(B(4,L))
      SB5L=SIN(B(5,L))
      CB5L=COS(B(5,L))
      SB6L=SIN(B(6,L))
      CB6L=COS(B(6,L))
      GGT(1,1)=CB4L
```

```
      GGT(1,2)=SB4L*SB5L
      GGT(1,3)=-SB4L*CB5L
      GGT(2,1)=SB6L*SB4L
      GGT(2,2)=CB6L*CB5L-CB4L*SB5L*SB6L
      GGT(2,3)=CB6L*SB5L+CB4L*CB5L*SB6L
      GGT(3,1)=CB6L*SB4L
      GGT(3,2)=-SB6L*CB5L-CB4L*SB5L*CB6L
      GGT(3,3)=-SB6L*SB5L+CB4L*CB5L*CB6L
      IF (I.GT.1) GO TO 119
      WRITE(58,118)
      DO 117 IA=1,3
  117 WRITE(58,116) (GGT(IA,IB),IB=1,3)
  116 FORMAT(5X,3(F10.6,3X),/)
  118 FORMAT(5X,*ELEMENTS OF COMPUTED GGT MATRIX FROM EULER
     1ANGLES ARE=*,//)
  119 CONTINUE
      AL(I)=ACOSZ(I)*GGT(1,1)+ACOSX(I)*GGT(1,2)+
     1 ACOSY(I)*GGT(1,3)
      AM(I)=ACOSZ(I)*GGT(2,1)+ACOSX(I)*GGT(2,2)+
     2 ACOSY(I)*GGT(2,3)
      AN(I)=ACOSZ(I)*GGT(3,1)+ACOSX(I)*GGT(3,2)+
     3 ACOSY(I)*GGT(3,3)
      FCI=B(1,L)*AL(I)**2+B(2,L)*AM(I)**2+B(3,L)*AN(I)**2
      ENELSP=Z(I)*BETA*SQRT(FCI)
      BB(1)=B(1,L)*AL(I)**2
      BB(3)=B(2,L)*AM(I)**2
      BB(5)=B(3,L)*AN(I)**2
      BB(2)=2.*SQRT(B(1,L)*B(2,L))*AL(I)*AM(I)
      BB(4)=2.*SQRT(B(1,L)*B(3,L))*AL(I)*AN(I)
      BB(6)=2.*SQRT(B(2,L)*B(3,L))*AM(I)*AN(I)
      AEFF2=B(7,L)*BB(1)+B(9,L)*BB(3)+B(11,L)*BB(5)+
     1 B(8,L)*BB(2)+B(10,L)*BB(4)+B(12,L)*BB(6)
      AMI=2.5-AJ1(I)
      IF(AEFF2.LT.(0.)) GO TO 109
      AEFF=SQRT(AEFF2/FCI)
```

```
      HYPFEN=AEFF*AMI
      CC(7)=B(7,L)**2+B(8,L)**2+B(10,L)**2
      CC(8)=B(7,L)*B(8,L)+B(8,L)*B(9,L)+B(10,L)*B(12,L)
      CC(9)=B(8,L)**2+B(9,L)**2+B(12,L)**2
      CC(10)=B(7,L)*B(10,L)+B(8,L)*B(12,L)+B(10,L)*B(11,L)
      CC(11)=B(10,L)**2+B(12,L)**2+B(11,L)**2
      CC(12)=B(8,L)*B(10,L)+B(9,L)*B(12,L)+B(11,L)*B(12,L)
      CKK=CC(7)*BB(1)+CC(9)*BB(3)+CC(11)*BB(5)+CC(8)*BB(2)+
     1    CC(10)*BB(4)+CC(12)*BB(6)
      AKK=SQRT(CKK/AEFF2)
      AI=3.5
      AI1=AI*(AI+1.)
      DELE3=(0.5*(B(7,L)+B(9,L)+B(11,L))*(AI1-AMI**2)-
     1 AKK**2*(AI1-3.*AMI**2)/2.-HYPFEN**2)/(2.*ENELSP)
      FC(I)=ENELSP+HYPFEN+DELE3
      ERR(I)=SQRT(FCI)*DELH(I)*FACTOR
      ERR(I)=1.
      GO TO 136
  135 CONTINUE
      FC(I)=HN(I)
      ERR(I)=1.
  136 CONTINUE
      IF(LX-1)110,110,120
  120 CONTINUE
      DO  235 IZ = 1,12
      D1(IZ) = 0.0
      DO  235 JZ = 1,12
  235 D2(IZ,JZ) =0.0
      IF(Z(I).EQ.0.) GO TO 110
      DDD=.5*AMI/(FCI*AEFF)
      C2(7)=DDD*BB(1)
      C2(8)=DDD*BB(2)
      C2(9)=DDD*BB(3)
      C2(10)=DDD*BB(4)
      C2(11)=DDD*BB(5)
```

```
      C2(12)=DDD*BB(6)
      BETAB=BETA*Z(I)
      GZ=SQRT(B(1,L))
      GX=SQRT(B(2,L))
      GY=SQRT(B(3,L))
      AZZ=SQRT(BB(1))
      AXX=SQRT(BB(3))
      AYY=SQRT(BB(5))
      AZ(1)=0.5*AL(I)/GZ
      AZ(2)=AZ(3)=0.
      AX(2)=0.5*AM(I)/GX
      AX(1)=AX(3)=0.
      AY(3)=0.5*AN(I)/GY
      AY(1)=AY(2)=0.
      ALL=ACOSX(I)
      AMM=ACOSY(I)
      ANN=ACOSZ(I)
      AZ(4)=GZ*(ALL*CB4L*SB5L-AMM*CB4L*CB5L-ANN*SB4L)
      AZ(5)=GZ*(ALL*SB4L*CB5L+AMM*SB4L*SB5L)
      AZ(6)=0.
      AX(4)=
     1GX*(ALL*SB4L*SB5L*SB6L-AMM*SB4L*CB5L*SB6L+ANN*CB4L*SBL)
      AX(5)=
     1GX*(ALL*(-CB6L*SB5L-CB4L*CB5L*SB6L)+AMM*(CB6L*CB5L-
     1       CB4L*SB5L*SB6L))
      AX(6)=
     1GX*(ALL*(-SB6L*CB5L-CB4L*SB5L*CB6L)+AMM*(-SB6L*SB5L+
     1       CB4L*CB5L*CB6L)+ANN*CB6L*SB4L)
      AY(4)=
     1GY*(ALL*SB4L*SB5L*CB6L-AMM*SB4L*CB5L*CB6L+ANN*CB6L*CB5L)
      AY(5)=
     1GY*(ALL*(SB6L*SB5L-CB4L*CB5L*CB6L)+AMM*(-SB6L*CB5L-
     1       CB4L*SB5L*CB6L))
      AY(6)=
     1GY*(ALL*(-CB6L*CB5L+CB4L*SB5L*SB6L)+AMM*(-CB6L*SB5L-
```

```
     1      CB4L*CB5L*SB6L)-ANN*SB6L*SB4L)
            DO 910 IA=1,6
            GB(IA)=(AZZ*AZ(IA)+AXX*AX(IA)+AYY*AY(IA))*BETAB/ENELSP
            IA1=IA+6
            C1(IA1)=0.
  910       C1(IA)=BETAB*GB(IA)
C           C1(IA) ARE DERIVATIVES OF ENELSP
            AXX=SQRT(BB(3))
            AYY=SQRT(BB(5))
            AZZ=SQRT(BB(1))
            F2(1)=2.*AZ(1)*(AZZ*B(7,L)+AXX*B(8,L)+AYY*B(10,L))
            F2(2)=2.*AX(2)*(AZZ*B(8,L)+AXX*B(9,L)+AYY*B(12,L))
            F2(3)=2.*AY(3)*(AZZ*B(10,L)+AXX*B(12,L)+AYY*B(11,L))
            DO 915 IA=4,6
            F2(IA)=2.*(AXX*AX(IA)*B(9,L)+AYY*AY(IA)*B(11,L)+
           1 AZZ*AZ(IA)*B(7,L)+(AXX*AY(IA)+AYY*AX(IA))*B(12,L)+
           2 (AXX*AZ(IA)+AZZ*AX(IA))*B(8,L)+(AYY*AZ(IA)+
           3 AZZ*AY(IA))*B(10,L))
  915       CONTINUE
            F4(1)=2.*AZ(1)*(AZZ*CC(7)+AXX*CC(8)+AYY*CC(10))
            F4(2)=2.*AX(2)*(AZZ*CC(8)+AXX*CC(9)+AYY*CC(12))
            F4(3)=2.*AY(3)*(AZZ*CC(10)+AXX*CC(12)+AYY*CC(11))
            DO 920 IA=4,6
            F4(IA)=2.*(AXX*AX(IA)*CC(9)+
           1AYY*AY(IA)*CC(11)+AZZ*AZ(IA)*CC(7)+
           1   (AXX*AY(IA)+AYY*AX(IA))*CC(12)+
           1(AXX*AZ(IA)+AZZ*AX(IA))*CC(8)+
           2    (AYY*AZ(IA)+AZZ*AY(IA))*CC(10))
  920       CONTINUE
            DO 925 IA=1,6
  925       C2(IA)=(-BETAB*HYPFEN*GB(IA)/ENELSP+
     1      (BETAB**2)*F2(IA)/(2.*(ENELSP**2)*HYPFEN))*AMI
C           C2(IA) ARE DERIVATIVES OF HYPFEN
            DO 927 IA=1,6
            IA1=IA+1
```

```
  927 C2(IA1)=(AMI**2)*BB(IA)/(0.5*FCI*HYPFEN)
      DO 930 IA=1,6
  930 AK2(IA)=((BETAB*AMI/(ENELSP*HYPFEN))**2)*(F4(IA)-
     1(2.*CCK/(ENELSP*HYPFEN))*(C1(IA)
     2*HYPFEN+ENELSP*C2(IA)))
      DO 935 IA=1,6
  935 C3(IA)=(ENELSP*(-0.5*(AI1-3.*(AMI**2))*
     1AK2(IA)-2.*HYPFEN*C2(IA))-
     1(0.5*(B(7,L)+B(9,L)+B(11,L))*(AI1-(AMI**2))-
     20.5*(AKK**2)*(AI1-3.*(AMI**2))-
     3HYPFEN**2)*C1(IA))/(2.*(ENELSP**2))
C     C3(IA) ARE DERIVATIVES OF DELE3
      F4(7)=2.*BB(1)*B(7,L)+BB(2)*B(8,L)+BB(4)*B(10,L)
      F4(8)=2.*(BB(1)+BB(3))*B(8,L)+BB(2)*(B(7,L)+B(9,L))+
     1 BB(4)*B(12,L)+BB(6)*B(10,L)
      F4(9)=2.*BB(3)*B(9,L)+BB(2)*B(8,L)+BB(6)*B(12,L)
      F4(10)=2.*(BB(1)+BB(5))*B(10,L)+BB(4)*(B(7,L)+
     1B(11,L))+BB(2)*B(12,L)+BB(6)*B(8,L)
      F4(11)=2.*BB(5)*B(11,L)+BB(4)*B(10,L)+BB(6)*B(12,L)
      F4(12)=2.*(BB(3)+BB(5))*B(12,L)+BB(6)*(B(9,L)+
     1B(11,L))+BB(2)*B(10,L)+BB(4)*B(8,L)
      DO 1237 IA=7,12
 1237 CK(IA)=-AKK*C2(IA)/(AEFF*AMI)+
     1F4(IA)/(2.*FCI*(AEFF**2)*AKK)
      DO 1236 IA=7,12
      AIA=0.
      IF (IA.EQ.7.OR.IA.EQ.9.OR.IA.EQ.11) AIA=1.
 1236 C3(IA)=(AKK*CK(IA)*(3.*AMI**2-AI1)+
     10.5*(AI1-AMI**2)*AIA-2.*HYPFEN*C2(IA))/(2.*ENELSP)
      DO 1235 IA=1,12
 1235 D1(IA)=C1(IA)+C2(IA)+C3(IA)
      GO TO 110
  109 WRITE(58,108) I
  108 FORMAT(5X,*NEG AEFF2 FOR I=*,I3)
      FC(I)=FM(I)
```

```
      DO 197 JJ=1,12
  197 D1(JJ)=0.
  110 CONTINUE
      RETURN
      END

      SUBROUTINE EULER(GGT,THETA,PHI,PSI)
C     SUBROUTINE EULER
C     THIS PROGRAMME CALCULATES THE EULER ANGLES THETA, PHI
C     AND PSI FROM THE DIRECTION COSINES OF G-SQUARE DIAGONAL
C     MATRIX.
      DIMENSION GGT(3,3),TPS(4,4,4),AMTRX(9),BMTRX(64,9),
     1 A(64),B(64),C(64),IA(64),IB(64),IC(64),ABSMT(9)

      SUBROUTINE EXAM(A,B,M,LF)
C     SUBROUTINE EXAM
      DIMENSION A(12,12),B(12),C(12)

      SUBROUTINE MATINV(A,N,B,M,DETERM)
C     SUBROUTINE MATINV
C     MATRIX INVERSION WITH ACCOMPANYING SOLUTION OF LINEAR
C     EQUATIONS
      DIMENSION IPIVOT(12),A(12,12),
     1 B(12,1),INDEX(12,2),PIVOT(12)
      EQUIVALENCE (IROW,JROW),(ICOLUM,JCOLUM),(AMAX,T,SWAP)

      SUBROUTINE JACOBI4(N,Q,JVEC,M,V)
C      SUBPROGRAM FOR DIAGONALIZATION OF MATRIX Q BY
C      SUCCESSIVE ROTATIONS
      DIMENSION Q(12,12),V(12,12),X(12),IH(12)

      SUBROUTINE JACOBI3(N,Q,JVEC,M,V)
C         SUBPROGRAM FOR DIAGONALIZATION OF MATRIX Q BY
C      SUCCESSIVE ROTATIONS
      DIMENSION Q(3,3),V(3,3),X(3),IH(3)
```